Resonance Ionization Mass Spectrometry of Calcium

Adrian Philip Land
Department of Physics and Astronomy, University of Glasgow.

Submitted for the Degree of Doctor of Philosophy, September 1990.

Acknowledgements

I would like to take this opportunity to give my thanks to some of the many people who have helped me in so many ways throughout this programme of research and in the preparation of this document.

To Ken, for keeping me on my toes.

To Mike T., for showing me the 'tweaks'.

To Paul, for user-friendly computer expertise.

To Ravi, for calculations and explanations.

To Chris, Bob J., Archie, Alistair, Ian and Bob M.,

for your friendship and good humour.

To Margaret, for turning sketches into pretty pictures.

To all the craftsmen of the Mechanical and Electronic Workshops,

for advice and technical support.

To my Family and Friends, for always being there.

To Kathy, my shining star, for love and friendship,

for making me smile.

Table of Contents

Summary

This thesis describes the design and development of a new Resonance Ionization Mass Spectrometer instrument at the Dept. of Physics and Astronomy, the University of Glasgow, and some of the early laser spectroscopy and mass spectrometry investigations carried out with the instrument.

The elemental trace analysis capability of the instrument has been measured to be better than 1ppm for both rubidium and calcium in complex matrices. Isotopic abundance ratios for calcium have been measured with an accuracy of $\pm 3\%$ and with a precision of $\pm 5\%$.

The laser ablation process has been investigated for a calcium metal sample for several ablation wavelengths. A good fit to data was obtained with a simple thermal process model. The laser ablation of calcium was observed to display a strong enhancement at a wavelength corresponding to a known two-photon resonant, one-photon ionization ("2+1") RIS scheme. The potential utility of this Resonant Laser Ablation process as an analytic technique is discussed.

The laser ionization spectroscopy of calcium has been investigated over the wavelength region 413nm to 437nm. Two series of "2+1" transitions were observed, both displaying a strong ion yield enhancement in the vicinity of an intermediate resonace. Single photon, bound-bound transitions from excited states were also observed. The populating mechanisms and relative populations for these excited states have been investigated. A further series of observed lines has been assigned to two-photon resonant transitions from excited metastable states to autoionization levels, lying above the first ionization potential. Several spectral features have not yet been identified, possible mechanisms are discussed.

A simple theoretical model for determining two-photon transition cross-sections is outlined. A population rate equation model has been developed to describe the dynamics of the resonance ionization process. These two theoretical models have been combined to generate theoretical ion yields for a "2+1" RIS scheme, a comparison with experimental data is presented.

Mass spectra for a calcium metal sample have been obtained using several 'competing' analytic techniques:

- Laser Ionization Mass Analysis (LIMA)
- Resonant Laser Ablation (RLA)
- Non-resonant post-ionization of laser ablated neutrals (SALI)
- Resonant post-ionization of laser ablated neutrals (RIMS)

Significant differences in the observed selectivities, and consequent sensitivities, are discussed with regard to the analytic utility of each technique.

The work on the laser spectroscopy and the mass spectrometry of calcium is solely that of the author.

Publications List

Investigation of the Effects of Gas Purification on the Background Laser Ionisation in Proportional Chambers.
S.L.T. Drysdale, A.P. Land, K.W.D. Ledingham, C. Raine, K.M. Smith, M.H.C. Smyth, D.T.Stewart, M. Towrie and C.M. Houston.
ALEPH 86-30 (distr. TPC-CAL) (1986).

Two- and three-photon ionisation transitions in caesium vapour.
C.M. Houston, S.L.T. Drysdale, R. Jennings, A.P. Land, K.W.D. Ledingham, R.P. Singhal, M.H.C. Smyth, D.T. Stewart and M. Towrie
Journal of Physics D: Applied Physics 21 (1988), S59-S62.

Molecular and Collisional Processes During Three Photon Ionisation Transitions in Caesium and Rubidium Vapours.
M.H.C. Smyth, S.L.T. Drysdale, R. Jennings, A.P. Land, K.W.D. Ledingham, R.P. Singhal, D.T. Stewart, M Towrie and C.M. Houston.
In *Resonance Ionisation Spectroscopy 1988*, Eds. T.B. Lucatorto and J.E. Parks
Inst. of Phys. Conf. Ser. No. 94, p. 73.

Application of Resonant Ionisation Mass Spectroscopy to Depth Profiling in III-V Semiconductor Devices.
C.J. McLean, J.H. Marsh, J.W. Cahill, S.L.T. Drysdale, R. Jennings, P.T. McCombes, A.P.Land, K.W.D. Ledingham, R.P. Singhal, M.H.C. Smyth, D.T. Stewart and M. Towrie.
In *Resonance Ionisation Spectroscopy 1988*, Eds. T.B. Lucatorto and J.E. Parks
Inst. of Phys. Conf. Ser. No. 94, p.193

Population Rate Equation Solution of a General Resonant Ionisation Scheme.
R.P. Singhal, A.P. Land, K.W.D. Ledingham and M.Towrie.
In *Resonance Ionisation Spectroscopy 1988*, Eds. T.B. Lucatorto and J.E. Parks
Inst. of Phys. Conf. Ser. No. 94, p. 69

The Glasgow Resonant Ionisation Mass Spectrometer.
M. Towrie, S.L.T. Drysdale, R. Jennings, A.P. Land, K.W.D. Ledingham, P.T. McCombes, R.P. Singhal, M.H.C. Smyth, D.T. Stewart, C.M. Houston and C.J. McLean.
In *Resonance Ionisation Spectroscopy 1988*, Eds. T.B. Lucatorto and J.E. Parks
Inst. of Phys. Conf. Ser. No. 94, p. 267

The Glasgow Resonant Ionisation Mass Spectrometer.
P.T. McCombes, S.L.T. Drysdale, R.Jennings, A.P.Land, K.W.D. Ledingham, R.P. Singhal, M.H.C. Smyth, D.T. Stewart, M.Towrie and C.J.McLean.
Accepted for publication in the Proceedings of the International Conference on Mass Spectroscopy, Bordeaux, France, August 1988.

Preliminary Results from the Glasgow Resonant Ionisation Mass Spectrometer.
R.Jennings, S.L.T. Drysdale, A.P. Land, K.W.D. Ledingham, P.T. McCombes, R.P. Singhal, M.H.C. Smyth, D.T. Stewart, M. Towrie, C.M. Houston and C.J. McLean.
Presented as a poster at the Adriatico Research Conference on the Applications of Lasers in Surface Science, held at the International Centre for Theoretical Physics, Trieste, Italy, August 1988.

Population Rate Equation Modelling fo a Resonant Ionisation Process
R.P.Singhal, A.P.land, K.W.D.Ledingham and M.Towrie
Journal of Analytic and Atomic Spectroscopy, 7, 599-606, 1989

Trace Analysis Using a Commercial Resonant Ionisation Mass Spectrometer
M.Towrie, S.L.T. Drysdale, R. Jennings, A.P. Land, K.W.D. Ledingham, P.T. McCombes, R.P. Singhal, M.H.C. Smyth and C.J. McLean.
International Journal of Mass Spectrometry and Ion Processes (1990), Vol. 96(3), 309-320

Characterisation of the Energy and Spatial Distributions of Neutrals Sputtered by Laser Ablation
P.T.McCombes, A.P.Land, K.W.D.Ledingham, R.P.Singhal and M.Towrie
Presented as a paper at the SPIE Technical Symposium on Laser Spectroscopy, Los Angeles, January, 1990

Resonant Laser Ablation (RLA)
C.J. McLean, J.H. Marsh, A.P.Land, A. Clark, R. Jennings, K.W.D. Ledingham, P.T. McCombes, A. Marshall, R.P. Singhal and M.Towrie
International Journal of Mass Spectrometry and Ion Processes (1990), Vol. 96(1), R1-R7

Observations on Carbon Clusters During Trace Elemental Analysis of Coal Samples by RIMS
R.P. Singhal, S.L.T. Drysdale, R. Jennings, A.P. Land, K.W.D. Ledingham, P.T. McCombes and M. Towrie
Submitted for publication in the International Journal of Mass Spectrometry and Ion Processes (1990)

Table of Symbols

The symbols in this table may be assumed to have the given meanings throughout this thesis, unless otherwise stated. Labels 'i' and 'j' represent upper and lower energy states in an atomic transition, respectively.

A_{ji}	Einstein coefficient for spontaneous emission from $j \rightarrow i$
B_{ij}	Einstein coefficient for absorption from $i \rightarrow j$
B_{ji}	Einstein coefficient for stimulated emission from $j \rightarrow i$
τ_{ji}	Natural radiative lifetime for decay from $j \rightarrow i$
$\Delta\nu_a$	Natural atomic linewidth
λ_{ij}	Wavelength of radiation for transition $i \rightarrow j$
ω_{ij}	Angular frequency of radiation associated with transition $i \rightarrow j$
E_{ij}	Energy gap between states i and j
f_{ij}	Oscillator strength for transition $i \rightarrow j$
σ_{ij}	Absorption cross-section for transition $i \rightarrow j$
P_{ij}	Stimulated transition rate from $i \rightarrow j$
$n_i(t)$	Instantaneous population density of state i at time t
F	Total angular momentum of given state
I	Nuclear spin angular momentum
J	Total electronic angular momentum of given state
m_F, m_J	Z-components of F, J, respectively
L, S	Orbital and spin angular momenta of given electronic state J, respectively

g_i	Statistical weight of level i
α_{ji}	The ratio of statistical weights g_j / g_i
n, n*	Principal and effective principal quantum numbers, respectively
C_{ij}	Clebsch-Gordan coefficient for transition $i \rightarrow j$
τ_L	Laser temporal pulse length
ϕ	Laser photon flux
Φ	Laser energy fluence
$\Delta\nu_L$	Laser linewidth
(π, ε_o, h, c, m_e, e)	Have their usual meanings.
R	Rydberg constant

---

1. Introduction

Resonance Ionization Mass Spectrometry (RIMS) is a new technique for solving problems. The 'problems' can be divided into two main types; detecting very small numbers of atoms or molecules, and investigating the spectroscopy of atoms or molecules. RIMS is a hybrid measurement technique, combining resonance ionization spectroscopy (RIS) with mass spectrometry. The RIMS technique shows great potential for expanding both the scale and versatility of its parent methods. The field has already been the subject of several books and major review articles [1-17]. In particular, Letokhov [1] provides an overview of RIMS as both an analytic and spectroscopic tool for the study of atoms and molecules; Fassett and Travis [5] illustrate the present state-of-the-art for RIMS as a technique for inorganic chemical analysis, Koppenaal [16] puts RIMS into context as one of many 'competing' branches of atomic mass spectrometry, Fig.1.1, and Axner [17] discusses RIS in the context of optical spectrometry, Fig.1.2.

In the following sections, the basic RIS/RIMS concept, some important areas of application and the experimental methods used to realize these will be discussed. The emphasis of the discusssion will tend to elemental, rather than molecular, studies, in line with investigations carried out in this work.

(1) Resonance Ionization Spectroscopy

When an atomic or molecular 'system' is ionized following a quantum state transition induced by narrow band electromagnetic radiation, it is said to have undergone "resonance ionization". The resonance occurs when the photon energy of the irradiating beam matches the energy gap between two quantum levels of the system under investigation.

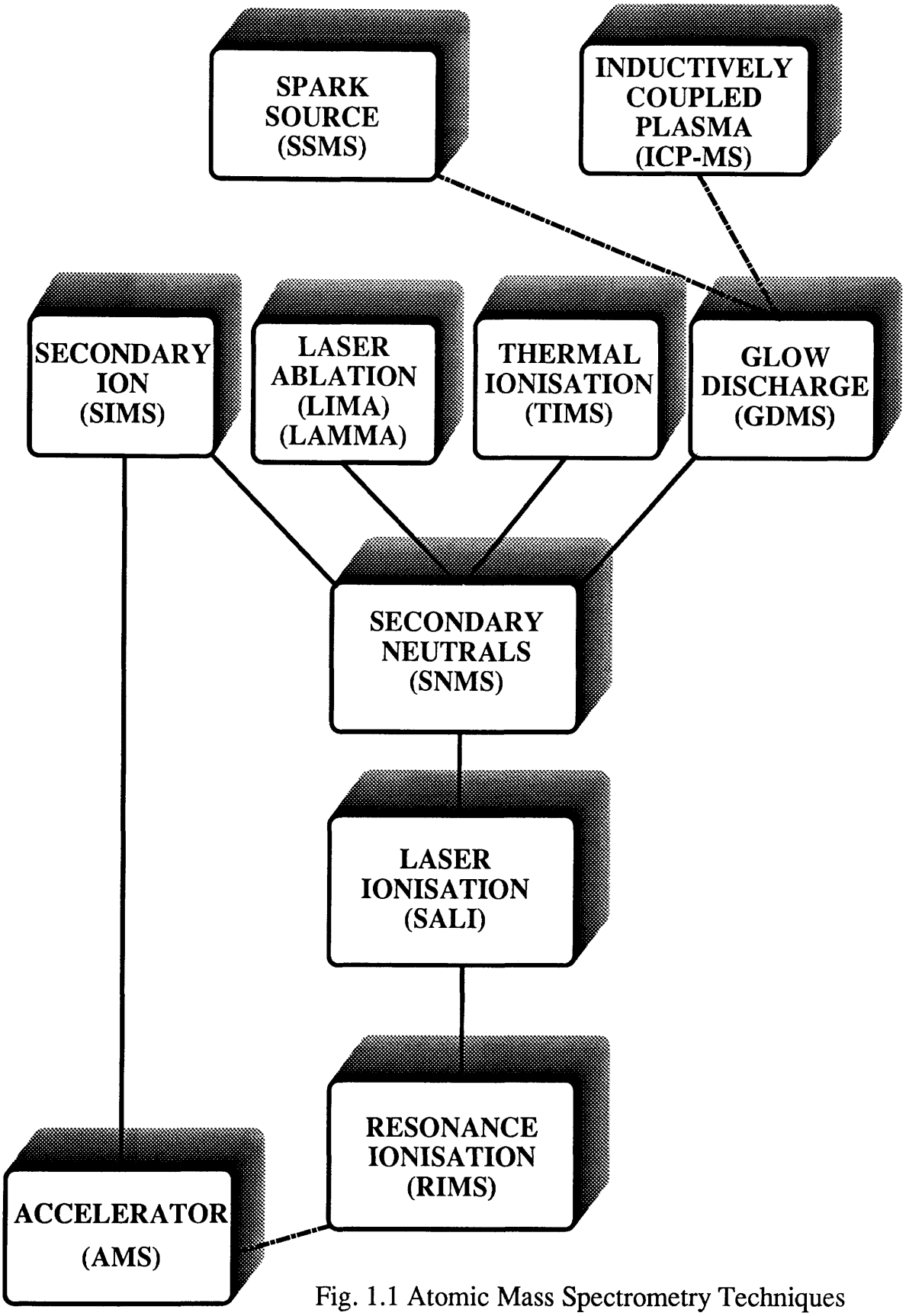

Fig. 1.1 Atomic Mass Spectrometry Techniques

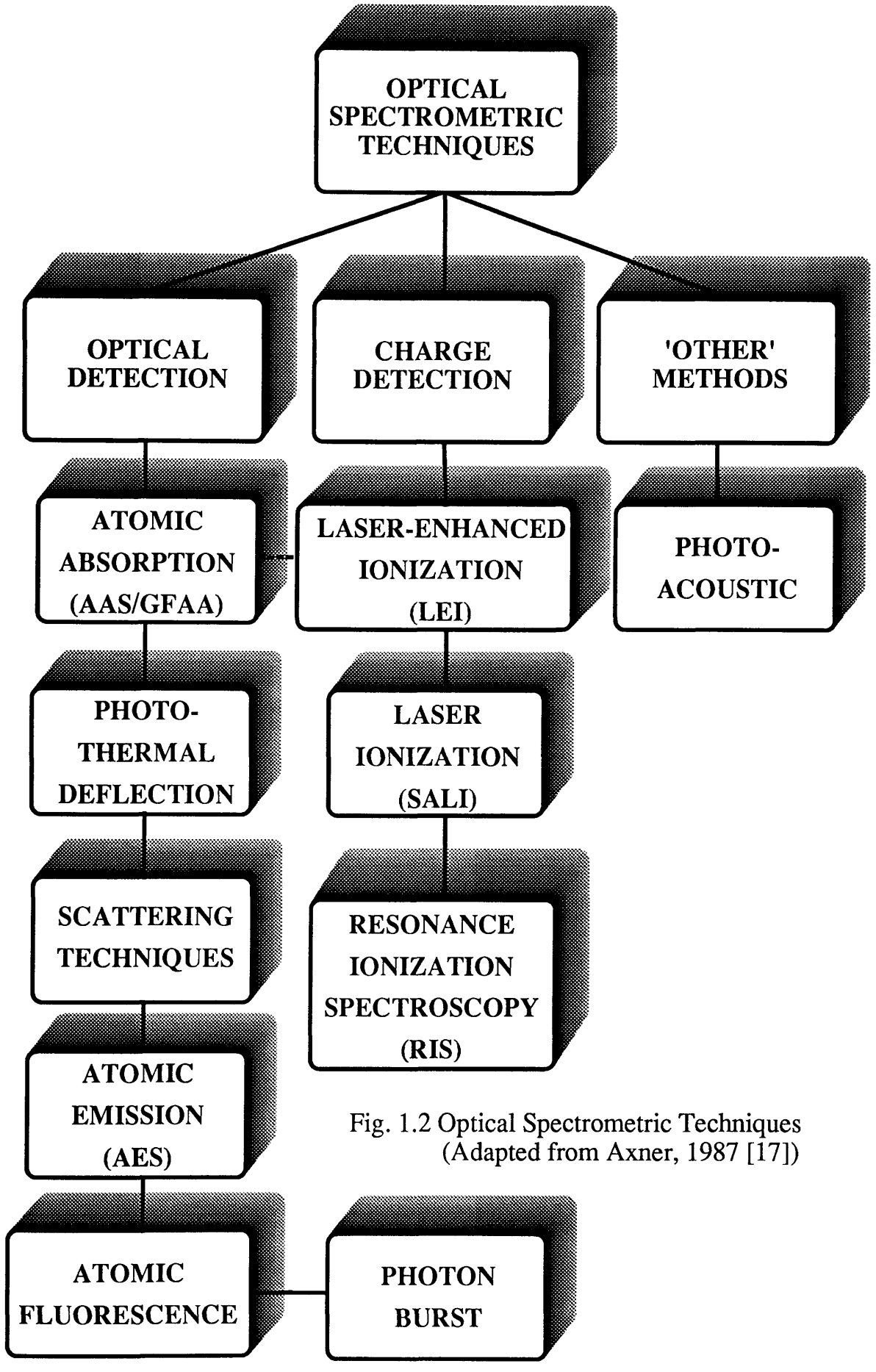

Fig. 1.2 Optical Spectrometric Techniques
(Adapted from Axner, 1987 [17])

The simplest example of resonance ionization spectroscopy (RIS) is illustrated by the energy level diagram in Fig. 1.1.1.

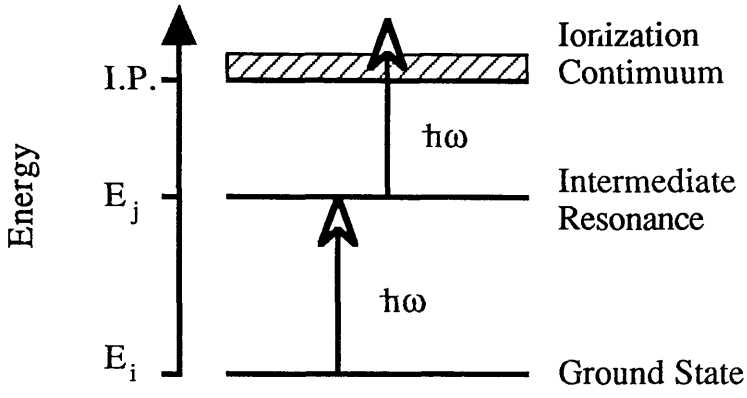

Fig. 1.1.1 Basic "1+1" RIS Scheme

A system in its ground state is resonantly excited to an intermediate excited state and is then ionized by absorption of a further photon. For most atomic and molecular transitions such a process requires photons in the ultra-violet (UV) to visible range of the spectrum (200-800nm). The concept of using such a resonant laser photoionization process for analytic measurements (in particular, the separation of atomic isotopes) was first proposed by Letokhov in 1969 [18].

The conceptual framework for the RIS process can be traced from Einstein's classical treatment of the interaction of atoms with a radiation field [19], through Fermi's Golden Rule [20] to the optical Bloch equations [21]. The practical realisation of RIS awaited the development of tunable, high spectral intensity light sources - dye lasers. Using the new dye laser technology, the RIS process was first demonstrated, with rubidium atoms, by Ambartsumyan, Apatin and Letokhov in 1971 [22].

The principal characteristics of RIS were summarized in a recent review article by Letokhov [10]. As an analytical chemistry technique, RIS

has three main features which make it highly attractive: *selectivity* , *versatility* and *sensitivity* . Every species of atom and molecule has its own unique set of energy levels - an identifying spectral "fingerprint". Tunable, narrow band radiation should thus allow any chosen state to be excited selectively (eg. a minor isotope may be selected in the presence of a far greater number of chemically nigh identical, but spectrally distinct, major isotopes). If sufficient spectral intensity is applied to the transition, then the process can be 'saturated', that is, every system in the selected state becomes excited. Hence, the RIS process should have a high analytic sensitivity . The power of RIS was demonstrated by Hurst, Nayfeh and Young in 1976, detecting single atoms of caesium within a gas proportional counter [23].

As a spectroscopic tool, RIS displays two further attributes which are of great appeal: *spectral* and *temporal resolutions* limited, in principle, solely by the intrinsic homogeneous broadening mechanisms of the system under investigation [10]. Spectral resolution is the ability to examine the fine detail of a system's internal structure, eg. atomic hyperfine structure. RIS can utilise the narrow-band laser and Doppler-free techniques developed in conventional spectroscopy, and can hence attain resolutions sufficient to probe the narrowest of spectral features. The temporal resolution of RIS is defined by the pulse lengths of the lasers employed. Existing, commercial laser technology can routinely achieve sub-picosecond pulse widths and hence even the short state lifetimes encountered in molecular species can be examined. Other spectroscopic techniques (eg optical absorption and emission spectroscopies) can achieve similar resolutions but generally require rather large amounts of sample material with which to work. The ability of RIS to make spectroscopic measurements on trace amounts of sample has been well demonstrated by Andreev et al [24]- Rydberg spectroscopy of the short-lived radioactive element Fr; by Niemax and co-workers for Yb [25], Ca and Li [26], and for studies on the positronium

'atomic' system by Chu and Mills [27].

Widespread interest in RIS as a viable, general purpose analytic technique was sparked by the review paper of Hurst et al in 1979 [15]. A simple theoretical framework for the atom/laser field interaction was developed and then used to derive basic requirements for efficient utilization of the RIS process. In particular, five variations on the basic RIS scheme were presented, which would allow all elements in the periodic table (except for He and Ne) to be ionized using existing laser technology. The schemes provide a useful guide to the difficulties that may be expected in ionising a given element, but are by no means definitive. Usually, many different excitation routes are feasible; eg. calcium (Ca) is listed under Scheme 2, but, as will be discussed in Chapter 4, this method was not used in this work, whilst four other methods were! The five schemes, in order of increasing complexity, are illustrated in Fig. 1.1.2 and their possible application to the elements in Fig. 1.1.3. Scheme 1 is the basic form described above with only one laser wavelength required. Scheme 2 uses frequency doubled light ($2\omega_1$) to effect the resonant transition, with the fundamental radiation (ω_1) ionising the excited state. Schemes 3 and 4 are 'doubly resonant', with a second colour (ω_2) being introduced to excite a further bound-bound transition before photoionization. This 'stepwise' excitation, and its extension to three or more colour schemes, adds greater selectivity to the process. Scheme 5 employs a 'two-photon' resonant transition, this special class of transition will be discussed in detail in Chapter 4. The relative cross sections for the transitions involved in the schemes will be detailed in a later section. The single laser schemes (1, 2, 5) have enjoyed the greatest popularity through their inherent simplicity.

The five basic Resonance Ionisation schemes

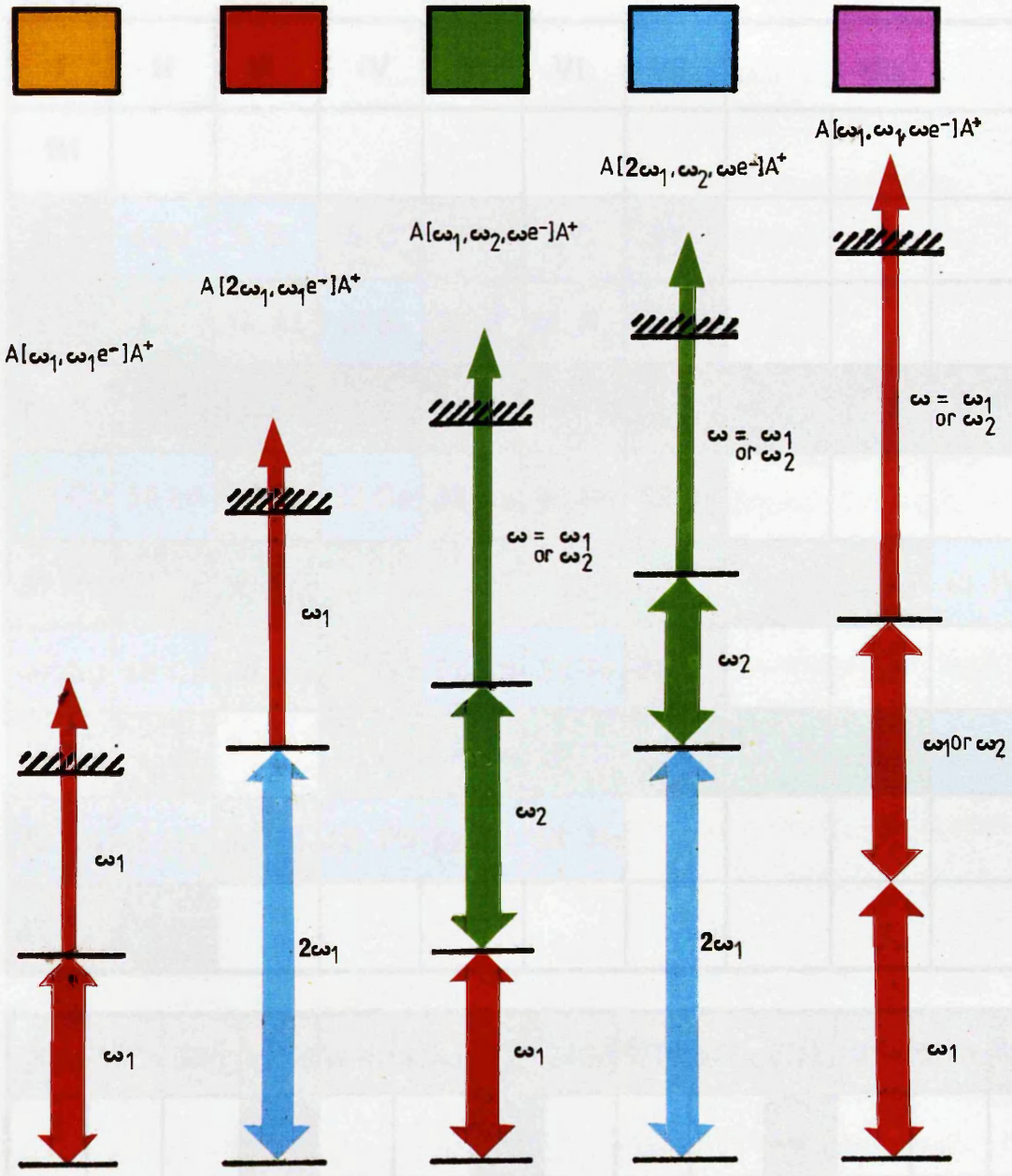

Application of the Resonance Ionisation schemes
to the periodic table

I	II	III	IV	V	VI	VII	VIII			0
1H										
3 Li	4 Be	5 B	6 C	7 N	8 O	9 F				
11 Na	12 Mg	13 Al	14 Si	15 P	16 S	17 Cl				
19 K	20 Ca	21 Sc	22 Ti	23 V	24 Cr	25 Mn	26 Fe	27 Co	28 Ni	
29 Cu	30 Zn	31 Ga	32 Ge	33 As	34 Se	35 Br				36 Kr
37 Rb	38 Sr	39 Y	40 Zr	41 Nb	42 Mo	43 Tc	44 Ru	45 Rh	46 Pd	
47 Ag	48 Cd	49 In	50 Sn	51 Sb	52 Te	53 I				54 Xe
55 Cs	56 Ba		72 Hf	73 Ta	74 W	75 Re	76 Os	77 Ir	78 Pt	
79 Au	80 Hg	81 Tl	82 Pb	83 Bi	84 Po					
87 Fr	88 Ra									

57 La	58 Ce	59 Pr	60 Nd	61 Pm	62 Sm	63 Eu	64 Gd	65 Tb	66 Dy	67 Ho	68 Er	69 Tm	70 Yb	71 Lu
			92 U			95 Am				90 Es				

(2) Resonance Ionization Mass Spectrometry

"The combination of resonance ionization spectroscopy with mass spectrometry was both obvious and natural.", Fassett and Travis, (1988) [5].

"The primary advantage of resonance ionization for MS (mass spectrometry) is the ability to avoid isobaric interferences in the ionization process; this advantage is necessary for the determination of ultratrace concentrations or extremely small ($<10^{-6}$) isotope ratios. A secondary advantage is the separation of the atomization and ionization processes, through which matrix-induced effects on atomization and ionization can be segregated and mitigated.", Koppenaal, (1988) [16].

The interfacing of RIS with mass spectrometry can be seen as providing benefits to each field, at the expense of greater experimental complexity. Although the basic RIS technique can provide a high degree of selectivity there are several major areas in which further discrimination is required, eg. elemental isotopic composition analysis, very high abundance sensitivity isotope ratio measurements and molecular fragmentation studies. In these cases a further degree of selectivity can be obtained by analyzing the RIS ions in a mass spectrometer, the hybrid technique known as resonance ionization mass spectrometry. 'Conventional' mass spectrometry is limited by the inefficiency and lack of selectivity inherent in the ionization processes employed. Measurements are sometimes simply not at all possible through limited available sample quantities and/or isobaric interferences. RIS can provide an efficient, highly selective ion source to help overcome these problems.

An important technique frequently used in mass spectrometry is that of "isotope dilution" [5, 63]. The use of isotope dilution allows a quantitative determination of a chosen element to be made through a precise isotope ratio measurement. Basically, a precisely known amount of a minor, possibly not

naturally occurring, isotope (the 'spike') of the element of interest is added to a precisely measured amount of sample. (eg. A ^{236}U spike could be used to determine the amount of ^{238}U present in a sample.) The sample undergoes a degree of processing (eg. acid dissolution) during which the spike isotope comes into chemical equilibrium with the sample. Provided that 'equilibrium' is maintained between the two isotopes at all stages of the process (chemistry, vapourization, ionization, etc.), a measurement of the ratio of spike isotope to the major elemental isotope of interest will give a quantitative measure of original elemental concentration in the sample. Hence, no knowledge of 'absolute' efficiencies (eg. mass spectrometer transmission) are required at any stage of the measurement, and hence the influence of sytematic errors is greatly reduced. (The isotope dilution method is also used with nuclear counting methods, with the spike being a short half-life radioisotope. For some studies, most notably medical, the use of radioactive materials is not desirable, and hence the ability of mass spectrometry to work with stable isotopes is of strong appeal.)

With sufficiently narrow band lasers (usually CW), individual isotopes can be selectively excited, utilizing spectral 'isotope shifts' [28]. This ability has led to great interest in the use of RIMS to make sensitive, very high 'abundance ratio' isotope measurements (eg. for isotope dating techniques) and for isotope separation work (eg. ^{235}U / ^{238}U). Abundance sensitivity is the ability to measure the level of a minor isotope in the presence of very much more prevalent major isotopes. RIS can typically provide spectral selectivities greater than 10^3 and up to 10^6 under favourable circumstances [29, 30]. RIMS is set to become the preeminent technology for commercial isotope separation over the next decade (AVLIS: atomic vapor laser isotope separation, in the USA [31]; LAPIS: laser photoionization spectroscopy in the USSR [32]). RIMS provides an ideal tool for spectroscopic studies on individual isotopes, particularly for rare or short-lived species (eg. Wen et al

on $^{10}Be:^{9}Be$ [33]; Kronert et al on neutron deficient gold isotopes [34]; Fearey, Miller and co-workers on Lu [35] and Pb/Bi mixtures [36]; Young, Donohue and Smith on the actinide [37] and lanthanide [38] elements; and the early (1976) work of Janes et al [39], Carlson et al [40] and Solarz et al [41] on $^{235}U:^{238}U$).

However, the linewidth of most high power pulsed dye lasers of the type frequently used for RIS generally exceeds any isotope shift in the analyte element. Hence, one might expect that under saturation conditions all isotopes would be excited with equal probability [42].

{Isotope shifts are usually in the range 0.3 -15GHz. The larger values being observed for the very lightest and heaviest of elements, with intermediate mass elements displaying relatively small values (eg. shifts of ≈15GHz have been reported for $^{10}Be:^{9}Be$ [33] and $^{235}U:^{238}U$ [39] respectively, whilst for $^{88}Sr:^{90}Sr$ a value of 0.7GHz has been measured [43].) Pulsed dye lasers typically have linewidths between 3 and 30GHz. CW dye lasers typically have linewidths of around 1MHz. (A convenient conversion to spectroscopic units is 30GHz≈1cm^{-1}) }.

If knowledge of the isotopic abundances present in a sample is required then a mass spectrometer is required to provide discrimination between the isotopes. The basic assumption that uniform isotopic excitation is induced by broad-band laser radiation has recently been shown to not be generally valid [44], "..the amount of ionization will depend on an intricate interplay between atomic and radiation parameters", Lambropoulos and Lyras (1989), [45]. This has important implications for the accuracy of isotope ratio measurements made with RIMS (and consequently for the accuracy of the determination of absolute elemental concentrations when isotope dilution methodology is employed).

Applying RIS to molecules is considerably more complex than with atoms. The added degrees of freedom possessed by many-body molecular

systems leads to considerably richer and more complicated spectra; sharp atomic spectral lines being replaced by broad rotational/vibrational band structure. Under conditions of intense illumination, as employed in RIS analysis, many molecules 'photodissociate' into a series of smaller, characteristic fragments. A true picture of such a process can only be built up by studying the mass spectrum of the resulting ions [12]. With the RIS technique it has proven to be possible to control the degree of fragmentation, from a predominantly molecular parent ion through to total atomic decomposition. Thus structural information for the molecule of interest can be obtained [46].

(3) Sample Vapourization

The preceding discussion has rather assumed that the sample of interest is in the vapour phase- this being a prerequisite for narrow spectral features and for efficient ion/electron collection. Therefore, the analysis of solid samples requires a vapourization (atomization) step before RIS can take place. (RIS has been demonstrated directly for samples in solution [47-49], but is generally impracticable.) All of the vapourization techniques in general use for RIS/RIMS have been used as the basis of independent analytic techniques. Frequently the sample atomization process is also used as the ionization mechanism ("ionization-through-vapourization": ITV). The separation of these two processes into distinct temporal and spatial regions (atomization and then 'post-ionization') is one of the major distinguishing features of RIS analysis. The sample vapourization step is usually highly inefficient as a means of creating free ions for mass spectrometric analysis, the majority of vapourized material consisting of free neutral atoms. Existing ITV techniques also show little selectivity and hence, are prone to

'interferences' (eg. isobaric interferences in mass spectrometry), which ultimately limit their measurement capability. When selectivity does occur in ITV, it is usually to the detriment of the analysis! Such 'selectivity' can result in the inability to produce an ion signal for certain elements (eg. high melting point or high ionization potential elements) or in large changes in relative ion yield dependent on the chemical composition of the sample - known as 'matrix effects'. To overcome these two major shortcomings, several new mass spectrometric methods have been developed to analyze the atomized neutral species following sample vapourization. The separation of the two processes into distinct stages allows each to be optimized independently. These techniques can be grouped together under the title "secondary neutral mass spectrometry" (SNMS) and utilize ion beams [50], electron beams [51], glow discharges [52], inductively coupled plasmas [53] , resonant laser (RIMS) and non-resonant laser [54-57] beams, respectively. RIMS is the only one of these methods which displays inherent selectivity. The selectivity of RIMS gives the very important benefit that many samples can be analysed without expensive and time consuming chemical processing (eg. with RIMS, ^{238}Pu can be measured in the presence of high amounts of its interfering isobar ^{238}U [42]).

Two parameters of the vapourization source which have a major influence on the efficiency of the RIMS analysis are the source 'duty cycle' and the source 'temperature(s)'. If the atomization source operates continuously (eg. a graphite furnace) and pulsed RIS lasers are employed, then there will be a "duty cycle" mismatch and hence sample utilization will be poor. (For a thermal atom source in vacuum and a short pulse length laser operating at 10Hz, only $\approx 10^{-5}$ of the atoms leaving the source are analyzed by the laser [58].) This problem can be overcome either by using CW lasers or, more commonly, by pulsing the atomization source (eg. pulsed laser ablation).

It is possible to define three distinct 'temperatures' associated with an atomization source: "internal (or, excitation)", "translational (or, hydrodynamic)" and "kinetic (or, thermal)" [59, 60]. All vapourization techniques, to one extent or another, result in energy being 'deposited' into internal degrees of freedom within the analyte system (eg. the excitation of metastable atomic states). This is frequently characterized by an 'internal temperature' for the vapourization process, which may be quite different from any 'translational' temperature induced by the process. In conjunction with the energy partition function, the internal temperature provides a guide for the excited state population distribution following atomization [59]. Since RIS is state selective (usually based on the ground state) this information can give a guide as to the expected fraction of the atomized analyte which can be accessed by the tuned lasers (eg. the high density of low lying states for uranium led to only ≈1/40th of the total atomic population being in the ground state following ion beam sputtering [61] whilst for thermally evaporated Re no excited state poulation was observed [62]). The "translational" and "kinetic" temperatures are related to velocities associated with the vapour ($T=\pi mv^2/8k$ [60]). These give a guide to the potential overlap between the resonant lasers and vapour from the source. The translational temperature is a measure of the velocity of the vapour perpendicular to the source. (eg. For an atomic beam from a thermal sample oven, the translational temperature is derived from the mean atomic velocity along the direction of the beam. For a sputtered plume, the translational temperature is related to the velocity of the centre of mass of the plume.) The kinetic temperature is a measure of the velocity spread in the vapour perpendicular to the major direction of translation. (eg. From an oven, the kinetic temperature is related to the beam divergence, and hence can have any value from a few mK up to the translational temperature. For a sputtered plume, the kinetic temperature is a measure of the rate of

expansion of the plume.) For a purely thermal source in which the vapour and source are in thermodynamic equilibrium, all three of these temperatures should be equal.

The vapourization methods most commonly used for RIS/RIMS analysis and their 'parent' ITV techniques are outlined in the following sections.

{ Note: In quoting analytic sensitivities the standard abbreviations ppm/ppb/ppt will be used to denote parts-per-million(10^6) / billion(10^9) / trillion(10^{12}) by-weight. These are equivalent to weight-for-weight measurements, eg. 1ng/g=1ppb. The suffix 'a' (eg. ppta) is used to denote atomic number concentration. For liquids analysis results are frequently quoted in the form weight/volume, eg. 1μg/l≅1ppb. Frequently the smallest detectable number of atoms or mass of analyte is quoted, eg. 1ng of ^{235}U. (A convenient conversion is : 10^{13} atoms≈1ng).}

(i) Electrothermal and Flame Vapourization

The simplest method of vapourising a sample is to place it in a hot environment and raise its temperature sufficiently for atoms to evaporate out of the source. The 'hot environment' can be provided in a flame or at a heated surface. The surface is usually either an electrically-heated metal filament or a graphite tube furnace. These technologies have been long developed as elements of the well established analytic techniques of thermal ionization mass spectrometry and atomic absorption spectroscopy, respectively

Thermal ionization mass spectrometry (TIMS) has long been the reference technique for highly accurate and precise isotope ratio measurements. When combined with isotope dilution methodology, TIMS becomes the standard reference technique for elemental composition measurements [5, 63] (the combined technique being known as isotope dilution mass spectrometry, IDMS). TIMS uses a heated filament

(1000-3500K) to both vapourize and ionize a sample under high vacuum conditions for subsequent mass analysis. Samples must undergo a large amount of chemical preparation to put them into a suitable form for 'loading' onto a filament. The loading process can involve simple drying [64] from solution, electroplating [65] or adsorption into resin beads which are then placed onto the filament [66]. The ratio of neutral to ionic species in the thermally desorbed plume is given approximately by the Saha-Langmuir equation: $n^+/n^0 = (Z^+/Z^0) \exp(W\text{-}IP)/kT$ Where, n^+/n^0 is the ratio of ions to neutrals in the plume, Z^+/Z^0 is the ratio of partition functions for the ions and neutrals, W is the filament work function, IP is the ionization potential for the analyte element, k is Boltzmann's constant and T is the filament temperature [67-69].

Generally, only a small fraction of material leaves the sample in the desired ionic state, the greater fraction being neutral atoms and molecules, and molecular ions [58]. The measurement capability of TIMS is limited by this inefficiency and by isobaric interferences which result from the lack of selectivity in the ionization process. The neutral atom population has been shown to have an excited state population distribution well described by the Boltzmann distribution for the filament temperature [62]. Mass discrimination effects (of the order, ≈0.4%) are known to exist in the ion formation process and this also limits the attainable isotope ratio measurement accuracy [42].

Much of the early RIMS analysis work was carried out on modified TIMS instruments and hence this combination is comparatively well documented and understood. Using thermal filament sources, RIMS has already been demonstrated for almost half of the elements in the periodic table [8]. When used solely as an atomization source the filaments are generally run at reduced temperatures (1000-2500K) compared with ITV methodology. As a source of free atoms for RIMS analysis, the thermal

filament has two major strengths: simplicity, and relatively well understood and characterized behaviour. Its principal drawbacks would appear to be the amount of chemical processing required and the poor duty cycle overlap when pulsed RIS lasers are used. Fassett et al have managed to alleviate the latter problem to a degree by pulsing the filament assembly [70]. Isotope fractionation effects in the neutral atom population of the thermal plume, similar to those observed for the thermal ion signal, are to be expected [42].

Using thermal filament sources, Walker and Fassett have undertaken 'state of the art' isotope ratio measurements on the Os-Re system using sub-nanogram samples [66]; Kronert et al have detected 10^{13} atoms of ^{239}Pu [71] and 10^{8} atoms of the short-lived ^{183}Au isotope [34]; and Gerke et al have measured a detection limit of 160 femtograms for Ca (limited by background contamination), using a gas filled thermionic diode detector [72].

The technologies of flame and graphite furnace atomization have largely been developed for use in atomic absorption spectroscopy (AAS), the preeminent technique for routine elemental trace analysis [73]. (When a graphite furnace is utilised for atomic absorption spectroscopy the acronym GFAA is frequently used.) For flame-AAS, the sample is introduced in liquid form to the gaseous flow used to fuel the flame (nebulisation). Atomization takes place within the intense heat of the flame itself. The analyte element is generally in thermal equilibrium with the flame and hence the flame temperature (2000-3000K) is a good measure of the internal temperature [17]. In GFAA the sample is vapourized through electrothermal heating within the graphite tube. Samples are usually inserted into the tube in liquid form with an inert buffer gas present at atmospheric pressure within the analysis volume. Atomization temperatures of 2000-3500K are usually employed. Detection of the analyte element of interest is accomplished through the wavelength-specific absorption of light. The determination of the optical absorption of a sample requires a measurement of the change in

the intensity of the light beam as it passes through the sample vapour. This can be done with great sensitivity, but is fundamentally limited by quantum fluctuations ("shot noise") in the light beam and the photodetector [74], and hence cannot approach the ultimate single atom detection limit of RIMS [10].

For RIMS analysis, the graphite furnace is used in two quite distinct fashions: firstly, as an enclosing analysis environment under atmospheric pressure of an inert buffer gas; and secondly, as an atomic beam source for analysis under high vacuum conditions.

The use of the former method, along with flame atomization, has developed into a specialised subset of RIS analysis, under the acronym laser enhanced ionization (LEI). This method relies on direct optogalvanic detection of the laser induced current, and as yet has not been interfaced with a mass spectrometer. LEI has been reviewed by Axner (1987) [17] and by Omenetto (1988) [75]. Detection limits, surpassing those attainable with the parent technique, have been reported for several elements (eg. 1pg/ml for In) [76].

Sample 'ovens' have long been used as atomic beam sources for spectroscopy [77]. The graphite furnace has been developed by Letokhov, Bekov and co-workers [13, 78] and by Bushaw, Whittaker and co-workers [79] to provide a suitable atom source for RIS analysis at the highest levels of sensitivity. The furnace is capable of directly vapourizing liquid or solid samples with a minimum of chemical preparation. Bekov et al have reported several ultra-high sensitivity measurements for trace elements in real samples (eg. Ru at a level of 1ppt in metal samples [80], <1ppb for Rh and Ir in geological materials [81], <0.1ppb for Ga in a solution containing less than 50pg of analyte [78], <2ppb for Al in high purity Ge and <0.3ppm for Al in blood samples [13].) Using CW lasers, Whitaker and co-workers have detected less than 0.3pg of ^{130}Ba with an abundance sensitivity of $>10^{10}$ [30]. Despite the inherent 'cleanliness' of the method, matrix dependent effects,

similar to those observed in GFAA, have been reported by Zilliacus et al [82].

Both flame and furnace sources are inherently "d.c." in nature and consequently display poor duty cycle overlap in operation. The enclosed furnace geometry is superior in this respect since it allows the sample to be 'retained' in the analysis volume for longer periods [83].

(ii) Laser Ablation

High power lasers have been used to 'process' (melt, modify, vapourize) materials for many years. Laser 'sputtering' refers to any process in which material is removed from a solid/liquid sample. Major reviews of the theory and application of laser sputtering are given by Vertes, Gijbels and Adams [173] and by Conzemius and Capellen [174]. Usually the terms 'ablation' and 'desorption' are used to describe those processes which result in sample vapourization (as opposed to 'macroscopic damage' processes such as exfoliation or hydrodynamic sputtering [84-87]). In this thesis, the term 'laser ablation' will be used, somewhat arbitrarily, to describe all processes which result in elemental vapourization of the bulk sample matrix, and 'laser desorption' will refer to vapourization of surface components (usually molecular) from a supporting substrate. Pulsed laser ablation was used as the vapourization method for much of the work reported in this thesis, the technique will be discussed more fully in Chapter 3, with only a brief outline given below.

As a vapourization source for mass spectrometric materials analysis the laser has several obvious attractions: solid and liquid samples can be analysed with little, if any, sample preparation; the method is inherently 'clean'; high spatial resolution can be obtained by focussing the laser to a tight spot ($\approx 1\mu m$, "microbeam"), and both surface and bulk analyses are possible through control of the laser power. Lasers have been used as ITV sources

for mass spectrometry since the early 1960's, with major interest being generated over the past decade, as is usually the case, by the availibility of commercial instruments (principally, LAMMA 500/1000, Leybold-Heraeus GMBH, Koln, W. Germany; LIMA, Cambridge Mass Spectrometry Ltd., Cambridge, UK). Usually fixed wavelength lasers (Excimer, Nd:YAG) are used for laser sputtering, the use of tunable lasers ("resonant laser ablation") will be discussed in Chapter 3. Laser desorption has become popular as a vapourization technique for large molecules in organic mass spectrometry [46]. Laser ablation has proven to be a popular and versatile tool for multi-element trace and isotope ratio analyses [16, 88, 89]. The techniques main strengths being its relative simplicity, high sensitivity and microbeam capability, its principal weakness being poor quantitation. Strong isotope fractionation effects (5-25%) have been reported for laser ionization studies, although it is not clear whether these reflect a true physical process or are instrument artifacts [88, 90].

Laser abalation suggests itself rather naturally as an atomization source for RIS analysis, the pulsed ablation process providing good duty cycle overlap for pulsed resonance ionization. Indeed, the first successful demonstration of RIS as an ionization source for mass spectrometry utilized laser ablation [91], and the first elemental trace analysis of a solid sample with RIS used an ablation laser [92]. This latter work, Mayo, Lucatorto and Luther (1982), remains the most sensitive analytic RIS measurement reported for laser ablation: 10ppta for Na in Si, using a gas proportional counter for detection. Beekman and Thonnard [93] claim a detection limit of 15ppb for Ga in Si, with good linearity and quantitation; their results for Al in steel samples, however, are comparatively poor in both these aspects. Williams and co-workers reported the relatively modest limit of 1ppm for Cr in a steel sample [94]. Using non-resonant laser postionization, Schueler and Odom [95] have found increases in sensitivity of between x100 and

x1000 over those obtained with standard ITV laser ablation in the analysis of high purity GaAs and HgCdTe.

As will be discussed in Chapter 3, laser ablation is generally found to be a process far from thermodynamic equilibrium. For example, Nogar et al [60] used 1.06μm pulses, with an intensity of $\approx 10^8$ W/cm^2, to ablate tantalum from a metal filament held at a base pressure of 1500K. They reported the following 'temperatures': internal, between 1500K and 2000K, hydrodynamic, 8500K and thermal, 450K (the boiling point for Ta is ≈5700K). However, velocities measured for both the ablation plume centre of mass and radial expansion are generally <1mm/μs, which should allow a high geometric overlap factor, see Chapter 3.

(iii) Ion Beam Sputtering

When a sample surface is bombarded with a beam of energetic particles, sample material is 'sputtered' off and the surface is effectively vapourized. The sputtering beam can consist of electrons, atoms or ions. For 'elemental' samples, the sputtered material consists largely of neutral atoms, some molecular species and a small fraction of atomic ions [96]. With 'molecular' samples (eg. peptides in glycerol solution) it is possible to eject intact high molecular weight species in both neutral and ionic forms, as well as a variety of molecular fragments [97]. Useful discussions on the physical processes involved in the sputtering process are presented by Robinson [98], Garrison and Winograd [99], and Winograd [100].

The analysis technique secondary ion mass spectrometry (SIMS) uses the sputtered ions (either positive or negative) for mass spectrometric characterization of the sample [101]. For SIMS analysis an energetic positive ion sputter beam is most commonly used (typically O_2 or Cs at keV energies). The "sputter yield", S, for ion bombardment with keV beams is typically S≈4, that is, for every incident ion four species are sputtered from

the sample [102]. An ion beam can be focussed down to sub-micron spot sizes and hence SIMS can provide high spatial resolution on a sample surface. The controlled way in which the sputtering process erodes away a sample surface provides an ideal tool for measuring a 'depth profile' for a sample. The combination of these two properties has led to SIMS becoming the predominant analytic technique where surface or structural information is required [103]. The measurement capabilities of SIMS anlaysis are limited by the standard difficulties inherent in ITV techniques: limited sensitivity, isobaric interferences and matrix effects. Typically, less than one in a hundred of sputtered species are in the ionic form required for SIMS detection. This fraction varies by many orders of magnitude between elements and is highly dependent on the sample matrix and any surface contamination [104, 105]. For surface studies (eg. catalysis), by definition, the amount of sample available for analysis is strictly limited and hence high sensitivity is required. To ensure that only the surface monolayer is analysed, SIMS must be operated in the "low dose" regime (low incident sputter energy and intensity) in which SIMS displays the lowest relative sensitivity. Matrix effects are a particular problem when quantitative 'dopant depth profiles' are required from inhomogeneous samples (eg. trace element dopants in multi-layer semiconductor devices) [106]. Isotope ratio bias effects are also commonly encountered in SIMS analysis, heavier isotopes of a given element generally being less efficiently ionized [107].

Many of the SNMS methods, mentioned above, have been combined with ion sputtering in attempts to overcome these limitations. Using electron beam postionization, Benninghoven and co-workers have reported much improved quantification but reduced sensitivity compared with standard SIMS analysis [51]. Becker and Gillen have developed the use of non-resonant laser postionization (surface analysis by laser ionization: SALI) with high intensity UV laser radiation. Enhanced sensitivity, approaching

ultra-trace levels, has been demonstrated [56]. The use of the glow discharge will be discussed in §(iv), below.

Much work has been carried out to develop the use of ion sputtering as an atomization source for RIMS analysis. (For RIMS analysis, an inert gas (usually Ar) sputter ion beam is preferred, this choice enhancing the ratio of sputtered neutrals to ions [108].) The combined technique holding out the promize of the structural capabilities of SIMS with the enhanced sensitivity, and relative freedom from matrix effects and isobaric interferences of RIMS.

The obvious potential for commercial applications, particularly in the semiconductor industry, has generated much research interest in the use of RIMS in conjunction with ion sputtering. Young et al [109] present a brief review of some of the early ion sputtering/RIMS experiments with an analysis of important experimental design parameters. Winograd and co-workers have studied many of the important parameters for the efficient interfacing of pulsed RIS lasers with ion sputtering (eg. ion pulse length, laser spot size etc.) [110]. In a later paper, the same group report a high sensitivity (<0.2ppb) analysis of indium in a silicon matrix, with good linearity over a large dynamic range (10^4) [111]. Downey and Hozack have compared SIMS with RIMS for the depth profile analysis of semiconductor (AlGaAs) devices [112]. Accurate dopant profiles were obtained directly in the RIMS analysis, showing matrix effects much reduced from those apparent with the SIMS data. Matrix effects have, however, been observed in the analysis of several metal samples (I, [104]; U, [108, 113]; U, Sm, [114]) in the presence of oxygen/surface metal oxides. Hutchinson et al [115] have investigated matrix effects, and the use of isotope dilution to alleviate the problems, for U in soil samples. Parks and co-workers have demonstrated good sensitivity (sub-ppm) and measurement linearity for trace impurities in a variety of high purity host matrices [106, 116].

To date, only pulsed RIS lasers have been used with sputter sources. The sputter ion beam can operate continuously but is more usually pulsed to provide greater sample utilization efficency, ion pulse lengths of 5μs being typical. For pulsed operation and typical experimental parameters, the real time duty factor is $\approx 10^{-4}$, with ≈30% of sputtered atoms available for laser irradiation [110]. Pellin et al [117] report an overall experimental collection efficiency of ≈5%. Effective internal temperatures for sputtered neutrals are dependent on the energy of the sputter ion beam, but are typically 1000-2000K for Ar^+ sputtering at ≈3keV [110]. Note that this is significantly 'cooler' than the 'temperatures' associated with the sputtering process itself and with the translational velocities of the sputtered plume ($\approx 10^4$ K) [118].

(iv) Glow Discharge

The glow discharge provides a simple and convenient method for ion sputtering of conducting solid samples. The discharge is stable, easily controlled and yields high sputtered densities [52]. The sample is used as the cathode for the discharge and the sputter ions are formed from a buffer gas, typically ≈1torr of Ar. Sputtered neutrals move away from the sample surface, through the 'dark space' region, and can be subsequently ionized in the discharge plasma. Ionization is induced largely through electron impact and Penning processes, the overall efficiency being small, <1% [52]. Ions formed in the discharge can be extracted into a mass spectrometer, giving rise to the technique 'glow discharge mass spectrometry' (GDMS). The separation of vapourization and ionization into distinct regions allows GDMS to be classified as a form of SNMS in its own right. The GDMS technique is claimed by one of its commercial manufacturers, VG Instruments Ltd., to be sensitive and versatile: "..detection limits better than 10ppb for most elements, below 1ppb in some cases..(for solid, conducting samples).." [119].

The obvious potential to increase the overall efficiency of the process

through use of resonance ionization has been investigated by Harrison and co-workers [120]. An enhancement of the ionization efficiency by a factor of fifty was reported for an iron sample. Through duty cycle considerations this represents a net loss in overall sensitivity with the 80Hz repetition rate laser employed, compared to that achieved with the discharge operated in its normal continuous mode. The relatively high gas pressure in the discharge should give rise to long residency times for analyte atoms in the probed volume and consequently a high duty cycle efficiency should be achievable through use of a pulsed discharge and a high repetition rate laser (eg. 1kHz excimer pumped dye systems). The high discharge pressure and 'temperature' also have important implications for the excitation processes. Atomic ground state populations will be depleted, leading to reduced sensitivity, but efficient collisional ionization of high lying states (discussed below) could help to redeem this.

(4) Ionization Mechanisms

Following resonant laser excitation there are several ways in which an atom can become ionized: photoionization, autoionization, field ionization or collisional ionization. Each method has its own set of distinct properties, strengths and weaknesses, these will be briefly outlined in the following sections.

(i) Photoionization and Autoionization

When an atom or molecule is raised to a higher charge state following absorption of a photon, it has undergone 'photoionization'. Marr [69] presents an overview of the various ionization processes that can result from the interaction of gases with a radiation field; and Hurst and Payne [4]

discuss some of the parameters important specifically to RIS. The five basic RIS schemes described in §1, above, each use photoionization from a resonantly excited intermediate state to a singly charged ionic state: $A^* + h\nu \rightarrow A^+ + e^-$. The process has the advantage of simplicity, the high intensity laser light required for the resonant transition(s) can frequently provide enough energy to also ionize the excited state. Many of the reports mentioned above have utilized photoionization; of the vacuum atomization results, only Letokhov, Bekov and co-workers do *not* use this method. The cross sections for excited state photoionization ($10^{-17} \rightarrow 10^{-21}$ cm^2) are, however, typically many orders of magnitude smaller than those for the resonant bound-bound transitions ($10^{-10} \rightarrow 10^{-14}$ cm^2) and hence, very high laser intensities ($10^8 \rightarrow 10^{12}$ W/ cm^2) are required to saturate such a step. Such high intensities usually require focussing for pulsed RIS dye lasers, and are not readily feasible for CW dye lasers. The need to focus the laser beams leads directly to a reduction in analytic sensitivity through a reduction in the amount of sample vapour analysed by the laser. Overly high power densities (those exceding required saturation levels) on bound-bound transitions can lead to 'light induced level splittings' which can actually reduce the total ion signal ! [4, 121] The selectivity of the process is also reduced through a disproportionate increase in non-resonant background ionization. These problems can to an extent be alleviated by using a separate high intensity, long-wavelength laser (eg. 10μm CO_2 or 1.06μm Nd:YAG) to ionize a highly excited state. This technique has been used by Bushaw, Whittaker and co-workers in their high sensitivity CW experiments with Ba [79].

Another possible way to enhance the efficiency of photoionization is through the resonant excitation of *autoionization* states: $A^* + h\nu \rightarrow A^{**} \rightarrow A^+ + e^-$. Such states will be discussed in Chapter 4. For the present discussion, suffice it to say that autoionizing resonances are

bound states existing above the first ionisation potential. They have relatively high cross sections ($>10^{-16}$ cm^2), and are known to exist for many elements (but not, in the optical spectrum, for the alkali metals). Such transitions can be relatively easily saturated, at the expense of a further tunable laser being required.

(ii) Field Ionization

If an intense electric field is applied to an atom in a highly excited Rydberg state, then the atom can *field ionize* [122]. This method has been highly developed for RIS analysis by Letokhov, Bekov and co-workers. Usually, several resonant steps are used to excite the atom to a high lying state (effective quantum number $n^* \approx 20$) and then a high voltage field pulse applied ($\approx$2kV/cm). Transitions to suitable high Rydberg states generally have cross sections ($\approx 10^{-15}$ cm^2) which are easily saturated with tunable dye lasers. Each system in the upper excited state becomes ionized, however, it is generally only possible to excite $\approx$1/2 of the ground state population into the upper state [13]. { More strictly: the field, E, required to ionize a Rydberg state n^* is given by, $E(V/cm) \approx 3 \times 10^8/(n^*)^4$. The fractional population, B, in the state, j, following multistep excitation is given by, $B = g_j / \sum_i (g_i)$, where g_i is the statistical weight of the resonant state i [13] .}

(iii) Collisional Ionization

For resonance excitation in the presence of a relatively high pressure (>0.1 torr) of buffer gas, excited states can become ionized through collisions. For a room temperature buffer gas, the dominant ionization mechanism is simple thermal-collisional with the neutral gas atoms, and only highly excited states (those within $\approx$kT of the continuum) are ionized. This method has been investigated by Houston et al [123] for the detection of Cs, and Smyth et al [124] for Cs and Rb, in gas proportional counters.

Gerke et al have used collisional ionization for the ultra-high sensitivity detection of Ca and U in a gas thermionic diode [72]. If the buffer gas itself is highly excited (eg. in a flame, plasma or glow discharge, as discussed above), then ionization can be induced through collisions with ions, electrons or excited state neutrals. Generally, the collisional mechanism is highly efficient, inherently continuous in operation, with the obvious attractions of being cheap and simple! High pressure sources can be interfaced with mass spectrometers through the use of differential pumping (eg. commercial GDMS, ICP-MS instruments). Bekov and Letokhov [13] have noted that the ultimate sensitivity attainable with such sources will be limited by impurities present in the buffer gas.

(5) Applications of RIMS Analysis

"Trace pollutants are, by definition, present in very small amounts in the presence of large quantities of other materials. Thus their detection presents the problem of getting a signal from a trace pollutant which is distinguishable from signals from the other materials present." Williams et al (1984), [94].

As originally stated, RIMS is very much an applications orientated technique, the applications lying broadly in the fields of fundamental spectroscopy and materials analysis. The major spectroscopic investigations carried out using RIMS have been noted in §1 and §2, above. This section will cover some of the important aspects of RIMS as an analytic technique and outline some of the fields in which RIMS analysis shows great potential (semicondutor materials, bio-medical, environmental and geological/archaeological studies). The selectivity and sensitivity of RIMS technology should help provide accurate, quantitative measurements at levels

below those attainable with conventional analytic techniques. The potential of RIMS to perform such measurements without chemical pre-processing may, in the long term, lead to quick and cheap routine analyses. A 'worked example' is presented to give a feeling for the potential capabilities of current RIMS technology.

(i) 'Worked Example'

The example will be based on an ion beam sputter source with pulsed laser ionization, the combination for which greatest commercial interest is displayed. The figures are based on those reported in the works mentioned in §3(iii), above, and are presented merely as guidelines.

Assume that a pulsed ion sputter beam with a current of 50μA and a pulse duration of 5μs strikes a high purity material. With a sputter yield of 4, this gives rize to a plume of 6.25×10^9 species, of which ≈70% will be in the required ground state. Further, the laser can irradiate ≈20% of these with an ionization efficiency of 100%. We have now created $\approx 8.75 \times 10^8$ ions. If ≈40% of these are transmitted through the mass spectrometer and detected with ≈40% quantum efficiency, then we have detected 1.4×10^8 analyte atoms in one pulse. If we now asssume that our laser repetition rate is 20Hz and that we are prepared to count for 15 minutes, we will detect a total of 2.52×10^{12} ions. For a precise analysis we require 1000 counts, and hence our sensitivity to trace impurities in a host matrix is $(1000/2.52 \times 10^{12}) \approx 0.4$ppba. Less than 20pg of sample (or approximately one monolayer, for an ion spot size of ≈1 mm^2) has been consumed in the analysis! The low count rate (≈1/s) would allow simple, precise counting electronics to be used. Obviously, this analysis has taken into account only the 'signal' values, with no consideration given to 'noise' sources which will in reality limit the measurements. Background levels will depend on the form (eg. purity) of the sample, RIS scheme employed and the discrimination afforded by the

mass spectrometer.

(ii) Semiconductor Materials

As semiconductor devices have become ever more compact and structurally complex, the requirements for methods of characterizing the devices have become ever more stringent. The analysis requirements of the semiconductor industry have been outlined by Smith and McGuire [125]. In this context, RIMS is perceived as having two important roles; detection of impurities at ultra-trace levels, below those attainable with other techniques, and quantitative depth profile analysis of dopant elements in multi-layer devices. Several of the key experiments demonstating the power of of RIMS have been mentioned in the preceding sections (ultra-trace analysis [13, 92, 117]; depth profiling [106, 112]). A RIMS instrument dedicated to semiconductor analysis is under development in the Dept. of Physics and Astronomy, University of Glasgow [126].

(iii) Bio-Medical Studies

Trace elements play a vital role in the metabolisms of all living creatures. To date, fifteen trace elements have been identified as being crucial to the health of human beings, "Acting as catalytic or structural components of larger molecules, they have specific functions and are indispensable for life.", Mertz (1981) [127]. Versieck [128] presents a highly comprehensive review of trace elements in human body fluids and tissues. Generally, these elements must be present in very closely regulated amounts at around the ppb level [127]. Lack of these elements leads to 'mineral deficiency' symptoms whilst their presence in higher concentrations can have toxic effects. The deletrious effects of xenobiotic elements (ie. poisons!) in macroscopic amounts is relatively well understood, however, the action of trace amounts of such elements is not at all well characterized [129] (eg. the

postulated link between Al and Crohns disease [130]). Hence, there is a great need for sensitive and accurate measurements of trace elements in biological materials. RIMS should display sufficient sensitivity to be of use in such determinations. More importantly, the selectivity and comparitive freedom from matrix effects should allow accurate measurements in a wide variety of biological materials with a minimum of chemical processing [131].

Important experimental results are those of Bekov and Letokhov for Al in blood [13], Fasset and co-workers for Fe in serum [132], and Moore and co-workers for Mo and Cu in serum [131] and for Si in a variety of biological reference materials [133].

(iv) Environmental Studies

There has been increasing concern over the effect that industrial pollutants are having on the environment (acid rain, the greenhouse effect, trace metals in water supplies, nuclear fallout etc.). There is a growing need for analytic techniques which can achieve levels of sensitivity and accuracy beyond those achievable with present methods, RIMS is perceived to fulfil these requirements.

A major area of concern is the presence of low-level radioactive materials in the environment eg. effluents from the nuclear power industry, decay products from nuclear weapons testing, and from 'civilian' nuclear reactor accidents. It has been suggested that the presence of trace amounts of long half-life, beta emitters (eg. ^{135}Cs) may present a long term public health hazard [134]. The potential for RIMS to achieve sensitivities higher than those attainable with nuclear counting techniques has been explored in detail by Houston [135]. Briefly, nuclear techniques only detect the radiation from a decaying nucleus, whilst RIMS detects the parent nucleus itself. For long lived species RIMS should display far higher counting rates and hence a greater attainable sensitivity. RIMS has the added major strength that

isotopic abundance information is readily available. This is of great importance in determining the origin of nuclear materials (eg. Pu pollution from nuclear power plants, weapons fallout and natural sources each displays its own characteristic isotope 'pattern'). Nuclear materials have been studied with RIMS by Donohue and co-workers [42, 114], Kronert et al [71], Rimke et al [136] and Gerke et al [72].

(v) Geological/Archaeological Studies

Although two quite distinct research fields, geology and archaeology have similar requirements for materials analysis capability: accurate and precise isotopic abundance information with high sensitivity, and ultra-trace element detection.

Isotope abundance analysis allows the 'age' of certain materials to be detemined through the technique of 'isotope dating' (eg. the well known ^{14}C dating method for organic materials). Briefly, if the relative concentration of a long-lived radio-isotope to a reference isotope is known for a sample at some initial time, then the age of the sample can be determined from the present day relative concentrations and a knowledge of the decay half-life for the radio-isotope (eg. ^{14}C:^{12}C). Standard nuclear counting techniques monitor the radiation from the radio-isotope (eg. the beta decay of ^{14}C to ^{14}N) or from some other radio-isotope further down the decay series. As mentioned above, the sensitivity of nuclear counting techniques is limited compared with that, in principle, attainable with mass spectrometry, and RIMS in particular. Three main difficulties exist for mass spectrometric isotope dating measurements; a very high abundance sensitivity is usually required ($>10^6$), the available sample size is frequently very small (eg. the Turin Shroud), and the isotopes of interest may be isobars (eg. ^{187}Os / ^{187}Re). The principal strength of RIMS in such measurements is the virtual elimination of isobaric interferences through its inherent selectivity.

Perhaps the most impressive demonstration of the power of RIMS has been in this field: the determination of the ^{81}Kr concentration in groundwater at a level of 1200 atoms/L ($\approx 3x10^{25}$ molecules), by Hurst, Parks, Lehmann and co-workers [137]. The chemical inertness of the krypton analyte is of crucial importance to the sensitivity of this measurement; for species other than the noble gases, chemical reactions will indubitably limit the attainable sensitivities to levels less than that reached for krypton. Walker and co-workers have used RIMS and isotope dilution techniques on the Os/Re system to date geological samples [66]. The possibilities of using RIMS to make ultra-high abundance sensitivity ($>10^{12}$) have been discussed by Lucatorto et al [29], Clark et al [28] and by Snyder et al [138].

Bekov and Letokhov have made a series of ultra-trace elemental determinations in ocean 'objects' and ancient geological sediments (eg. noble metals in seawater at ppt levels) [139], and in sedimentary rocks (Rh at ppb levels) [81]. (The former representing the first shipborne RIMS analyses!)

(6) The Choice of Calcium

As indicated in the title of this thesis, this work concentrated on the RIMS analysis of calcium (Ca). (Some of the important chemical and physical properties of calcium are given in Table 1.) Given the choice of some 84 stable elements from which to choose, the decision to work with calcium bears some justification.

In many ways calcium is a model system for the development of RIMS methodologies. It has a large mass range of stable isotopes, with both odd and even nuclear spins, and with a very large range of abundance ratios. Its atomic spectroscopy, both bound and autoionization, is rich, but comparatively well documented and understood. Calcium has a relatively low ionization potential and its resonance ionization is readily achieved with

Table 1. Calcium Data

Atomic number: 20

Atomic weight: 40.08 g/mol ; Density: 1.54g/cm^3

Principal oxidation number: +2 ; Electronegativity: 1.0

Atomic radius: 0.196nm ; Ionic radius: 0.099nm

Melting point: 1120K ; Boiling point: 1760K

[From, *Science Data Book*, Ed. R.M. Tennent. Oliver Edinburgh, 1971]

Atomic ground state: $4s^2\ {}^1S_0$ Ground state of Ca^+: $4s\ {}^2S_{1/2}$

First ionization potential: 6.115eV = 49,306.1cm^{-1} [198]

Natural isotopic abundance ratios: [147]

Isotope	Mass(amu)	% Abundance
40	39.96	96.982
42	41.96	0.642
43	42.96	0.133
44	43.96	2.057
46	45.95	0.003
48	47.95	0.182

Radioisotopes and half-lifes:

$^{41}Ca,\ T_{1/2} = 1.03 \times 10^5 a$; ^{45}Ca, 165d ; ^{47}Ca, 4.54d

Nuclear spins: Even neutron number, =0, Odd = 7/2

visible wavelengths. By a fortuitous gift of Nature, the 'layout' of the atomic level structure is well suited to measurements on the two-photon intermediate resonance enhancement effect, to be discussed in detail in Chapter 4. Calcium also displays a number of similarities, in both spectral and chemical characteristics, to uranium. This allows calcium to be used for the development of methods suitable for the analysis of uranium without the radiation and chemical toxicity hazards associated with the noxious substance [140].

There are many interesting and demanding applications for the analysis of calcium itself. Since calcium accounts for some 3% of the earth's crust and is present in the human body in macroscopic quantities (≈0.05%), the need for an ultra-trace analysis technique such as RIMS may not at first be entirely obvious! The potential uses of RIMS in calcium analysis are based on its abilities to make precise and accurate isotope ratio measurements on small amounts of sample materials with minimal chemical preparation, and to make very high abundance sensitivity measurements. In the former category are medicinal chemistry, geological and cosmochemistry studies, and in the latter studies in archaeology/paleoanthropology and fundamental particle physics. These various possibilities are outlined below.

Calcium plays a crucial role in the human metabolism. Knowledge of the pathways that calcium follows in the body, its localised concentrations and its rate of absorption from food intake are all important for the understanding of metabolic function. The 'microlocalised' (≈1μm) distribution of Ca in biological samples has been investigated by Burns and File [141], using a SIMS instrument. Combining the very finest of sputter ion sources available (ø≈100nm) with the sensitivity of RIMS should allow such studies to be carried out at the single cell level [142]. The study of calcium absorption is of great topical interest in medicinal chemistry [143]. Published results have utilized the standard method of stable isotopic tracers [144],

combined with various mass spectrometry techniques (TIMS [145], SIMS [143] and field desorption MS [146]). Chemical processing is required in all of these cases to overcome background and achieve adequate sensitivity. RIMS has the potential selectivity to work directly with unprocessed samples (blood, urine etc.) and its high sensitivity should allow smaller samples to be analyzed.

The large fractional mass range covered by the calcium isotopes makes it likely to display mass dependent isotope fractionation effects. These are of interest to geologists and cosmochemists [147, 148]. Here, the potential ability of RIMS to make accurate and precise isotopic abundance measurements on small samples (eg. rare meteorite fragments) is of interest.

Perhaps the most challenging problem for the RIMS analysis of calcium is to make the very high abundance ratio (10^{-15}) measurements required for the ^{41}Ca:^{40}Ca isotope pair. (^{41}Ca is formed from ^{40}Ca by thermal neutron absorption.) It has been suggested that ^{41}Ca isotope dating might prove a useful new tool in the archaeologist/ paleoanthropologist's kitbag of technologies [149, 150] (in much the same way as ^{12}C:^{14}C is used at present).

With its 10^5 year half-life, ^{41}Ca should be of use in dating calcium-bearing samples (eg. bones) from the Pleistocene age (125,000 to 730,000 years ago), a period not covered by any of the existing archaeometric techniques. (The combination of the long half-life and the ^{41}Ca decay mode, electron capture to ^{41}K with emission of only soft x-rays and low energy Auger electrons, makes nuclear counting techniques impracticable.) The technical problems for mass spectrometry are, however, formidable. The first reported measurement on the abundance ratio of ^{41}Ca:^{40}Ca was from a meteorite sample [151], a value of 3.8×10^{-12} being obtained, using highly sophisticated accelerator mass spectrometry (AMS)

[152]. This 'high' value indicating the strong neutron irradiation history of the meteorite. It is only recently that the abundance ratio of ^{41}Ca:^{40}Ca in contemporary samples ($2x10^{-14}$ - $3x10^{-15}$) has been established [153]. Even here, a large degree of sample pre-enrichment was required to make the measurements feasible. The most popular arrangement for AMS work is to use a negative ion source and a tandem mass spectrometer [152], RIMS does not fit obviously into such a scheme. If, however, a cyclotron type accelerator were to be utilised, then RIS would provide a sensitive positive ion source with an added degree of selectivity. More speculatively, it may be possible to make a 'standard' RIMS instrument which could achieve the required abundance sensitivity without recourse to the even greater costs and experimental complexities of AMS. Such a possibilty has been discussed by Lucatorto and co-workers [29]. More specifically, using CW lasers, Whitaker and Bushaw have demonstrated isotope selectivities of 10^6 for ^{136}Ba:^{137}Ba (isotope shift ≈200Mhz) solely in the laser excitation stage [30]. Calcium has a very similar spectroscopy to barium (both being alkaline earth elements), and isotope shifts in the range 400MHz to 4GHz have been measured [154], thus a selectivity of at least that obtained for Ba may be expected. State of the art mass spectrometers can achieve abundance sensitivities greater than 10^9 [155, 156], and consequently a total instrument selectivity of $>10^{15}$ would seem to be feasible with existing technology.

A proposed measurement in the field of fundamental particle physics has even more demanding requirements: the detection of 10^4 atoms of ^{41}Ca with a selectivity of 10^{16}! An instrument which could dispaly such capabilities would become a sensitive solar neutrino detector [157], providing complementary information to the existing Ar/Cl detector of Davis and co-workers [158]. (^{41}Ca can be formed from absorption of a solar neutrino by ^{41}K: $^{41}K + \nu_e \rightarrow (^{41}Ca)^+ + e^-$). Much of the above

discussion on the prospects for RIMS in ^{41}Ca dating apply equally well to this problem. It is, however, evident that further improvements are required in both the selectivity of the resonance ionization step and in the mass spectrometer's abundance sensitivity before a RIMS analysis of an unenriched sample becomes feasible even in principle.

The laser spectroscopic and mass spectrometric studies carried out on calcium samples will be detailed in the following chapters.

---

2. Instrumentation

A complete RIMS instrument is a large, complex system. The system under development in the Department of Physics and Astronomy, University of Glasgow, that was used throughout this work, is shown schematically in Fig. 2.1. The system will henceforth be referred to as the "Kratos Machine", after the supplier of the main vacuum system (Kratos Analytic, Manchester, UK). The various major component sub-systems are discussed in detail below.

(1) Analysis Chamber and Mass Spectrometer

This is a large ultra-high vacuum (UHV) system into which the sample is inserted for analysis, Figs. 2.1.1 (a), (b). The system is constructed almost entirely of stainless steel (SS) to allow for 'clean' UHV conditions. Samples enter the main chamber through a fast insertion lock (Kratos XSAM-800). The sample can be changed and UHV conditions reestablished within about 10 minutes. The main chamber consists of a SS sphere with a variety of ports facing radially towards the centre. The sample is mounted on a SS 'sample stub', spring-clipped to the sample manipulator, at the centre of the sphere. A sample stub is shown in Figs. 2.1.2 (a), (b). The sample manipulator (Kratos XYZ- θ) is used primarily in the sample insertion operation, although it does allow for small movements of the sample during analysis if required.

Directly in front of the sample sits the ion optic assembly. The first optic and the sample stub comprise the 'ion source' region, Fig. 2.1.3. The ion optics were designed by Dr. M. Towrie (Departmental Research Fellow). Only ions created within a certain region of the ion source are extracted into the mass spectrometer, this is called the 'acceptance volume'.

The acceptance volume was measured using resonance ionization of

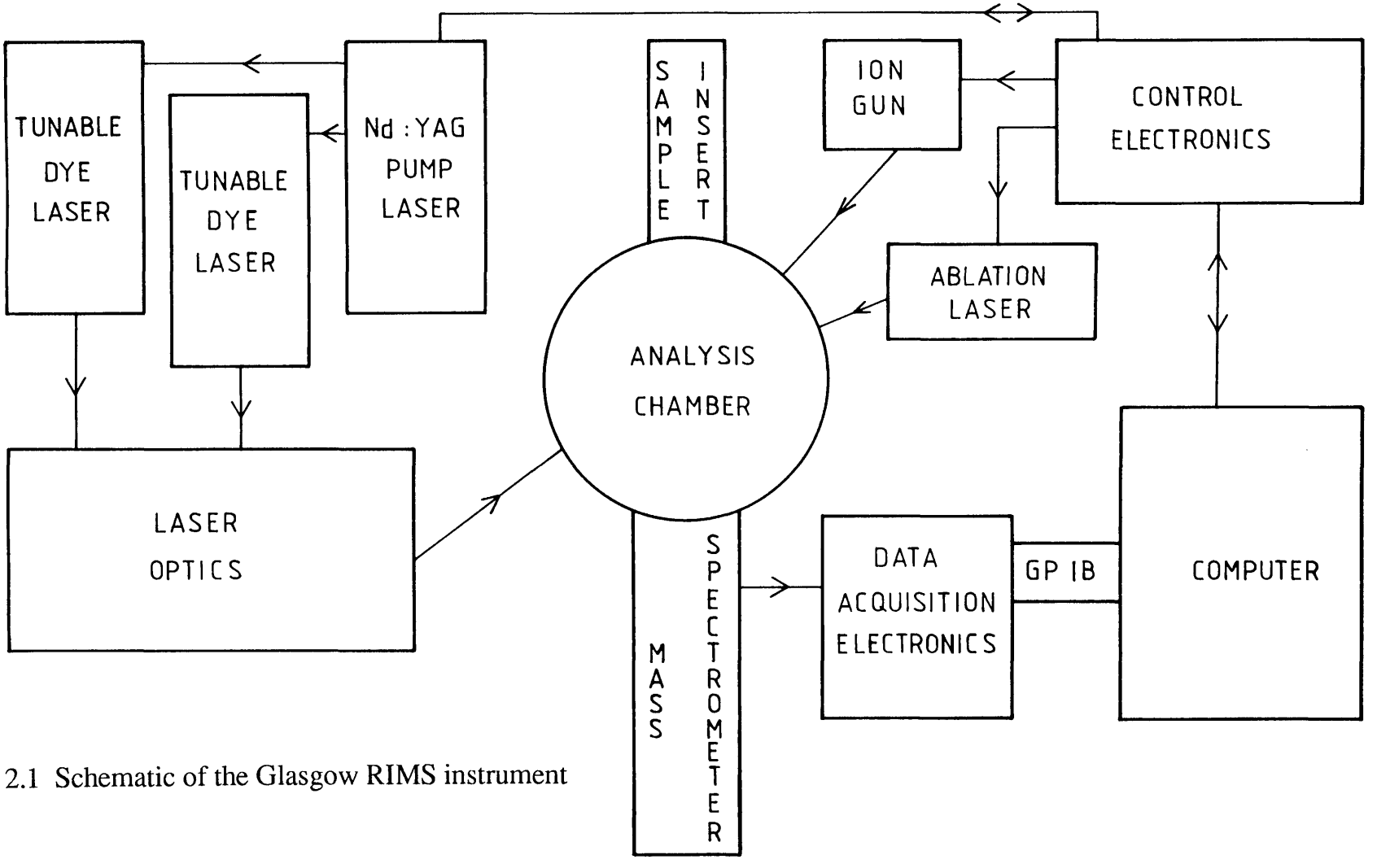

Fig. 2.1 Schematic of the Glasgow RIMS instrument

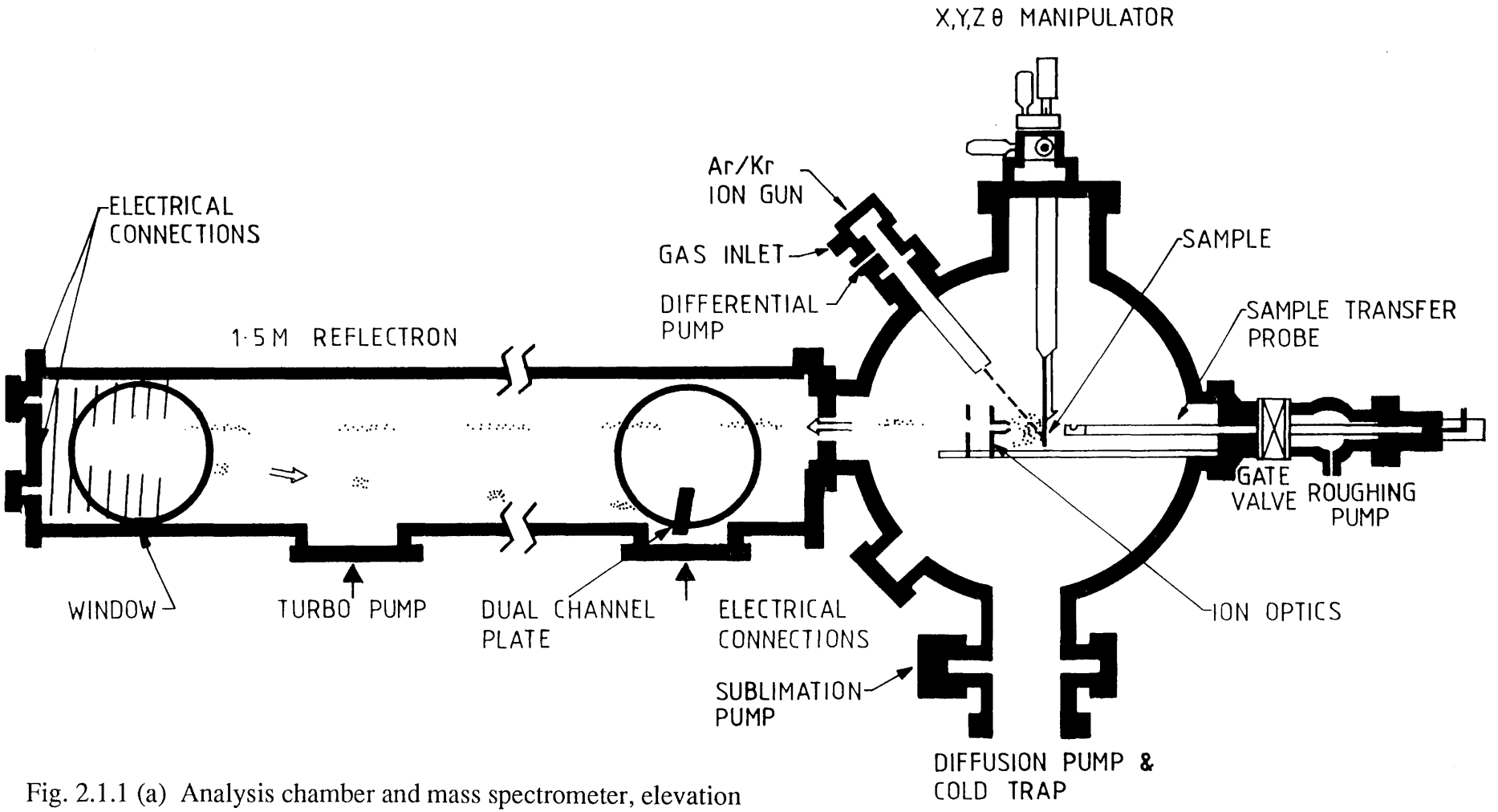

Fig. 2.1.1 (a) Analysis chamber and mass spectrometer, elevation

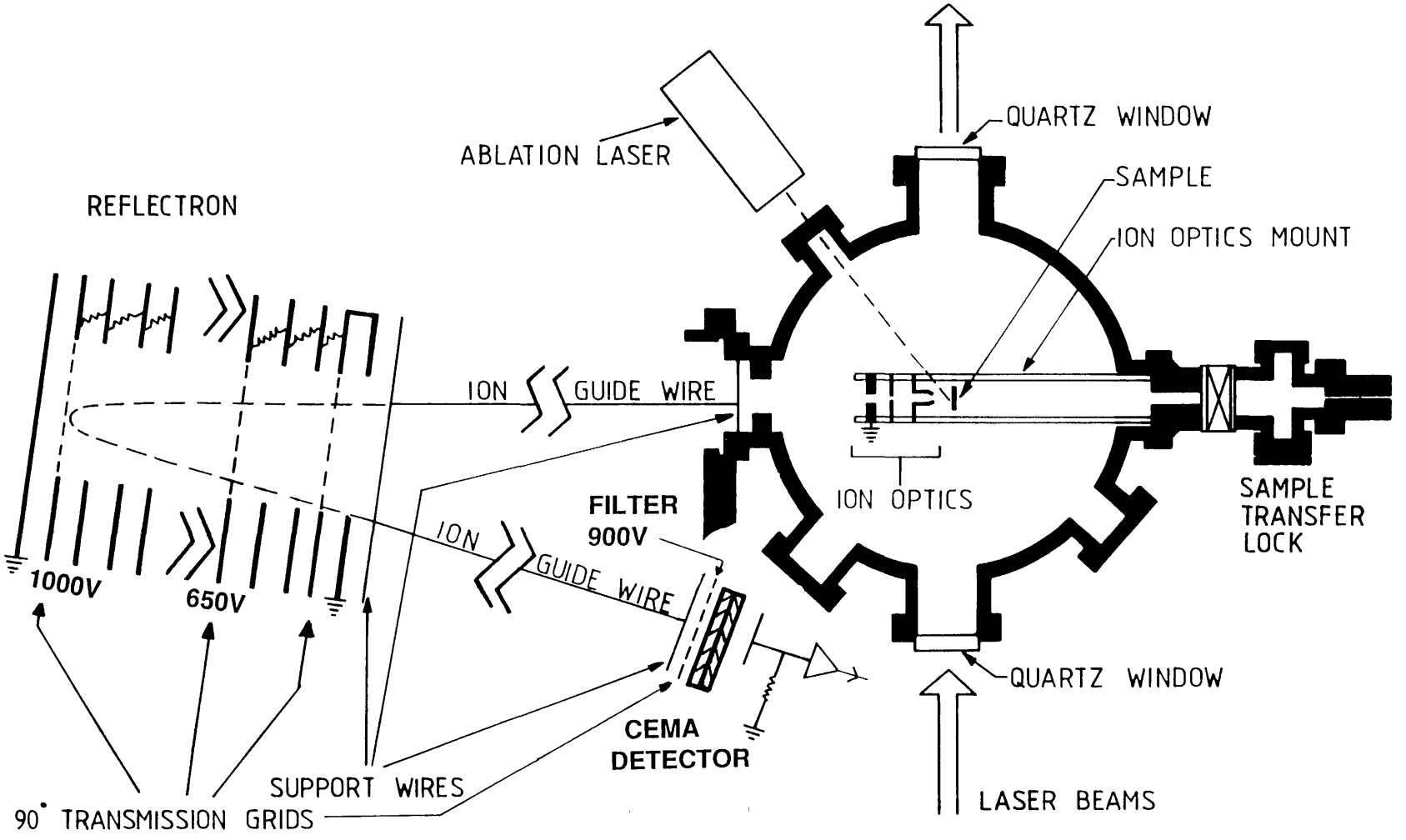

Fig. 2.1.1 (b) Analysis chamber and mass spectrometer, plan

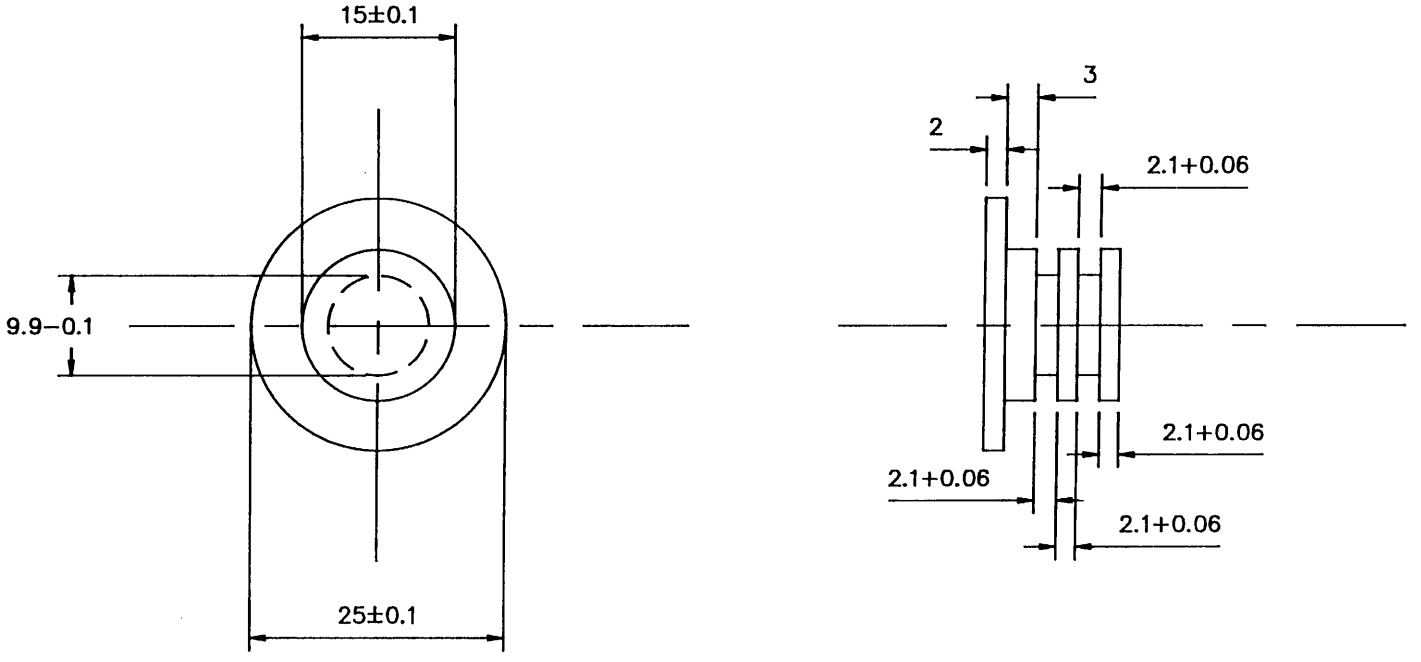

Fig. 2.1.2 Sample stub

unless otherwise specified TOLERANCES are						
one place (0) ±0.76 (±0.030)	DRAWN	DATE	SCALE	ISSUE	MATERIAL	DRAWING No
two place (00) ±0.39 (±0.015)	T.L.N.	11/12/89	2:1	3	STAINLESS STEEL 316	LIS--0025
three place (000) ±0.13 (±0.005)						

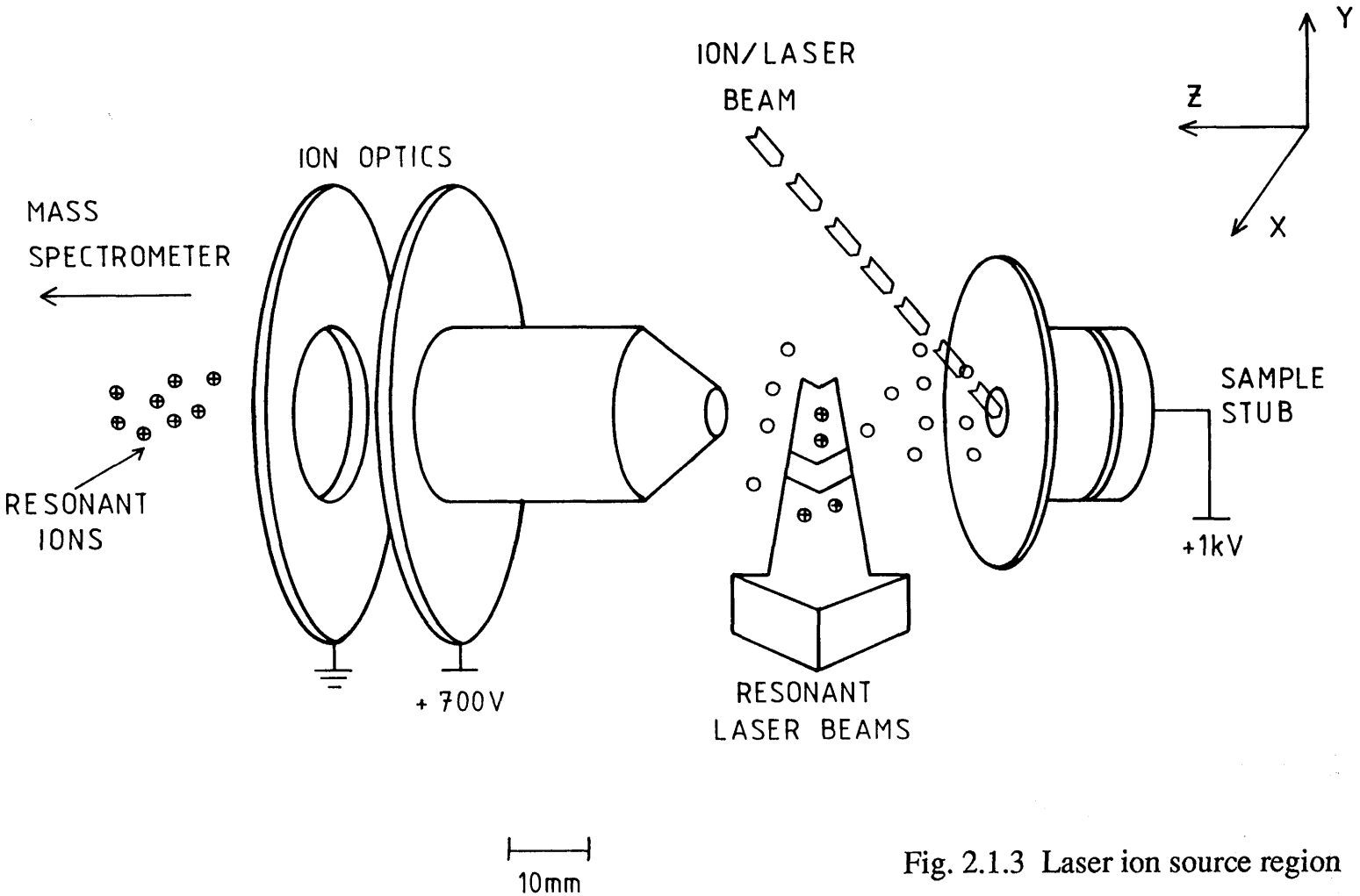

Fig. 2.1.3 Laser ion source region

background organic impurities in the vacuum (to be discussed more fully in Chapter 3), Figs. 2.1.4 (a), (b). The form shown in (a) arises from the action of both low and high energy filters in the mass spectrometer, discussed in detail below. The asymmetric and off-centre form shown in (b) is thought to be due to a slight misalignment between the ion optic assembly and the rest of the mass spectrometer.

The mass spectrometer (MS) works on the time-of-flight (TOF) principle. Ions created during the ionizing pulse within the source region receive (approximately) equal kinetic energies from the static electric field. The ion optics extract ions from the source region into a field-free drift tube. In the drift tube, ions separate out in time according to their charge/mass ratio. Hence the mass spectrum of ions created can be obtained by measuring the relative arrival times at the detector. Ideally, ions would be created instantaneously, within an infinitesimal volume and would have equal (preferably zero) kinetic energies. In practice, none of these conditions are met, and the mass resolution is restricted. The major resolution limiting factor for all laser and SIMS based TOF systems is the spread in initial kinetic energies of the ions.

To help overcome this limitation, the Kratos machine employs a commercial "Reflectron" electrostatic mirror [159] (Cambridge Mass Spectrometers (CMS), Cambridge, UK), Plate 1. This largely compensates for the spread in kinetic energies of ions leaving the source region by focussing the ions temporally at the detector. Briefly, high energy ions penetrate deeper into the reflecting fields, and hence must travel further, than ions of a lower energy. The field gradients within the electrostatic mirror can be arranged to focus the arrival times of ions at the detector.

The CMS Reflectron requires only two external voltages to be supplied: a 'reflect' voltage, applied to the final grid in the mirror, and a 'retard' voltage, applied to a grid near the top of the mirror stack. An internal resistor chain

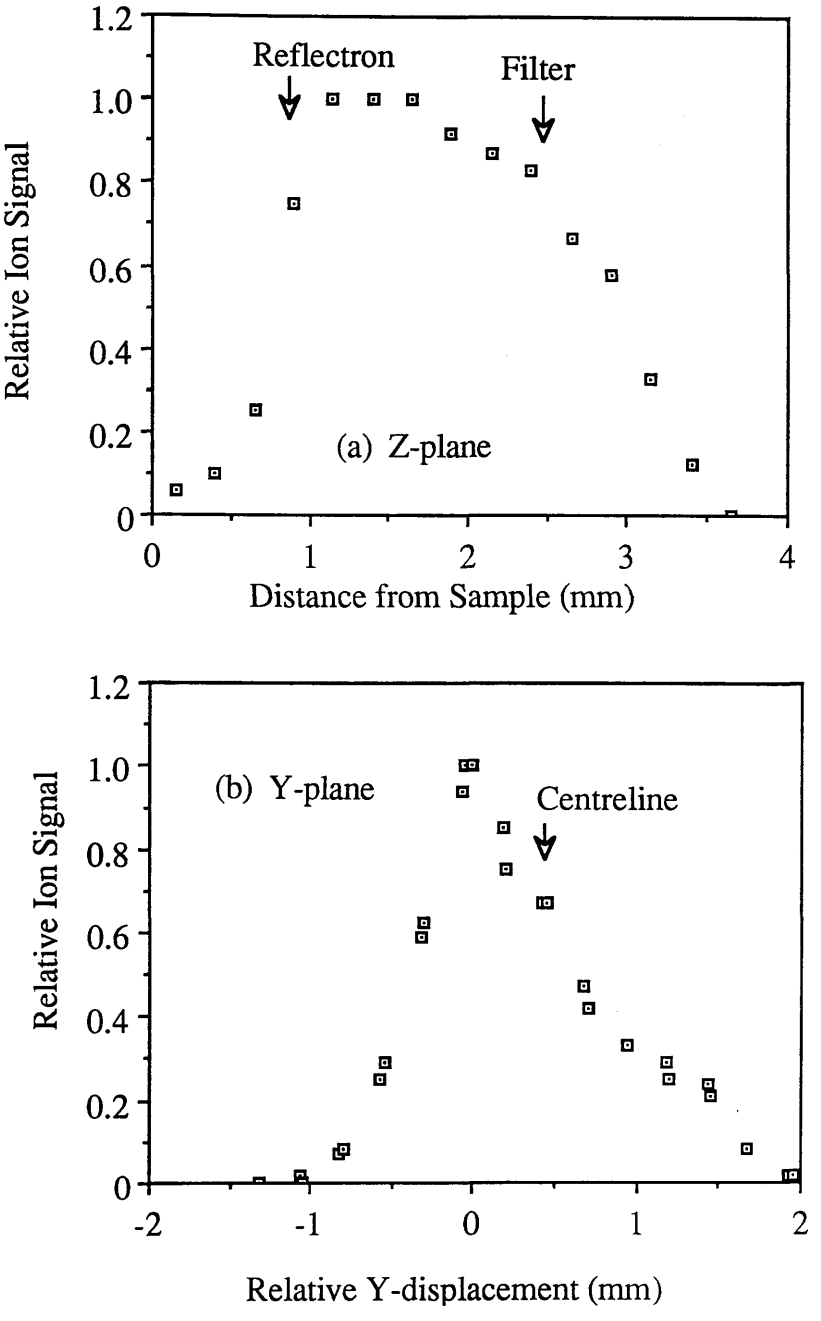

Fig. 2.1.4 Ion acceptance volume for the mass spectrometer

Plate 1. The CMS Reflectron electrostatic mirror

sets the relative potentials of the remaining eighteen plate electrodes. The reflect voltage sets an upper energy limit for reflection of ions. The Reflectron therefore acts as a very efficient high energy filter: ions created at potentials greater than the reflect voltage pass through the rear grid and are grounded on the earthed back plate. This provides a high degree of suppression for ions generated in the atomization process whilst still retaining high transmission for RIMS ions, which are created in a region of lower field potential. For a given reflect voltage, the retard voltage determines the degree of energy compensation attainable with the Reflectron and hence the overall mass resolution.

Defining the mass resolution to be R=M/ΔM,where ΔM is the FWHM of the peak at mass M, then a conventional Wiley-McLaren type TOF system (no energy compensation) [160] will typically have R≈200 and a Reflectron system R≈2000 [161]. The CMS Reflectron is designed for optimal transmission of ions with energy 3.5keV. At this energy a ^{40}Ca RIMS ion had a measured flight time of ≈30μs and a time FWHM of ≈30ns, giving a mass resolution of R=500 (the factor of 1/2 arising from the quadratic dependence between mass and flight time). This comparatively low value was due to the combination of the large resonant laser beam diameter (ø≈1mm) and the high extract field (≈300V/cm) typically employed in this work. (The attainable resolution is at present limited to R≈1000 by the temporal resolution (10ns) of the data acquisition electronics, discussed below, and by the pulse length (10ns) of the resonant lasers.) This sharp ion pulse led to problems with electrical ringing at the detector output. It was found that it was possible to achieve the same resolution at reduced voltage levels in the MS, with longer ion flight times and proportionally greater peak widths, ≈60μs and ≈60ns, respectively. This reduced the degree of ringing at the detector output and hence it was decided to run the MS at a reduced voltage of 1kV.

The reduction in operating voltage for the MS was only possible through

the use of a device known as an 'electrostatic particle guide' (EPG) [162]. This consists of a length of fine wire, strung along most of the ion flight path and held at a small negative potential (≈-6V). This provides a degree of correction for radial dispersion of the ion packet. With the Reflectron at its design operating voltage it was possible to enhance the ion transmission by at least a factor of two through use of the EPG. At the lower MS voltage used throughout this work almost no ion signal was detected without the EPG in use, but almost the full ion signal amplitude could be recovered through applying a potential to the wire.

The system's ability to measure the mass of an ion peak was calibrated using the extended, regular mass spectrum obtained from carbon clusters formed in the laser ablation of a graphite sample, (to be more fully discussed in Chapter 3). The results are shown in Fig. 2.1.5. The carbon clusters give clear, known mass peaks from 12amu to over 2000amu. Experimental masses were calculated assuming a simple quadratic dependence between mass and time of flight, and an offset correction factor. Hence, at least two mass peaks must be assigned to calculate the two unknowns. A simple routine has been incorporated into the data analysis software to perform this calculation for any two specified peaks, and to scale the spectrum accordingly. For the data shown, peaks at masses 12amu and 132amu, respectively, were utilized. The results show good linearity over a large mass range. The calculated mass accuracy is relatively poor at higher masses through limited precision in the calculated extrapolation from the lower mass region, this being defined by the resolution of the mass peaks. Greater accuracy could be achieved by using more than two assigned mass peaks and applying a least-squares fitting procedure to extract the required constants.

Early tests on the MS, in all modes of operation, showed large background ion signals with little obvious time structure. These were identified as low energy ions resulting from 'signal ions' scattering , and

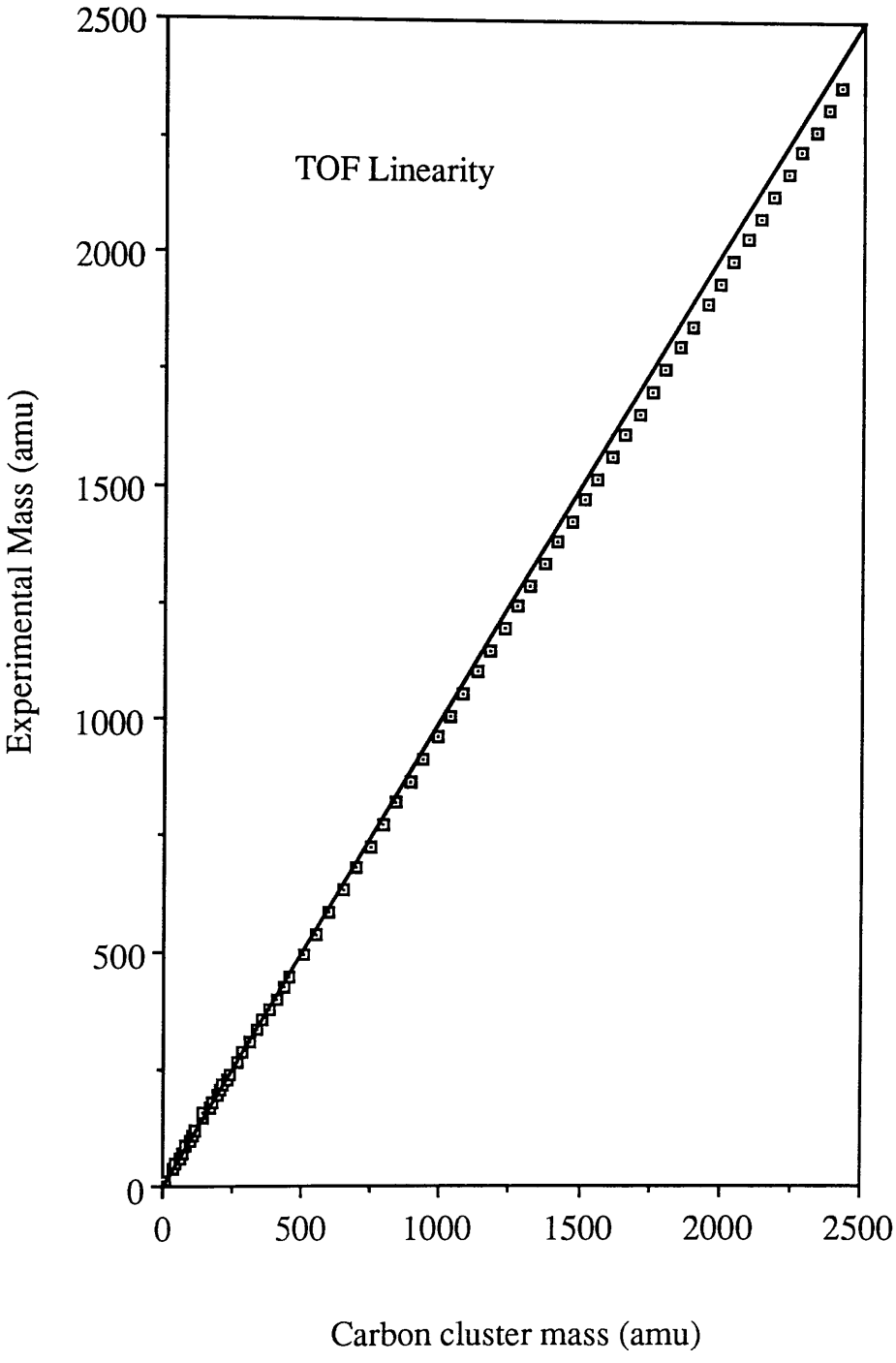

Fig. 2.1.5 Linearity and accuracy of mass measurements.
The straight line shows the ideal system response.

initiating secondary ion emission, from the grids in the Reflectron. This background was largely eliminated by placing a further grid immediately in front of the detector, held at a potential just below that of the signal ions, to act as a low energy filter.

Ions must pass through an effective total of four grids, each of 90% transmission, in travelling through the MS. This sets an upper limit on the ion transmission of ≈60%.

The ion detector is a dual channel electron multipier array (CEMA) [163] (Galileo 3025-10V, Galileo Electro-Optics Corp., MA, USA). This has a specified, quantum detection efficiency of >40% for low energy ions and a current gain of $x10^7$. Into a matched 50Ω load impedance, the FWHM of the output electron current pulse is specified to be <1ns, which should give rise to a voltage pulse amplitude of >80mV [163]. On first use (January,1988), the single ion amplitude was measured at 6mV. This was thought to be partly due to exposure of the CEMA to air during system assembly and also due to the lack of impedance matching between the detector anode and the matched 50Ω cable system employed for the data acquisition electronics. Considerable ringing and pulse overshoot were apparent for large ion pulses. The single ion amplitude decreased with time over the several months of machine operation. By March, 1989 single ions were not readily apparent above the noise floor of 1mV. A further problem was only realized towards the end of this investigation. The CEMA was supplied with biasing as shown in Fig. 2.1.6 (a). The lack of bias between the rear plate of the CEMA and the collector anode is believed to have resulted in reproducibility problems, particularly with isotope ratio measurements, this will be discussed more fully in Chapter 5. After some experimentation, the wiring scheme shown in Fig. 2.1.6 (b) was adopted, initial results suggesting a marked improvement.

The detector and low energy filter assembly is shown in Plate 2. The dual CEMA is visible as a thin wafer in the centre of the plate, the filter is mounted

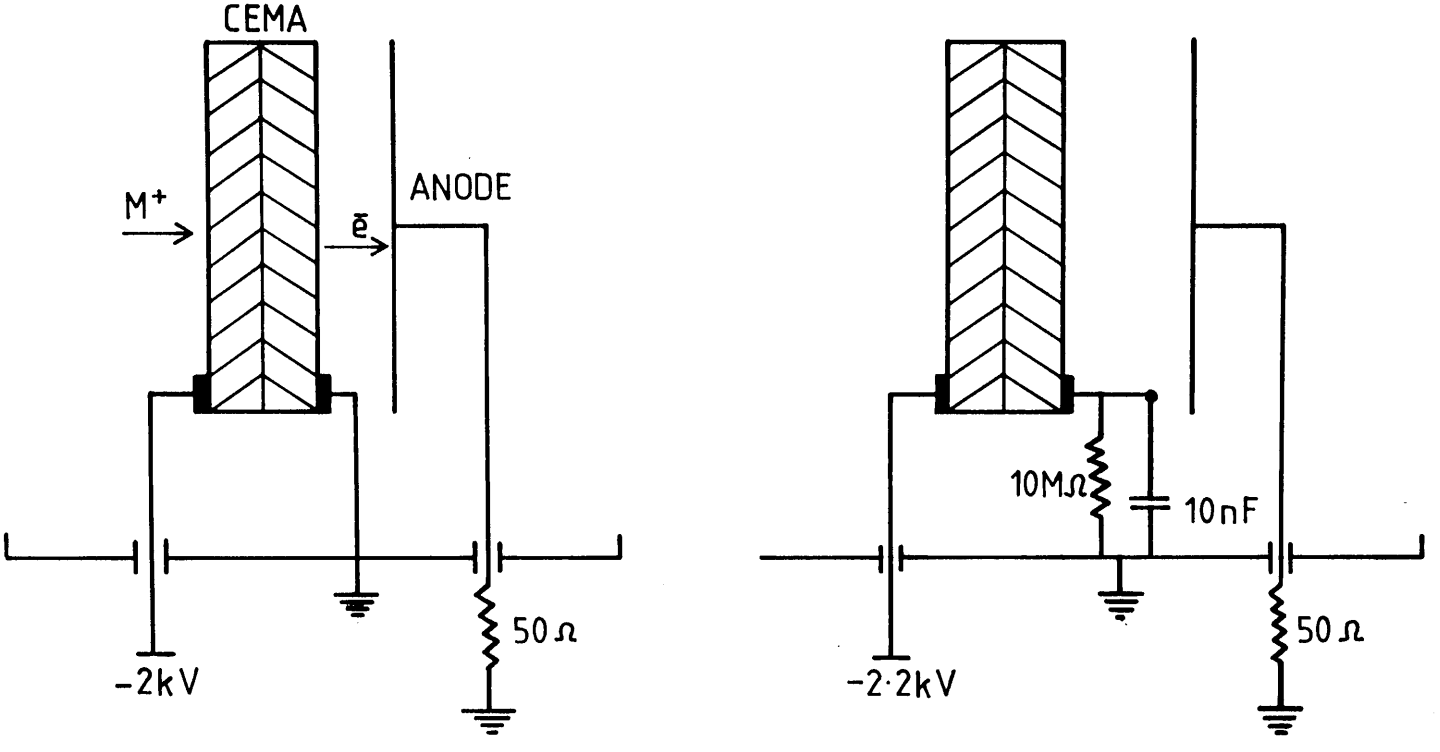

Fig. 2.1.6 (a) Original detector biasing (b) Modified arrangement

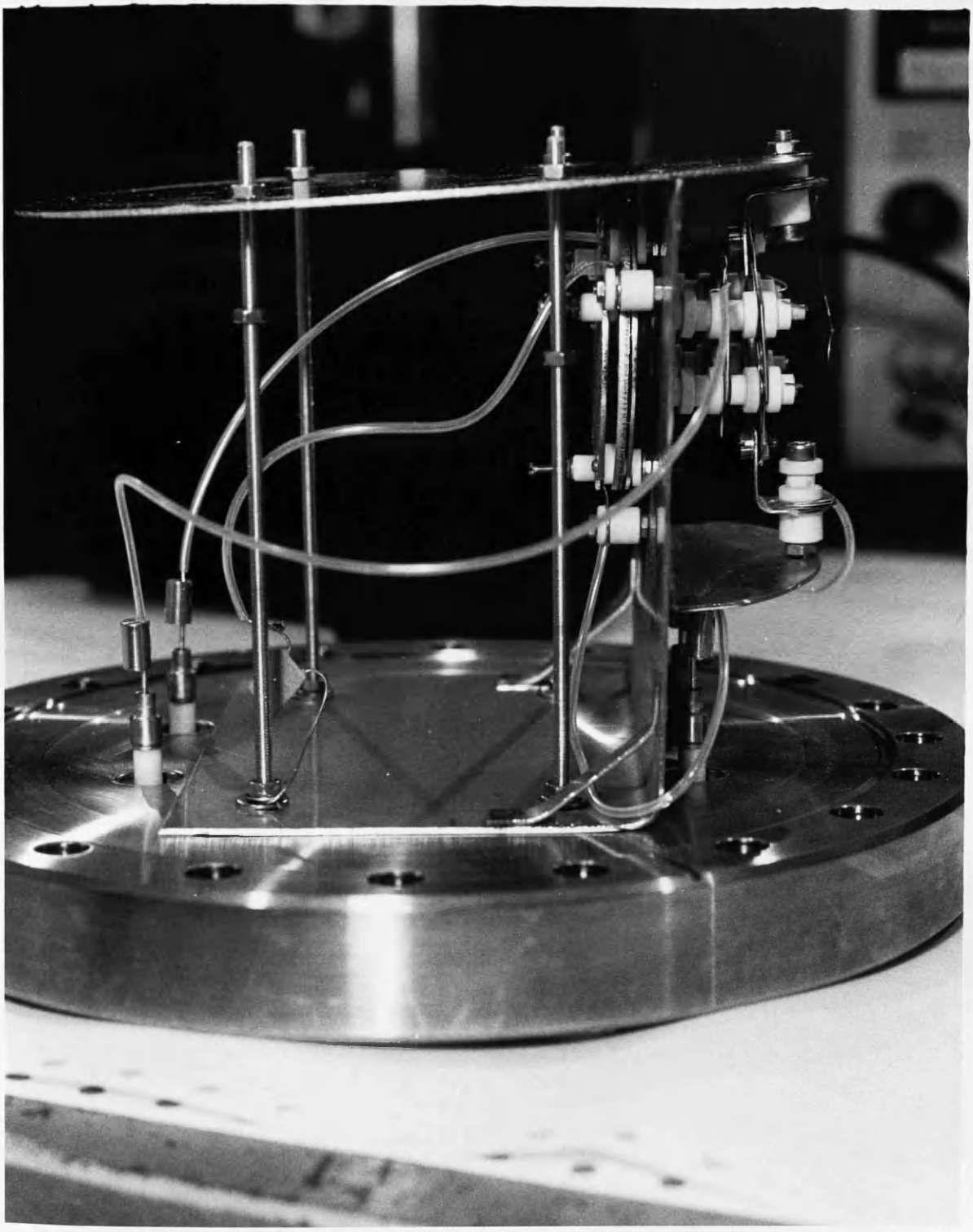

Plate 2. The dual CEMA detector and low energy filter assembly

directly in front of the detector. The earthed plate above the detector provides a screen against stray ions in the drift tube. The fine EPG wire is just visible to the right of the filter.

The main chamber is pumped by a large oil diffusion pump (Edwards Difstak 160/700ls^{-1}, Edwards High Vacuum, Crawley, UK) fitted with a liquid nitrogen cold trap, and by a titanium sublimation pump (Kratos XSAM-800). A turbomolecular pump (Edwards ETP6/200ls^{-1}) is fitted to the drift tube. Vacuum pressure is monitored by an ionization gauge (Kratos VC-22 IG) in the main chamber. The system routinely operates at a base pressure of below 10^{-9} torr, the limit of the vacuum gauge.

(2) Atomization source

The sample material can be atomized either through ion sputtering or laser ablation.

(i) Ion sputtering

The system is fitted with a MiniBeam 2 Ion Gun (Kratos MB-2). This is designed to deliver a d.c. current (<30μA) of gas ions (usually argon) into a small spot (<1x1mm^2) at energies of up to 5keV. The gun has no provision for rejection of energetic neutral or contaminant ionic species at the output.

For use on the TOF system it was necessary to devise a method of pulsing the gun's output. The method most frequently employed to achieve this is on other ion gun models is to sweep a d.c. beam acros a narrow aperture [164]. The small dimensions of the gun's lens stack and the limited gun-to-sample distance (<5cm) did not allow this to be done here. Instead, it was decided to pulse the ion formation process within the gun itself [165]. The gun's ion source region is shown in Fig. 2.2.1. Ion formation was modulated by applying

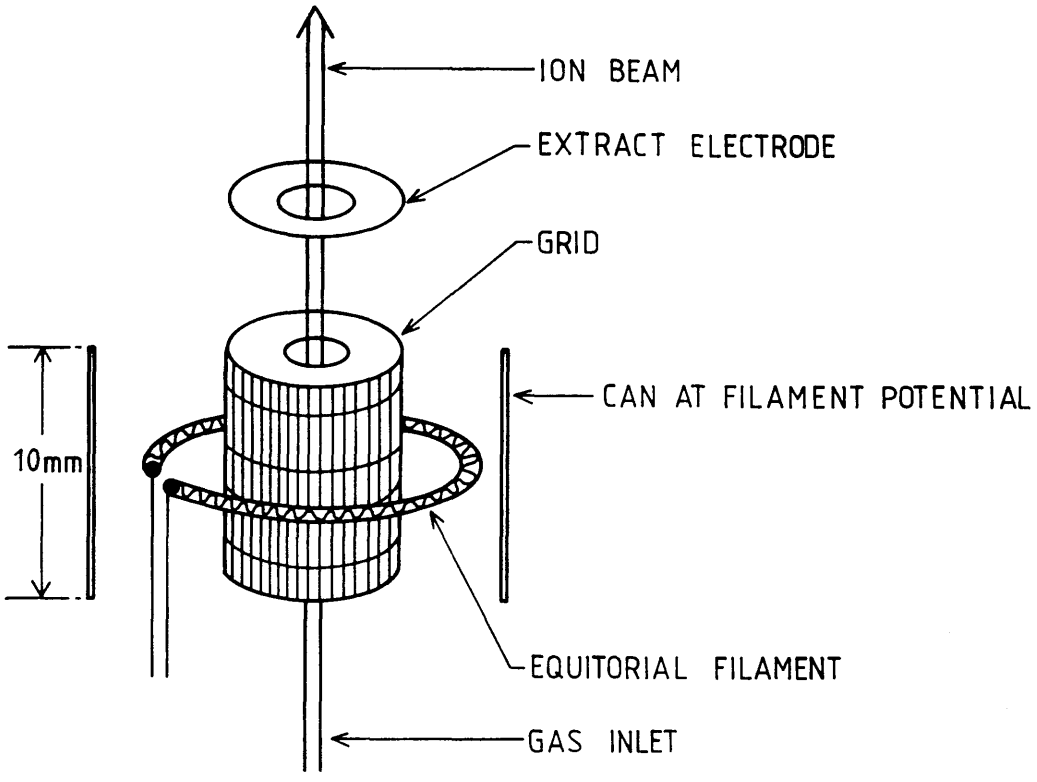

Fig. 2.2.1 Kratos Minibeam-2 Ion Gun source region

Fig. 2.2.2 Voltage pulse and relative electrode potentials

(Where: E_0 is the ion beam energy; V_{EXT} the extract potential; V_{FIL} the filament potential and V_{GRID} the potential of the grid)

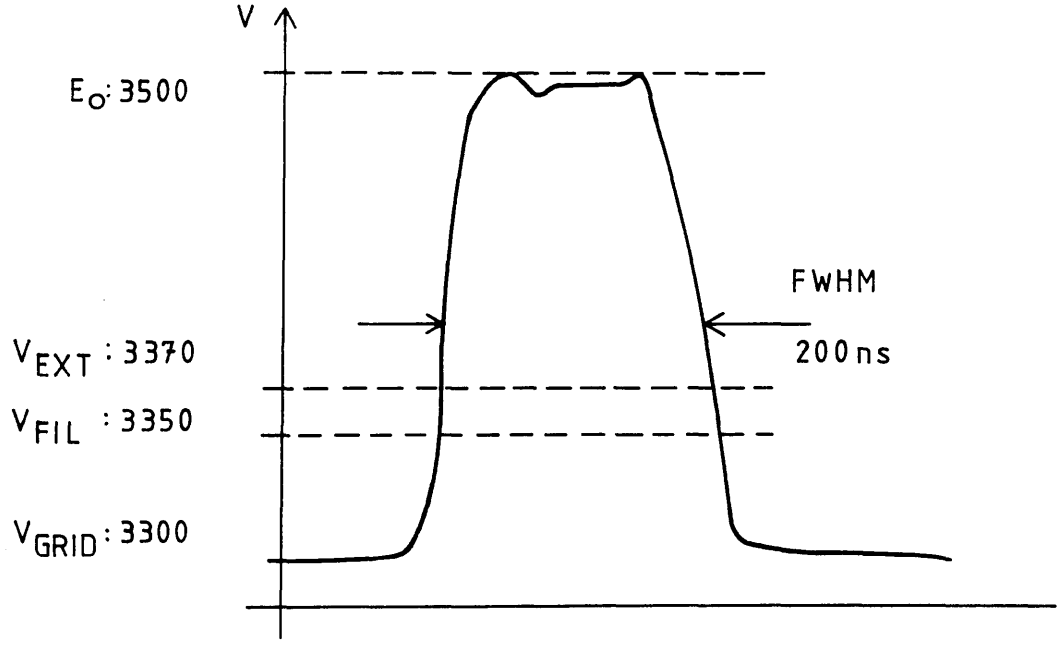

a voltage pulse between the grid and the filament. The voltage pulse and the relative potentials of the various electrodes are shown in Fig. 2.2.2. The circuit used to generate the pulse is given in Fig. 2.2.3. The resulting current pulse is mirrored in the shape of the TOF-SIMS peak, shown for aluminium in Fig. 2.2.4. The long tail indicates a large spread in kinetic energies for the ions leaving the gun's ion source. This is thought to be due to two main reasons; a large extract volume (defined by the extract potential and the grid potential) and scattering of ions by the high residual neutral gas pressure.

The d.c. ion current from the gun was measured by floating an ammeter between the sample stub and the high voltage power supply providing the electrical bias for the sample stub. It was possible to obtain up to 50μA of current from the gun into a spot size of $\approx 5mm^2$, see below. The pulsed ion current could be monitored using the capacitor de-coupling arrangement shown in Fig. 2.2.5. For pulse lengths >2μs it was possible to achieve ≈5μA pulses. However, the current amplitude diminished rapidly for shorter pulse lengths. For the narrowest pulses obtained (≈0.5μs), the current pulse was barely visible, indicating an amplitude of ≈1μA.

Workers at CMS have shown that it is possible to achieve very short pulses (<60ns) with a similar gun by lowering the gas pressure and by fine tuning the source voltages [166]. Unfortunately, these adjustments lead to a much reduced current amplitude (<1pA) and were consequently not utilized in this work.

The gun suffered from reliability problems, particularly at higher operating voltages. It was therefore necessary to operate the gun at reduced energy (<3.5keV) for reliable operation to be achieved.

With the ion gun running, the working pressure in the system rose to $\approx 5 \times 10^{-8}$ torr.

The gun is designed for operation normal to the sample surface, with an earthed sample and a gun to sample distance of 1". In such a configuration the beam shape is specified to be circular with a diameter of <1mm. In the Kratos

Fig. 2.2.3 High voltage pulser (floating)
0·1μs – 5μs, ≤ 300V

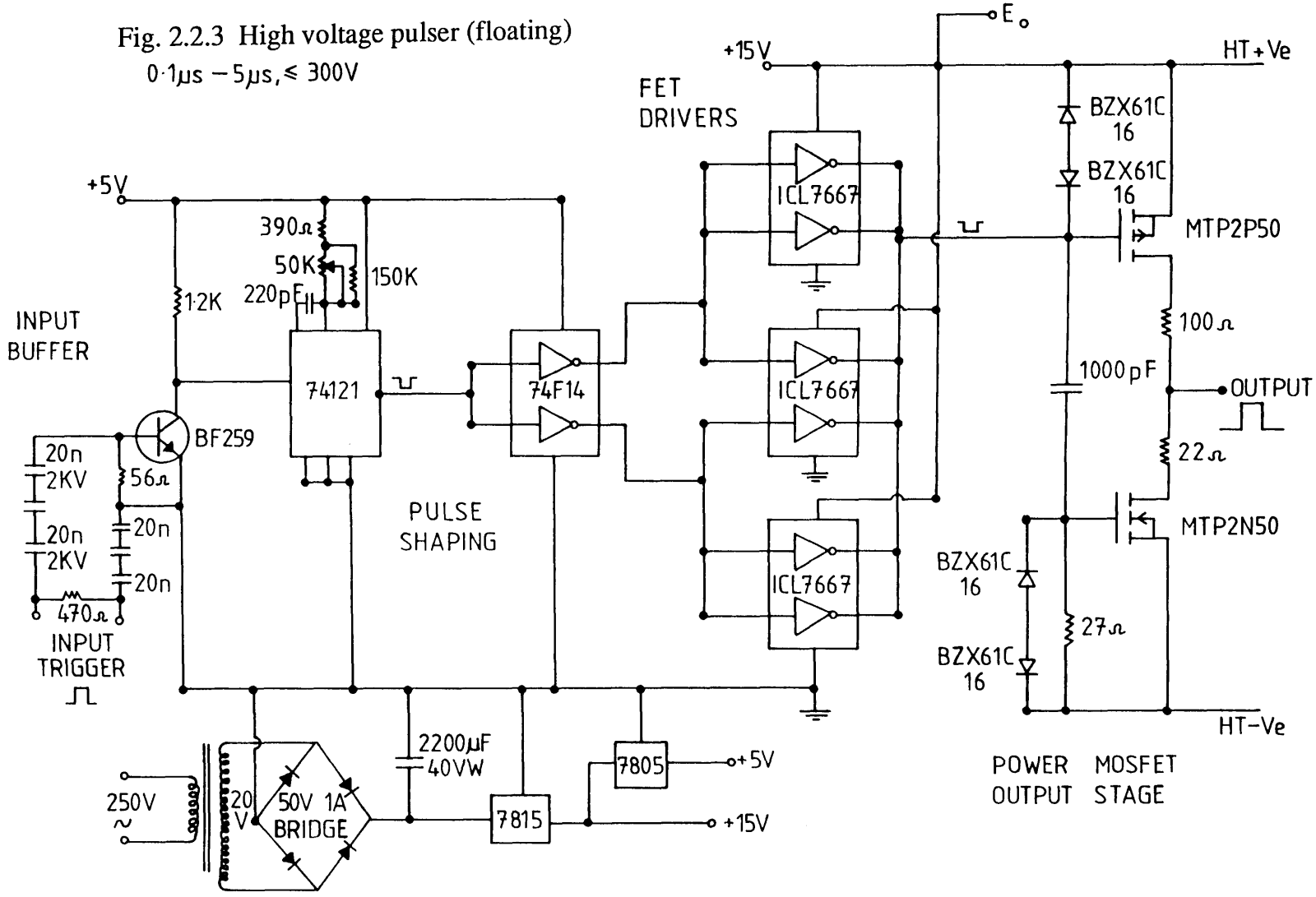

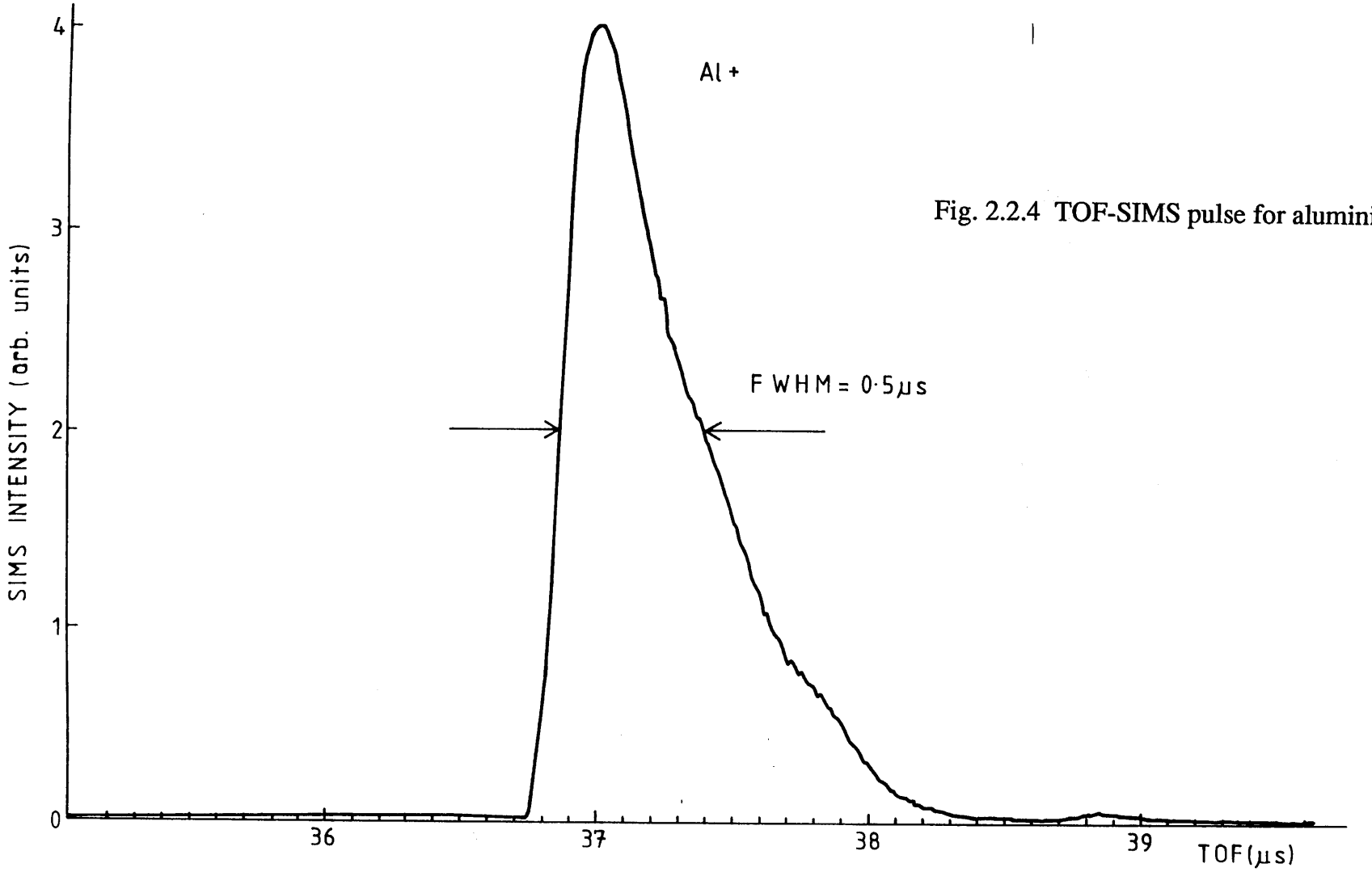

Fig. 2.2.4 TOF-SIMS pulse for aluminium

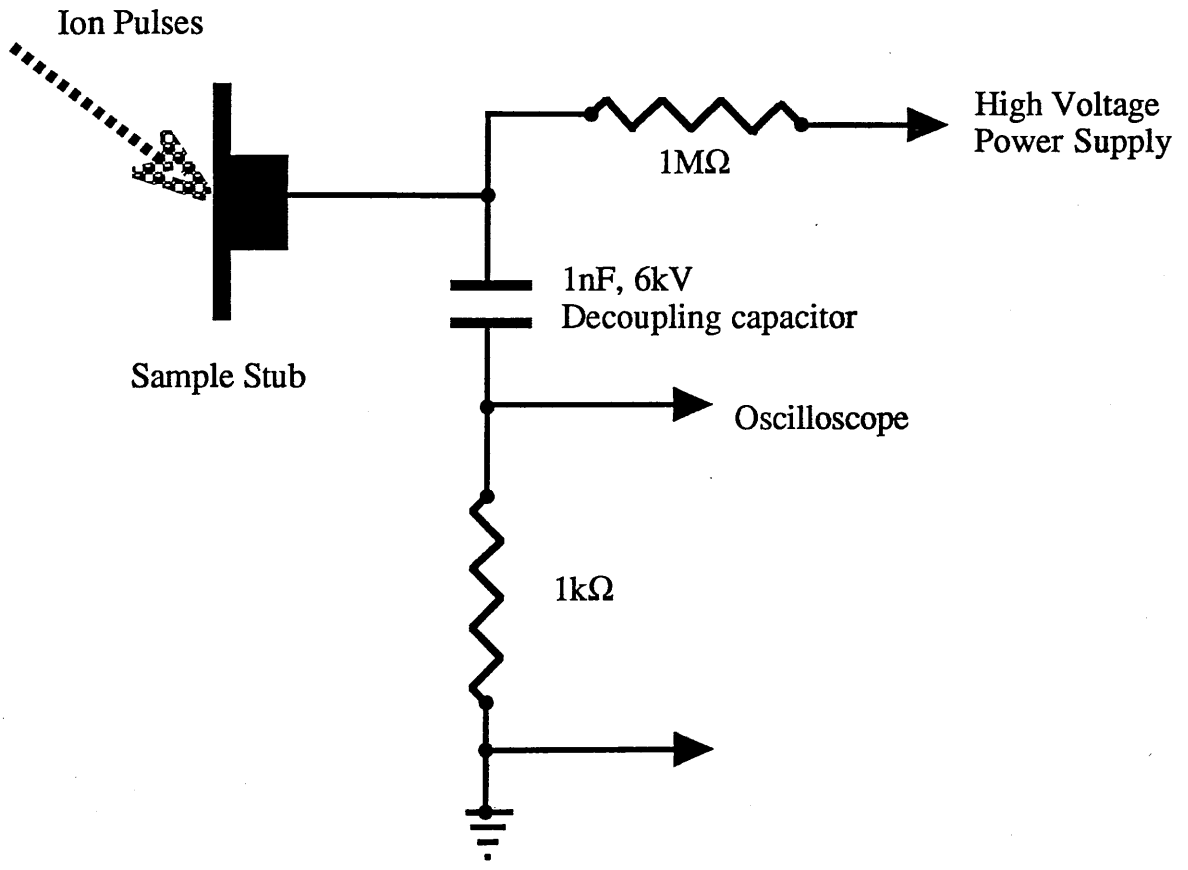

Fig. 2.2.5 H.V. decoupling circuit for monitoring primary ion pulses.

machine the gun's lens stack is at 45° to the sample , the distance to the sample is 2" and the sample is typically held at +1kV, with a field gradient of 300V/cm extending to the first optic. These less than optimal conditions led to an approximately elliptical spot shape, with area $\approx 5mm^2$.

(ii) Laser ablation

A Q-switched Nd:YAG laser was also available for sample atomization (Quantel YG585, Quantel, Cedex, France). The fundamental 1.06μm radiation and its first three harmonics (532, 355, 266nm) were each available. The laser is specified to have a TEM_{00} beam, which is ideal for ablation purposes. However, this was found not to be the case in routine operation. Several distinct hot-spots were observed in the spatial profile (as measured on photographic burn-paper) and these were noted to be time varying. To overcome this problem a ceramic disc diaphragm was inserted into the laser oscillator cavity. This modification also reduced the total available power by a factor of three in the fundamental, to ≈100mJ. The ouput power at 1.06μm was measured to have a pulse to pulse variation of ± 5% and a mean drift of ±6% over an hour of operation. The harmonic generating crystals were not temperature stabilized and this led to drifts in the output power of the harmonics, particularly so for the third and the fourth. Throughout most of this programme of work the fundamental output was preferred for its greater stability. The pulse length is specified to be 15ns. The laser head incorporates a simple optical variable attenuator to allow for precise adjustments of the output power. The ablation spot size and position on the sample were adjusted using a quartz lens of focal length 50cm.

(3) Tunable lasers and optical system

The complete optical system is shown in Fig. 2.3.1. Two pulsed, tunable dye lasers (Spectron SL4000, Spectron Laser Systems, Rugby, UK) are available, both pumped by harmonics generated in a Q-switched Nd:YAG laser (Spectron SL2Q+SL3A). The first ('blue') dye laser is pumped at 355nm and covers the wavelength range from 380nm to 750nm. The second ('red') laser is pumped at 532nm and covers from 550nm to 750nm. In each case the longer wavelength limit being defined by the mechanical scan mechanism in the laser head. Both lasers consist of an oscillator cell cavity and either one or two amplifier cells. The lasers are specified to deliver >20mJ/pulse in the red and >10mJ/pulse in the blue, in a pulse length of 12ns and with a linewidth of $0.1cm^{-1}$ (3GHz). The temporal profile of a dye pulse was measured using a fast photodiode (ITL TF1850, Instrument Technology Ltd., Hastings, UK) monitored on a fast (high bandwidth) oscilloscope (Tektronix 7904/7A24, Tektronix, ORE, USA), Figs. 2.3.2 (a), (b). The output polarisation is linear.

The red laser was relatively easy to operate and routinely delivered 10mJ/pulse. The blue laser, however, proved to be extremely awkward to work with, it frequently taking many hours to achieve laser action at all. The blue laser typically delivered <1mJ/pulse. Pulse energies were measured using calibrated joulemeters (<1mJ, Molectron J-09, Molectron Detector Corp., CA, USA; >1mJ, Gentec ED200 , Gentec, Ottawa, Canada). The spectral output of the blue laser was discovered to be less than pure laser emission with quantities of amplified spontaneous emission (ASE) being produced at all times. This will be discussed in detail in Chapter 4.

Each dye laser has an independent wavelength scan control box. These allow a target wavelength and a scan speed to be specified. The lasers are specified to have a high degree of scan linearity and precise resetability. Early

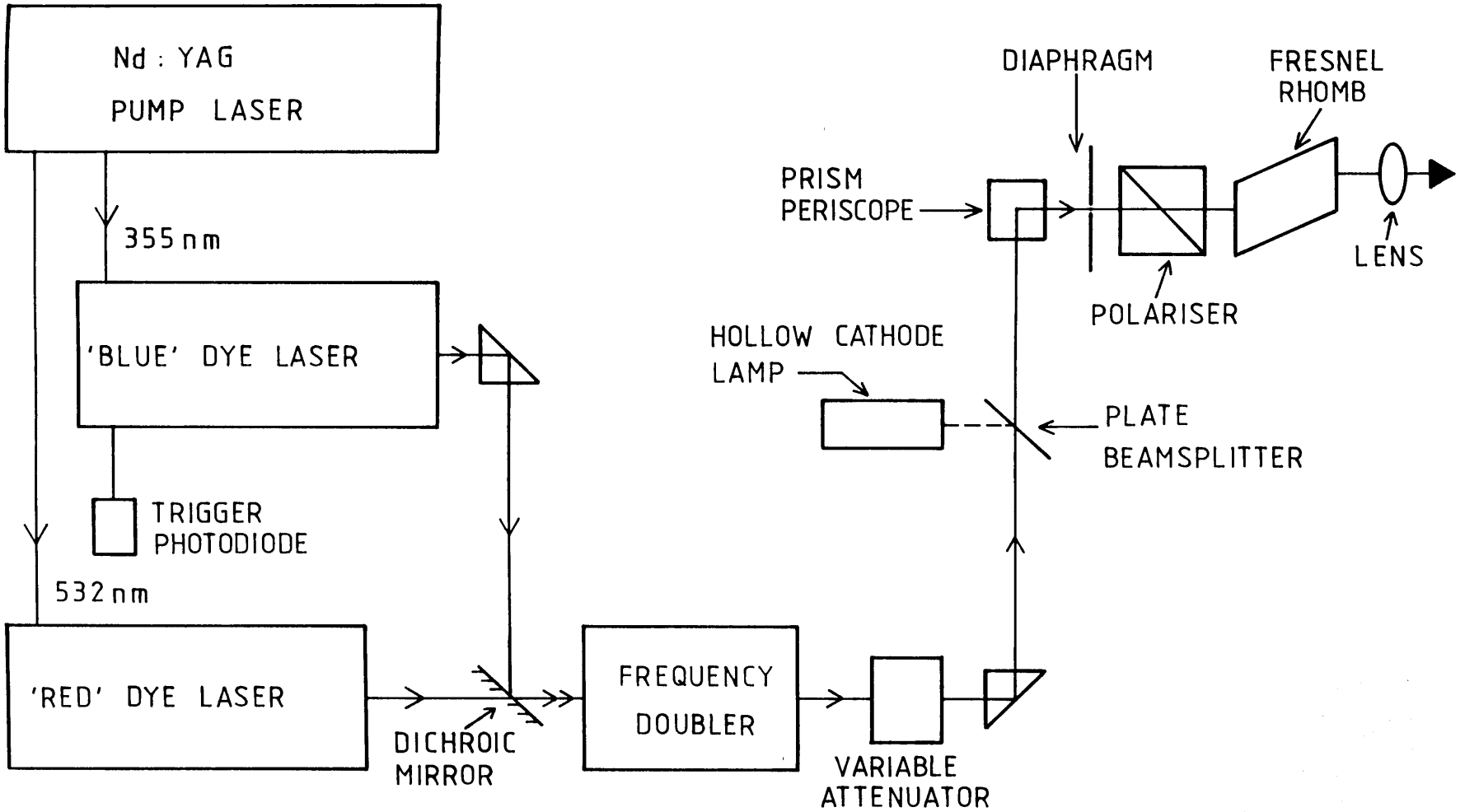

Fig. 2.3.1 Tunable lasers and beam delivery optics

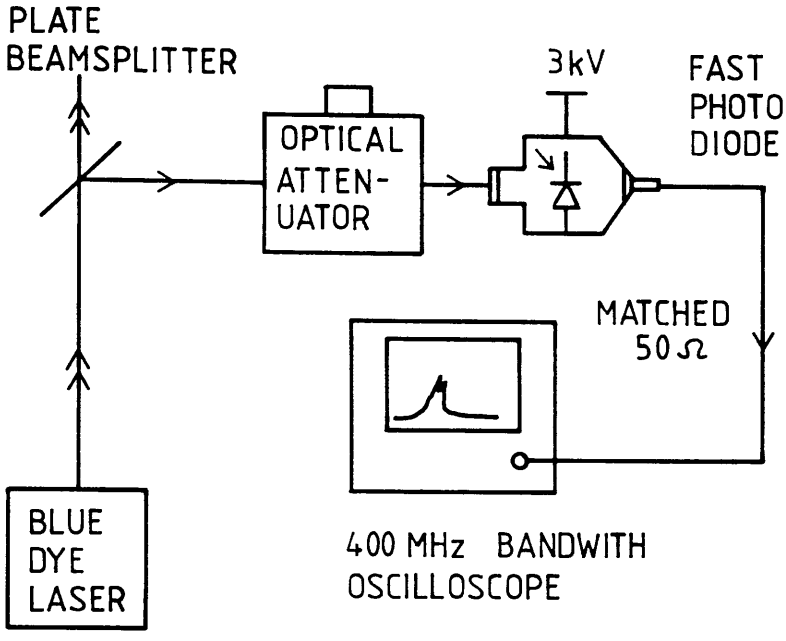

Fig. 2.3.2 (a) Arrangement for laser pulse temporal profile measurement

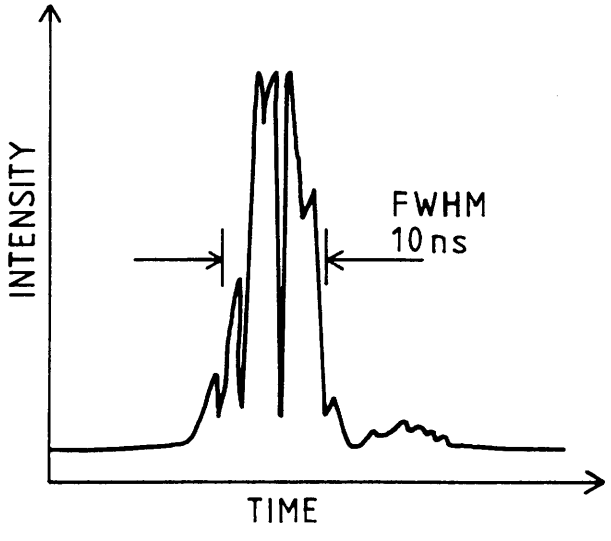

Fig. 2.3.2 (b) Typical temporal profile of a dye pulse

tests showed that both lasers failed to meet specification in both respects, illustrated in Fig. 2.3.3. The figure shows two consecutive wavelength scans monitored on a hollow cathode lamp, allowance was made for 'backlash' between the scans. The manufacturers affected some degreee of improvement by rebuilding the scan mechanisms in the laser heads. The problem does, however, appear to have resurfaced over the last few months of laser use. Wavelength stability was measured to have a thermal drift coefficient of $+0.2cm^{-1}/^{o}C$.

An autotracking frequency-doubling unit (Inrad J-12 "Autotracker", Interactive Radiation Inc., NJ, USA) was also available for the generation of tunable UV radiation (280-370nm).

The laser wavelength was calibrated by monitoring the optogalvanic effect (OGE) signal from a Uranium/Argon hollow-cathode lamp (Juniper 4165, Spectronic Services, Leeds, UK) and comparing this with standard reference tables [167-170]. The power supply provided with the lamp was somewhat 'rudimentary', outputting large amounts of electrical noise. This was rebuilt and satifactory operation obtained.

The laser beams were steered into the MS using right-angled quartz prisms. When two or more colours were required, the beams were combined using dichroic mirrors (Newport Dichroic Edge-Filters, Newport Corp., CA, USA). Purity of linear polarisation was ensured through use of a high quality polarising cube (Newport 10FC16PB.3) positioned immediately before the MS. The polarisation could be changed to circular by inserting a Fresnel rhomb (Spindler and Hoyer 33-7852, Gottingen, West Germany) after the linear polariser. The beams were focussed into the chamber with a quartz lens of focal length 40cm. This was mounted on a precision X-Y translation stage to allow the beam positions to be moved precisely within the ion source region. Largely through reflective losses, typically less than half of the power generated at the laser output was delivered to the source region. The beam

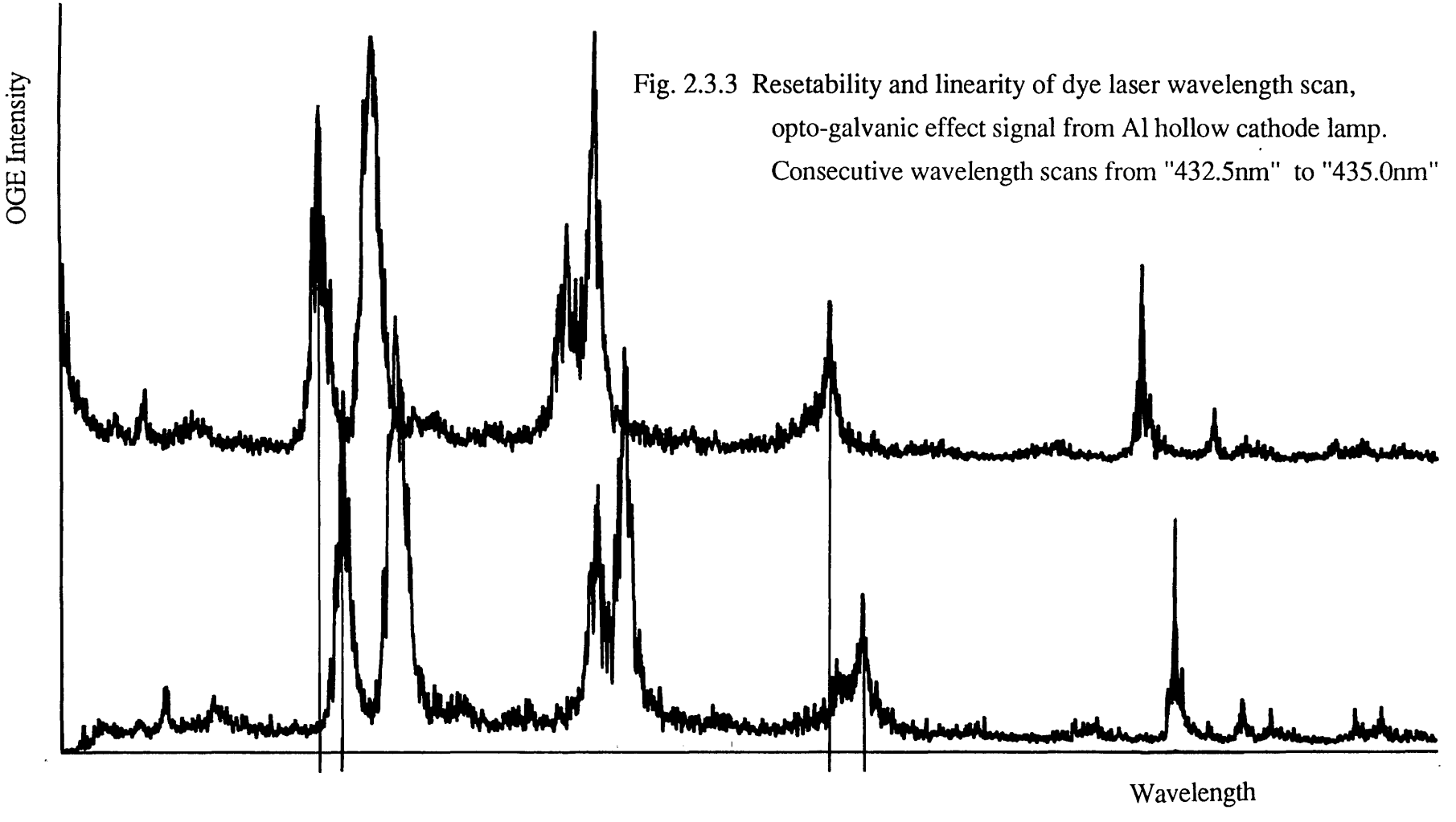

Fig. 2.3.3 Resetability and linearity of dye laser wavelength scan,
opto-galvanic effect signal from Al hollow cathode lamp.
Consecutive wavelength scans from "432.5nm" to "435.0nm"

intensity could be varied using a precision variable optical attenuator (Newport 935-5).

(4) Data Acquisition and Control Electronics

The data acquisition (datac) system is required to measure and process transient ionization signals from the MS and to monitor other experimental parameters (eg. laser power) on a pulse to pulse basis. The control electronics system is required to synchronize the firing of the pulsed atomization source and the ionizing lasers, and provide status and timing signals to the datac system. The system runs under custom software control from an IBM-PC compatible computer. This 'communicates' with the datac and control systems via a GPIB bus. The complete system is shown in Fig. 2.4.1, a detailed discussion of each sub-section is given below.

(i) Data Acquisition

The system is built around two commercial CAMAC units: a LeCroy 2261 transient recorder and a LeCroy 2259 multichannel ADC (LeCroy, Spring Valley, NY, USA). The technology of transient recorders is discussed in Stults et al [171]. The performance of transient recorder based datac systems for isotope ratio measurements with pulsed ion currents (as encountered in this work) have been investigated by Simons [90] and Fassett et al [172].

The 2261 transient recorder is used to measure the pulsed ion signal from the mass spectrometer. The input of the 2261 was configured to accept signals in the range -1.9V to +0.1V. The ion signal from the detector could be either amplified (LeCroy VV100B Pre-amp) or attenuated (Hatfield precision 50Ω attenuator LE10/50, Hatfield Instruments, Plymouth, UK) to match this range. The preamp has excellent noise and linearity performance but displays poor

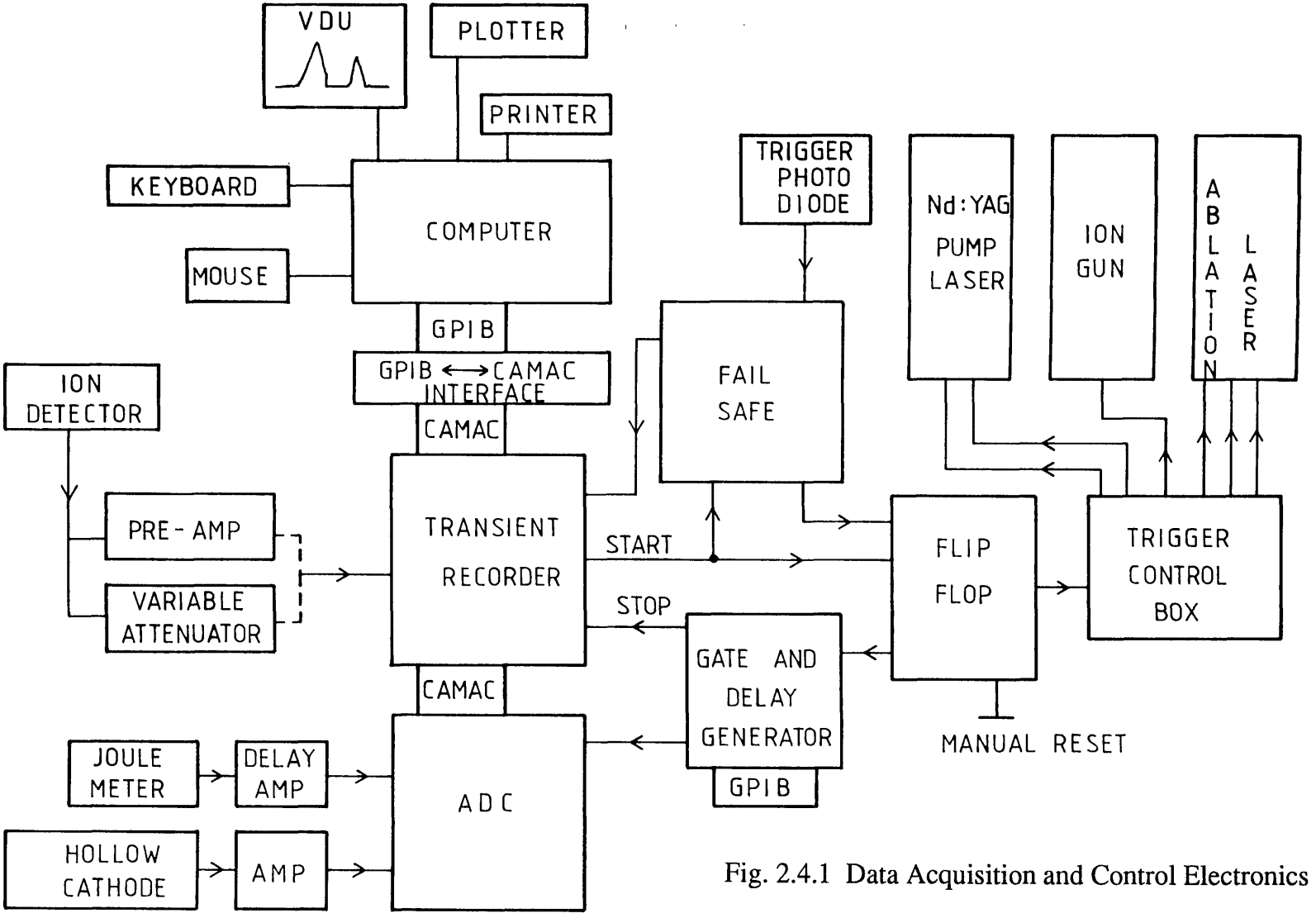

Fig. 2.4.1 Data Acquisition and Control Electronics

overdrive characteristics: input pulses of amplitude >250mV give rise to a large and extended overshoot. The 2261 uses a custom charge coupled device array to store a transient event. The array has 640 time bins, the width of each being set by the period of a clock oscillator. Two clock rates were routinely employed: 20MHz, giving 50ns time bins, and 100MHz, giving 10ns time bins. The total measured 'time-window' is thus 32μs for 20MHz, and 6.4μs for 100MHz. The stored charge in each bin is digitized by an 11-bit ADC, giving at best 1mV resolution over the 2V input range. For this work the 2261 was used as an analogue current integrator, although simple changes to the computer software control (discussed below) should allow it to perform in a digital pulse counting mode. Using an electronic test pulse and precision variable attenuator, the effective dynamic range of the ion signal measurement chain (pre-amp, transient recorder, computer analysis) was measured to be >60dB, Fig.2.4.2 (a) (plot (b) will be discussed below). Using the circuit shown in Fig.2.4.3 (a), the precision and stability of the measurement chain for isotope ratio measurements was measured to be better than $\pm$0.5% for an 'isotope ratio' of forty. A sample output from this measurement is given in Fig. 2.4.3 (b). The 2261 has an inherent noise level of $\approx$3mV and displayed a significant baseline drift with time, these points will de discussed in detail in section (iii), below. The 2261 cannot be used independently in a CAMAC crate since it does not generate the crucial "LAM interrupt". The 2259 ADC is used to set LAM, and hence must always be gated even if not otherwise required.

The 2259 ADC has 12 peak-sensitive input channels sharing a common gate input (ie. all input peaks must overlap within the gate period, typically 1μs). The 2259 has an input range of 0 to -2V, an 11-bit ADC, and hence an effective resolution of 1mV. Typically only two channels were used, monitoring resonant laser power and OGE intensity. Standard nuclear spectroscopy amplifiers were used to shape and delay the required joulemeter and hollow-cathode pulses.

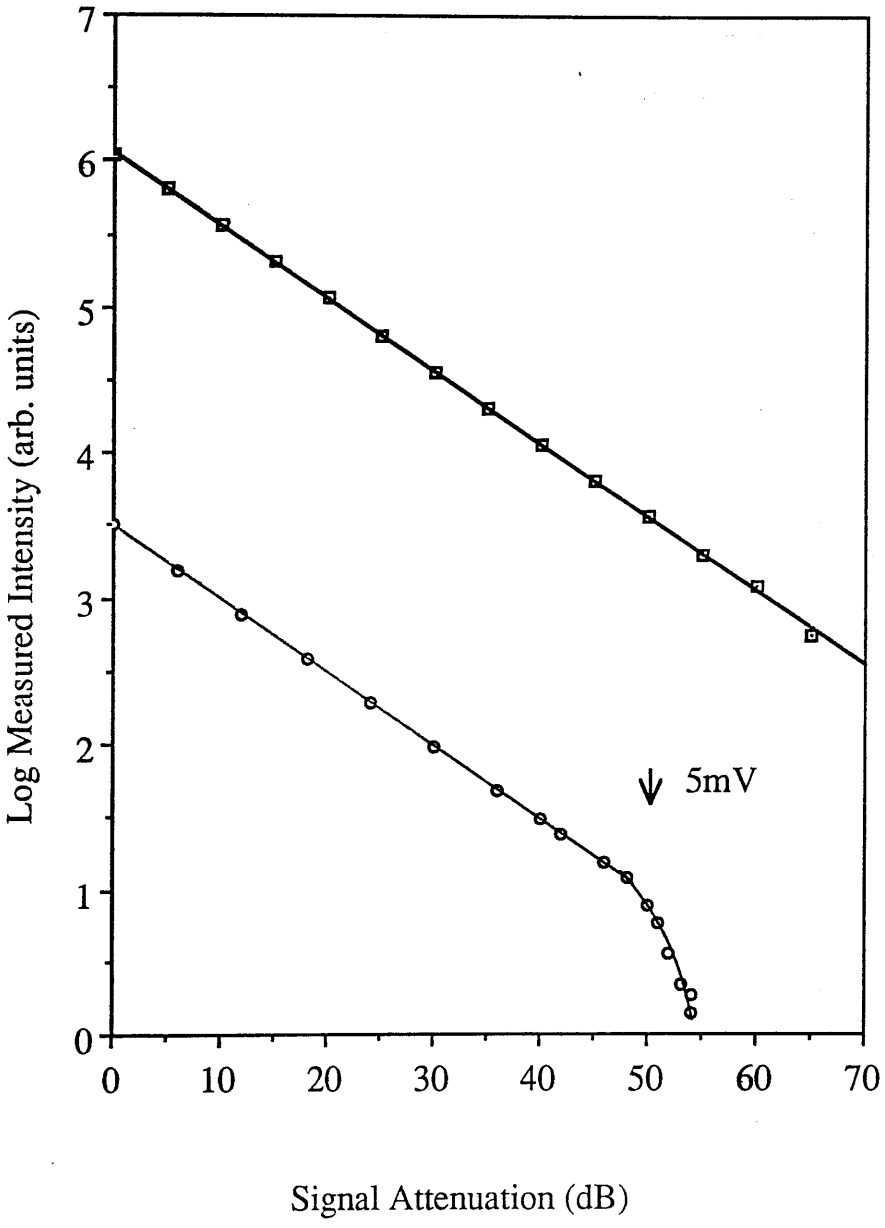

Fig. 2.4.2 (a) [] Linearity of ion signal measurement system, 20Hz 'flip-flop' operation, no discriminator

(b) O Initial baseline correction only, 10Hz operation, discriminator at 3mV. Offset for clarity

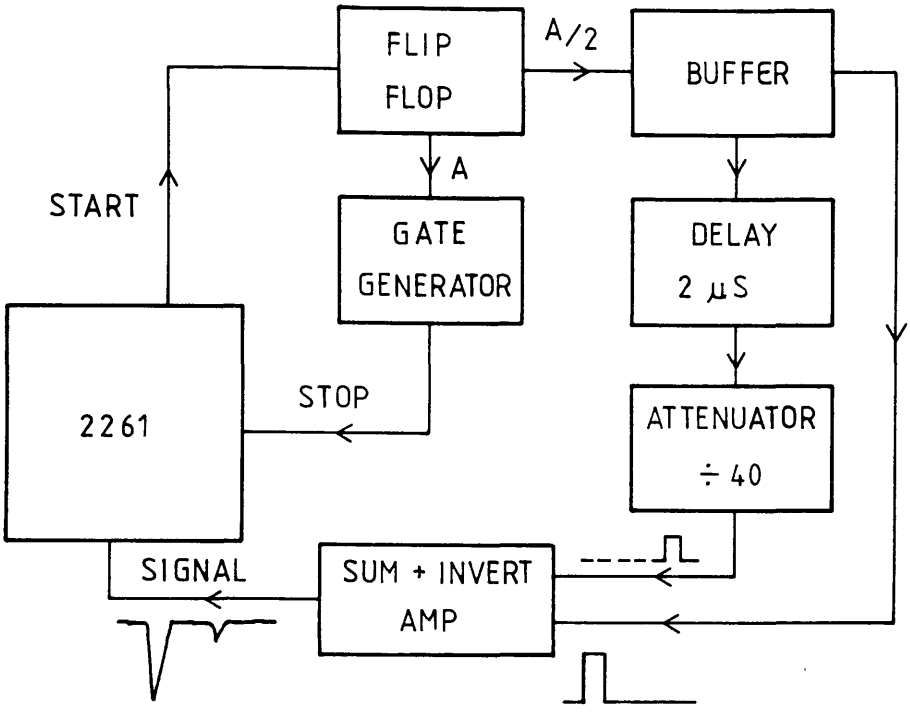

Fig. 2.4.3 (a) Test circuit for isotope ratio precision and stability measurements

Fig. 2.4.3 (b) Sample data spectrum from precision/stability measurements, summation of 1000 pulses

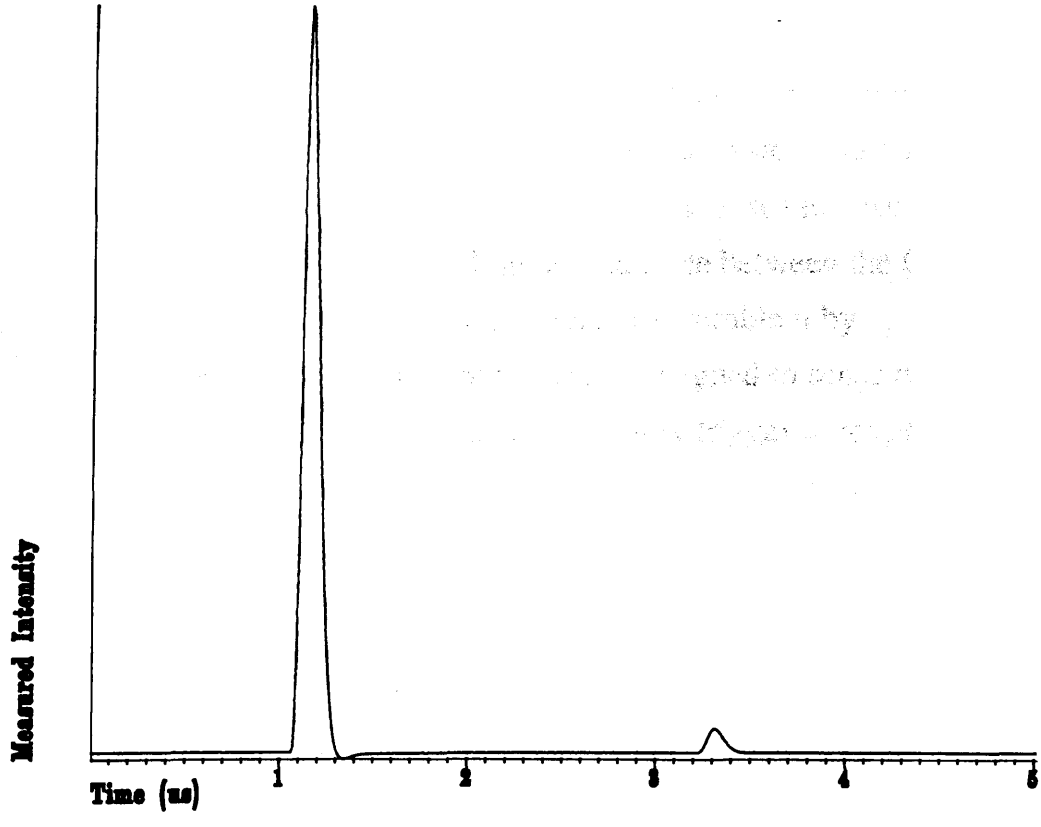

(ii) Control Electronics

The datac sequence is initiated by a start signal from the computer. A series of logic units and gate-and-delay generators then automatically trigger the atomization pulse and the ionization laser. An independent 'trigger control box' was designed and built to deliver the numerous pulses required to fire the two laser systems in precise synchronicity. Standard digital techniques are used to generate the fixed timing delays. The critical timing delay between the firing of the Q-switches of the two lasers is set by a precision analogue monostable. Timing gates for the 2259 and the 2261 are generated by a precision delay generator (SRS DG535, Stanford Research Systems Inc., CA, USA) triggered from a fast photodiode. As will be discussed in greater detail below, it was found to be necessary to correct for the baseline of the 2261 on a pulse to pulse basis. To achieve this, the computer software was set to run at 20Hz and a special flip-flop circuit was designed and built to trigger the lasers at their required 10Hz rate, and to deliver a 'dummy' trigger to the datac timing electronics.

The system should continue to cycle in this closed loop for as long as the computer generates a series of start pulses. However, the system has some intermittent fault at work: periodically (every 10k shots or so) the cycle 'stalls'. This is thought to be due to a fault in the interface between the CAMAC modules and the computer. It was decided to avoid this problem by incorporating a 'fail-safe' unit into the loop. This is designed to sense that the cycle has stalled, clear the 2261 and generate a dummy trigger to reinitiate the cycle. This works well, the system will now run reliably for any length of measurement.

(iii) Computer and Software

The computer is required to initiate the datac cycle and collect, analyze and display (on line) data from the 2259 and 2261 units. Two main Fortran programs were developed: SPEC, for laser spectroscopy investigations; and READ2261 for mass spectrometry. Control signals are sent to, and data received from the CAMAC unit (LeCroy 8901-A) and the SRS digital delay generator via a GPIB bus (NI GPIB-PC 2A, National Instruments, TX, USA). The core of each program consists of a series of GPIB interface calls. Some high-level subroutines from the LeCroy CATALYST software suite were also utilized. Display routines are from the HALO graphics kernel package (Media Cybernetics, MD, USA).

Obtaining accurate data from the 2261 proved to be rather onerous. The measured value from each time-bin must be corrected against the baseline value for this individual time-bin (equivalent to a d.c. offset). At first this baseline value was measured only once at the start of an experimental run. It was later noticed that the baseline was subject not only to random noise fluctuations, as expected, but also to large drifts over the course of a measurement. This problem has largely been eliminated by correcting each time-bin on a pulse to pulse basis, hence the flip-flop arrangement discussed above. Use of this technique also uncovered another subtlety in the 2261's behaviour. The unit is highly temperature sensitive, to the extent that great care must be taken to ensure that the unit is addressed at as near a constant rate as possible. A timing difference of 1ms between data ('flip') and baseline ('flop') loops in the READ2261 program being readily apparent in a baseline shift.

For each laser pulse, the program SPEC stores the integrated ion signal over a specified interval of the time spectrum read from the 2261 (eg. over the Ca^{40} peak) and also any chosen ADC channels. Hence, as the laser wavelength is scanned (independently) a laser spectroscopy spectrum is recorded. In

principle, several ion peaks can simultaneously be monitored.

READ2261 lets the system perform very much as a digital storage oscilloscope in 'summation' mode. Each complete 2261 spectrum is read into a summation buffer for a specified number of shots- typically several thousand laser pulses. The program can also communicate, over the GPIB interface, with the SRS delay generator. This allows the time position of the spectrum to be scanned, and hence a picture of the entire mass spectrum to be built up.

The programs allow for an optional 'software discriminator' to be used, in principle giving an improved signal to noise ratio. Care must be exercised in using this facility: the combination of baseline noise and a discriminator can give rise to low level non-linearities. This point is illustrated in Fig.2.4.2 (b). This facility should really only be employed when the single ion amplitude is at least twice the noise level.

Once stored, data can be further analyzed and hard-copy obtained using various custom programs. In paricular, a large and sophisticated software suite, PLOT, has been developed by Mr.P.T.McCombes (SERC postgraduate student) to analyze mass spectra in a 'user-friendly environment'. PLOT performs the time to mass scaling of spectra (as discussed above) and gives quantitative peak area analysis. The signal intensity for a mass peak was measured by integrating over the peak width, equivalent to analogue current integration. This required a degree of subjective assessment, particularly when peak shapes were corrupted by electrical ringing, and consequently contributed to measurement imprecision.

---

3. Preliminary Investigations

This chapter will detail some of the preliminary investigations carried out on the Kratos Machine. The purpose of these early experiments was largely to determine optimal operating parameters for the instrument for both analytic and spectroscopic investigations.

(1) Background Laser Ionization

Much of the early work in the LIS Group at Glasgow focussed on the laser ionization of trace organic impurities within vacuum systems. The doctoral thesis of M. Towrie [175] provides an in-depth review of this field. These early investigations yielded two major results of great importance to ultra-trace RIMS analysis. Firstly, in even the cleanest of UHV systems, there always exists a partial pressure of aromatic hydrocarbon impurity gases, primarily phenol and toluene [176]. (The recent results of Marshall et al (1990) [236] suggest that aniline may also be a significant contaminant.) The presence of plastic materials inside of the vacuum system or the use of synthetic oil diffusion pumps can significantly increase the levels of such contaminants. Secondly, aromatic hydrocarbons can be ionized with very high efficiency using UV radiation (<300nm) in a one photon resonant, two photon ionization process ("1+1"). The frequency quadrupled output from a Nd:YAG laser (266nm) has been shown to be a particularly effective ionizing wavelength, lying close to a major resonance for the aromatic structure. For low laser fluences (<100μJ/mm^2) it is possible to obtain parent ion molecular peaks (eg. at 92 amu for toluene), but at higher

fluences (>100μJ/mm^2) extensive fragmentation takes place, giving rise to ions at many masses below that of the parent [176, 236].

The implications for RIMS analyses using high intensity UV radiation are quite clear, ultimately the attainable sensitivity will be limited by isobaric interferences arising from laser ionization of hydrocarbon impurities present in the vacuum system. This problem has indeed been encountered by Fassett and co-workers in their analyses of I [177], Re and Os [66].

From a pragmatic, experimental point of view, background ionization can be put to good use, providing a source of free neutrals, with uniform spatial distribution throughout the ion source region, at the expense of no effort from the user! Thus, an ion signal could be generated in the Kratos Machine simply by introducing a tightly focussed beam at 266nm into the source region. This simple process is the way in which the mass spectrometer's acceptance volume was mapped out (see Chapter 2).

As mentioned above, the use of high intensity UV laser beams can give rise to extensive fragmentation of the impurity hydrocarbons, the mass spectrum obtained from the Kratos Machine is shown in Fig. 3.1.1 (a). The background pressure in the system was <1x10^{-9} torr. Clearly some large hydrocarbon species is constituent within the vacuum, the most likely candidates being the oils used in the rotary and diffusion pumps. The diffusion pump oil, tradename "Santovac" (C.V.C., Rochester, N.Y., U.S.A.), has the chemical structure of a poly-phenyl ether, Fig. 3.1.1 (b), comprising a long chain of aromatic groups, an ideal candidate for fragmentation under UV irradiation.

(2) Pulsed Ion Gun Results

The basic Kratos Minibeam ion gun, and the modifications made to allow pulsed operation, have already been described in Chapter 2. Several

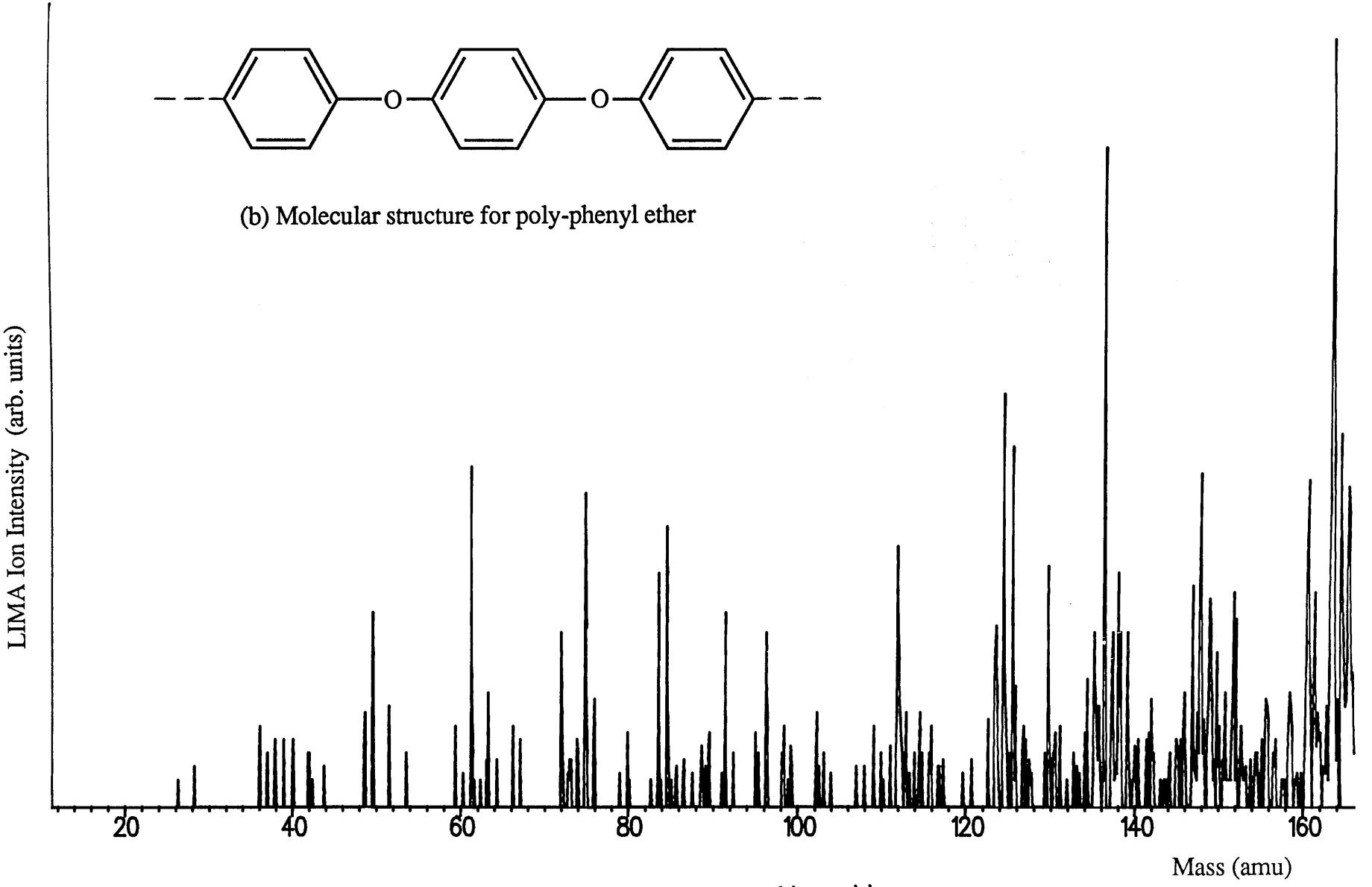

Fig. 3.1.1 (a) Laser ionization (266nm) of background impurities

major difficulties were immediately encountered in operating the ion gun. Reliability was poor even at reduced operating voltages (3.5kV cf. the specified 5kV), electrical sparks and arcing necessitating frequent major rebuilds of much of the electronic circuitry. The need to run at a reduced voltage in turn led to a poor primary ion beam spot size on the sample surface. Using a sample made from a mixture of graphite and calcium carbonate, spot sizes were estimated from the fluorescence clearly visible from the sample surface with the gun running in continuous mode (see Chapter 5 for details of the sample preparation). The best spot size and shape achieved was roughly elliptical, with length ≈4mm, width ≈2mm, and an estimated area of ≈5mm^2.

With the mass spectrometer set to transmit ions generated at the sample surface, it was possible to obtain crude time-of-flight SIMS spectra, an example from the graphite/calcium carbonate sample is shown in Fig. 3.2.1. The observed ion signal was low, but quite usable. Clearly the mass resolution was limited by the temporal width of the ion sputter pulse, the individual calcium isotopes could not be resolved.

Attempts to generate a signal using laser postionization of sputtered neutrals met, however, with only limited success. The first experiment attempted, involved using the ion gun in d.c. mode to sputter rubidium atoms from a RbCl sample. A blue postionization laser was then scanned over the wavelength range 415-430nm. With the transient recorder gate set to cover the mass range 85-87amu (i.e. both Rb isotopes), the mass spectrum shown in Fig. 3.2.2 was obtained. However, when the ion gun was pulsed, only the most tenuous of signals were observed. Both resonant and non-resonant lasers were used, a wide range of delay times and relative beam positions were tried, and both rubidium and calcium samples were investigated. This disappointing result is thought to be due to both the low primary ion beam current intensity (and the consequent low density of sputtered neutrals

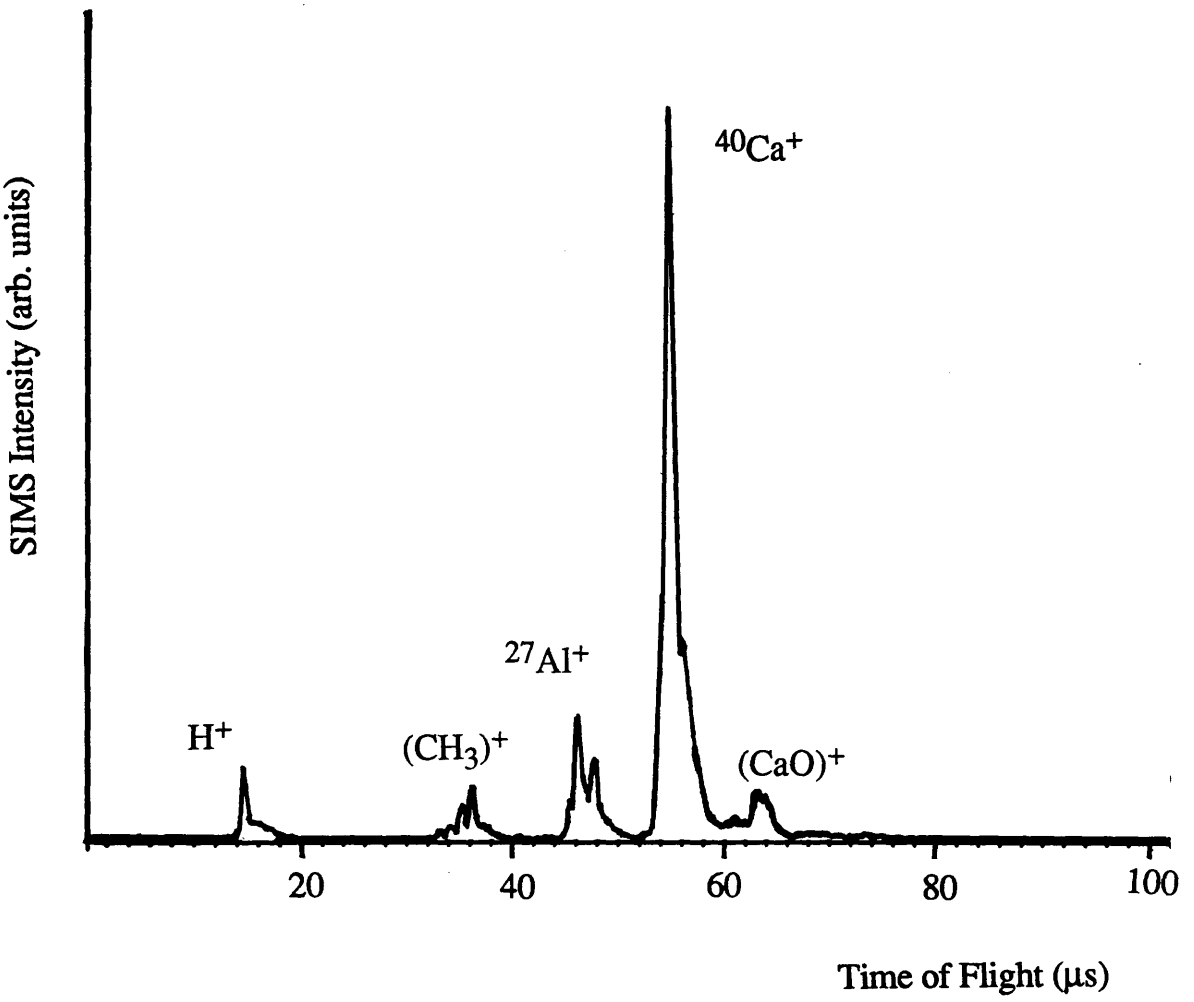

Fig. 3.2.1 TOF spectrum for Ca SIMS ions

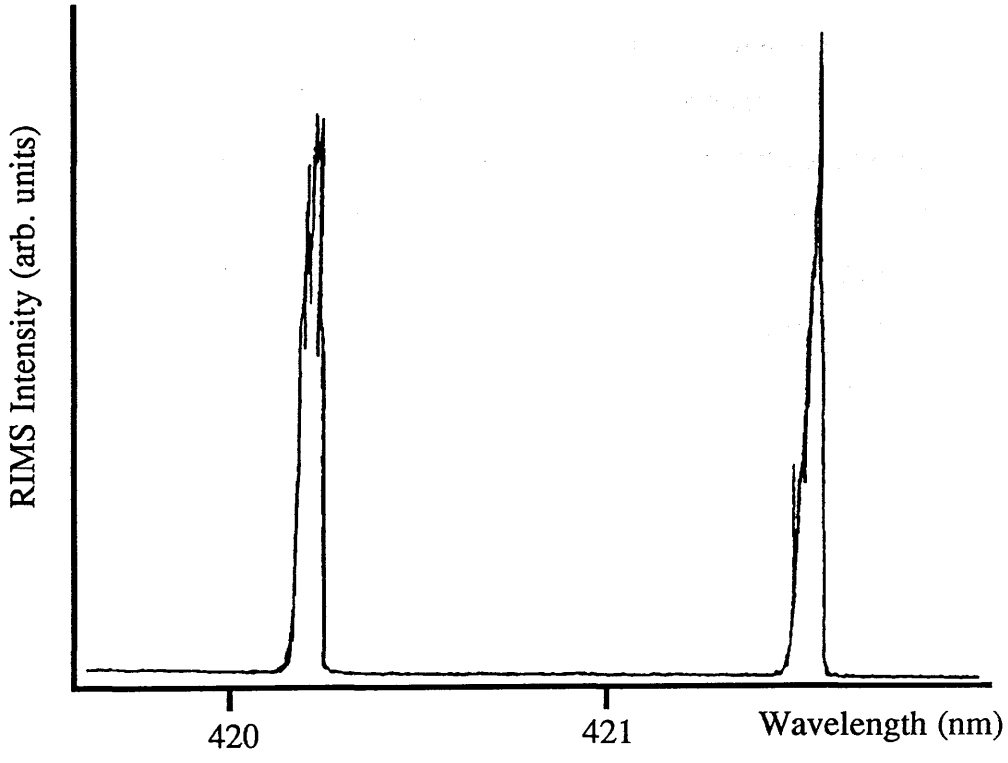

Fig. 3.2.2 RIMS spectrum for Rubidium

available for post-ionization) and the low geometric overlap between the ionization lasers and the sputtered plume. The poor reliability of the gun severely limited attempts to improve upon these results.

In direct comparison, it was found to be relatively straightforward to generate large laser postionization signals when utilizing laser ablation as the atomization technique. In light of these observations, further development effort with the Minibeam gun on the Kratos Machine was not felt to be warranted and all subsequent experiments were conducted utilizing laser ablation. (In a separate series of experiments, Mr. C.J. McLean of the LIS group has obtained good experimental RIMS data using a similar ion gun. The high reliability of this particular gun has allowed a systematic programme of instrument optimization to be carried out, with consequent benefits in measurement capability.)

(3) Laser Ablation Studies

From an experimental standpoint, laser ablation has several very great strengths as an atomization technique. With readily achievable intensities, sufficient ions are generated in the ablation process to generate a mass spectrum. An example of such a 'LIMA' spectrum is shown in Fig.3.3.1, the ablation wavelength was 1.06μm, the fluence ≈5mJ/mm^2, and the sample again was the graphite/calcium carbonate mixture. The short pulse length of the ablation laser (≈10ns) allows high mass resolution to be achieved routinely, giving clear isotopic identification. This ability to generate such high quality spectra, without the added complexity of postioinzation lasers, was found to be most useful in setting up the instrument.

A series of experiments was conducted to determine various important parameters of the ablation process, and consequently how best to harness

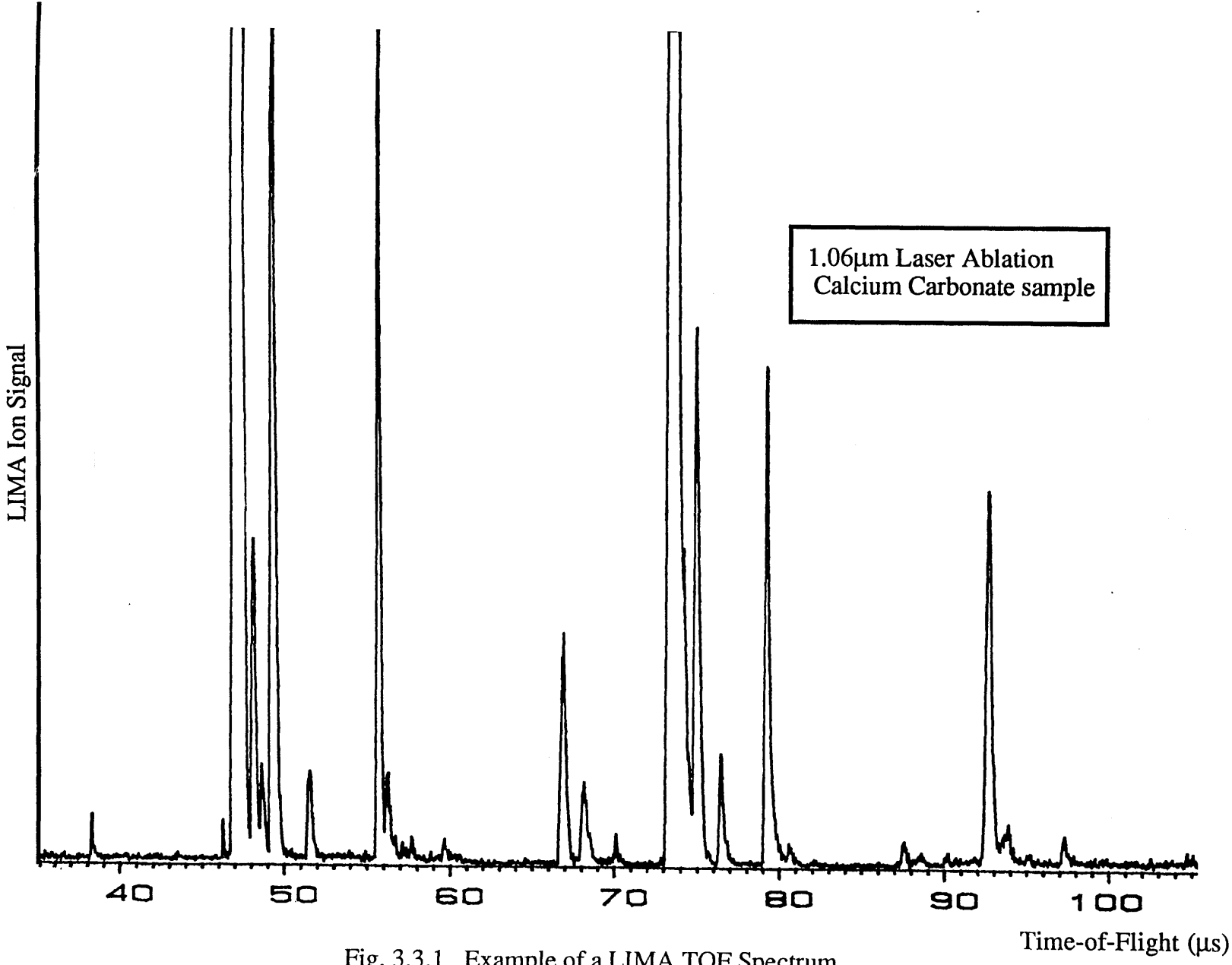

Fig. 3.3.1 Example of a LIMA TOF Spectrum

laser ablation as an atomization source for RIMS. For all of these measurements a simple calcium metal sample was used, again see Chapter 5 for sample preparation details. For all measurements, the ablation beam struck the sample surface at an angle of ≈45° to the normal.

(Subsequent to these early measurements, much further research into the laser ablation process has been carried out in the LIS group, some of these results have been reported in McCombes et al 1990, [178].)

(i) Ion and Neutral Yield Variations with Ablation Fluence

The first and simplest experiment to be carried out ,was to investigate the change in the LIMA ion signal as the laser ablation fluence was varied. An ablation wavelength of 1.06μm was used, with a spot size of $1mm^2$, as defined by an aperture in the beam path, and with a simple aluminium metal sheet as a sample. Laser pulse energy was measured with a calibrated Gentec joulemeter. The results are shown in Fig. 3.3.2(a). The signal intensity is observed to level off at a fluence of $\approx 2mJ/mm^2$ (corresponding to a flux of $2x10^7$ W/cm^2), far below the levels typically employed for LIMA analysis (10^{10} W/cm^2). At saturation fluences, the time-of-flight spectrum was observed to be degraded, with severe peak broadening and instability being evident. This is thought to be due to the space charge effect generated by the large number of LIMA ions created at higher ablation fluences.That is, the same absolute number of ions can be created at lower fluences with large spot sizes as with intense, tightly focussed beams.

The mass spectrometer was then set to reject LIMA ions and to accept the lower energy postionization ions (reflect potential < sample potential). It was, however, noted that it was possible for a significant LIMA signal to 'break through' for ablation fluences $>2mJ/mm^2$. This would seem to corroborate the idea that the observed LIMA saturation is due to a space charge effect. A dense electron cloud in front of the sample will reduce the

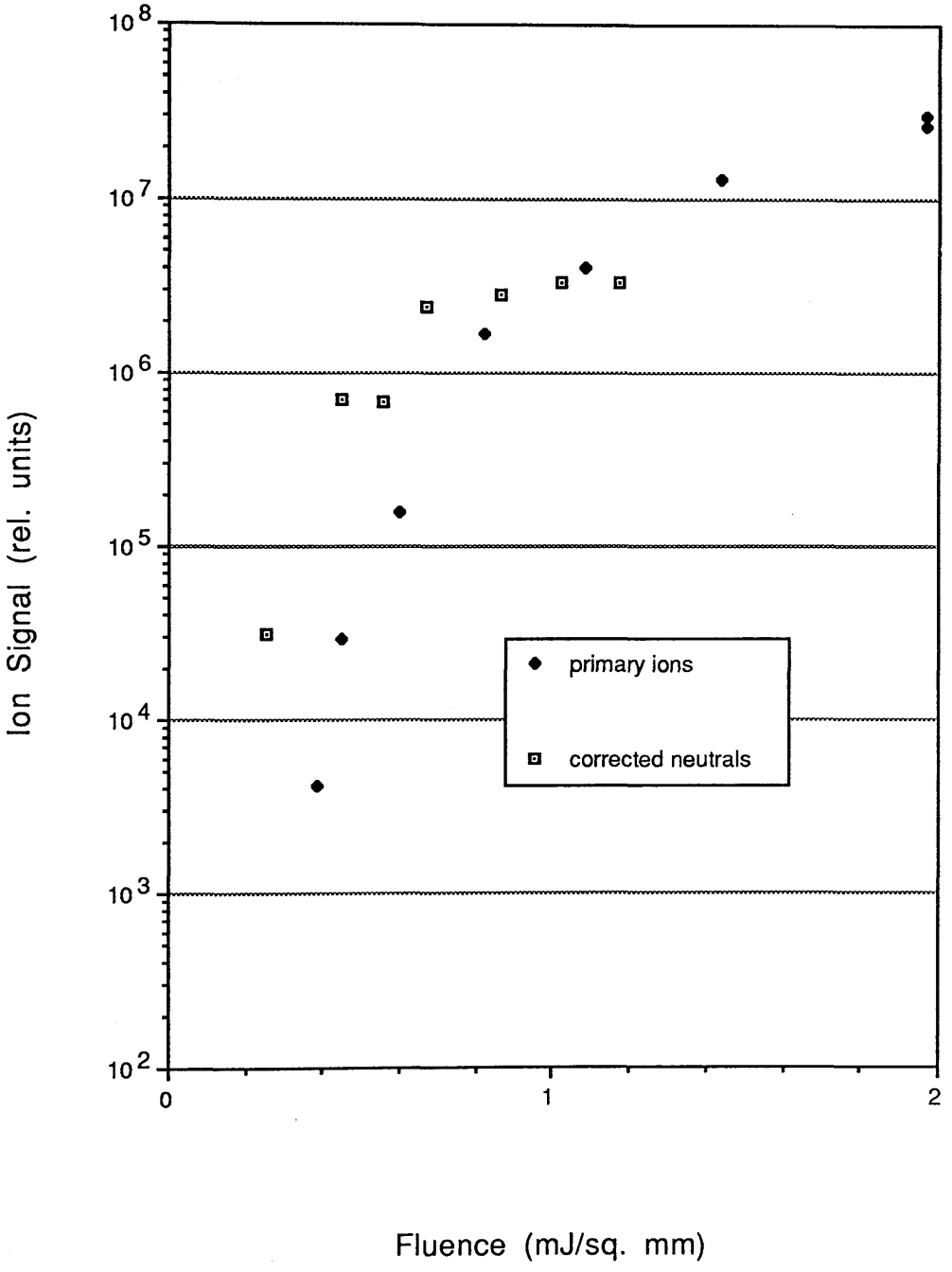

Fig. 3.3.2 (a) Aluminium neutral atom yield / laser ablation fluence
(b) Aluminium LIMA ion yield / laser ablation fluence

effective potential that positive ions are accelerated through, and consequently lower the kinetic energy of the ions.

Ablated, neutral aluminium atoms were then postionized using the fourth harmonic (266nm) of the Spectron Nd:YAG laser, the results are shown in Fig. 3.3.2 (b). The RIMS data is observed to saturate at a lower fluence level, $\approx 1 mJ/mm^2$, than observed for the LIMA data. For ablation fluences $>1 mJ/mm^2$, the time-of-flight spectrum obtained with postionization of ablated neutrals was observed to become distorted and unstable.

The experiment was then repeated with a calcium metal sample. A blue laser beam was introduced into the source region to effect resonance ionization of laser ablated neutral calcium atoms. The blue beam passed parallel to the sample surface, at a distance of ≈2mm, with a time delay of ≈2μs, and was loosely focussed. Broadband amplified spontaneous emission (ASE) excited the first transition, with the laser emission being tuned to a further bound-bound transition and thence photoionizing this upper excited state (see Chapter 4). The variation in RIMS intensity with laser ablation fluence was then measured, see Fig 3.3.3, with a close similarity to the aluminium results being observed. With the calcium sample and an ablation fluence of $\approx 1 mJ/mm^2$, it was possible to obtain RIMS ion signals several hundred times more intense than obtainable with LIMA, see Chapter 5.

These data sets suggested that an ablation fluence of between one and four (mJ/mm^2), for a $1 mm^2$ ablation spot size, would be optimal for RIMS analyses with the Kratos Machine.

(ii) Energy Distribution of Ablated Neutrals

In the above experiment, the delay time between ablation laser and ionization laser pulses was set at ≈2μs, the value which gave rise to the greatest signal intensity. The effect of varying this delay time was then investigated. The experimental arrangement remained similar to that noted

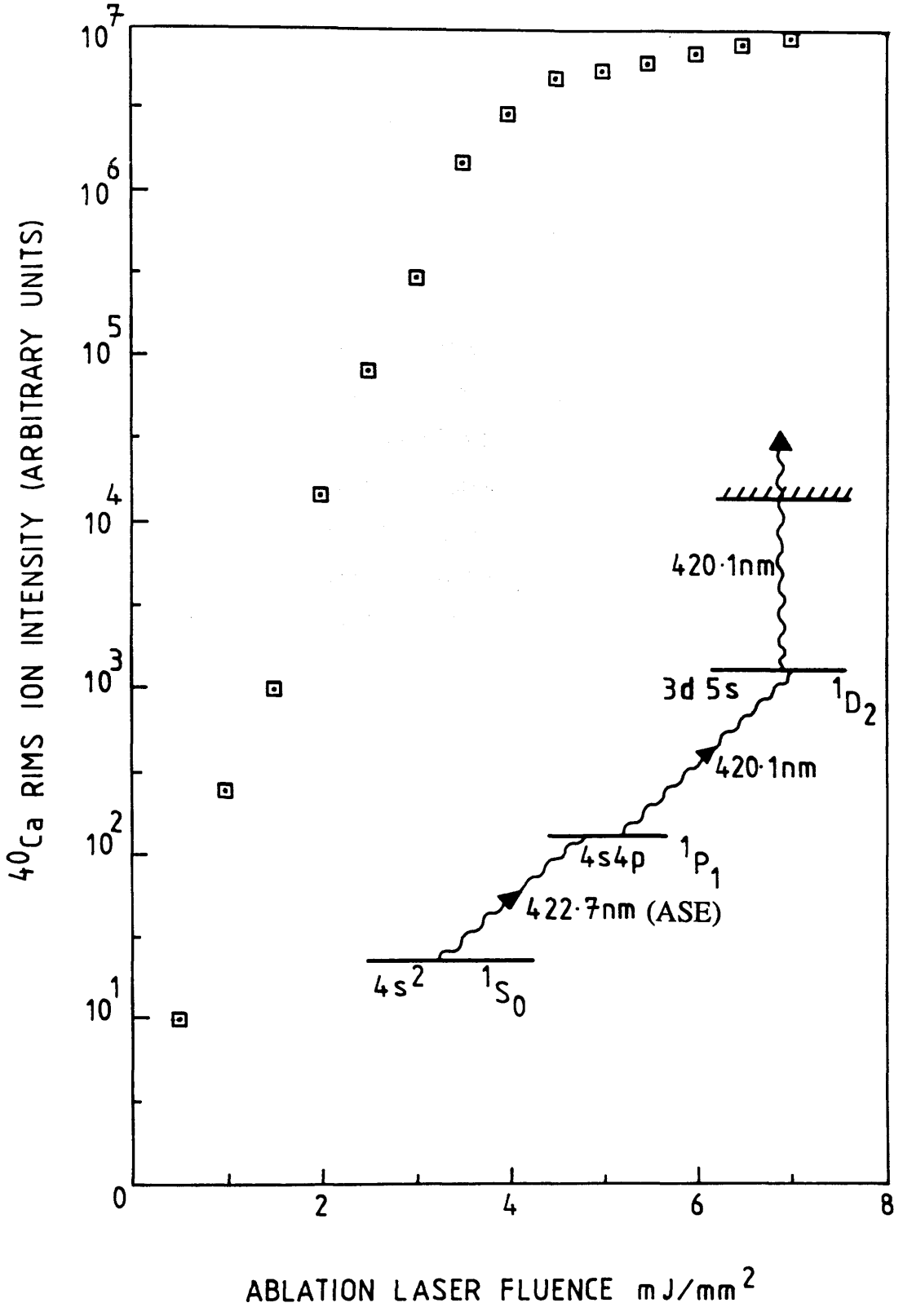

Fig. 3.3.3 Variation in Ca laser ablation neutral yield with increasing ablation fluence

above, with the following exceptions. The resonant laser beam was tightly focussed, giving rise to a stable, close to saturation, ion signal. Measurements were made for ablation wavelengths of 355nm, 532nm and 1064nm. The fluence was adjusted for each wavelength to give similar absolute ion signal intensities, values were typically $1 \rightarrow 2 mJ/mm^2$. The results are shown in Fig. 3.3.4, the theoretical curves fitted to the data will be discussed below. Within experimental uncertainty, the distribution is observed to be independent of wavelength. The distribution has a maximum at $\approx 2\mu s$, and more than 80% of the plume is contained within a $4\mu s$ 'window' around the peak. This would suggest that a high geometric overlap is attainable with quite moderate resonant laser beam diameters ($\approx$4mm).

The data was analyzed by Dr. R.P. Singhal of the LIS group. A computer model, based on the analysis of Chen and Yeung (1988) [179], was developed to predict the temporal and spatial distribution of ablated neutrals. The model requires as input, the mass of the element of interest, the velocity distribution of neutrals perpendicular to the sample surface and a plume expansion coefficient, a. The theoretical curve obtained assuming a Maxwellian velocity distribution at the boiling point of calcium (1758K) and with a=o is given by the solid curve in Fig. 3.3.4. Using the measured expansion coefficient, a=0.075, (see next section) the fit to data improves dramatically, shown by the solid curve in Fig.3.3.4. Whilst this excellent fit may be fortuitous, it would seem to provide firm evidence that the laser ablation is largely a thermal evaporation process for the parameters employed in these experiments.

{The basic physical processes involved in laser ablation are known to change with the ablation intensity [176, 180]. Below $\approx 10^8$ W/cm^2 the process is largely a simple thermal effect, with ablated material simply evaporating from the sample surface- as observed above. For higher intensities the process becomes much more complicated; a shock-wave can be created in the

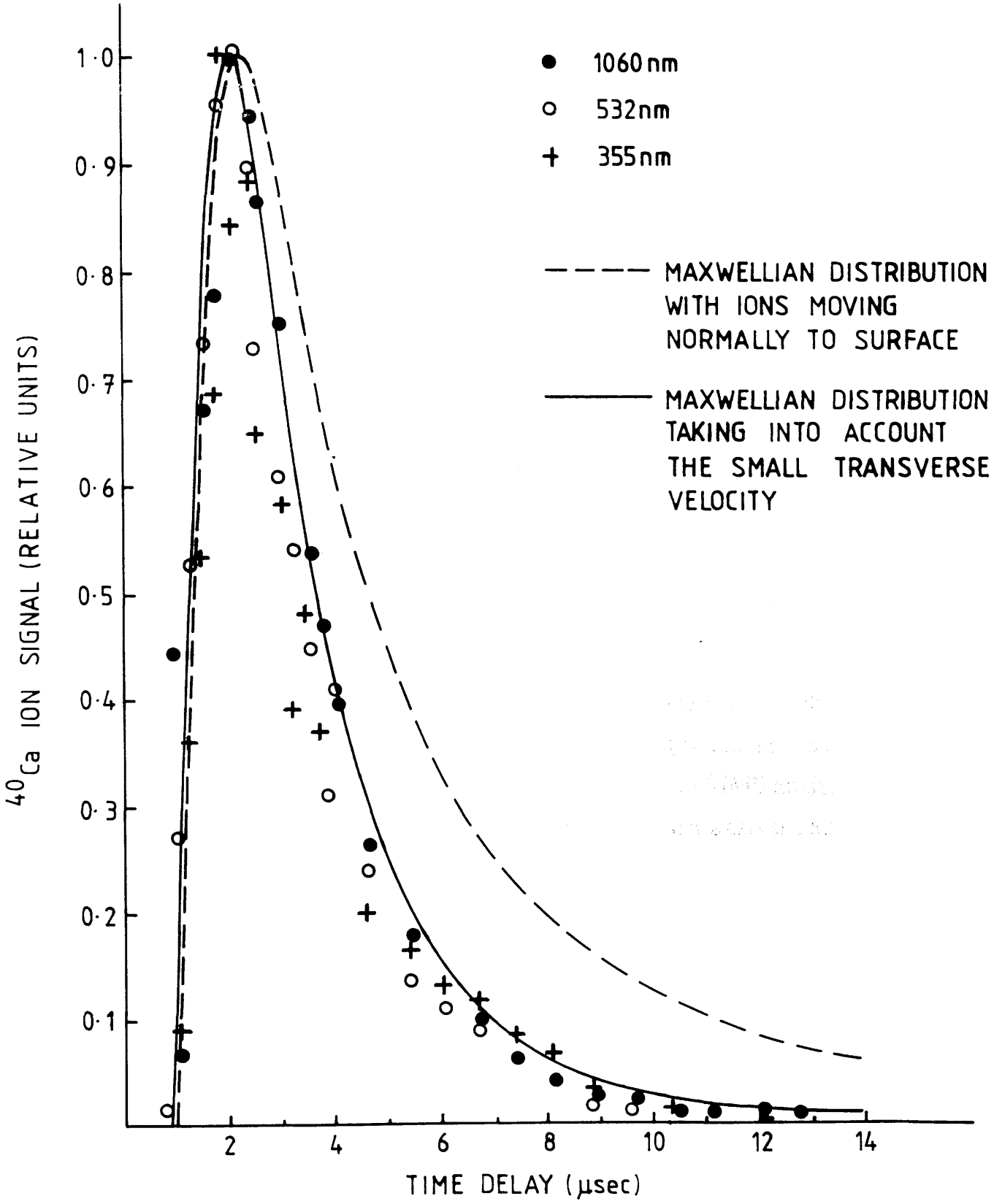

Fig. 3.3.4 Ca RIMS ion signal versus time delay between ablation and ionization laser pulses

sample, leading to the formation of a high density, hot plasma from which sample material is ejected [173]. Measurements on the 'temperatures' associated with the ablation plume provide a method by which to probe the basic ablation process. Quite different results have been reported in the literature. Nogar et al [60] used 1.06μm pulses, with an intensity of $\approx 10^8$ W/cm^2, to ablate tantalum metal from a filament held at a base temperature of 1500K. They reported the following temperatures (see Chapter 1), internal, between 1500K and 2000K, hydrodynamic, 8500K, and thermal, 450K (the boiling point of Ta is ≈5700K). Evidently, a process far from thermodynamic equilibrium. Beekman and Callcott [59] used 1.06μm pulses to ablate samarium with an intensity of $\approx 10^9$ W/cm^2. They found the following temperatures, internal, ≈1640K, hydrodynamic, ≈1240K, and, thermal, ≈1200K (boiling point for Sm, ≈2200K).}

For the low ablation intensities achievable with the present set-up of the Kratos Machine, the neutral yield will initially be skewed towards more volatile elements in the sample, giving a distinct bias for surface analyses. However, for a bulk analysis, the ablation products will reach a steady-state equilibrium accurately reflecting the bulk composition (in much the same way as is found for the varying elemental sputter yields in SIMS analysis). At the much higher ablation intensities used in pure LIMA analysis, all elements can be vapourized with very high efficiency, leaving the variation in ionization efficiency and matrix effects to skew the results.}

(iii) Expansion of the Laser Ablation Plume

In order to estimate the beam spot sizes, for both ablation and ionization lasers, which would give optimal geometric overlaps, it was necessary to understand the way in which the ablation plume expanded as it moved away from the sample surface. Several authors have reported such measurements [179,181], but generally for conditions quite different to those of relevance

to this series of experiments. Dr. M. Towrie devised a simple method by which to determine the rate of plume expansion for the experimental parameters relevant to our investigations, see Fig.3.3.6. The ablation spot size was defined to be a circle with diameter 1mm by a circular aperture placed in the beam path. A glass plate was held parallel to the sample surface at a distance of 10mm. After several thousand laser shots, at an ablation fluence of ≈5mJ/mm^2, a circular deposit of calcium metal could be observed to have been ablated onto the glass slide. This deposit was examined under a travelling microscope, a series of concentric rings (interference fringes) being observed. From the dimensions of the outermost ring, the transverse velocity of the plume expansion was estimated to be ≈0.075 that of the normal velocity (i.e an expansion coefficient of, a=0.075). In other words, at the ablation fluences employed here, neutrals leave the sample surface in the form of a well collimated atomic beam (normal temperature =1758K, transverse temperature =28K). This has several important consequences. Firstly, an ablation spot size of ≈1mm diameter should optimally 'fill' the acceptance volume of the mass spectrometer, see Fig. 2.1.4. The geometrical overlap between the plume and the resonant laser beams should remain high up to quite large distances from the sample, which should be beneficial to the efficient rejection of LIMA ions. Finally, the Doppler width of spectral lines, $\Delta\nu_D$ in the plume can be calculated from,

$$\Delta\upsilon_D(\text{MHz}) \cong \frac{215}{\lambda(\mu\text{m})}\sqrt{\frac{T(K)}{m(\text{amu})}} \qquad (3.3.1)$$

For ^{40}Ca in the ablation plume (and transverse excitation) this gives a low value of ≈430MHz (to be discussed again in Chapter 5). This may have important implications for RIMS isotope selectivity measurements using laser ablation as the atomization technique.

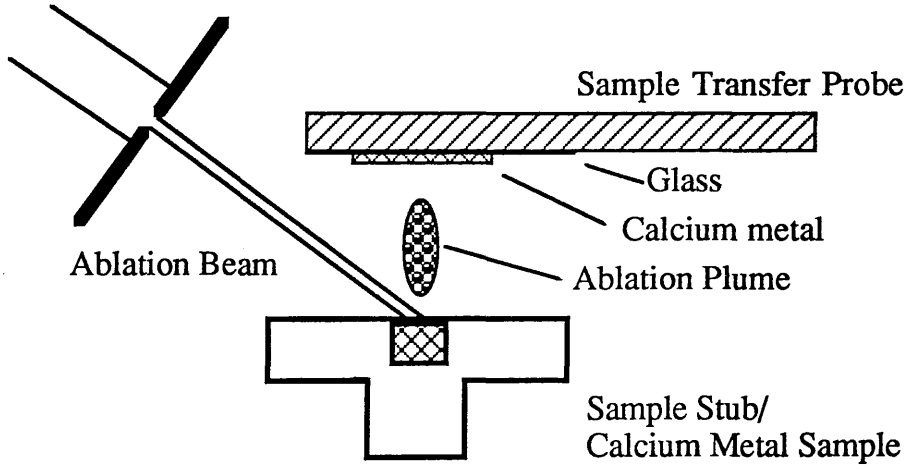

Fig. 3.3.6 Schematic of Ablation Plume Expansion Experiment

(iv) Cluster Formation in Laser Ablation

In Chapter 2, a mass calibration graph was shown, Fig. 2.1.5. This utilized the extensive, regular series of mass peaks obtained from laser ablation of a graphite substrate. The LIMA mass spectrum obtained for laser ablation of graphite at a wavelength of 532nm and at a fluence of $\approx 10 mJ/mm^2$ is shown in Fig. 3.3.7. (This high fluence helped to promote cluster formation at higher masses, but also contributed to the observed poor mass resolution.) This spectrum provides not only a convenient method for mass calibration, but can be interpreted to gain insight to the fundamental process of cluster ion formation [237]. The spectrum divides into two quite distinct sections. For lower mass clusters, containing up to 31 carbon atoms, stable peaks occur for both odd and even numbers of atoms in the cluster, C_n , $1 \leq n \leq 31$. For the higher mass clusters, only those containing an even number of carbon atoms give rise to stable peaks, C_{2m} , $m \geq 16$. Clusters were visible above the noise floor up to C_{214} , improvements in the system's signal to noise ratio may extend this limit.

The physics of cluster formation and structure has become a major research field in its own right, and has been recently reviewed by Maier (1989) [182]. Both neutral and ionic clusters are formed from collision processes that take place within the high temperature plasma which forms immediately above the sample surface during high intensity ablation [173, 182, 183]. The spectrum shown in Fig. 3.3.7 is almost identical to that obtained by Rohlfing et al [219]. This is an interesting comparison to make, since the spectrum obtained in this work is a measure of the cluster *ions* produced in the ablation process, whilst Rohlfing et al analyzed *neutral* cluster products (utilizing laser postionization of neutral clusters produced in a supersonic helium jet following laser ablation) [219]. Both sets of results

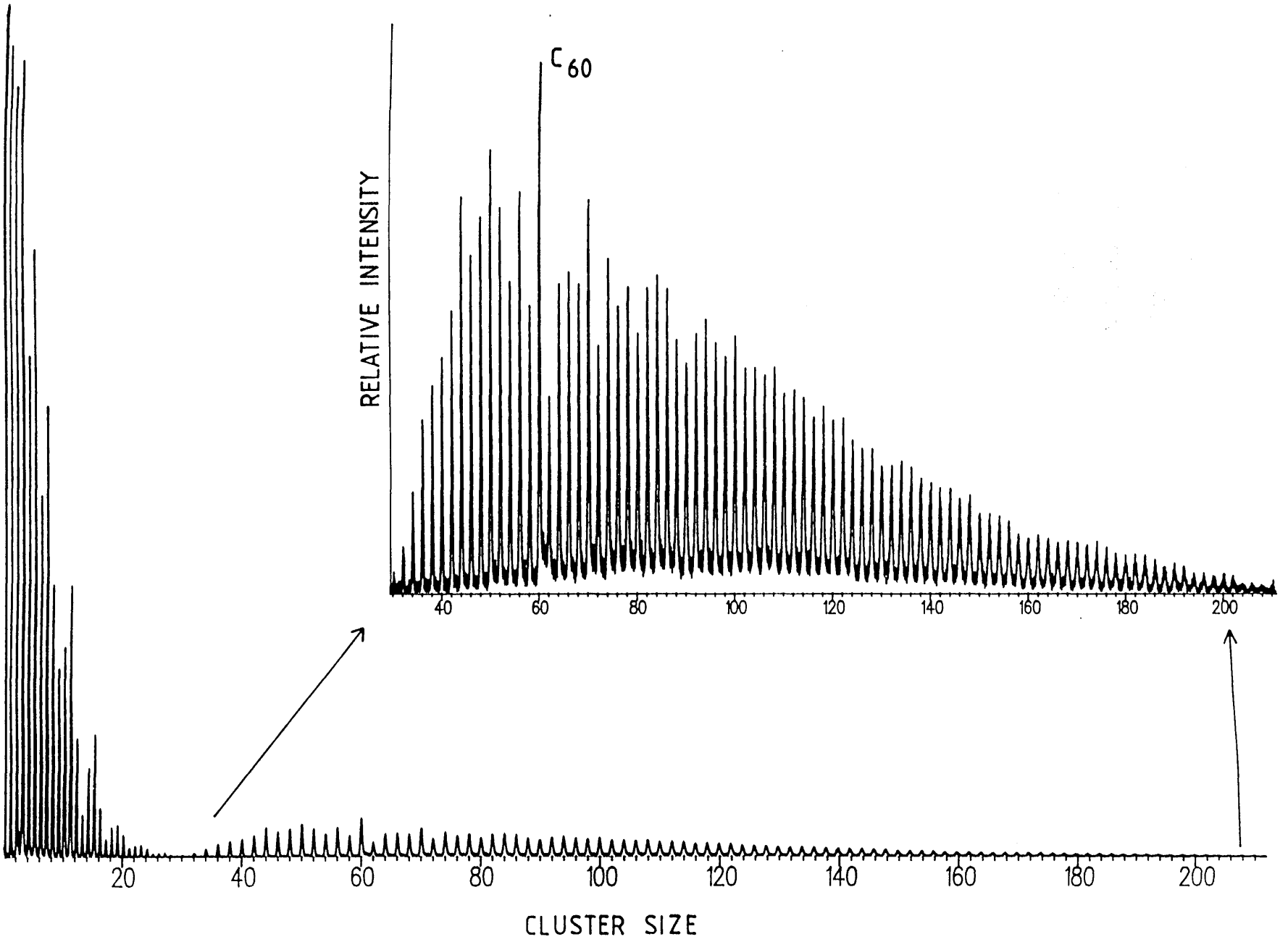

Fig. 3.3.7 Carbon clusters LIMA mass spectrum

clearly show very distinct signal enhancements for the C_{60} and C_{70} clusters, evidently these cluster sizes have a preferred stable structure. Also, clusters C_{62} and C_{72} are much reduced in intensity in comparison with their neighbours. The lower mass clusters are believed to have either an open linear chain structure or a simple ring structure [238]. The larger clusters are thought to have closed spheroidal shell structures [238]. In particular, the C_{60} cluster is now believed to have the elegant and sophisticated structure known as "Buckminsterfullerene", [220, 238], see Fig. 3.3.8.

Two important aspects of the cluster mass spectrum, Fig.3.3.7, can be analyzed for information on the cluster formation process [237]. Firstly, as demonstrated in Fig. 2.1.5, the measured cluster masses follow very closely the quadratic dependence expected for the ideal time of flight analyzer. This implies that the clusters must all be formed close to the sample surface and on a relatively short time scale. This precludes metastable decay of large clusters as the primary mechanism for formation of smaller clusters. Secondly, assuming that the Reflectron perfectly compensates for the initial energy spread of ions, the measured cluster ion temporal peak width can be related to the timescale of ion formation. For clusters, C_n, with $n>32$, the measured peak width (FWHM) is constant at ≈450ns; for the range $16<n<32$, the width reduces to ≈350ns; but for the lowest mass clusters the width increases to ≈650ns, Fig. 3.3.9. These values suggest the following model for cluster formation. Following the rapid temperature rise of the surface induced by laser ablation, a high temperature and high pressure gas 'cloud' is formed immediately above the surface. This gas will then rapidly expand outwards, forming the laser ablation plume. As the plume expands, the pressure within the plume will rapidly decrease. From the time measurements given above, it can be seen that formation of clusters in the $16<n,32$ range requires the highest pressure to form, whilst those of the

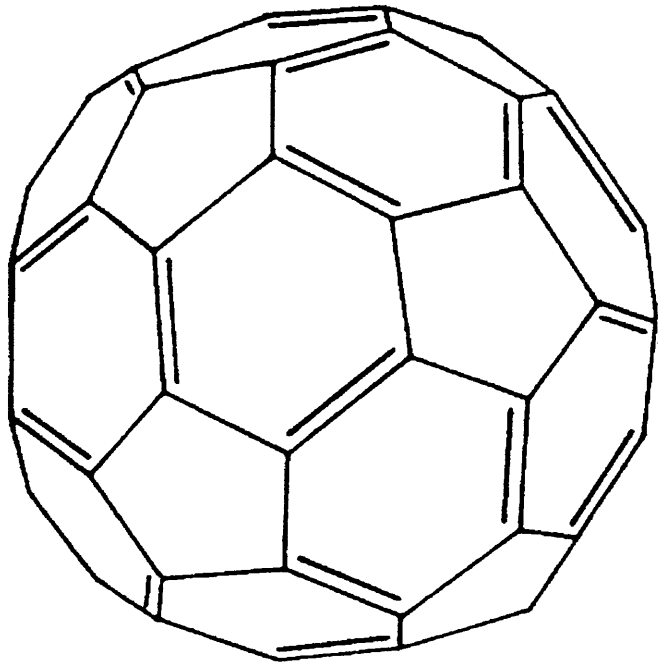

Fig. 3.3.8 Proposed Structure for C_{60}, "Buckminsterfullerene"

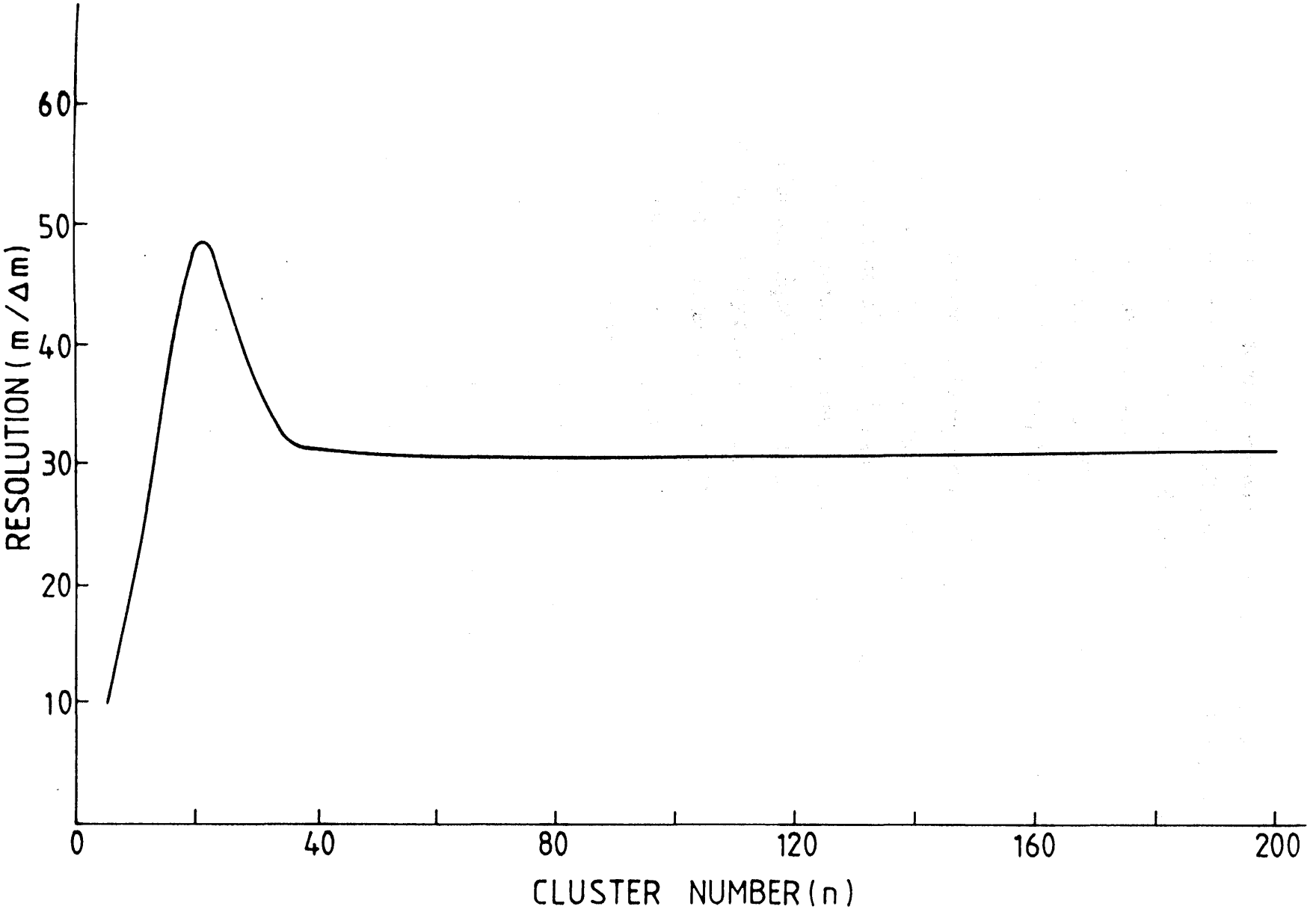

Fig. 3.3.9 Variation in carbon cluster mass peak width with cluster number

lowest masses can form over a wider range of conditions. The constant width of the higher mass, closed shell structures suggests that these all form independently of each other over a well defined range of temperature and pressure. Further work is in progress in the LIS group to examine the basic cluster formation process in greater detail (eg. changing the laser ablation intensity should change the temperature and pressure of the initial gas phase.)

Cluster formation can be regarded as a specialized form of matrix effect. Ablation of a pure elemental sample would ideally give rise only to a monomeric ion signal, instead, many different mass channels become populated. This phenomenon has several implications for laser ablation as an atomization technique for RIMS. If ablation ions are not effectively suppressed, then they may present a source of 'isobaric' interferences. An example of this problem is given in Chapter 5, for the analysis of rubidium in a predominantly graphite matrix. Formation of the simplest cluster, the 'dimer' Ca_2, was observed during several of the analyses carried out on the calcium metal sample, this will be discussed again in Chapter 5. Whilst cluster formation of the element of interest is unlikely during an elemental trace analysis, the activity of such matrix effect processes highlights a potential shortcoming for the laser ablation technique, see Fassett and Travis [5] for a discussion of this problem.

(4) Resonant Laser Ablation (RLA)

The results discussed in this section have been published in McLean, Land et al, 1990 [184]. (Note added in proof: The RLA process is currently being investigated in great detail by the LIS group at Glasgow, the publication by Wang et al (1990) [239] details some of this ongoing research.)

For the results detailed in the preceding section, laser ablation was carried out at fixed wavelengths defined by the Nd:YAG laser. Verdun, Krier and Muller [185] observed that it was possible to enhance the LIMA ionization yield by tuning the ablation wavelength close to known atomic transitions of the element of interest. Using a transmission ablation geometry instrument (LAMMA-500), measurements were made for Cu, Cd and Mo in a variety of sample matrices. Ablation fluences were reported as typically $\approx$100mJ/mm^2. Resonant enhancements of $\approx$x5 were obtained, although spectral lines were observed to be much broader ($\approx$0.5nm) than those expected for vacuum atomic transitions. No estimate of absolute wavelength accuracy was given and hence it is not clear if spectral lines were shifted as well as broadened with respect to their vacuum values.

The very first 'resonance ionization' data to be obtained with the Kratos Machine [186] utilized this 'Resonant Laser Ablation' (RLA) concept. A concentrated solution of rubidium chloride was deposited onto a graphite substrate and allowed to dry. A blue laser beam was arranged to pass across the sample surface at grazing incidence ($\approx$3°). The laser wavelength was then scanned across known rubidium spectral transitions, 5s $^2S_{1/2} \rightarrow$ 6p $^2P_{3/2}$ (420.2nm) and 5s $^2S_{1/2} \rightarrow$ 6p $^2P_{1/2}$ (421.6nm). The ablation ion signal for Rb was observed to have strong resonances close to the known transitions, see Fig. 3.4.1. (The wavelength calibration system was not yet operational when this data was taken and hence no precise data for the actual

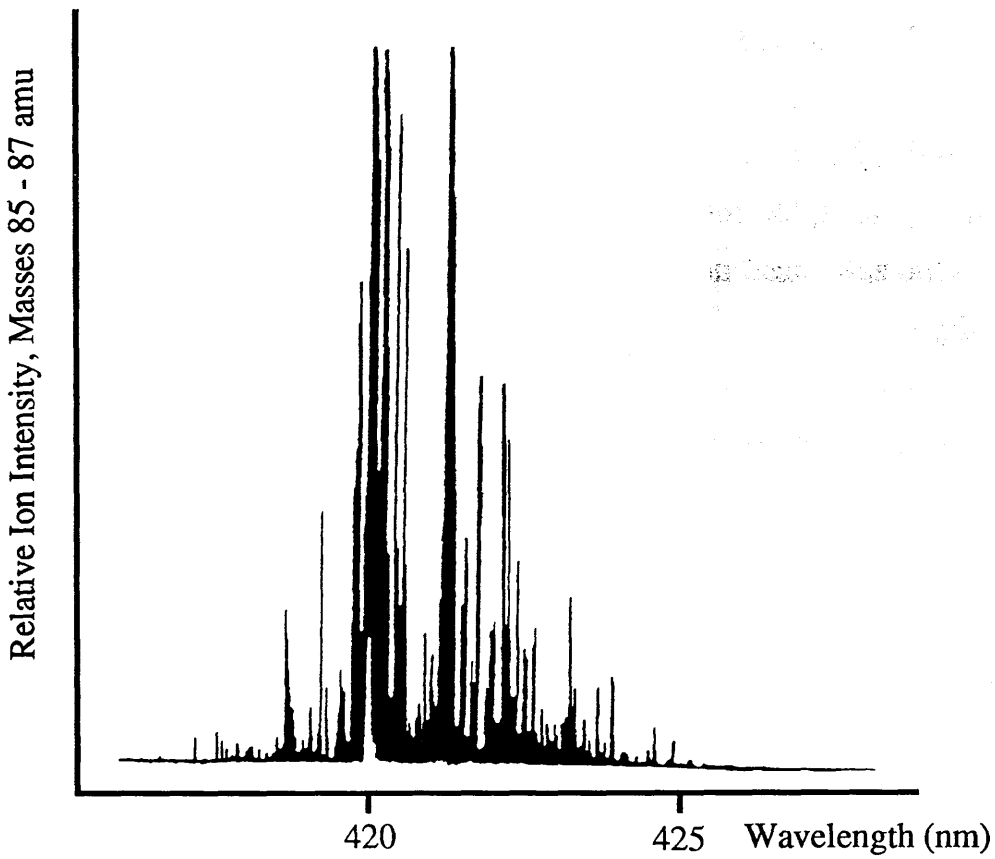

Fig. 3.4.1 Resonant Laser Ablation of Rubidium

wavelengths involved was available.) The resonances are significantly broader than those obtained under 'normal' RIS conditions (Fig. 3.2.2), much as observed by Verdun et al [185]. The background ionization structure (at the bases of the main peaks) is thought to be due to photodissociation/ionization of small Rb molecules (eg. RbCl).

The resonant laser ablation process was investigated for the calcium metal sample. The sample was rotated to ≈3° from the normal position, and a red laser beam allowed to strike the surface. The ablation beam was only loosely focussed, resulting in an ablation area of ≈3mm^2. The wavelength was then scanned through the region of a known two-photon resonant transition from the ground state, $4s^2\ ^1S_0 \rightarrow 4s5s\ ^1S_0$ at 600.125nm. For ablation fluences typical of those employed in non-resonant ablation (≈1mJ/mm^2), large ion signals were obtained, but no resonant structure was observed. However, when the ablation fluence was lowered to ≈30μJ/mm^2 the resonance spectrum shown in Fig. 3.4.2 (a) was obtained. At the resonant wavelength, it was possible to obtain an ion signal with an ablation fluence of only ≈1μJ/mm^2. By way of comparison, the wavelength scan was repeated in 'normal' RIMS mode, using resonant postionization of laser ablated neutrals (ablation at, 1.06μm, 4mJ/mm^2), see Fig. 3.4.2 (b). Wavelength calibration spectra were taken during both RLA and RIMS scans, see Fig. 3.4.2 (c). In both cases the measured resonance wavelength agreed with the known transition wavelength to within experimental error. The linewidths obtained in the RLA and RIMS spectra (≈0.02nm) are also identical within experimental uncertainty.

Although these results are quite different to those obtained by Verdun et al [185], the observations made here are entirely consistent with their proposed model for the RLA process. Verdun et al proposed that RLA be considered as consisting of two distinct processes. Firstly, the 'leading edge' of the laser ablation pulse vapourizes part of the sample surface, free

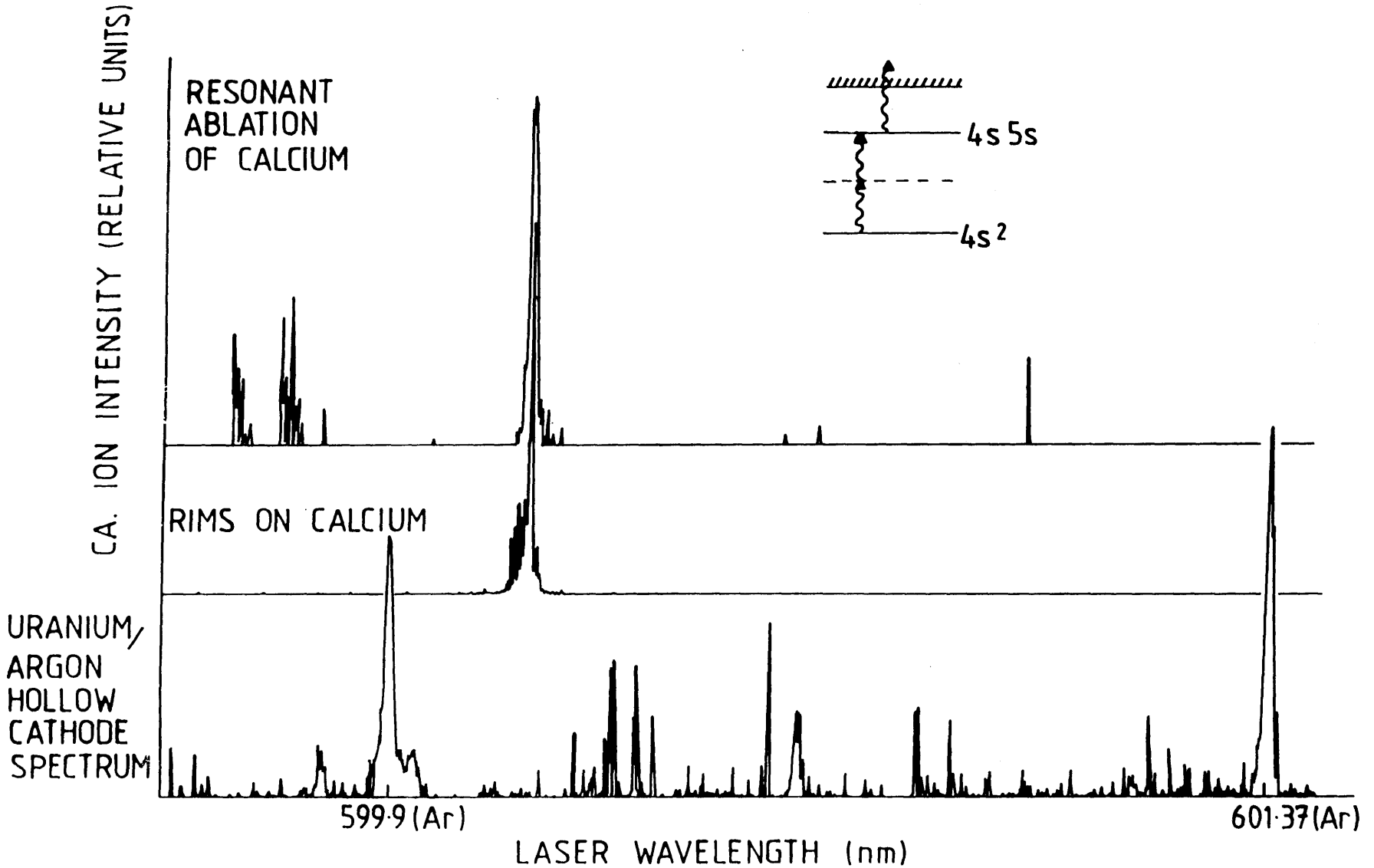

Fig. 3.4.2 (a) Resonant Laser Ablation of Ca (600.1nm)

(b) RIMS of Ca (600.1nm)

(c) Wavelength calibration OGE spectrum

neutral species then move away from the sample surface (as discussed in §3 above). Secondly, free neutral species liberated in the first step can then be ionized in free space, as happens during a normal RIS process.The following simple calculation would seem to lend some credence to this proposal. For a velocity of ≈1mm/μs, atoms created early in the ablation pulse will have moved a distance of ≈10μm from the sample surface during the 10ns duration of the pulse, a distance considerably greater than typical atomic bond lengths (<0.1nm). That is, it is possible for atoms to be 'transferred' from a matrix bound state (where broad, shifted spectral lines are to be expected) to a free vacuum state during the ablation laser pulse. Obviously this model will fail to some extent when the density of material in the ablation plume is such that atoms do not have sufficient time to move away from the close interferences of their neighbours (eg. inelastic collision broadening [222, 239]). This may be one reason why the results obtained here are quite different to those of Verdun et al [185].

The success obtained with the red wavelength transition prompted further investigations at blue wavelengths (415-425nm) where stronger atomic transitions were expected (see Chapter 4). Results in this region were, however, far less clear. It was possible to obtain ablation ion signals with very low fluences, ≈1μJ/mm^2, and resonant structure was observed. However, no degree of reproducibility could be achieved, entire spectral lines would disappear and then reappear seemingly at random. Several lines not apparent in RIMS spectra were occasionally observed. At times no resonant structure at all could be observed, only a broad and uniform continuum, even for very low ablation fluences. Time did not permit a detailed investigation of these phenomena, it is felt that a much more tightly controlled experiment (primarily, sample surface quality and laser spectral parameters) than that attempted here will be required to unravel the processes occurring in this spectral region.

In a separate series of experiments, conducted by Mr. C.J. McLean of the LIS group, similar RLA results were obtained for both Al and Ga from a semiconductor AlGaAs matrix. These results are detailed in McLean et al 1990, [184]. The measured spectra for the RLA of Al and Ga are shown in Figs. 3.4.3 and 3.4.4, respectively.

Evidently the RLA technique holds quite some promise as a surface analysis method, potentially offering a degree of RIS selectivity without the need for separate atomization and ionization sources. In Chapter 5, the utility of RLA as an analytic technique is compared with other laser mass spectrometry techniques.

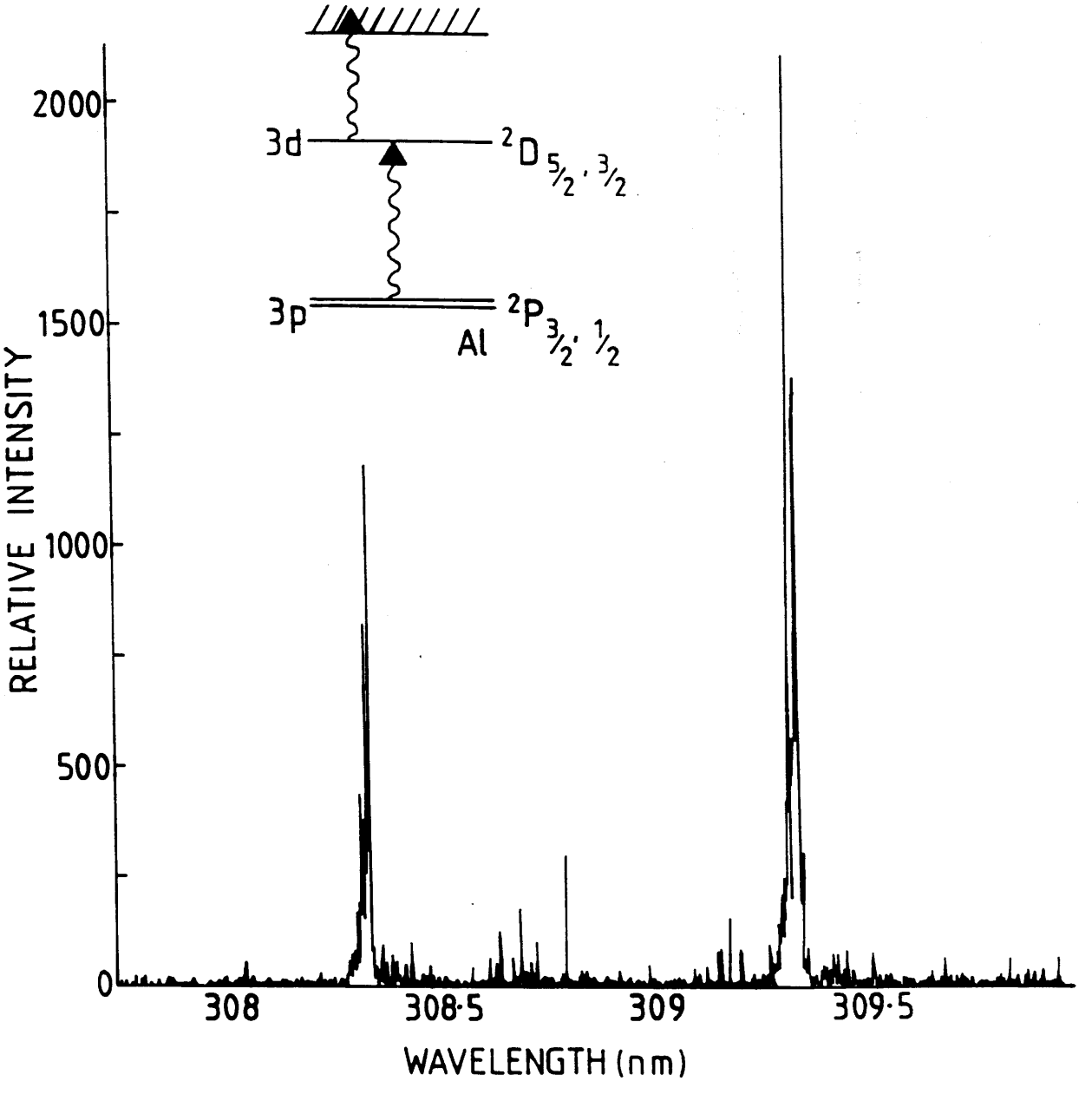

Fig. 3.4.3 Resonant Laser Ablation of Aluminium

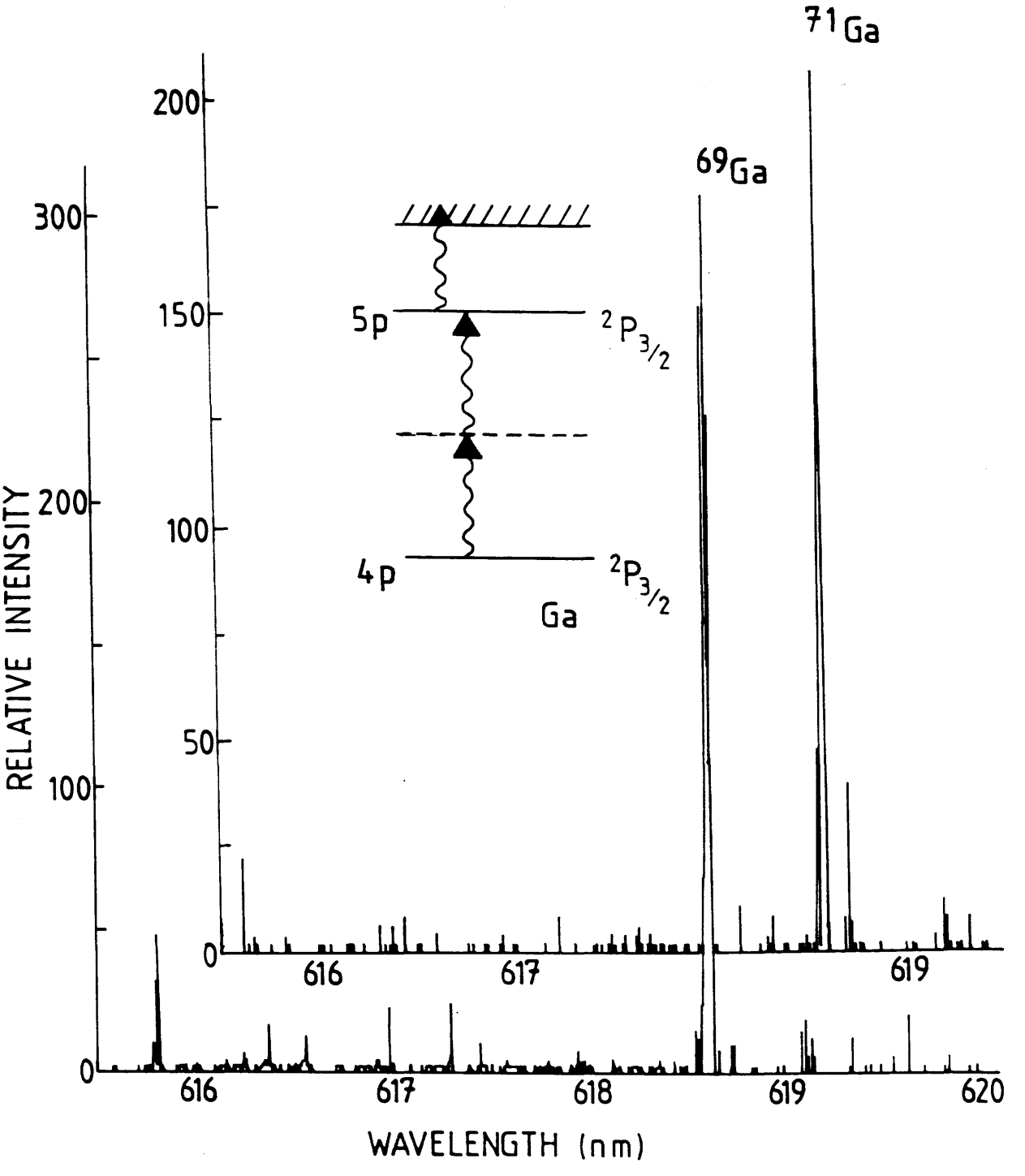

Fig. 3.4.4 Resonant Laser Ablation of Gallium Isotopes

4. Calcium Laser Spectroscopy

The resonance ionization spectroscopy of calcium was studied over the wavelength range 413-437nm. The principal aim of these investigations was to examine the degree of enhancement possible in a two-photon resonant excitation process through the close proximity of an intermediate state. As well as the expected series of two-photon resonant, one-photon ionization ("2+1") transitions, two further sets of spectral lines were observed. These have been identified as one-photon, bound-bound resonances originating from excited states, and two-photon resonant transitions from excited states to autoionization levels, respectively. A sample spectrum of raw data is shown in Fig. 4.1. The experimental techniques used to generate spectra are outlined in §4.1; a brief outline of the known spectroscopy of atomic calcium is presented in §4.2; the observed line series are discussed in §4.3 - §4.5; and finally, §4.6 contains some suggestions for improving the future performance of the Kratos Machine for laser spectroscopy investigations. Details of the basic atomic theory used throughout this chapter are contained in Appendix A.

(1) Experimental Method

The instrumentation and computer software used throughout these experiments have been detailed previously in Chapter 2 . The custom software programme *SPEC* was written specifically to collect laser spectroscopy data from the RIMS instrument. For each laser pulse, the program *SPEC* stores the ion signal integrated over a specified interval of the time spectrum (read from the transient recorder), and also reads out any chosen ADC channels. Hence, as the laser wavelength is scanned, a

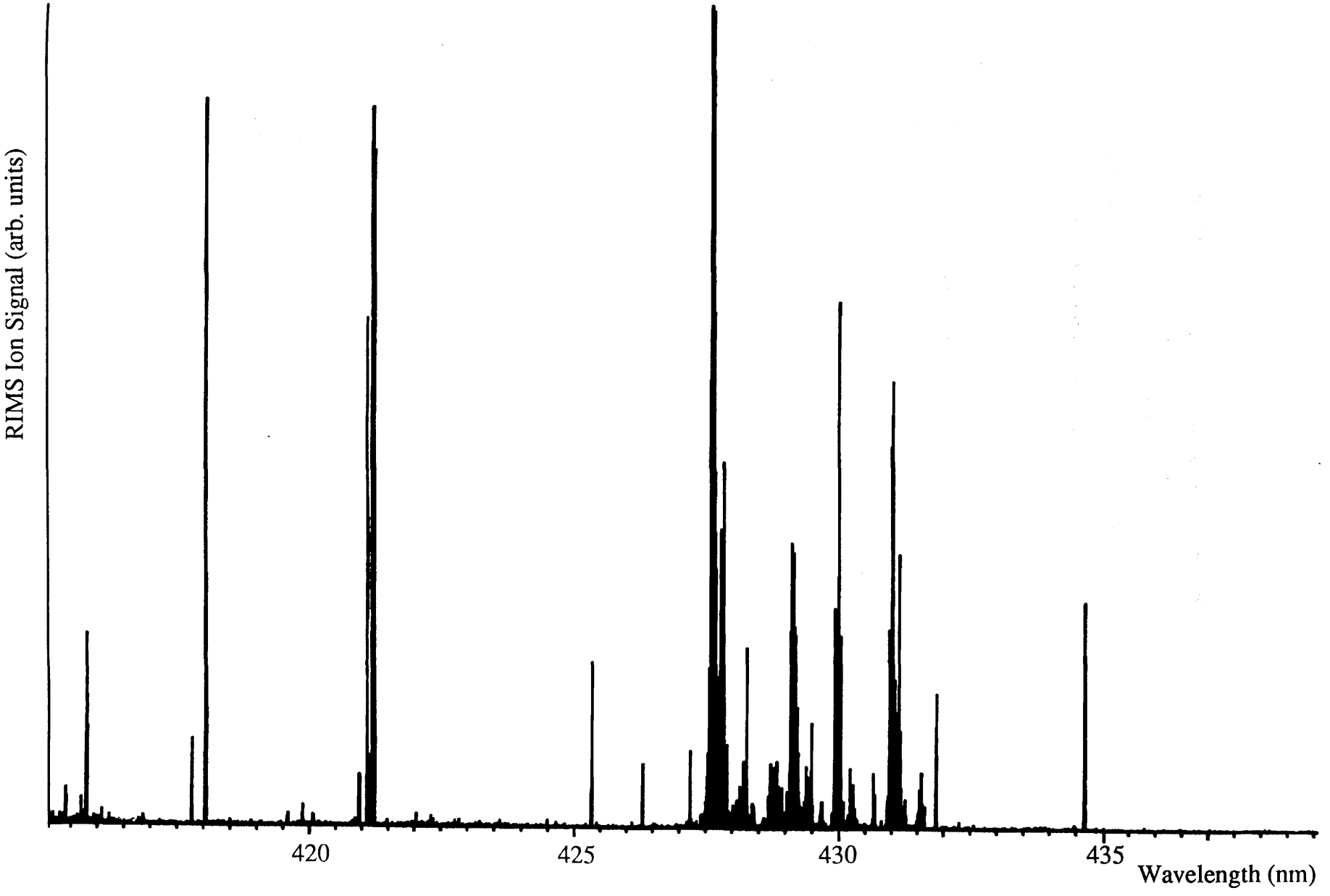

Fig. 4.1 Sample RIS Spectrum for Calcium, 415 - 440nm

wavelength spectrum is recorded. In principle, several ion peaks can simultaneously be monitored. For all of the spectra presented herein, the time window was set for the m/z=40 ion peak, hence any feature observed in a spectrum must be linked to an atomic/molecular system which gives rise to an ion with nominal m/z=40. Only two ADC channels were routinely utilized, monitoring the laser pulse energy and the wavelength calibration signal from the hollow cathode lamp, respectively.

Spectra were smoothed using simple software routines to alleviate pulse to pulse variations in laser output, and consequently to ease visual interpretation of the data. Final wavelength assignment for spectral features was performed manually, using linear interpolation from known OGE lines. Note, the conversion between energy and wavelength units was made consistent with the OGE reference work of Keller and co-workers [166, 170] through the relation:

$$1\,\mathrm{eV} = \frac{1239.8546}{\lambda(\mathrm{nm})} \rightarrow 8063.2553\ \mathrm{cm}^{-1} \qquad (4.1.1)$$

As discussed in Chapter 2, the poor linearity of the dye laser scan mechanisms led to limitations in the achievable accuracy and precision of wavelength assignment. Typically, limits of uncertainty were $\approx\pm 0.04$nm ($\approx 3\mathrm{cm}^{-1}$ for a one-photon transition, or $\approx 6\mathrm{cm}^{-1}$ for a two-photon process). The computer software is in the progress of being upgraded to allow wavelength calibration to become largely automatic, much as has already been accomplished for mass spectra.

For scans over which it was important that the laser power be kept as constant as possible, a simple manual stabilization procedure was employed. Firstly, the lowest laser power likely to be encountered within the wavelength region of interest was established, and then, the power throughout the run was attenuated to this level with the variable optical

attenuator through continual manual observation and adjustment. With practice, this procedure was found to be effective to the ±5% level.

For all of the spectroscopic analyses, a simple calcium metal sample was used, with laser ablation at 1.06μm as the vapourization technique.

(2) Calcium Atomic Energy Levels

As a member of the Column II elements of the periodic table (the 'alkaline earths'), calcium is an important system for the detailed understanding of basic atomic structure. The existence of two optically active valence electrons outside a complete shell provides a model system for the analysis of inter-electron coupling effects [187, 201]. Not only are all energy levels associated with single valence electron excitation shifted relative to their hydrogenic analogs, but there exists the possibility of new series of states formed through the simultaneous excitation of both outer electrons. One most interesting possibility allowed by two electron excitation is that of *autoionization*, this phenomenon will be discussed in §4.5, below. The existence of such doubly excited states was first postulated by Bohr in 1923 [188], and confirmed experimentally by Russell and Saunders in 1925 [189], through studies on the spectra of the alkaline earths. Calcium is well described by the "L-S" (or, 'Russell-Saunders') -coupling scheme, and states have a well defined parity, simplifying interpretation of spectra.

An energy level diagram for most of the known atomic structure of calcium is shown in Fig. 4.2.1. The figure can be conveniently divided into left and right hand sections. To the left, are the single electron excitation states (4sns, 4snp, 4snd etc, in both singlet and triplet configurations), built upon the $4s^2\ ^1S_0$ ground state, and converging to the first ionization potential $4s\ ^2S_{1/2}$ (ground state of the Ca^+ ion). To the right, are the two electron

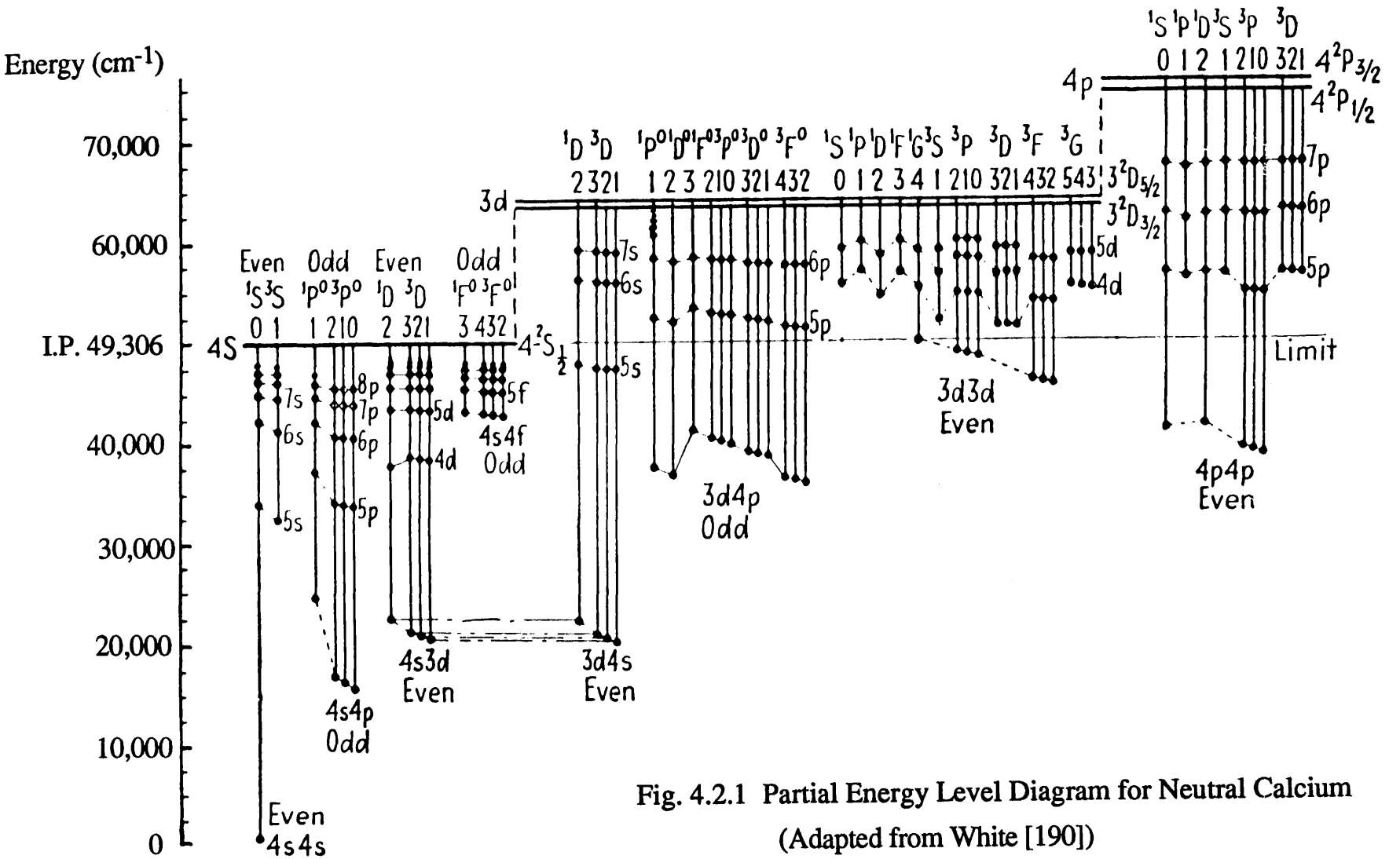

Fig. 4.2.1 Partial Energy Level Diagram for Neutral Calcium
(Adapted from White [190])

excitation states (3dns, 3dnp, 4pnp etc, singlets and triplets), converging to excited states of the Ca^+ ion.

The atomic spectroscopy of calcium has been studied in some detail by various authors, several of the key papers are referenced below. The classic NBS compilation of atomic energy levels by Moore, 1958, [191] is not particularly helpful, being fairly limited in scope, rather inaccurate and containing several misidentified configurations. The most comprehensive and reliable work is that of Risberg [192], listing some 275 spectral emission lines from a hollow cathode lamp. Accurate term values are given for most of the bound series and for several autoionization states.

The bound, even-parity, J=0, 2 states (principally 4sns $^1S_0$ and 4snd $^1D_2$) have been studied extensively by Borgstrom and Rubbmark [193] and by Armstrong, Esherick and Wynne [194]. In a separate paper, Armstrong et al present an extensive listing of the 4snp $^3P_{012}$ series [195]. The work of Armstrong and co-workers [194, 195] is of particular interest since it utilized the RIS technique to generate spectra. A simple gas-filled heat-pipe/ionization chamber was used as the source/detector for their experiments. The ionization mechanism was not clarified, but was thought to be due to collisional processes between the high Rydberg states under investigation and neutral buffer gas atoms. Similar studies have been undertaken in the LIS Group at Glasgow for Cs [123] and Rb [124] in gas-filled proportional counters.

The 4snp $^1P_1$ series has been detailed through absorption spectroscopy by Brown, Tilford and Ginter [198], who also present the most comprehensive and accurate listings for most of the odd-parity, doubly excited series (3dnp $^1P_1$, 3dnp $^3P_1$, 3dnp $^3D_1$, 3dnf $^1P_1$, 3dnf $^3P_1$ and 3dnf $^3D_1$). Connerade et al [187] report several lines from the odd-parity

4pns $^3P_1$, 4pns $^1P_1$ and 4pnd $^1P_1$ series, extending up to the second excited state of the Ca^+ ion. No published data were found for the even-parity AI states, the only available data being the preliminary, unpublished work of Wynne [199].

(3)Two-Photon Spectroscopy

(i) Background and Theory

Interesting discussions on both the theory and practice of two-photon spectroscopy are given by Grynberg and Cagnac [200] and by Letokhov [1].

When an atom or molecule is stimulated from one quantum state to another through the 'simultaneous' absorption of two photons it is said to have undergone a 'resonant two-photon transition'. Such a process is attractive for RIMS analysis for two main reasons. Firstly, compared with a '1+1' RIS scheme, the use of a two-photon process greatly extends the attainable ionization potential, and hence the range of elements accessible to the method. Secondly, through use of counter-propagating beams, a two-photon excitation can be made Doppler-free [200], with consequent gains in both selectivity and sensitivity [29]. The selectivity can be improved since the linewidths of any interfering background systems are not Doppler broadened. This point is most important if a high degree of isotope selectivity is required in the excitation scheme. The potential improvement in sensitivity arises from the interaction of the counter-propagating beams with all transverse velocity components of the Maxwellian distribution [29]. An excellent example of the potential of two-photon, Doppler free RIMS is given by Wen et al [33], in their measurements on the ^{10}Be:^9Be isotope pair.

The major drawback associated with two-photon excitation is that the values for transition cross-sections are typically much lower than those

encountered for one-photon transitions. Compared with one-photon processes, much higher laser fluences are required to saturate a two-photon process, leading to reduced excitation efficiency and increased non-resonant background ionization. { Many one-photon transitions can be saturated with less than $1\mu J/mm^2$, whereas, a two-photon process can typically require $1J/mm^2$ (assuming a laser pulse length of $\approx$10ns). [2]} From an experimental standpoint, a laser beam generally has to be brought to a tight focus to achieve sufficient ionization efficiency for a two-photon process, leading to a much reduced geometric overlap with the analyte vapour.

The two-photon process is usually conceptualized as involving a one-photon excitation to a "virtual" intermediate state, followed by a further 'quasi-simultaneous' one-photon transition from the virtual state to an upper excited state. Cross-sections for such 'virtual' processes are known to be very small. The above 'model' leads to a very simple, 'back of the envelope' calculation: total cross-section $\approx$ product of two one-photon transitions, one resonant and one non-resonant, (giving $\approx 10^{-32}$ cm^4) and the period of the illuminating radiation field ($\approx 10^{-15}$ s, for an optical transition), giving an overall magnitude of $\approx 10^{-47}$ $cm^4 s$. Perhaps a more helpful way of thinking about the two-photon process is to consider what the virtual state actually 'consists of'. Noting that spectral lines are not infinitesimally sharp, but resonances with wings extending out to all energies, the wavefunction for this intermediate state must be formed from the weighted sum of all states for which a one-photon transition from the lower level is possible. That is, the 'first' photon actually excites to some degree all possible single step transitions. Obviously, the transition probability to any given state is small since the photon energy will generally not lie close to the transition line center. As the photon energy comes closer to matching the energy gap between the lower level and a given intermediate state ('*X*'), the proportion of state *X* present in the total intermediate state will increase, until, in the

limiting case, we have a one-photon resonant transition. This line of reasoning leads to the concept of 'intermediate resonance enhancement', whereby the total two-photon cross-section is enhanced through the close coincidence of a suitable intermediate energy level with the energy of the illuminating photons. In practice, this means that the upper level for a two-photon process is specified to be one with energy level closest to being double that of a level with a one-photon transition from the lower level. By way of a concrete example, for calcium, only 4s4p $^1P_1$ at 23652.3 cm^{-1} can be reached with a single visible photon from the ground state. The level with energy closest to double this value, and with correct spin and parity for a two-photon transition from the ground state, is 4s8d $^1D_2$ at 46949.0 cm^{-1}. Consequently this might be expected to have the largest transition strength for a two-photon transition in the visible.

The quantum mechanical calculations used to quantify these concepts are presented in Appendix A, only the final result is required for further discussion here. Fig. 4.3.1 shows the system under consideration.

We can define the two-photon cross-section from $i \rightarrow f$ through the relation between transition rate from $i \rightarrow f$, P_{if}, and resonant laser photon flux, ϕ, given by,

$$P_{if} = \sigma_{if}\phi^2 \qquad (4.3.1)$$

Where, P_{if} has units sec^{-1}, σ_{if} $cm^4 sec$ and ϕ is the laser intensity in photons cm^{-2} sec^{-1}. With this definition, Equation 4.3.2 gives the two-photon cross-section from level i to level f, allowing for the existence of a single intermediate enhancing level r,

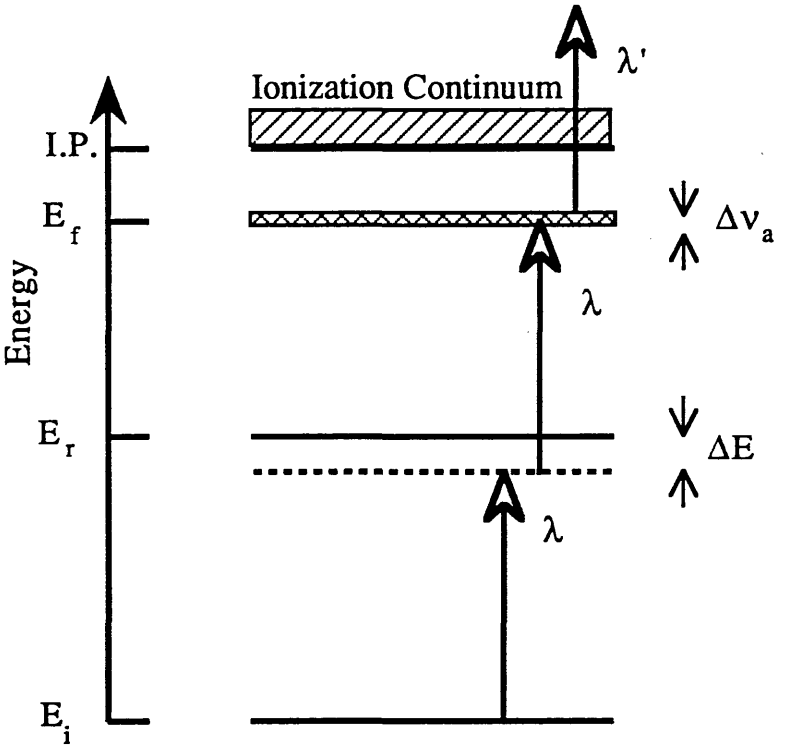

Fig. 4.3.1 Schematic for the "2+1" RIS scheme

$$\sigma_{if} = \frac{K f_{ir} f_{rf}}{\Gamma E_{ir} E_{rf} (\lambda \Delta E)^2} \sum_m |C_{ir} C_{rf}|^2 \qquad (4.3.2)$$

Where, K is a known constant, f_{ij} is the oscillator strength for transition $i \rightarrow j$, Γ is the broader of the natural linewidth for the upper excited state and the laser linewidth, λ is the laser wavelength, ΔE is the energy mismatch with level r, C_{ij} is the Clebsch-Gordan coefficient for the transition $i \rightarrow j$, and the summation is over all magnetic hyperfine states. For efficient excitation, the conditions given in (4.3.3) must be fulfilled,

$$P_{if} = \sigma_{if} \phi^2 >> \frac{1}{\tau_L} , \frac{1}{\tau_f} \qquad (4.3.3)$$

(Where, τ_L is the laser pulse length and τ_f is the upper state lifetime.)

Consider now how this cross-section will vary as a laser is scanned over a series of two-photon resonant transitions, eg. from the calcium ground state, $4s^2\ ^1S_0$ to the Rydberg series 4snd $^1D_2$. The oscillator strength f_{ir} is a constant, the Clebsch-Gordan term will remain constant over the series, and the product ($E_{ir}\, E_{rf}\, \lambda^2$) will change only slowly and smoothly. The expression becomes dominated by the energy mismatch term $1/(\Delta E)^2$ and the atomic properties of the upper excited state, f_{rf}/Γ. For an unperturbed series the latter term should also vary only slowly and smoothly, leaving only the energy mismatch term. Consequently, a measure of the relative two-photon excitation probability over an unperturbed series of spectral lines should show a simple resonant behaviour, with a peak intensity for the state closest to fulfilling the condition $E_{ir}=E_{rf}$. This, in essence, was the basic experiment that was planned for the calcium laser spectroscopy investigations. A single dye laser was scanned over the wavelength region 413-437nm, covering the

two-photon transition series, $4s^2\ ^1S_0 \rightarrow 4snd\ ^1S_0$ (n=8, 13) and $4s^2\ ^1S_0 \rightarrow 4snd\ ^1D_2$ (n=7, 11), allowing a comparison with theory to be made for two independent series.

The actual experimental measurement that is made, is not the relative two-photon cross-section, but the relative ionization probability. Hence, the effect of varying photoionization cross-sections from the upper excited states must also be taken into consideration. A population rate equation (PRE) computer model has been developed in the LIS group for expressly this form of calculation. The model is described in detail in Singhal et al (1989) [202], with a summary contained in Appendix B of this work. The final output of the PRE model is a set of relative ionization yields, directly comparable with the experimental data.

For this work, it was assumed that only the $4s4p\ ^1P_1$ state contributed to the intermediate enhancement. The theoretical model requires knowledge of several different sets of atomic parameters, for calcium many of these are directly available from the literature. Energy levels were taken from the papers mentioned in §4.2, above. Clebsch-Gordan coefficients were calculated after the methods given by Edmonds [203], see Appendix A for details. Oscillator strengths were calculated from the state lifetime measurements of Hansen, (1983) [204], using Eqn. 4.3.4 [205],

$$f_{ij} = \left(\frac{2\pi m_e \varepsilon_0 c^3}{e^2} \right) \frac{g_j}{g_i} \frac{1}{\tau_{ji} \omega_{ij}^2} \qquad (4.3.4)$$

Where, m_e and e are the mass and charge for the electron, respectively, c is the vacuum speed of light, ε_0 the vacuum permittivity, g_k the degeneracy of the state *k*, τ_{ji} the radiative lifetime for decay from $j \rightarrow i$ ($\tau_{ji}=1/A_{ji}$), and

ω_{ij} the angular frequency associated with the energy gap $E_j - E_i$.

Hansen's results [204] indicate that the $^1S_0$ series is basically unperturbed over the region of interest, but that the $^1D_2$ series is strongly perturbed in this vicinity by the $4p^2\ ^1D_2$ and $3d5s\ ^1D_2$ states. { A perturber state must have the same total angular momentum, J, and the same parity as the series it effects [194]. The closer in energy that a perturber state lies to a level, the greater the degree of perturbation experienced by that level.}. Coincidentally, the 4s8d-state, which might have been expected to have had the largest intermediate resonance enhancement, is also the state closest in energy to the perturbing 3d5s state. In fact, Hansen was unable to obtain a lifetime measurement for $4s8d\ ^1D_2$, indicating that the transition strength from this state to $4s4p\ ^1P_1$ is much lower than that of its neighbouring D-states. This anomaly suggested a rather interesting possibility: instead of using state lifetimes to determine relative ionization probabilities, the above theory could be 'inverted', with the relative ionization measurements allowing a state lifetime to be extracted. Hence, it was hoped that if a good fit to data could be obtained, then a first measurement of the radiative lifetime of the transition $4s8d\ ^1D_2$ to $4s4p\ ^1P_1$ could be made.

Very little information on absolute photoionization cross-sections for excited states of calcium was found in the literature. Apel et al, 1987, [65] suggest a value of $\sigma_I = 5x10^{-18}$ cm^2 for the $4s4d\ ^1D_2$ state, and Ditchburn and Hudson, 1959, [206] obtained a value of $\sigma_I = 6x10^{-19}$ cm^2 for the ground state $4s^2\ ^1S_0$. Excited state values were calculated through extrapolation from these two values using the "n^{*-3}" rule given by Hurst and Payne, [2]. Where, n* is the effective principal quantum number, calculated from the Ritz Formula for Rydberg series [192],

$$n^* = \sqrt{\frac{R}{T_n}} \qquad (4.3.5)$$

Where, T_n is the term energy (the energy gap between state *n* and the ionization potential) for the state with principal quantum number n, and R is the Rydberg constant.

Final values used as input to the PRE model and the resulting calculated cross-sections (from Eq. 4.3.2) are given in Table 4.3.1. Clearly the model predicts significantly higher values for the cross-sections than would typically be assumed for two-photon processes. The accuracy of the calculation was checked by repeating the process for the case (Ca: 4s4d $^1D_2$) examined by Apel et al [65]. Good agreement was found, indicating that no basic arithmetic errors had been perpetrated.

(ii) Experimental Results

Using Coumarin 420 blue dye, it was possible to perform a constant laser power scan over the wavelength region 413-437nm, with a fluence of $\approx 500\mu J/mm^2$. At this fluence, if the cross-sections predicted by the model outlined above are correct, then the two-photon transitions would all be pumped close to saturation. Fig. 4.3.2 is a typical example of the data obtained, only two-photon transitions originating from the ground state are labelled.

The spectrum shown in Fig. 4.3.2 was taken using linearly polarised light, the effect of changing to circularly polarised light is shown in Fig. 4.3.3. Two-photon transitions from the $^1S_0$ ground state to $^1S_0$ excited states are forbidden for circular polarisation (see Appendix A). This effect can be quite clearly seen in comparing Figs. 4.3.2 and 4.3.3, with almost all

State	n*	τ (ns)	λ (nm)	$\sigma_{2\omega}(cm^4s)$	$\sigma_I(cm^2)$
4s8s $^1S_0$	5.67	125	435.7	$8.97x10^{-42}$	1.09x10-20
4s9s	6.67	206	426.9	$4.55x10^{-41}$	6.69x10-21
4s10s	7.66	294	421.5	$3.78x10^{-40}$	4.42x10-21
4s11s	8.66	420	417.9	$1.55x10^{-41}$	3.06x10-21
4s12s	9.66	594	415.4	$4.57x10^{-42}$	2.20x10-21
4s13s	10.66	808	413.6	$2.10x10^{-42}$	1.64x10-21
4s7d $^1D_2$	5.94	224	432.8	$7.99x10^{-41}$	6.57x10-19
4s8d	6.82	-	425.9	-	4.34x10-19
4s9d	8.57	232	418.2	$3.18x10^{-40}$	2.19x10-19
4s10d	9.47	271	415.8	$1.13x10^{-40}$	1.62x10-19
4s11s	10.39	425	414.0	$4.43x10^{-41}$	1.23x10-19

Table 4.3.1 Parameter table for two-photon resonance enhancement.

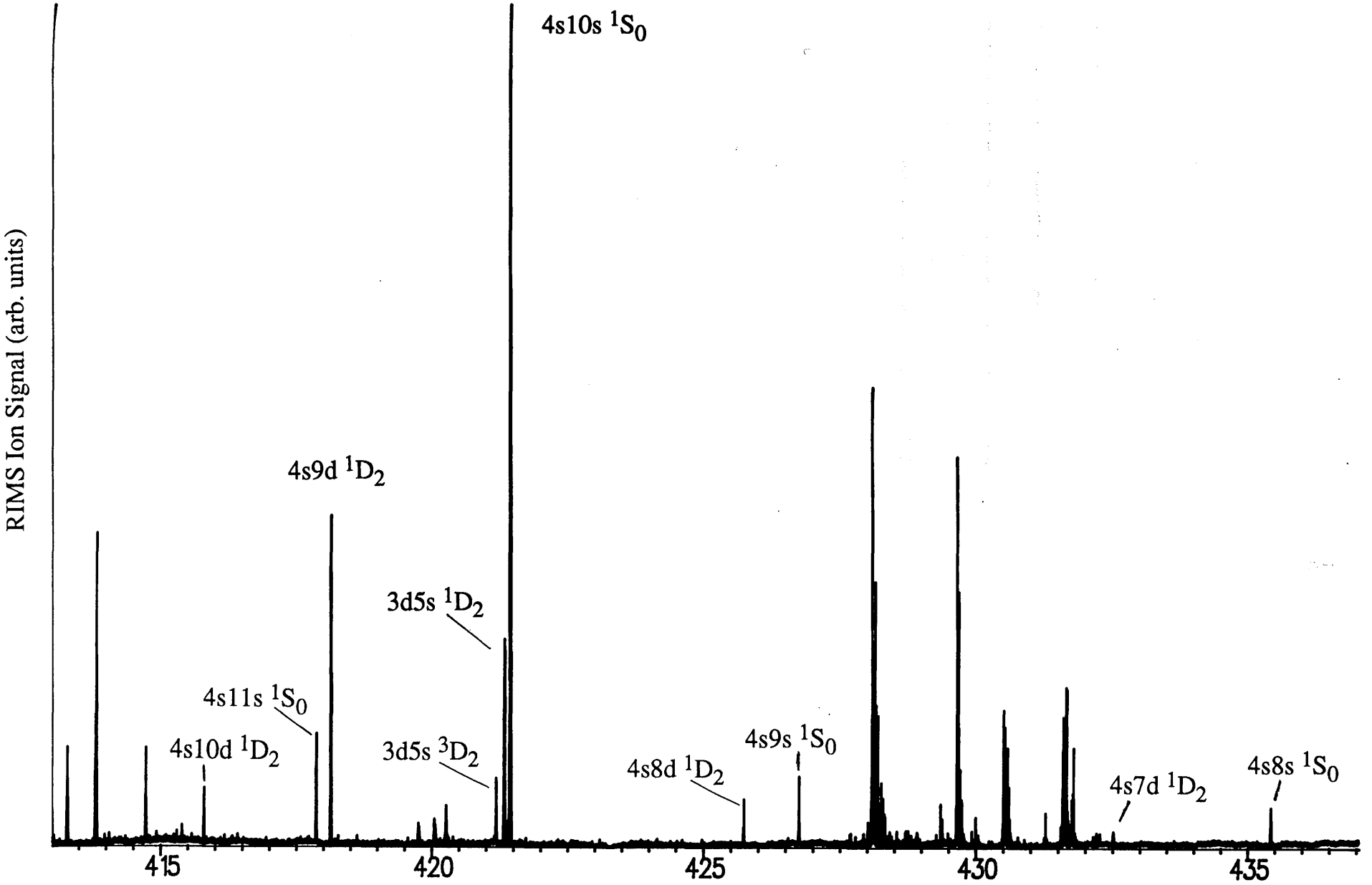

Fig. 4.3.2 Resonance Ionization Spectrum for Calcium,
Linear Polarisation, 413 - 437nm

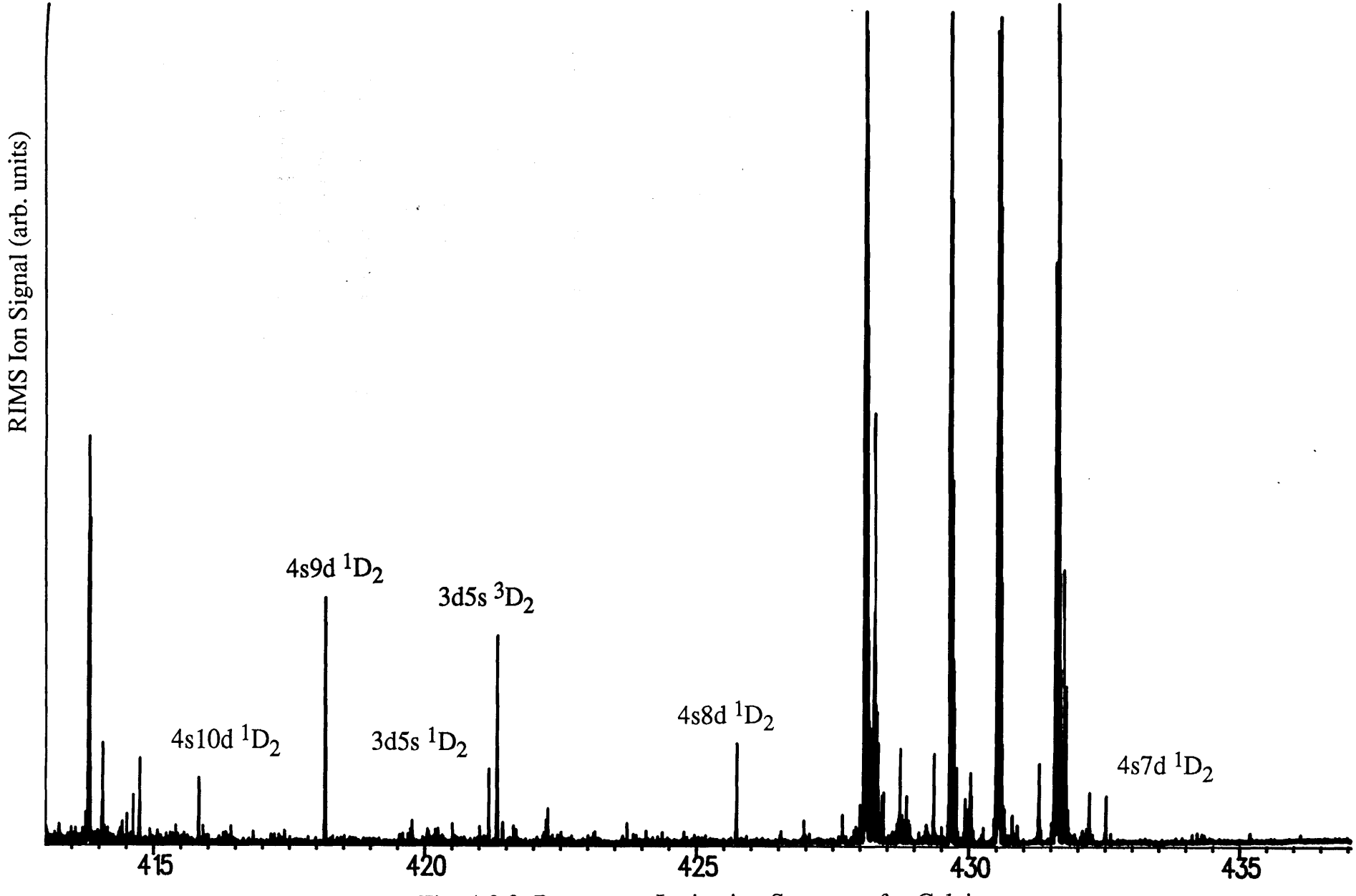

Fig. 4.3.3 Resonance Ionization Spectrum for Calcium, Circular Polarisation, 413 - 437nm

evidence of the $^1S_0 \rightarrow {}^1S_0$ series being erased in the latter. Although absolute measurements were not made during this programme of work, consideration of the Clebsch-Gordan coefficients for the $^1D_2$ transitions would suggest that the absolute cross-sections for this series should increase x3/2 in going from linearly to circularly polarised light [207].

At a basic, qualitative level the data agrees well with the intermediate resonance enhancement model concept outlined above. A clear resonance effect is observed for the 4sns $^1S_0$ series, with the strongest spectral feature being the 4s10s line- that expected to have the greatest enhancement. For the 4snd $^1D_2$ series, the 4s8d line is indeed suppressed (in line with Hansen's findings [204]), with 4s9d as the strongest member of this series, again as might be qualitatively expected. It was possible to reproduce the relative intensities of the various spectral lines at the ±35% level over several scans performed on different days. Final experimental results are the averages over these various runs. The experimental results and the PRE model predictions for the relative ionization yields for the two series are given in Table 4.3.2. As can be seen, when using the calculated two-photon cross-sections, the PRE model's predictions do not at all correspond to the experimental data. Instead, the PRE model suggests that the two-photon steps are saturated, with the total ion yield following the unsaturated photoionization cross-sections. Most interestingly, there is a reasonable correlation between the normalized two-photon cross-sections and the experimental ion yields.

There are two most likely explanations for the discrepancy. One, the calculated two-photon cross-sections are too high by several orders of magnitude, which would seem to be the 'easiest' explanation. However, the good agreement between theory and experiment found by Apel et al [65], using the same model, does lend some credibility to the model's vialbility.

State	$\sigma_{2\omega}$	σ_I	Ion Yield (Theory)	Ion Yield (Expt.)
4s13s $^1S_0$	0.6	37	27	<1
4s12s	1.2	50	42	<1
4s11s	4.1	69	74	14
4s10s	100.0	100.0	100.0	100
4s9s	12.0	151	151	11
4s8s	2.4	247	223	4
4s11d $^1D_2$	14.0	56	56	11
4s10d	35.6	74	74	16
4s9d	100.0	100.0	100.0	100
4s8d	-	198	-	20
4s7d	25.0	300	308	6

Table 4.3.2 Experimental and theoretical relative ion yields for "2+1" RIS scheme in calcium. S-state values have been normalized to the values for 4s10s, D-state values to those for 4s9d.

Two, the observed 'resonance' is due not to the two-photon cross-sections, but rather to a coincidental resonance in photoionization cross-section. Whilst such a proposition may be stretching the bounds of reasonable coincidence, Connerade et al [187] have, in fact, observed several series of autoionization states in the spectral region which would be reached by the ionization photon. The observed series [187] in this region 4pns $^1P_1$ and 4pnd $^1P_1$ both have the correct parity and angular momenta for one-photon transitions from the two-photon excited states.

Obviously, much further work is required to clarify this issue. The next step must be to eliminate the uncertainties introduced through lack of knowledge of the photoionization cross-sections. This could be done by saturating the photoionization transition. If, however, the ionization cross-sections are as low as originally anticipated, Table 4.3.1, then very high laser fluences (>1J/mm^2) would be required to effect saturation. The only practical way of doing this, would be to use the residual fundamental 1.06μm radiation from the Spectron Nd:YAG pump laser. This has sufficiently short wavelength to ionize all of the states of interest. One added benefit of this scheme would be the lack of multiphoton background ionization even at the very high fluences required. If it should prove to be possible to saturate the photoionization step, then the two-photon cross-sections could be measured using the power dependence curve method of Letokhov and co-workers [1], see also Appendix B. That is, the total ion yield should be measured over a large range of fluences; at lower fluences, the yield curve should be quadratic, and at high fluences the curve should flatten off into saturation. The variation in photoionization cross-section with wavelength could be investigated by introducing a second blue dye laser to scan over the spectral region of interest whilst leaving the original blue laser tuned to a two-photon resonance.

Two other two-photon transitions originating from the ground state

were observed, these were identified as those to 3d5s $^1D_2$ (the main perturber for the 4snd $^1D_2$ series) and 3d5s $^3D_2$. This latter line was the only intercombination line observed during this investigation, highlighting both the strong adherence to LS-coupling for the calcium system and the strong state mixing between singlet and triplet states for the 3d5s state, discussed by Armstrong et al [194].

(4) Bound-Bound, One-Photon Spectroscopy

As can be clearly seen from the spectra shown in the preceding sections, two-photon transitions originating from the ground state by no means account for all of the observed spectral features. The only known one-photon transition from the ground state in this spectral region is that to 4s4p $^1P_1$ at 422.7nm. Since this level would require absorption of a further two blue photons to become ionized, a very low cross-section process, clear observation of this transition was not expected, indeed identification of this line from the data was not possible.

Most of the strong and reproducible lines have been identified as bound-bound, one-photon transitions originating from excited states 4s4p $^1P_1$ and 4s4p $^3P_{012}$. One-photon, bound-bound transitions have much higher cross-sections than those typically encountered for the two-photon processes discussed above. From a known radiative lifetime, the absorption cross-section is given approximately by,

$$\sigma_{ij} = \frac{g_j}{g_i} \frac{\lambda_{ij}^2 A_{ji}}{8\pi\Delta\nu_a} \qquad (4.4.1)$$

Where $\Delta\nu_a$ is the atomic linewidth for the transition, and all other terms have their previously defined meanings. Excited state transitions in the optical region typically have cross-sections of $\approx 10^{-13}$ cm^2 and hence can be saturated with laser fluences of order 1μJ/mm^2, for ≈10ns laser pulses. For all the studies carried out during these investigations, laser fluences were always >40μJ/mm^2 and hence it was expected that any one-photon, bound-bound transitions would be heavily saturated. (By comparison, the two-photon lines were expected to be far from saturation at the fluences employed here.) When a transition is driven into saturation it becomes broadened ("power broadening", [205]). This effect allows one- and two-photon transitions to be easily differentiated, through comparison of the relative linewidths ('sharp' line= two-photon, 'broad' line= one-photon), illustrated in Fig.4.4.1.

(i) Transitions from 4s4p $^1P_1$

Three strong lines around 420nm (the "Gang of Three") were identified as transitions from 4s4p $^1P_1$ to 4s10s $^1S_0$, 3d5s $^1D_2$ and 3d5s $^3D_2$, respectively. Weak transitions were also tentatively identified as transitions to 4s9s, 4s11s $^1S_0$ and 4s8d, 4s9d $^1D_2$. The 4s4p $^1P_1$ state is known to have a short radiative lifetime (4.67ns, [204]) for decay to the ground state. Consequently, any population excited into this level during the ablation process would have had ample time to decay during the delay (≈2μs) between ablation and resonance ionization.

It is suggested that this level was populated by radiative absorption from the ground state stimulated by amplified spontaneous emission (ASE) emitted from the blue dye laser. As discussed in Chapter 3, the output from the blue dye laser was known not to consist solely of a pure laser line, but also of a broadband emission over much of the range of the dye- ASE.

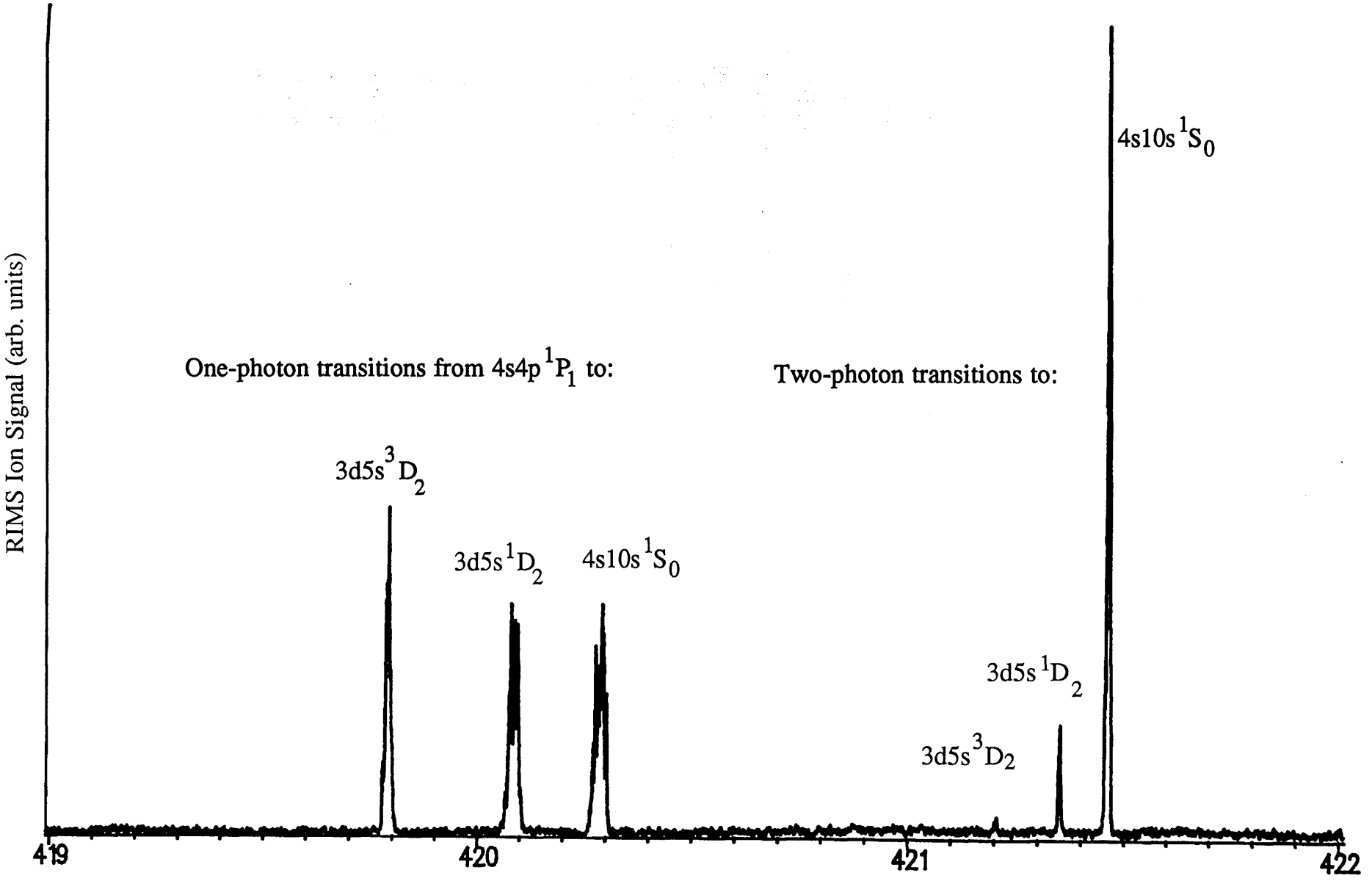

Fig.4.4.1 Calcium RIS Spectrum, 419 - 422nm,
Relatively broad ($\approx 2cm^{-1}$) one-photon and narrow ($\approx 0.8cm^{-1}$) two-photon lines

{ The generation of ASE is discussed in most basic laser physics textbooks (eg. Eastham [208]), only a brief outline of the problem is presented here. If the laser medium (in this case the laser dye) is pumped with sufficient intensity, then it is possible for a spontaneously emitted photon to undergo gain amplification as it passes through the pumped volume, hence Amplified Spontaneous Emission. The properties of ASE are dependent on the laser medium (eg. dye concentration) and gain volume geometry, but independent of the laser oscillator cavity. ASE is only partially coherent (a degree of laser 'speckle' can frequently be observed) and can be relatively intense (at one point, the ASE from the red dye laser had sufficient intensity for the autotracking frequency doubling unit to 'lock on' to the emission!!). The lack of coherence arises from the random nature of the spontaneous emission process. Compared with 'true' laser radiation (that arising from oscillations within the cavity), ASE has a broader bandwidth and a wide angular divergence. These two parameters, in principle, allow ASE to be differentiated from laser radiation and consequently filtered out of the beam. However, the ASE will still have contributed as a significant loss factor for laser power, draining population that could have contributed to the laser action. With the Spectron dye lasers, ASE generation was observed from both the oscillator and amplifier cells over a wide range of operating conditions. Whilst ASE from the oscillator cell was observed to be relatively divergent, sufficient intensity was generated along the optical axis to allow amplification from the amplifier cell. Attempts at spatially filtering the oscillator emission and changing the relative geometries of oscillator and amplifier cells gave little improvement. Introduction of an optical delay line between oscillator and amplifier pump beams also had little effect. The problem was compounded by the generally poor quality of laser beam obtainable from the oscillator cavity; pulse energy was always limited to <1mJ, and both the spot shape and beam divergence were poor. It would

seem that these lasers have been designed for efficient operation in the red region of the spectrum and consequently suffer in the blue. The best compromise situation that was achieved, involved using only the laser oscillator, with the full 355nm beam pumping a dilute dye solution. }

Very little intensity is required to saturate the $4s^2\ ^1S_0 \rightarrow 4s4p\ ^1P_1$ transition; Eqn. 4.4.1 gives $\sigma=2.7\text{x}10^{-9}$ cm^2, which would require a saturation fluence of only $\approx$0.2nJ/mm^2 for a 0.1cm^{-1} linewidth source, or $\approx$1μJ/mm^2 over a 10nm range. Although no spectral energy density measurements were undertaken for the ASE, it does not seem unreasonable that sufficient intensity was available to effect significant excitation to the $4s4p\ ^1P_1$ level.

The hypothesis that ASE from the blue laser was responsible for populating the $4s4p\ ^1P_1$ state was investigated in the following experiments. A second, red dye laser beam was arranged to illuminate the ionization region collinearly with the blue beam. This red laser was tuned to the one-photon, bound-bound transition $4s4p\ ^1P_1 \rightarrow 4p^2\ ^1D_2$ at 585.75nm, with an intensity $\approx$1mJ/mm^2. Absorption of either a red or a blue photon would provide sufficient energy to effect ionization from this D-state. The following observations were made: with only the red laser on, no ionization signal was observed; with both blue and red beams present, a large signal was observed for *all* wavelengths of the blue laser, but only for a very sharply defined resonance region for the red laser. Very little increase in ionization was apparent as the blue laser was scanned through the wavelength region of the P-state transition, suggesting that the ASE was capable of pumping the transition at near saturation levels.

The presence of ASE could have very important implications for both the sensitivity and the selectivity of a RIMS analysis. For example, if the intention was to utilize a two-photon excitation scheme originating from the

ground state, then this preferred excitation 'channel' would be in direct competition with the ASE channel for ground state population, with a consequent loss in sensitivity. The presence of relatively intense, broadband radiation has very obvious potential for increasing 'non-resonant' background ionization.

These effects are well illustrated in Fig. 4.4.2 . This spectrum was one of the first collected with the Kratos machine, before the nature of the ASE problem was appreciated. The dye used, Bis-MSB, covered the wavelength range 415-425nm, and seemed particularly prone to generating ASE. Copious amounts of 'non-resonant' background ionization are visible for all wavelengths, particularly so at the edges of the dye. The Gang of Three is clearly visible as the three intense lines in the centre of the spectrum. It is suggested that the 'non-resonant' ionization could in fact be better described as being 'doubly-resonant'!! That is, firstly ASE 'resonantly' excites population from the ground state to the P-state, as discussed above; secondly, this population is then further resonantly excited to any upper excited levels that lie within the range of the dye (principally the Gang of Three); and finally, these upper states are then photoionized by either ASE or laser photons. It was not possible to quantify the problems associated with the ASE (eg. the fraction of ground state population depleted by the ASE): the amount of ASE generated appeared to depend on many different parameters (eg. dye used, age of dye, pump power, temperature, laser oscillator cavity alignment etc.), and varied in an unpredictable fashion.

A problem similar to the ASE observed here has been reported by Nogar and Keller [233]. In their studies on the RIS spectrum of lutetium (a '1+1' scheme), several relatively intense satellite lines were observed on either side of the known central peak. These were discovered to result from efficient excitation of the 'central' transition by optical sidebands present in the laser emission. Although the sidebands were weak in comparison with the

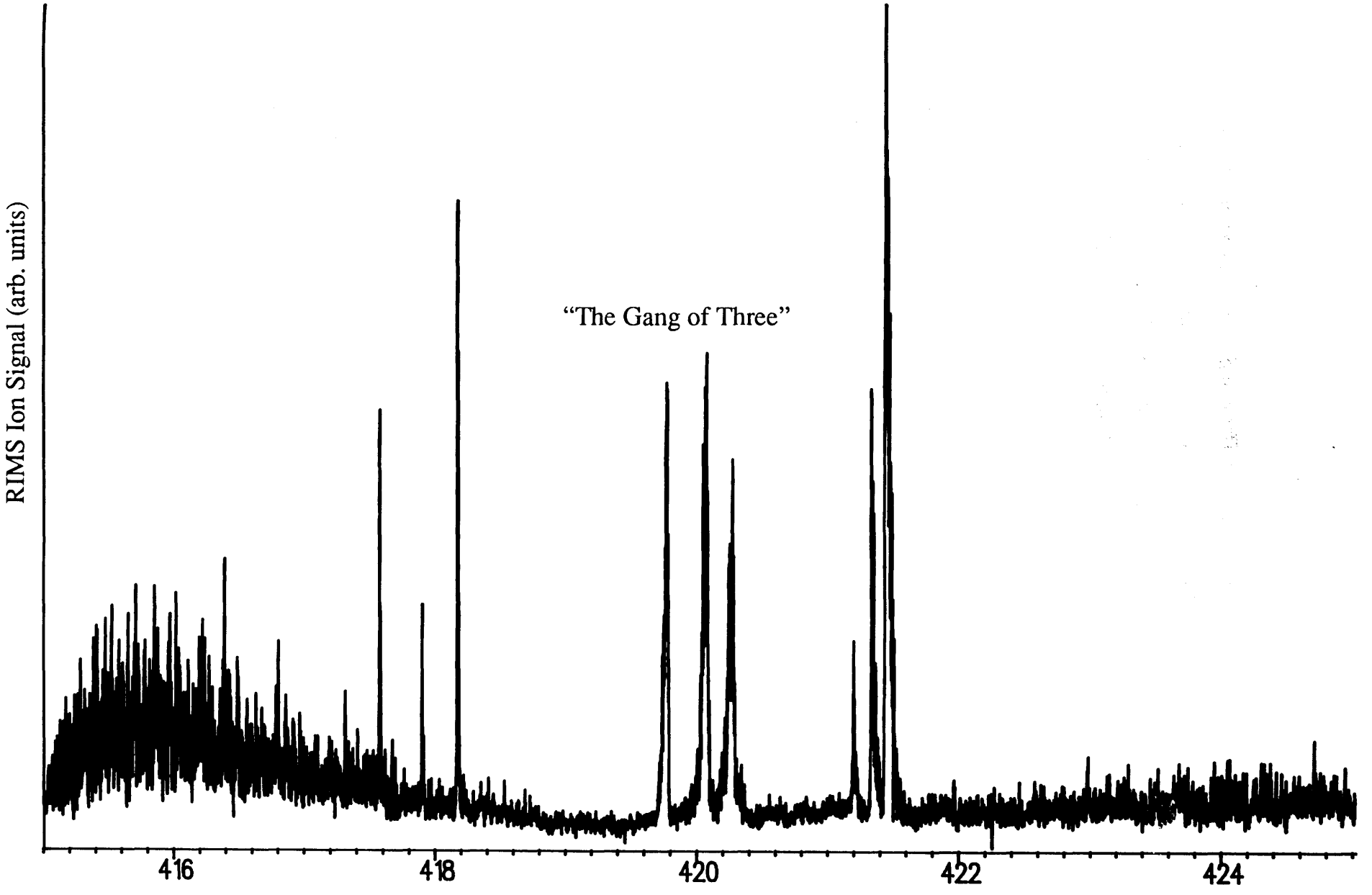

Fig. 4.4.2 Calcium RIS Spectrum, 415 - 425nm

Large background ionization due to ASE

main laser line (<1%), they had sufficient intensity to drive the strong one-photon bound-bound transition near to saturation. As with ASE, sidebands may prove to be a parameter which must be tightly controlled if the limits of analytic sensitivity and selectivity are to be reached.

(ii)Transitions from 4s4p $^3P_{012}$

One of the earliest experiments undertaken in the calcium studies, involved non-resonantly postionizing ablated neutrals with the 266nm and 355nm harmonics from the Nd:YAG. For both wavelengths, absorption of two photons is required to photoionize the calcium ground state. Twice as much power was available at 355nm than at 266nm, hence it was expected that the ion signal obtained with 355nm would be four times that with 266nm (following from the quadratic dependence expected for the two-photon process). In practice, however, it was possible to achieve considerably more ionization with the 266nm wavelength beam. Tight focussing of the laser beam was required in both cases to achieve reasonable ionization signals. Power dependence curves were taken for both wavelengths, see Fig. 4.4.3. The curve for 355nm shows the expected quadratic response for a non-resonant two-photon ionization process (gradient $\approx$2 on a log-log plot). The curve for 266nm is, however, more nearly linear (gradient $\approx$1 on a log-log plot) and appears to be close to saturation for the higher fluences. This suggests, that at 266nm, a one-photon ionization process is dominating. It was noted that it is possible for population in the metastable 4s4p ^3P states to be ionized by only one photon at 266nm whilst requiring two photons at 355nm. Hence, it was hypothesized that a significant population was being excited into the metastable ^3P states during the ablation process. {Note, the observed 'saturation' with 266nm only indicates that most of the population in the ^3P state is being efficiently ionized, the majority of the neutral population (in the ground state) will be excited with much less efficacy.}

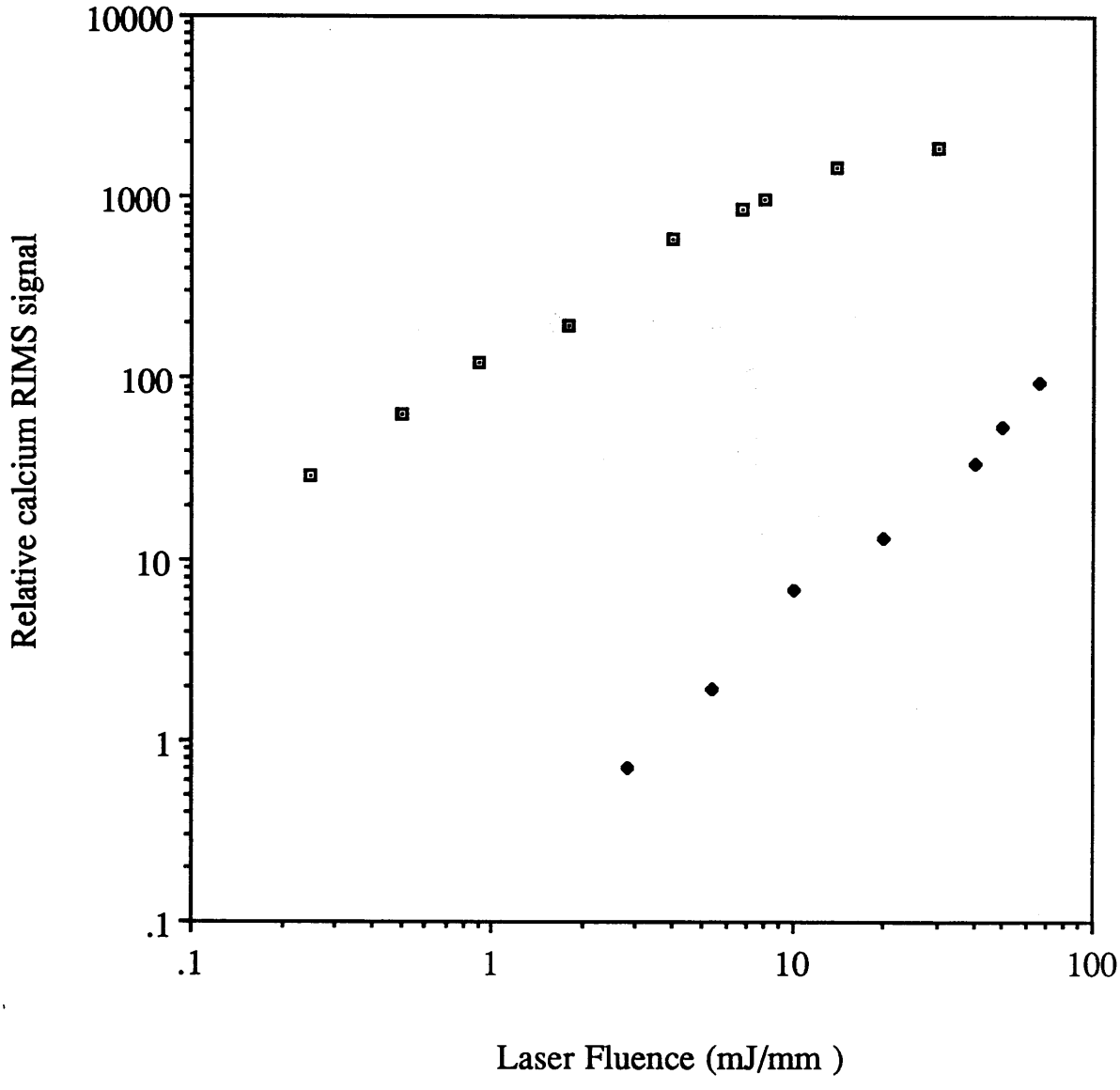

Fig. 4.4.3 Power dependence curves for Ca SALI

▫ 266nm ♦ 355nm

This hypothesis was investigated further using resonant laser ionization.

The spectral region around 430nm contains a multitude of lines, several of comparable strength to those discussed above. This wavelength region is shown expanded in Fig. 4.4.4. Six of these lines have been identified as comprising the one-photon, bound-bound multiplet $4s4p\ ^3P_{012} \rightarrow 4p^2\ ^3P_{012}$, Table 4.4.1, below.

Transition	λ expt. (nm)	λ lit. [192] (nm)
$^3P_1 - ^3P_2$	428.36	428.31
$^3P_0 - ^3P_1$	428.96	428.94
$^3P_1 - ^3P_1$	429.88	429.90
$^3P_2 - ^3P_2$	430.26	430.26
$^3P_1 - ^3P_0$	430.76	430.78
$^3P_2 - ^3P_1$	431.83	431.87

Table 4.4.1 One-photon transitions from $4s4p\ ^3P_{012} \rightarrow 4p^2\ ^3P_{012}$

Many of the smaller lines in this region are tentatively identified as two-photon transitions from $4s4p\ ^3P_{012}$ to autoionization states, to be discussed in the following section. Several relatively intense lines in this portion of the spectrum, however, have not yet been assigned. Most of the unassigned lines are quite broad, suggesting either saturated one-photon, bound-bound atomic transitions or possibly molecular transitions. Further investigation is required to clarify this issue. The ability of *SPEC* to monitor several mass peaks simultaneously, should be of great use in monitoring any molecular resonance effects (eg. the ratio of Ca to the Ca_2 dimer could be

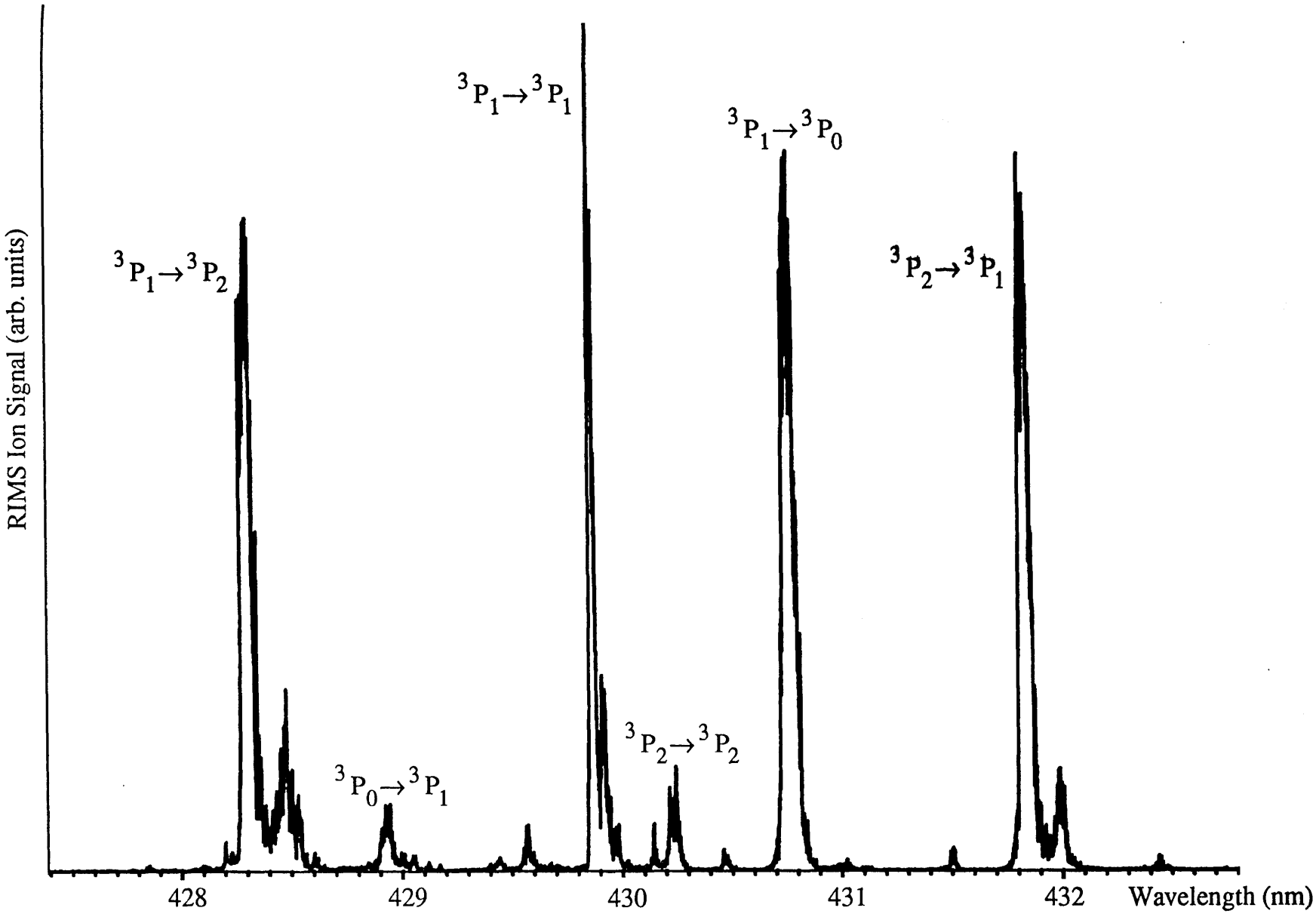

Fig. 4.4.4 Calcium RIS Spectrum, 427 - 433nm
Excited state $^3P \rightarrow {}^3P$ transitions

monitored throughout a wavelength scan).

The only radiative decay channel open to the 4s4p ^3P states is to the $^1S_0$ ground state, a forbidden transition under L-S coupling. Consequently, these states are metastable, with a lifetime of ≈0.4ms [209]. This long timescale (compared with the microsecond delay between ablation and postionization) allows for the possibility that these states are populated during the ablation process. The link between the ablation process and the metastable population was established by comparing the relative intensities of spectral lines originating from ground state and metastable populations, respectively, at different laser ablation intensities. This is illustrated qualitatively in Figs. 4.4.5 (a, b); at higher ablation powers (b) the relative proportion of metastable population increases.

An attempt was made to quantify the relative populations of ground and metastable states in the following way, see Fig. 4.4.6. The laser and optics were aligned to allow a blue laser beam and the frequency-doubled harmonic (UV) of a red beam to pass collinearly through the ionization region. The blue dye laser tuned to the 4s4p $^1P_1$ resonance at 422.7nm, the red laser was tuned to a sufficiently short wavelength to allow direct photoionization of both ^1P and ^3P states. The intensity of the blue was then attenuated until the one-photon transition was just saturated. The UV beam was kept at low intensity to give only a small correction for direct photoionization from the ground state. Consequently, the photoionization step was far from saturation. With the major assumption that the one-photon photoionization cross-sections from the ^1P and ^3P states are similar, a measure of the ionization signal with the blue beam present (ground state) and then absent (metastable) allows the relative populations to be measured. For an ablation intensity of ≈4mJ/mm^2, typical of that used throughout this work, the relative fraction of population in the metastable states 4s4p $^3P_{012}$ compared

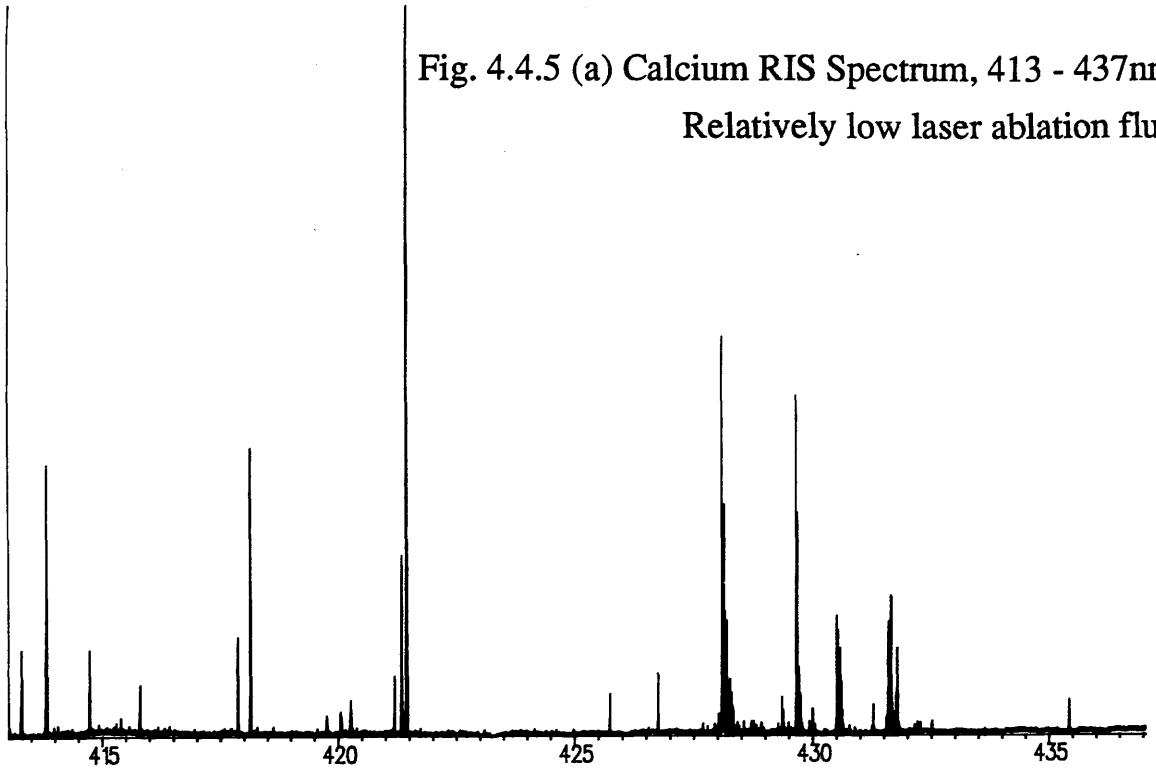

Fig. 4.4.5 (a) Calcium RIS Spectrum, 413 - 437nm
Relatively low laser ablation fluence

Fig.4.4.5 (b) Calcium RIS Spectrum, 413 - 437nm
Relatively high laser ablation fluence

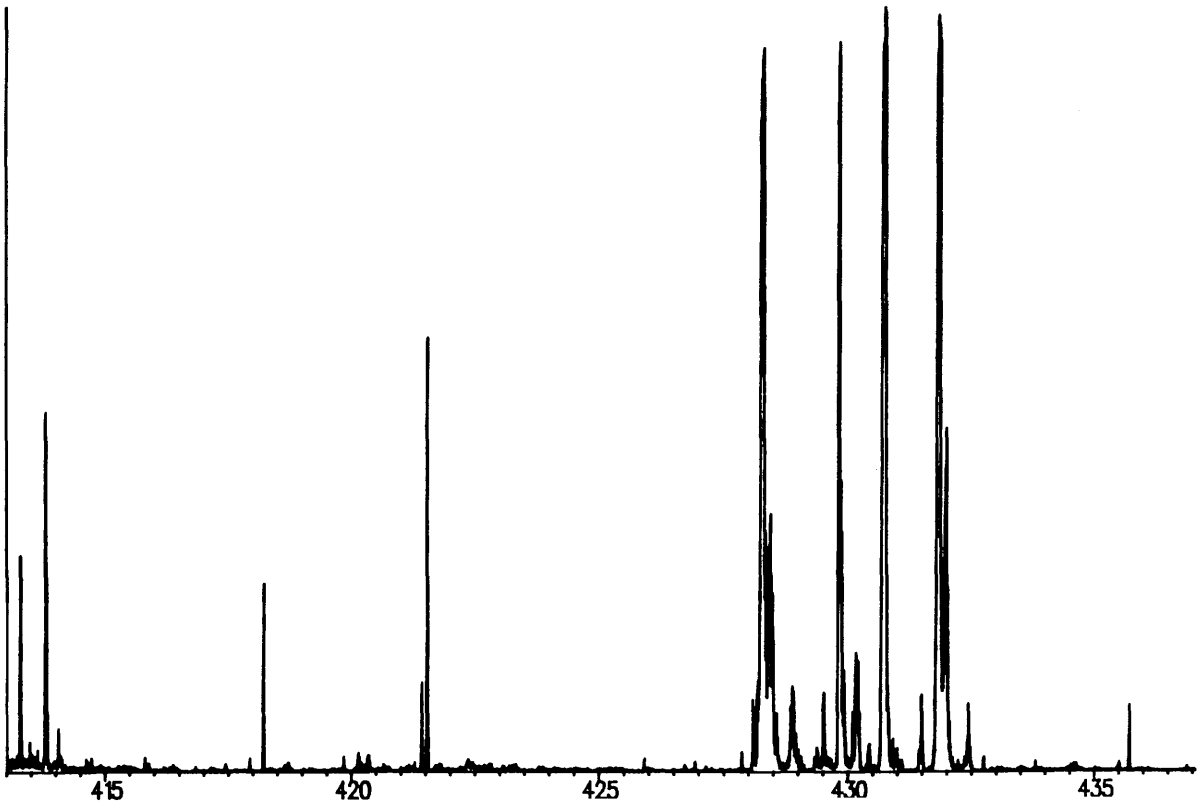

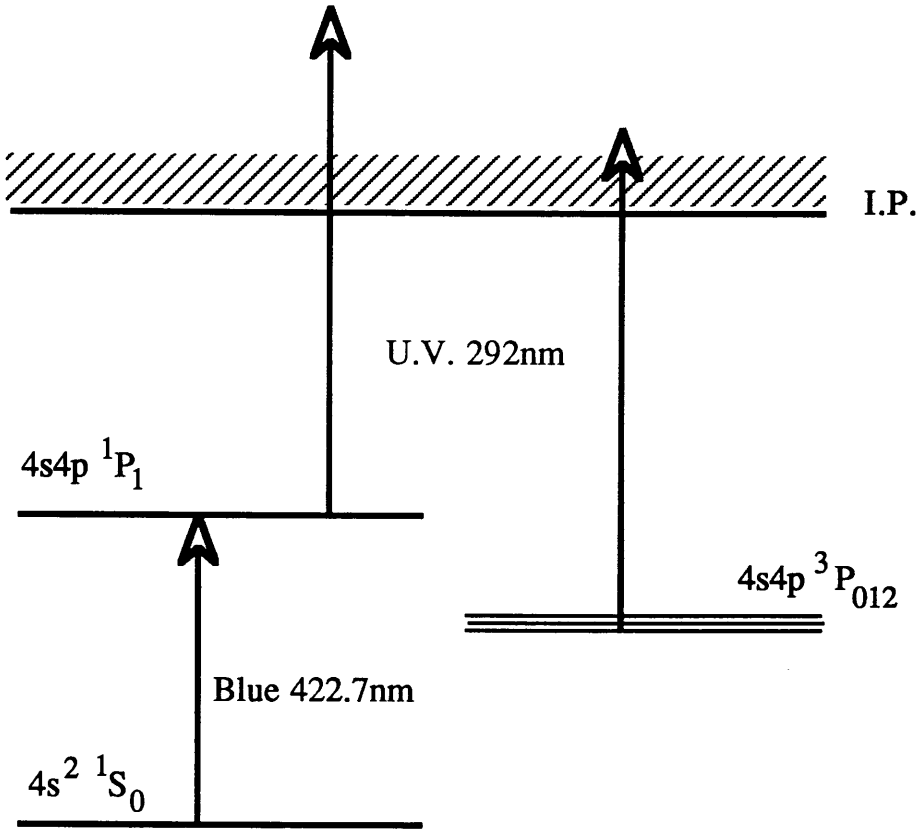

Fig. 4.4.6 Relative populations of $4s4p\ ^1P_1$ and $4s4p\ ^3P_{012}$ states.

to the $4s^2\ {}^1S_0$ ground state was measured to be ≈5%. For lower ablation fluences (<0.4mJ), however, this fraction was noted to diminish rapidly, values were measured in the range 0.05% to 0.005%. Time did not permit the systematic study which these results suggest is required to understand fully the dependence of internal excitation on ablation fluence. Ideally, these measurements should be made with the ionization step saturated. (In order to avoid a large photoionization signal directly from the ground state, or from other excited states, it would be best to use bound-bound transitions from the 1P and 3P states to higher excited states, followed by photoionisation with a long wavelength photon, eg. the Nd:YAG fundamental, 1.06μm.)

Potentially, these measurements of relative populations could be converted into internal excitation temperatures for calcium atoms in the ablation plume through application of the Maxwell-Boltzmann distribution (a value of 4300K is obtained for ablation at 4mJ/mm^2, and 2900K - 2200K for the lower fluences). Similar measurements have been carried out by Fasset et al [58] and by Beekman and Callcott [59], to obtain diagnostic measurements for thermal vapourization and laser ablation sources, respectively. However, it is not clear that such a calculation is valid for the present example. Both Fasset et al [58] and Beekman and Calcott [59] were concerned with high densities of low-lying states, which might be expected to be in thermal equilibrium, and which have relatively long lifetimes for radiative decay to the ground state. For calcium, however, only relatively energetic excited states exist. Presumably, many different states will be populated during the ablation process, the relative efficiencies for populating states being determined by the ablation plume constituents, 'temperature' and detailed atomic collision parameters. Once populated, these excited states will rapidly decay down in a cascade process until making a transition to a metastable state. Apart from the ground state, only two low lying states are metastable;

the 4s4p ^3P states, which will act as a very natural 'sink' for excited triplet states, and 4s3d $^1D_2$ (which must violate either parity conservation or LS coupling to decay), which could be a terminus for high lying P- and F-states. A detailed examination of the spectral data yielded only one weak line which could be assigned to a transition originating from this latter level, 4s3d $^1D_2 \rightarrow$ 4s5f $^1F_3$ at 435.5nm. A further possible transition, 4s3d $^1D_2 \rightarrow$ 4s7p $^1P_1$ at 424.05nm, was not observed. However, these findings agree well with tabulated oscillator strengths for these two transitions [209], the F-state transition having a very low value (considerably less than for the $^3P \rightarrow {}^3P$ transitions discussed above) and the P-state transition given no listed value.

In summary, two quite distinct processes (ASE photoexcitation and 'thermal' excitation during laser ablation) have been noted which may compromise the degree of both the sensitivity and selectivity routinely attainable with the existing Glasgow RIMS instrument. Both mechanisms deplete the ground state population available for RIMS analysis and consequently decrease the achievable sensitivity. The degree of problem introduced through excitation in the ablation process will vary greatly between elements, obviously becoming more prevalent at higher masses where the density of low lying states increases. The presence of matrix atoms in excited states will increase the probability of background ionization, again compromising RIMS performance. Evaluating the efffect of ASE is much more problematic. In some cases its presence could have negligible effect, save for the deleterious effects on laser power. In others, as was found for calcium, the efffects could be quite significant. Fortunately, ASE is not a fundamental problem, it is one which can be eradicated through the design of suitable laser systems.

(5)Autoionization States

"Autoionization states are bound atomic states whose energy levels relative to the outer valence electron lie above the ionization limit", Letokhov, 1987, [1].

Letokhov [1] provides an interesting discussion of both the theory behind AI states and their relevance to RIS studies. Briefly, autoionization (AI) states can decay either through a 'normal' radiative transition to a lower level, or by emitting an electron, 'autoionizing'. This new channel being opened up through coupling between the AI state and the continuum states of the atomic ion plus free electron. The major significance of such states for RIS analysis is that the cross-section to an AI state (frequently, $>10^{-16}$ cm^2) is much greater than that to the surrounding continuum (typically, less than 10^{-18} cm^2). Thus, utilization of AI resonances should yield benefits in both sensitivity and selectivity over conventional photoionization. The utility of AI states for RIMS analysis has been demonstrated by Janes et al [39], Carslon et al [40] and Solarz et al [41], all for U; Bekov et al for Yb [234], Rimke et al [235] for Gd and Tc, and Whitaker et al [30] for Ba.

As mentioned in §4.4, above, a series of narrow, low intensity lines observed in the region around 430nm are tentatively assigned to two-photon transitions from the 4s4p ^3P states to autoionization states. The lines can be seen as the fine low-level 'grass' throughout Fig. 4.5.1. Brown et al [198] give comprehensive listings of the odd parity AI states present in the portion of the spectrum which the postulated mechanism would probe. A reasonable correlation can be achieved for transitions to the 3dnp $^3D_1$, 3dnf $^3P_1$ and 3dnf $^3D_1$ series, Table 4.5.1. Many similar lines, however, remain unassigned. The postulated assignment of these lines is made uncertain by the poor wavelength measurement accuracy attainable during the course of this work. The high density of states in this region would require a wavelength

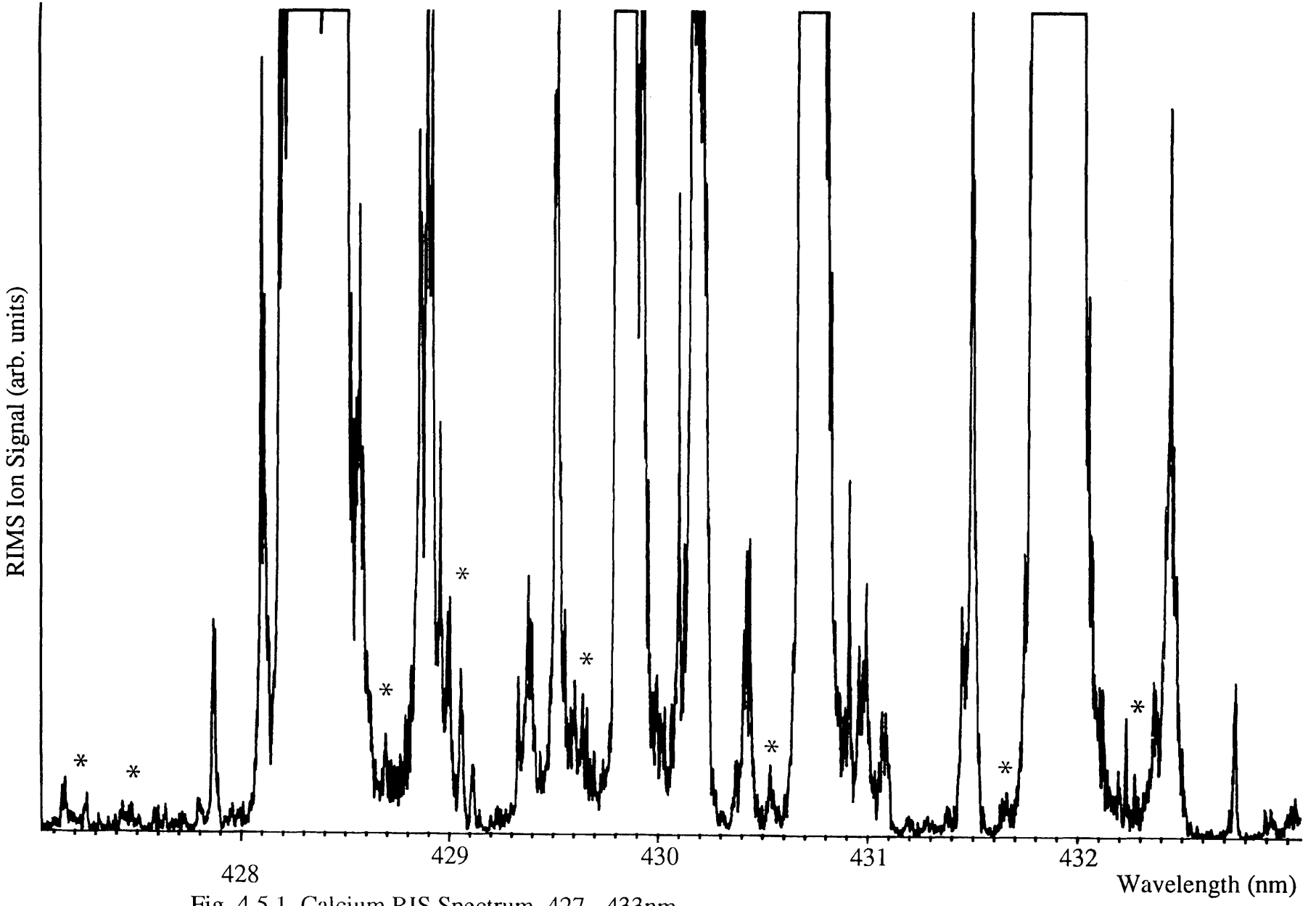

Fig. 4.5.1 Calcium RIS Spectrum, 427 - 433nm
Two-photon transitions from excited triplet states to AI states, "*"

Transition	$\lambda_{expt.}$ (nm)	$\lambda_{lit.}$ [198] (nm)
$^3P_1 \rightarrow$ 3d10p $^3D_1$	433.80	433.75
3d11p	430.49	430.53
3d12p	428.20	428.23
$^3P_1 \rightarrow$ 3d9f $^3P_1$	431.04	431.04
3d10f	428.60	428.61
$^3P_1 \rightarrow$ 3d8f $^3D_1$	435.03	435.05
3d9f	431.52	431.53
3d10f	429.10	429.07
3d11f	427.26	427.24
$^3P_2 \rightarrow$ 3d12p $^3P_1$	429.04	429.06
3d13p	427.45	427.41
$^3P_2 \rightarrow$ 3d9f $^3P_1$	432.28	432.28
3d10f	429.61	429.59
$^3P_2 \rightarrow$ 3d11p $^3D_1$	431.52	431.51
3d12p	429.45	429.50
3d13p	427.55	427.52

Table 4.5.1 Two-photon transitions from 4s4p $^3P_{1\,2}$ to AI states.

accuracy capability of better than ±0.001nm for unambiguous assignments to be made.

The potentially high ionization efficiencies available through AI states is, however, made very clear by the very observation of an ion signal through such a 'difficult' route.

(6) Suggested Improvements

Three major areas for further development of the Glasgow RIMS instrument for spectroscopic analysis can easily be identified; tunable laser sources, atomization technique and ion source design.

As has perhaps become clear through the discussions in this chapter, the present dye laser systems in use at Glasgow are less than ideal for routine RIMS analysis. Interestingly, and at times most frustratingly, there now exists new types of laser which should prove to be most suitable for RIMS analysis in general, and would have been ideal for the experiments carried out in this programme. Optical parametric oscillators (OPO) and tunable solid-state lasers, in particular Ti:sapphire, have recently begun to deliver the range of performance hitherto only accessible with dye lasers. Ledingham and Singhal (1990) [240] have recently prepared a critical assessment of the potential of such new solid-state sources for RIMS analysis. Messenger [210] gives a brief review of the new tunable solid-state laser systems and some of their applications. A single OPO, pumped with the third harmonic (355nm) from a pulsed Nd:YAG laser, could cover the range from 400nm to 2μm; and with sufficient power to allow efficient frequency doubling down to 200nm. All of the tunable solid-state laser systems operate in the near infra-red (eg. Ti:sapphire, 670-1150nm; Alexandrite, 720-800nm) but provide sufficient power (>1W in CW operation) to allow

efficient frequency doubling into the blue/UV region. Frequency doubled Ti:sapphire would have allowed the entire wavelength region of interest in this work to be covered with solid-state convenience and none of the practical problems found with dye laser operation (dye aging, chemical toxicity etc.) Also, the use of Ti:sapphire would have eliminated the ASE problem encountered with the blue dye laser: frequency doubling and filtering of residual fundamental wavelengths providing a simple way of eliminating ASE.

Undoubtedly, such new laser sources will have a major role to play in helping RIMS analysis to reach its full potential.

Laser ablation is undoubtedly a very simple method by which to provide a high pulsed density of neutral species for analysis. However, as an atomization source for spectroscopic investigations, several limitations are clear. The amount of material ablated per laser shot will vary with ablation laser power and consequently the density of analyte material available for analysis will also vary. This will ultimately limit the degree of accuracy attainable in making relative intensity measurements (by comparison, atomic beam sources, ovens, filaments etc, can provide highly stable reservoirs). Pulsed ion sputtering may also prove to be superior in this respect.

Finally, the existing ion source region has two main weaknesses for laser spectroscopy; the extract volume is quite small (see Chapter 2) and a relatively high electric field exists in the analysis volume. The former point becomes important when large wavelength ranges are scanned and small movements of the laser beam in the source become unavoidable through changes in the refractive index for beam optics. Thus, at present, small changes in beam position can lead to relatively large changes in measured signal intensity. The presence of the extract electric field (≈300V/cm) in the ion source will lead to Stark shifts and splittings of spectral lines (particularly high lying states), to the obvious detriment of high resolution

spectroscopy [194,205]. One simple solution would be to apply the extract field only after the laser ionization has taken place, by applying a pulsed voltage potential to the first optic. Such a pulse would require a very fast rise time (>30V/ns) in order to preserve mass spectral resolution.

---

5. Laser Mass Spectrometry

This chapter will describe some of the early mass spectrometric investigations carried out on the Kratos Machine. Three major areas were studied: the elemental trace analysis capability of the instrument; the accuracy and precision of isotope ratio measurements; and the comparitive 'abilities' of various laser ionization mass spectrometry techniques.

(1) Trace Analysis

The ability of the Kratos Machine to undertake elemental trace analyses was investigated both for calcium and rubidium. These results have previously been reported in Towrie et al (1989), [212]. In both cases, complex sample matrices were prepared to provide a more realistic simulation of the ability of the RIMS instrument to deal with 'real-world' samples.

(i) Rubidium Measurements

The rubidium measurements concluded a series of experiments conducted in the LIS group primarily by Drs. M. H. C. Smyth and M. Towrie. For the rubidium measurements, the sample was prepared in the following fashion. NBS standard reference material coal (SRM 1632a) and high purity graphite powder were mixed 1:1 in precisely weighted amounts. The NBS coal has a certified rubidium content of 30ppm. The graphite powder served several purposes: to 'dilute' the coal sample, act as a mechanical binding agent, and to make the final sample pellet conducting [115]. The powders were mixed and homogenized using a glass pestle and mortar. The resulting mixture contained rubidium at a concentration of 15ppm. This final powder was then compressed, using a 10-ton manual

press, into a solid pellet form directly within a 10mm diameter hole drilled into the centre face of a sample stub (Fig. 2.1.2). A sample 'blank' was prepared in a similar way using only the graphite powder.

Laser ablation, at a wavelength of 532nm and a fluence of $\approx 4 mJ/mm^2$, was used as the atomization technique. A two colour resonance ionization scheme was utilized. A blue photon at 421.7nm (Stilbene 420 dye) excited the neutral rubidium from the 5s $^2S_{1/2}$ ground state to 6p $^2P_{3/2}$. This excited state was then photoionized using the 532nm second harmonic from the Spectron Nd:YAG pump laser. The resulting time-of-flight spectrum is shown in Fig. 5.1.1. The two rubidium isotopes, ^{85}Rb and ^{87}Rb, are clearly visible and in approximately the correct isotope ratio. The background level in this spectrum is ≈1ppm. The Rb ion signal was observed to diminish to below the noise floor when the resonant laser was detuned from resonance. No signal above background was observed for the graphite sample blank. At the time these results were taken, the data acquisition electronics and software were still in the early stages of development, and consequently some of this background was probably due to electronic noise. The two broad peaks, bracketing the rubidium isotopes, were produced by unsuppressed carbon cluster ablation ions, C_7 and C_8, as discussed in Chapter 3. The mass spectrometer was then set to transmit ions created in the ablation process. The time-of-flight spectrum resulting solely from laser ablation is shown in Fig. 5.1.2. The absence of visible peaks for the rubidium isotopes in this figure confirms that, for the ablation parameters employed here, significantly more neutral species are formed in the ablation process than ionic forms.

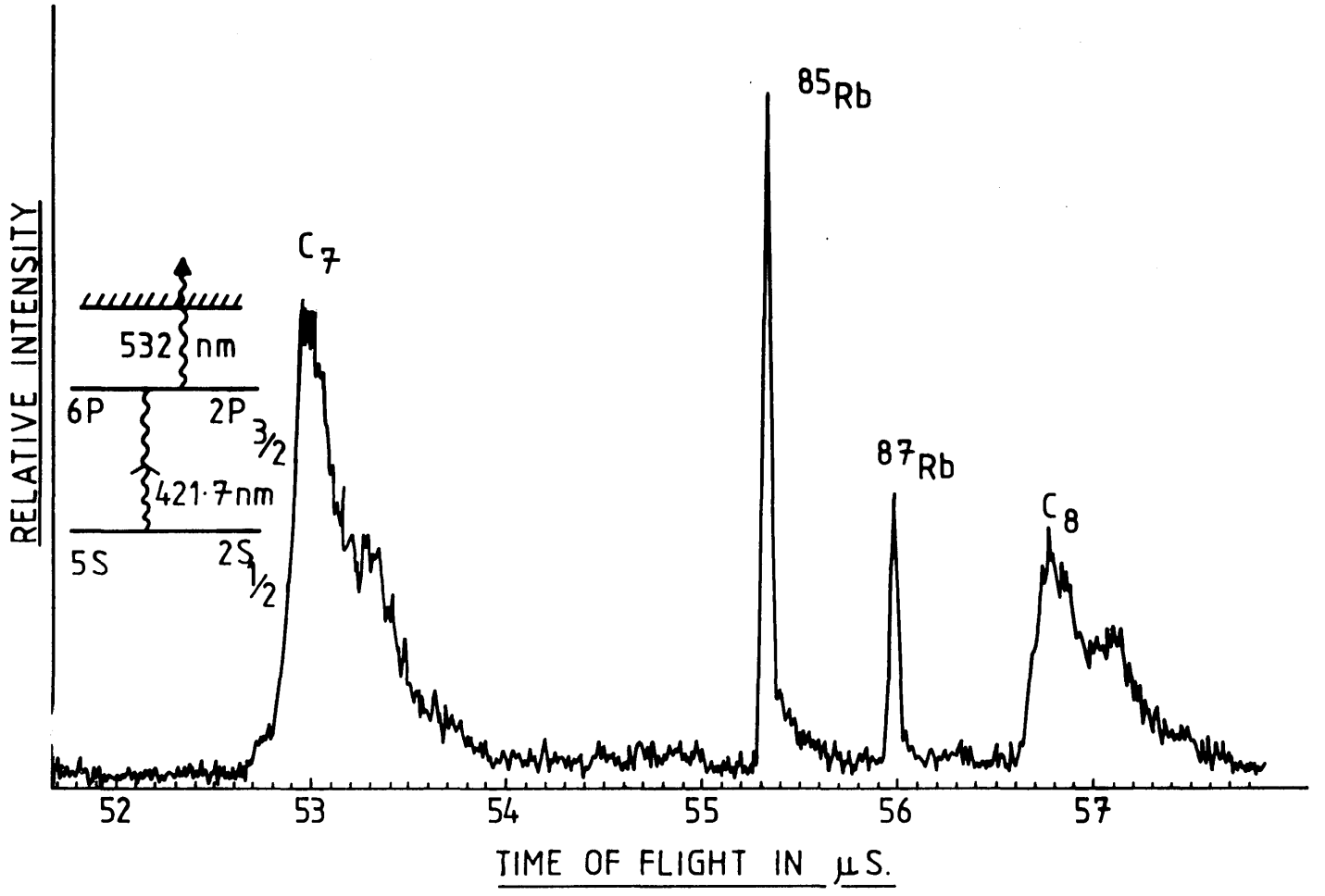

Fig. 5.1.1 RIMS of Rb isotopes, coal/graphite sample,15ppm

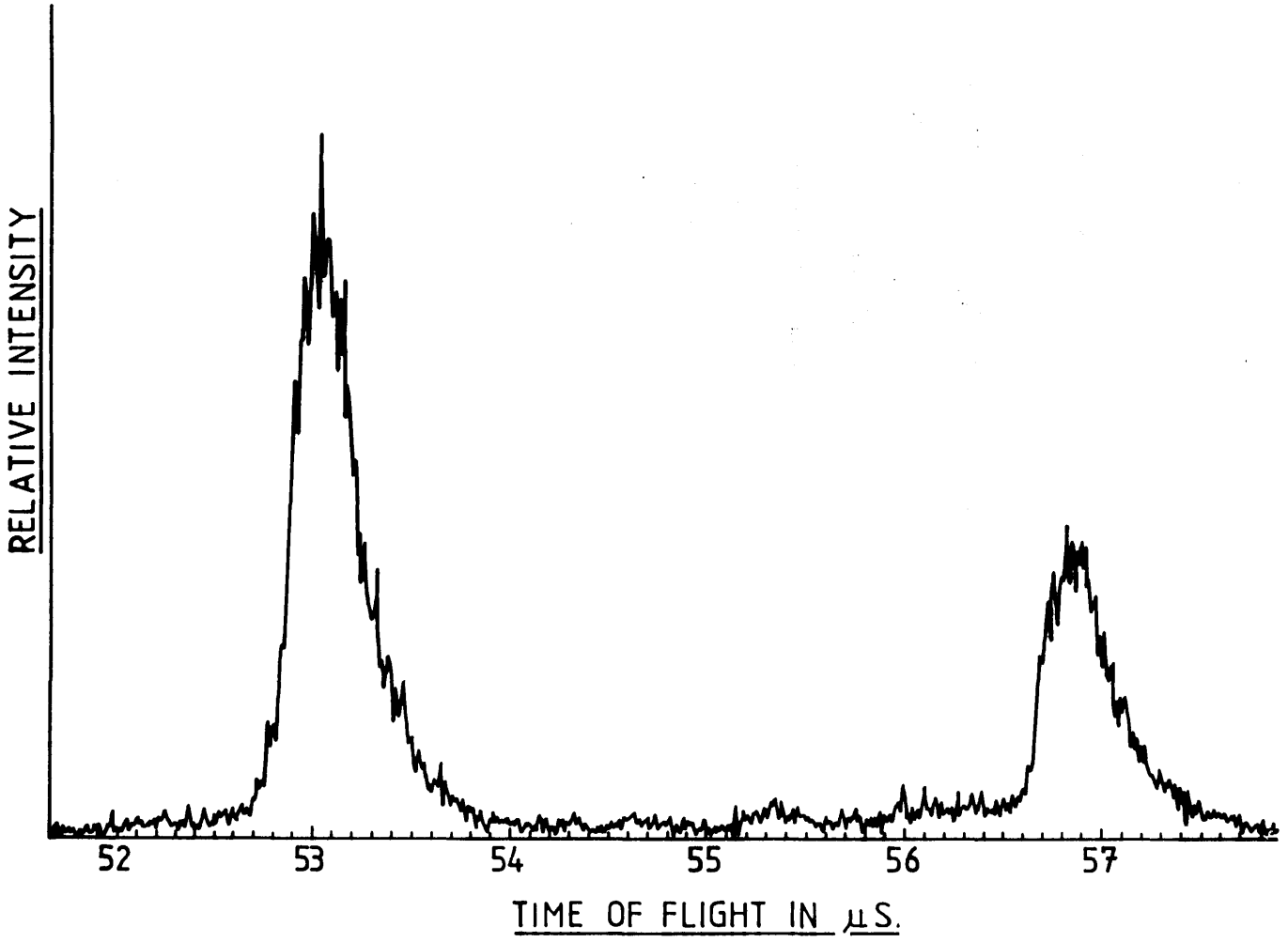

Fig. 5.1.2 Laser ablation of Rb coal/graphite sample

(ii) Calcium Measurements

The early measurements carried out with calcium were very similar to those described above for rubidium. A sample pellet was formed from a 1:4 weighted mix of high purity calcium carbonate and graphite powders. Obviously, the resulting sample contained calcium in far from trace quantities. However, the minor isotope ^{46}Ca was present at a level of only ≈3ppm. Laser ablation (532nm, 4mJ/mm^2) was again utilized as the atomization technique. A one colour, two-photon resonant, three-photon ionization scheme was employed using yellow/green photons at 536.1nm: $4s^2\ ^1S_0 \rightarrow 4s4d\ ^1D_2$. The resulting time-of-flight spectrum is shown in Fig. 5.1.3. Again, the background noise is at a level of ≈1ppm. All mass peaks displayed sharply resonant behaviour as the wavelength was scanned, demonstrating the lack of isobaric interferences.

These early results demonstrate well the capability of RIMS to undertake trace analysis measurements at the ppm level on complex samples without chemical preprocessing. The most significant problem raised by these investigations was the need to suppress background ions formed in the laser ablation process. Whilst the Reflectron provides a high degree of energy filtering, further development would seem to be required in this area to allow routine operation at the sub-ppm level.

Work is in progress in the LIS group to develop an elegant ion-optical solution to this problem, Fig. 5.1.4, [212]. By using a multi-element ion lens, it is possible to arrange for a field reversal to take place between the sample and the first optic. Ions created on the sample side of the reversal will be attracted back towards the sample, whilst ions on the optics side will be extracted into the mass spectrometer. One added advantage of this scheme, is that it should be possible to create RIMS ions in a comparatively low electric field region, with consequently reduced problems with Stark shifts and splittings (see Chapter 4.)

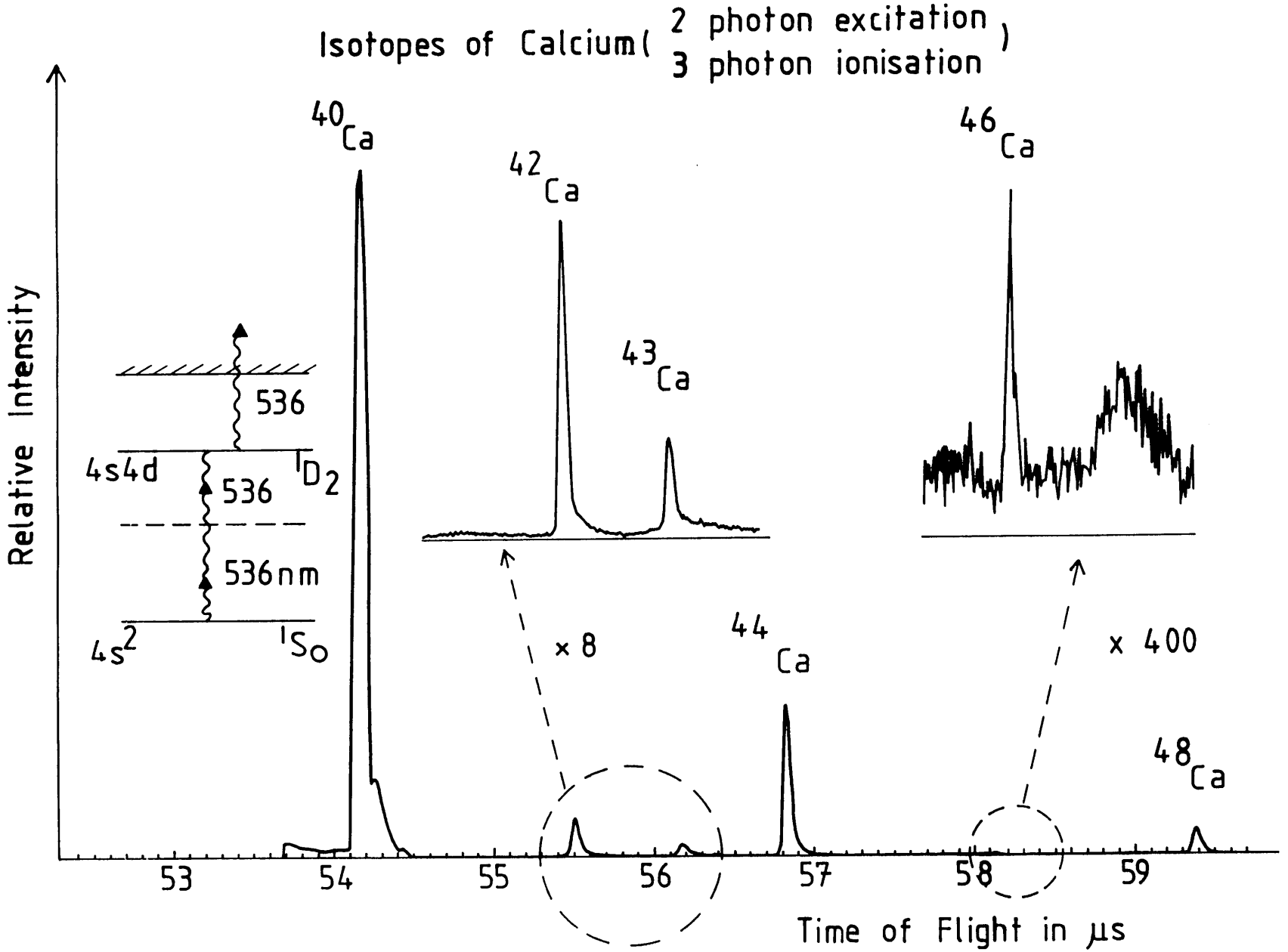

Fig. 5.1.3 RIMS of Ca isotopes, ^{46}Ca at 3ppm

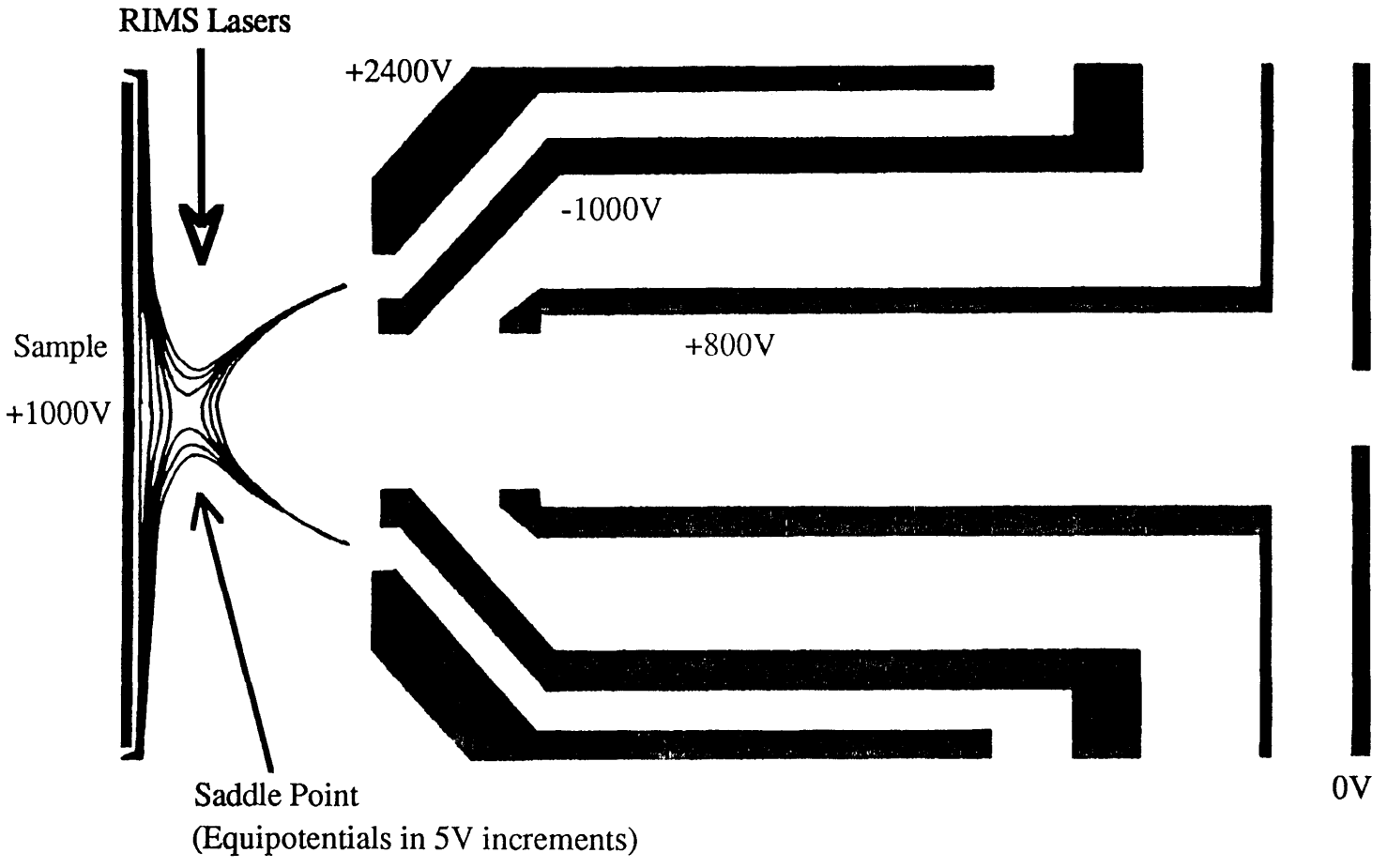

Fig. 5.1.4 Proposed ion optics arrangement for efficient suppression of background LIMA or SIMS ions

(2) Isotope Ratio Measurements

(i) Discussion and Preliminary Results

The ability to make isotope ratio measurements is a very important performance parameter for a mass spectrometry technique. Such information is of direct interest in sample characterization, helps to illuminate isobaric interferences and allows internally quantified results to be obtained through the isotope dilution methodology [5, 63]. RIMS was originally envisaged as being capable of playing two distinct roles in isotope ratio analysis: utilizing narrow linewidth lasers, individual isotopes could be selectively excited, and, with broad band laser sources, all isotopes of a chosen element could be equally excited, giving direct isotope ratio measurements [2]. Whilst narrow linewidth techniques (principally CW lasers) have demonstrated excellent performance characteristics [30, 35], some systematic problems are begining to be recognized for broad band, pulsed laser excitation methods [44, 45].

Some preliminary investigations were carried out on the Kratos Machine to assess the instrument's capabilities for precise and accurate isotope ratio measurements. As discussed in the Chapter 1, calcium is an excellent system for the study of isotope ratios: the stable isotopes span a large mass range (40-48amu); the isotope abundance ratios cover a very large dynamic range, ^{40}Ca:$^{46}Ca \approx 25{,}000{:}1$, but also ^{43}Ca:$^{48}Ca \approx 3{:}4$; and both odd and even nuclear spin stable isotopes are present. The isotope shifts and hyperfine structure for the calcium isotopes have been measured by several authors: Lorenzen et al (1983) [154] provide a valuable summary covering a variety of one- and two- photon transitions from the ground state. Shifts range from a few hunderd megahertz (eg. ^{48}Ca-^{46}Ca, 1-photon, 4s4p $^3P_1$, 441MHz) up to several gigahertz (eg. ^{48}Ca -^{40}Ca, 2-photon $\rightarrow$ 3d5s $^1D_2$, 4.367GHz).

Andl et al (1982) [213] studied the $4s^2\ ^1S_0 \rightarrow 4s4p\ ^1P_1$ transition in detail, and Brinkmann et al (1974) [214] provide a most interesting account of an early use of RIS for isotope selection. The Spectron dye lasers used throughout this programme of work have a specified linewidth of $0.1cm^{-1}$ (≈3GHz), considerably greater than the doppler-broadened linewidths expected in the laser ablated plume (<0.5GHz, Chapter 3), but comparable with the isotope shifts and hyperfine structure noted above.

Although early isotope ratio results were promising, [212], marked reproducibility problems were subsequently encountered. As mentioned in Chapter 2, the gain of the channel plate ion detector was observed to decline severely over the several months of operation, ultimately prohibiting accurate measurements on minor peaks. For this reason, measurements concentrated on the two major isotopes, ^{40}Ca and ^{44}Ca, present naturally in the ratio 47.15:1, [147]. The measured ratio for this isotopic pair varied, seemingly randomly, between 32:1 and 102:1 (!), utilizing a variety of RIS transition schemes.

Several authors have reported difficulties in making isotope ratio measurements using similar equipment and methodologies to those employed here [44, 215]. There is a growing consensus that many of these problems are of a fundamental nature, brought about through subtleties of the basic light-field/atomic interaction (laser mode structure, temporal profile, wavelength stability, hyperfine interactions etc., [45]). Given the comparatively large isotope shifts present on the transitions being utilized (eg. ^{40}Ca -^{44}Ca, $4s^2\ ^1S_0 \rightarrow 4s10s\ ^1S_0$, 1.616GHz, [154]) some problems were perhaps to be expected. It was hoped, however, that problems of this nature would be clarified by slowly scanning the laser wavelength across a spectral line and observing any variation in the measured isotope ratios. Irreproducibility was such that these measurements were at best inconclusive, a trend apparent on one run being negated by the results of the

following day's efforts. Obviously some other source(s) of error was 'dominating' the situation and masking the potentially interesting photo-physics.

Various other possible sources of confusion were considered. Micro-inhomogenities in the isotope distribution within the sample matrix could play a role, but no improvement was found upon changing to a simple metallic calcium sample. The position of the ionizing laser within the ion source will probably play a role, since it is unlikely that ion transmission for different masses is entirely uniform from within the source region. Again, however, no systematic, reproducible trend was detected. One interesting possibility, is that of an isotope bias effect in the distribution of neutrals within the ablation plume. Certainly, for the 'thermal spike' ablation model outlined in Chapter 3, lighter isotopic species may be expected to move away from the sample surface faster than heavier species, leading to a shift in temporal distributions between the isotopes (see, Fig. 3.3.4). This could be investigated by measuring the isotope ratio for a variety of delay times between ablation and ionization pulses. Early results, however, again showed no reproducible trends. Simons [90] reported a systematic problem with isotope ratio measurements on a commercial LAMMA instrument, ultimately traced to a detector saturation problem. Here, however, no simple correlation between measured ratio and signal size was observed. Finally, one major problem source was discovered. As noted in Chapter 2, the channel plate detector was supplied with a somewhat unorthodox biasing arrangement, see Figs. 2.1.6 (a). Once modified to a more conventional form, Fig. 2.1.6 (b), a marked improvement was immediately evident. Presumably, a complex space-charge effect between the ends of the multiplier channels and the collector anode was causing at least part of the irreproducibility problems.

The final set of data collected for this programme of work consisted of

two independent sets of fifteen measurements of the ^{40}Ca:^{44}Ca ratio. Laser ablation (1.06μm, 4mJ/mm^2) and a 2+1 RIS scheme ($4s^2\ ^1S_0 \rightarrow 4s10s\ ^1S_0$, 421.5nm), provided the atomization and ionization processes, respectively. Each measurement consisted of a mass spectrum collected over 1000 laser shots. The results for the average of each run were, 48.2±1.1 and 47.3±2.2, respectively, where the quoted uncertainty is equal to one standard deviation. The scatter of data appears to be quite random, with no correlation with time or signal size evident, despite a change in absolute signal size of ≈x2. These results correspond to an accuracy of better than ±3% and a precision of ±5%.

Whilst most encouraging, these results are obviously very much a beginning, still far from the fundamental Poisson statistics limit that Fassett and Walker [66] have shown is approachable with pulsed RIMS technology. The various parameters which are expected to influence ratio measurements, discussed above, will have to be investigated in detail. Only then will the Kratos Machine's ability to make accurate and precise isotope ratio measurements on a routine basis be made clear.

(ii) Polarisation Effects

As discussed in Chapter 4 and Appendix B, the polarisation of the laser light can play a major role in the observed spectroscopy. Principally, two-photon transitions between J=0 states are allowed for linear polarisation, whilst being forbidden for circular polarisation (see Figs. 4.3.2 and 4.3.3). For an atomic system with a nuclear magnetic moment, however, this restriction is lifted. Balling and Wright (1976) [216] have proposed a novel method by which these simple, but powerful, selection rules can be 'harnessed' to allow laser isotope separation without the need for narrow linewidth lasers. In principle, their method can be used to separate all isotopes with different nuclear spins (eg. I=0, 1/2, 3/2). For calcium, of the

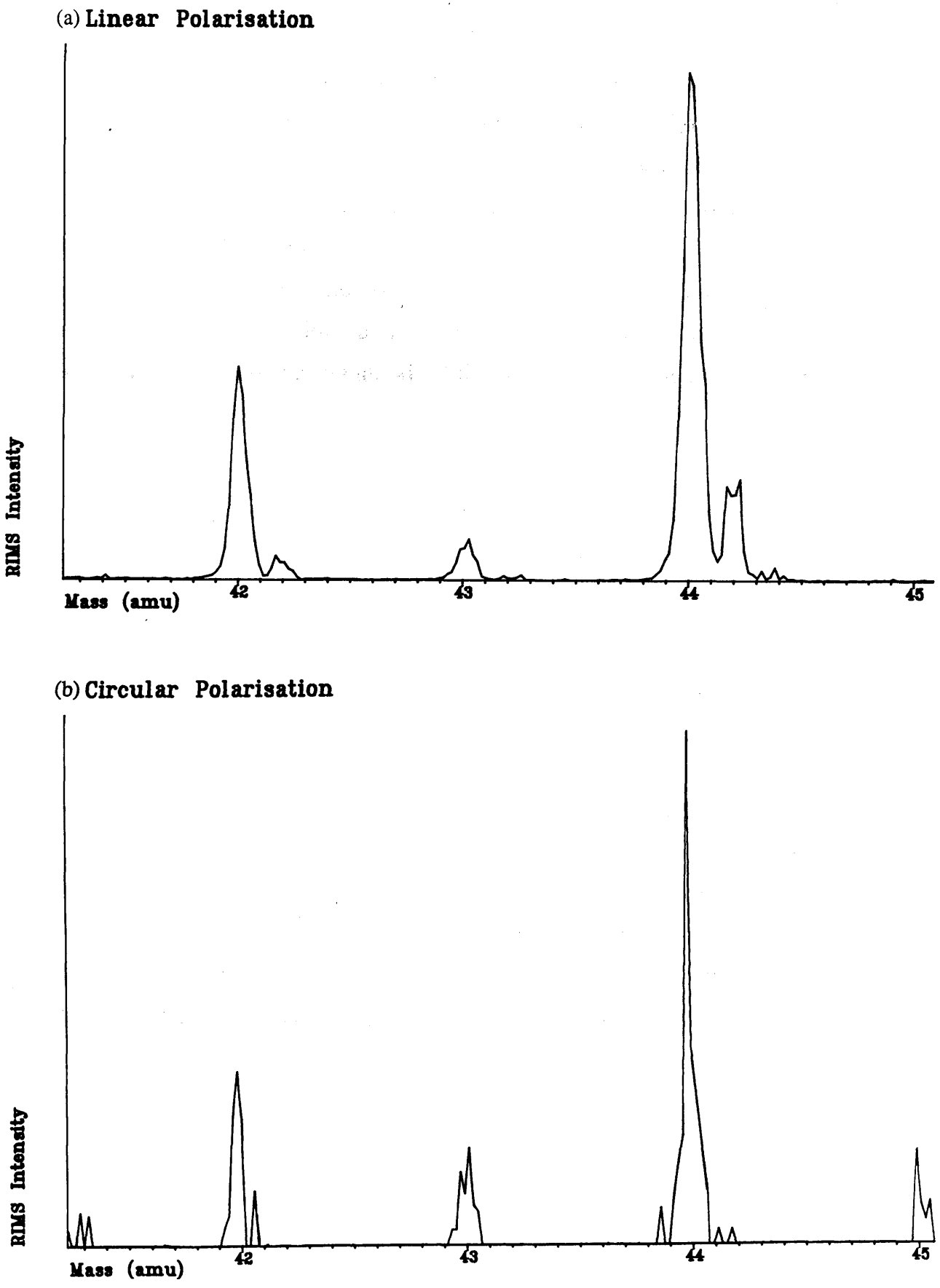

Fig. 5.2.1 RIMS of Ca isotopes, see text for details

naturally occurring stable isotopes, only ^{43}Ca has a non-zero nuclear spin (I=7/2). As discussed in Chapter 1, however, there is much interest in the possibility of measuring the rare, radioactive ^{41}Ca isotope (also I=7/2), such a measurement requiring excellent differentiation against the dominant ^{40}Ca. Balling and Wright's original scheme [216] envisaged using a two colour, 1+1+1, RIS scheme. Here, the possibility of utilizing a two-photon excitation was investigated. In principle, this should allow a greater possible odd/even enhancement whilst still allowing all of the benefits of two-photon excitation, discussed in Chapter 4 (eg. Doppler-free excitation), to be retained.

The two-photon transition $4s^2\ ^1S_0 \rightarrow 4s10s\ ^1S_0$ was investigated. A high quality of linear polarisation was assured through use of a Newport Beam Polarising Cube (>99% polarisation purity). The mass spectrum, covering the calcium isotopes 42, 43, 44, obtained with linearly polarised light is shown in Fig. 5.2.1 (a). A Fresnel rhomb was used to transform the linear polarisation into circular polarisation, the resulting quality of polarisation was not measured, but was estimated to be ≈95% (from consideration of the rhomb's specifications and the achievable accuracy of alignment) . From Balling and Wright's calculations [216], this quality of polarisation should enhance the odd/even ratio ≈x2. The comparative mass spectrum obtained with the circular polarisation is shown in Fig. 5.2.1 (b). The absolute intensity of signal in (b) is much reduced from that in (a) through practical problems in re-aligning the laser beam after insertion of the rhomb. The measured ratio of the even isotopes $^{42}Ca/^{44}Ca$ remained constant over the two runs, whilst the relative level of the odd isotope ^{43}Ca increased by a factor of 3.4 (which would correspond to a 97% pure circularly polarised beam). Improving the quality of polarisation to 99.9% would, in principle, give an enhancement of ≈x100. Evidently this method does hold some real promise for enhanced isotope separation in the calcium system.

(3) Comparison of Laser Mass Spectrometry Techniques

It was possible to use lasers to generate an ion signal in several different ways on the Kratos Machine: basic laser ablation ('LIMA'); resonant laser ablation ('RLA'); non-resonant laser post-ionization ('SALI'); and finally, resonant laser post-ionization ('RIMS'). A qualitative comparison of these various methods was undertaken using a simple calcium metal sample.

The calcium sample was formed by placing a single granule of the metal into a 3mm diameter well in the centre of a sample stub, and then compressing the rough granule with a 10 ton manual press until a good fit was obtained. The surface of the stub/sample was then rubbed flat using emery paper, a reasonable surface finish was achieved, although distinct grain boundaries were visible. The freshly cut metal surface was distinctly white and shiny, but tarnished rapidly in air to a dark matte gray. When ablated at high laser fluences (>10mJ/mm^2) under vacuum, the surface was observed to 'clean up', but then slowly return to a tarnished state over a period of a few hours, despite the UHV environment. This simple observation has important consequences for sample handling/preparation for sensitive surface analyses.

Each final mass spectrum shown is built up from four consecutive runs, each of 4000 laser shots, with the time window stepped in 30μs intervals for each run. (The transient recorder was run with a 20MHz sampling rate, giving a temporal resolution of 50ns and a maximum window for each run of 32μs.)

(i) Laser Ablation

The mass spectrometer was adjusted to allow efficient transmission of ions created at the sample surface by raising the 'reflect' potential on the reflectron ion mirror to a value greater than that of the sample.

(a) LIMA

LIMA has become a popular method for elemental trace analysis, especially so when a micro-imaging capability is required [16, 90, 174]. The most commonly employed ablation laser for LIMA analysis is the frequency quadrupled Nd:YAG at 266nm. The very high ablation fluences, >10J/mm^2, used in commercial LIMA instruments could not be reached on the Kratos Machine: the need to focus the ablation laser external to the vacuum system resulted in comparatively large ablation spot sizes (10^{-8} mm^2, compared with, 10^{-12} mm^2 on commercial instruments), and consequently much lower power densities for similar total ion yields. The ablation spectrum obtained using 266nm at a fluence of ≈5mJ/mm^2 into a spot diameter of ≈1mm and at a 45° angle of incidence, is shown in Figs. 5.3.1 (a, b). Evidently the sample surface consists of more than simply pure calcium metal! Basic elemental peaks are also clearly present for Na(23amu), Al(27) and K(39, 41), Cr(52) and Co(59). Many of the remaining peaks can be assigned to simple calcium ion molecular forms, eg. CaO(56amu), the dimer Ca_2(80), Ca_2H_3(83), Ca_2O(96) etc. Unequivocal identification of the remaining low intensity peaks was not possible with the available mass measurement accuracy, most of these probably arise from hydrocarbon impurities adsorbed onto the sample surface.

The experiment was repeated using the infra-red 1.06μm fundamental radiation from the ablation Nd:YAG, the results are shown in Figs. 5.3.2 (a, b). Most interestingly, this spectrum is very similar to that obtained with the UV wavelength ablation, indicating that the basic ablation process is largely independent of wavelength for the conditions employed here. This observation is consistent with a simple thermal evaporation process for laser ablation, see Chapter 3.

Both the major strength and ultimate weakness of the LIMA approach,

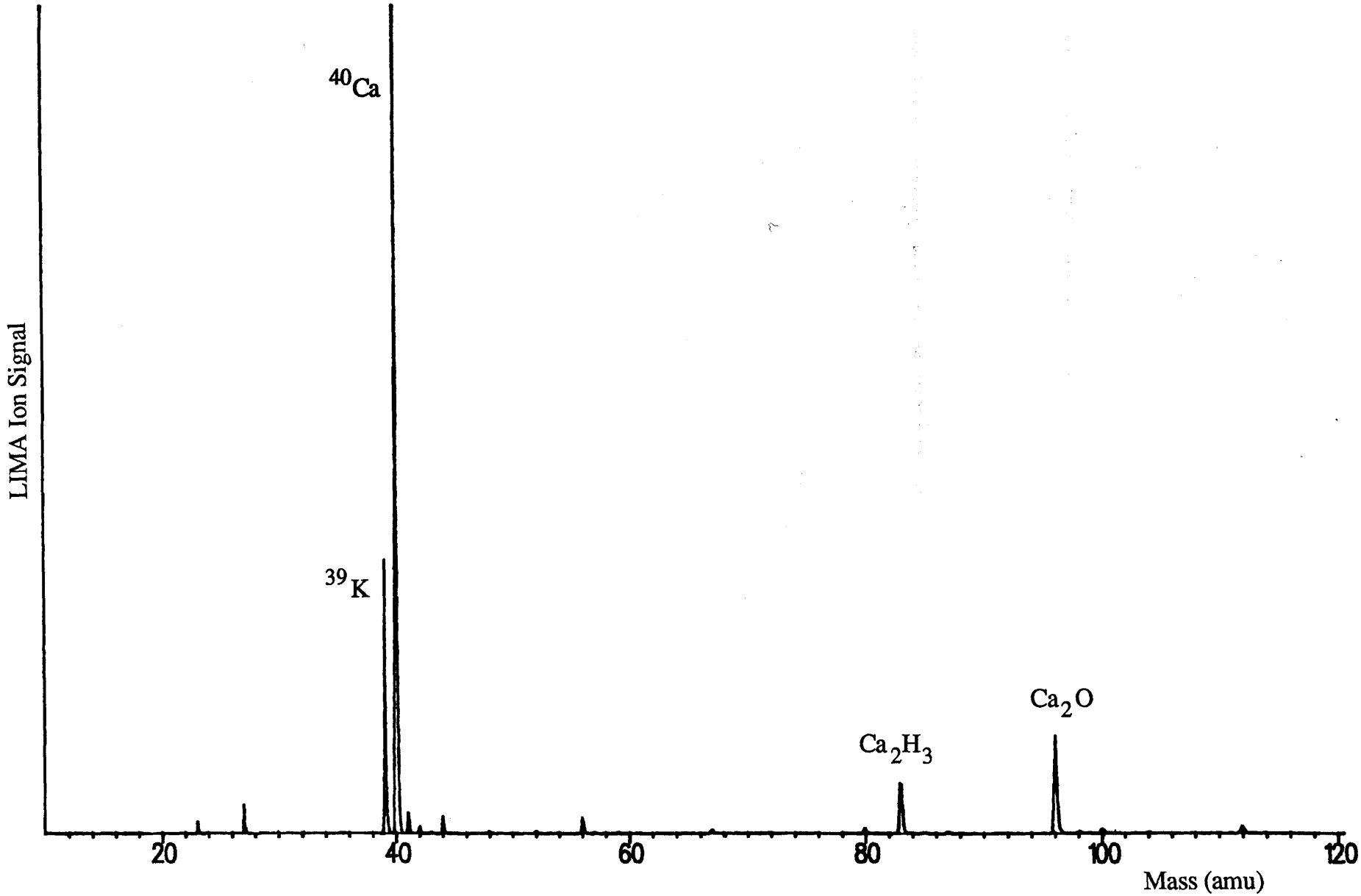

Fig. 5.3.1 (a) LIMA Mass Spectrum, 266nm Ablation

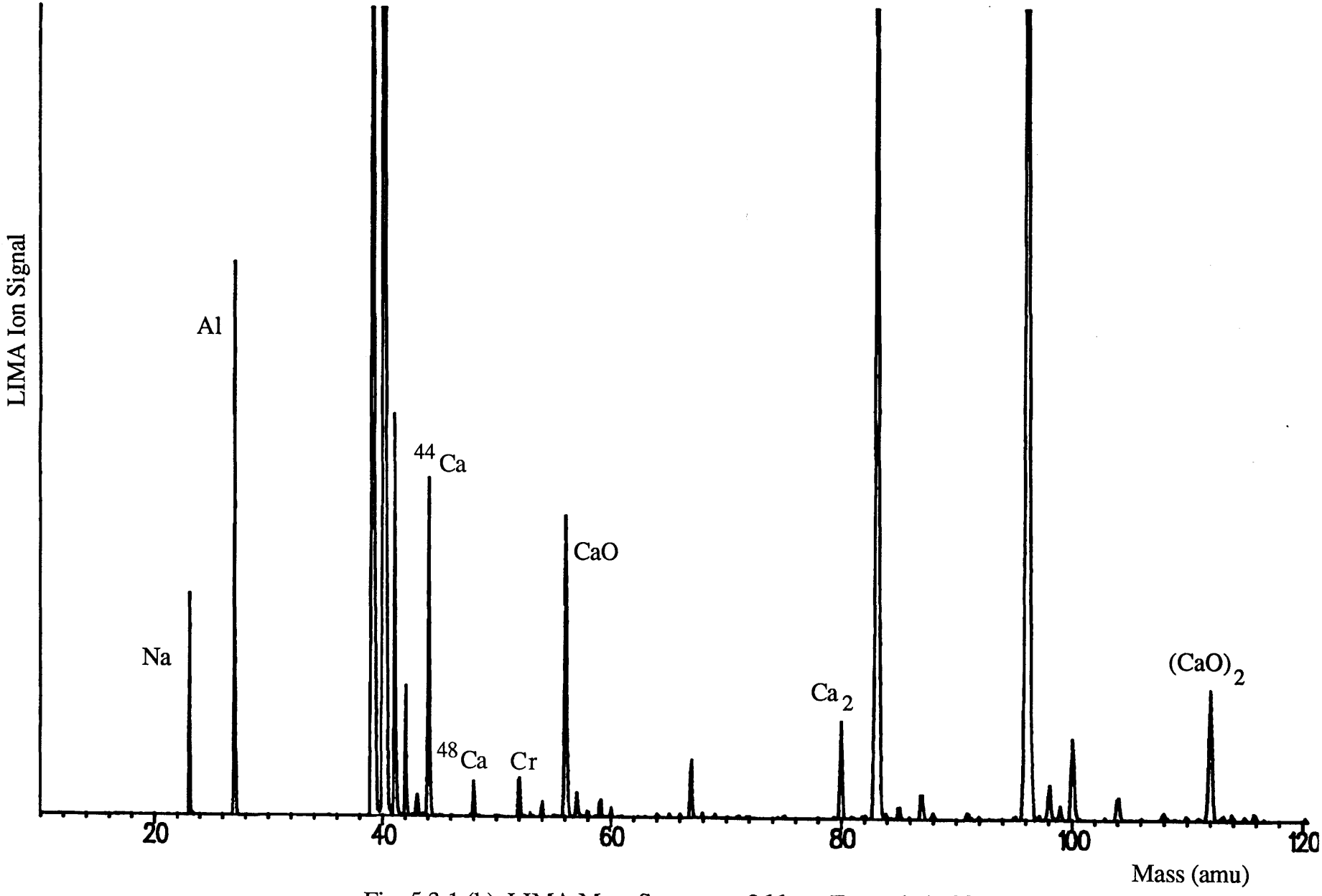

Fig. 5.3.1 (b) LIMA Mass Spectrum, 266nm, Expanded x20

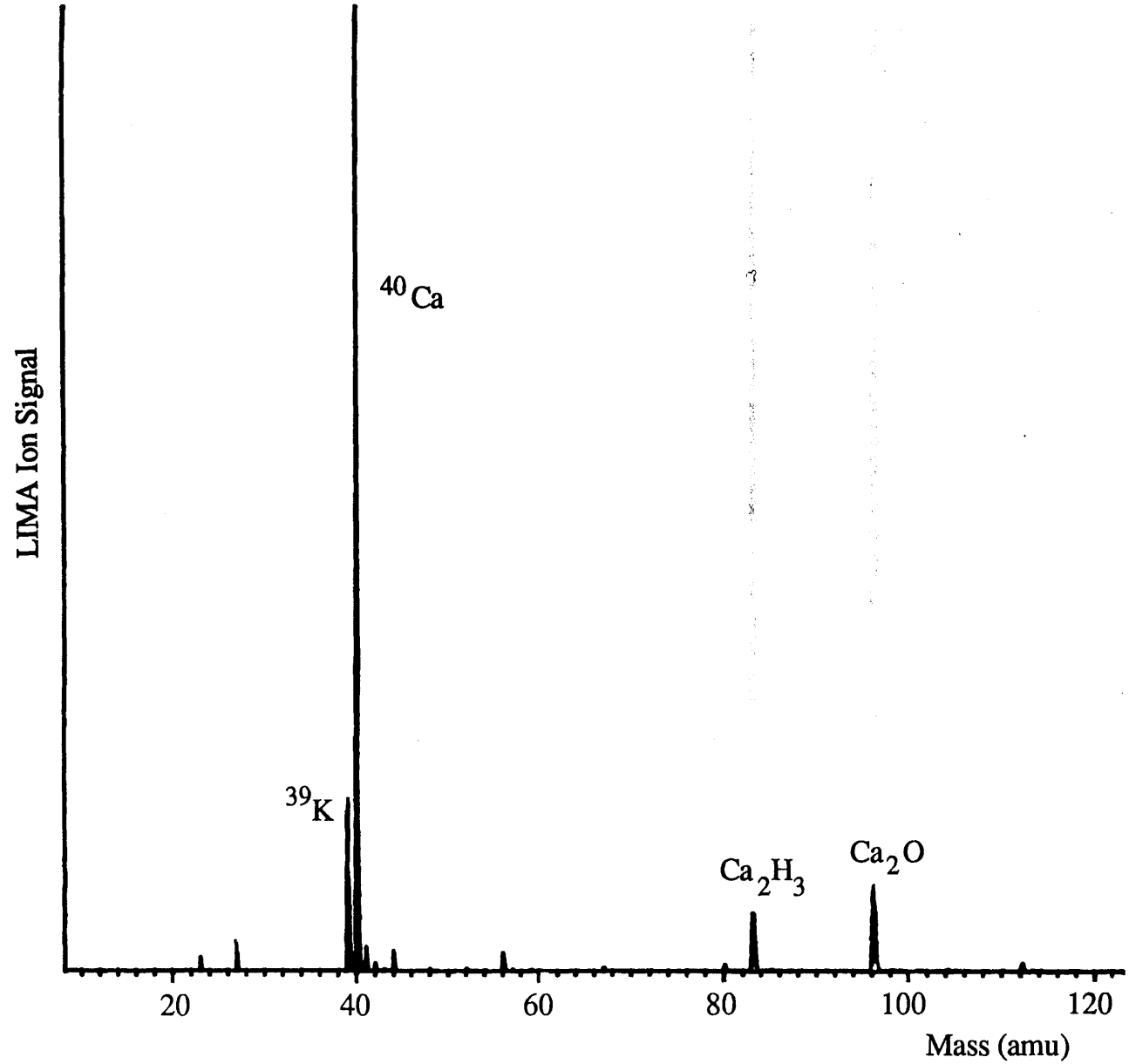

Fig. 5.3.2 (a) LIMA Mass Spectrum, 1.06μm Ablation

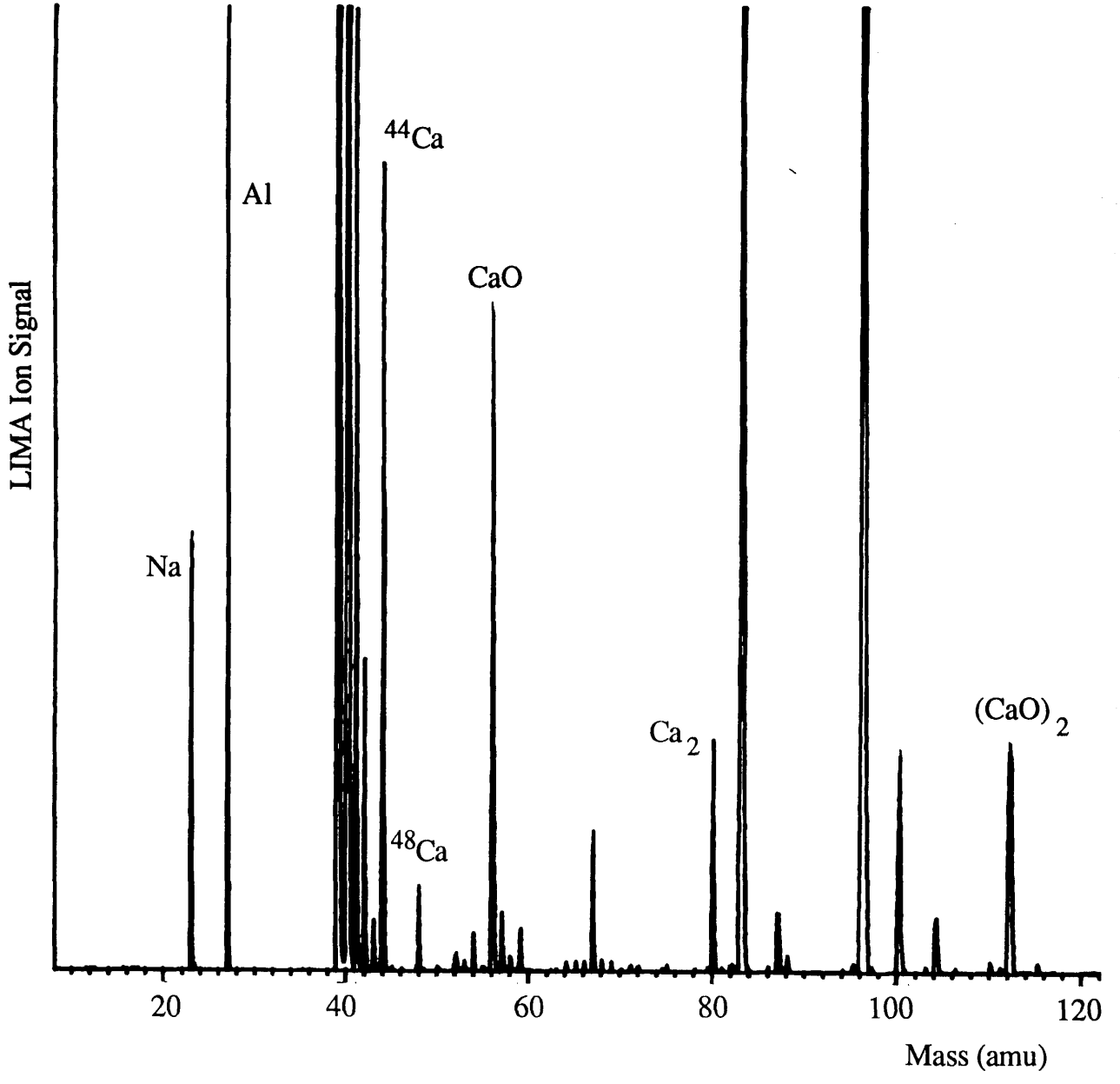

Fig. 5.3.2 (b) LIMA Mass Spectrum, 1.06μm, Expanded x40

as discussed in Chapter 1, are evident in the above spectra. All elements present in the sample are ionized to some degree, giving a rapid multi-element analysis capabilty. However, this inherent lack of selectivity in the ionization process must ultimately limit the attainable sensitivity through isobaric interferences. LIMA is known to be prone to strong matrix effects, [2, 5, 174], thought to be due to the very high ion densities occurring near the sample surface during the ablation process. This is well demonstarted by the observation of relatively strong ion peaks for elements such as Al, Na and K which are present only in small proportion in the sample, and by the strong Ca ion molecular peaks.

(b) Resonant Laser Ablation (RLA)

The novel technique of resonant laser ablation (RLA), as detailed in Chapter 3, gave rise to a quite different mass spectrum, Figs. 5.3.3 (a, b). Note the comparatively high scale multiplication factor (x1000) in (b) compared with that for the non-resonant ablation of Figs. 5.3.2, 5.3.3 (x20), above. The 2+1 ionization scheme at 600.1nm was again utilized, with the ablation beam at grazing incidence, ≈3°, and a fluence of ≈30uJ/mm^2. The only elemental line clearly observed is at ^{27}Al, molecular ions are limited to CaO and the dimer Ca_2 plus some of its hydrides. Clearly the RLA technique is comparatively free of both the major weaknesses of non-resonant ablation, demonstrating high selectivity and low matrix effects. However, as will be shown below, RLA does not display the full strength of RIMS in either of these aspects, the high ionization density in close proximity to the sample surface remaining a limiting factor. The sensitivity of the RLA approach is not clear from these results, although sensitivities at least as great as those attained with LIMA should be expected. One very obvious strength must be the very high geometric overlap between 'ablation' and 'ionization' beams.

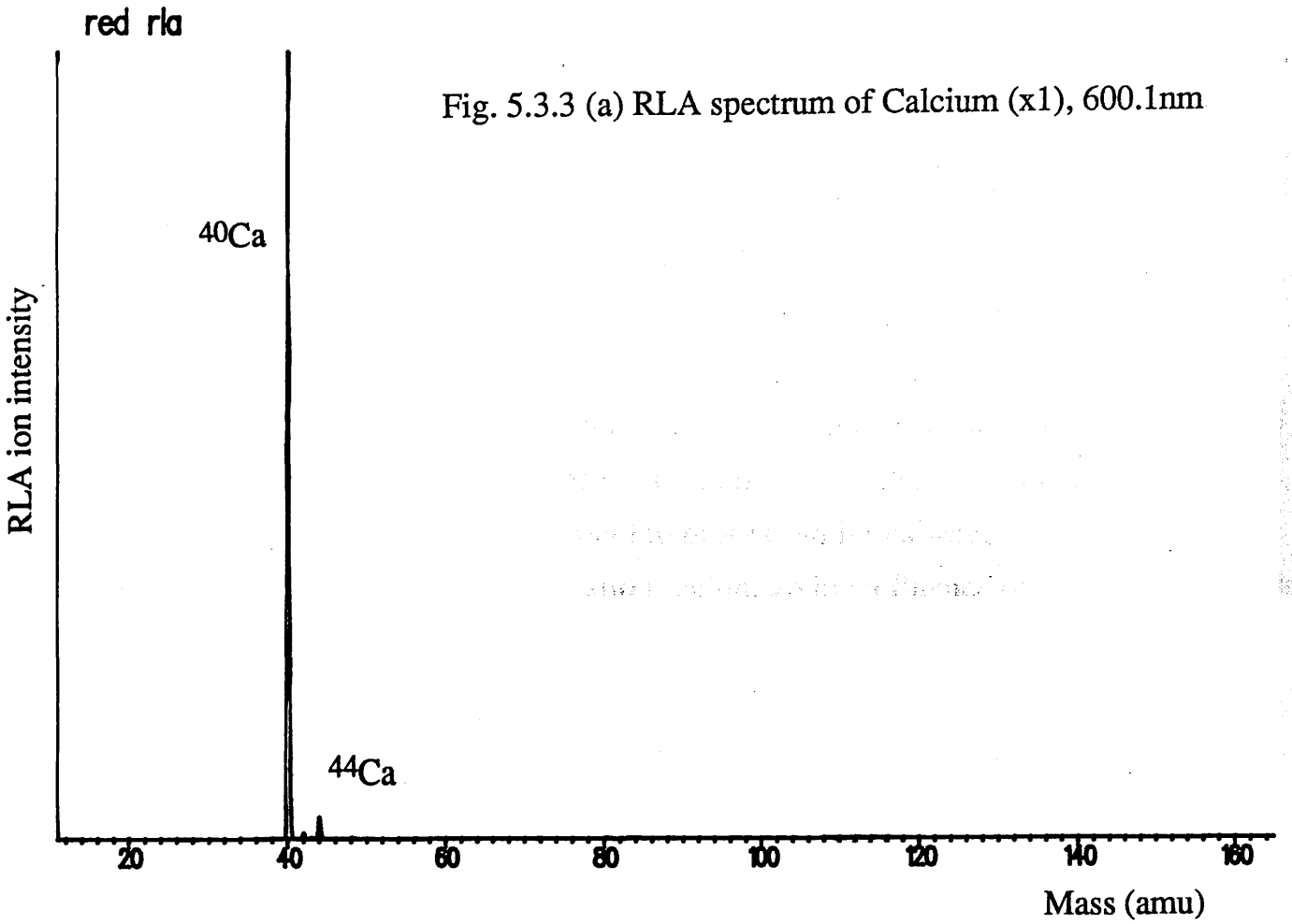

Fig. 5.3.3 (a) RLA spectrum of Calcium (x1), 600.1nm

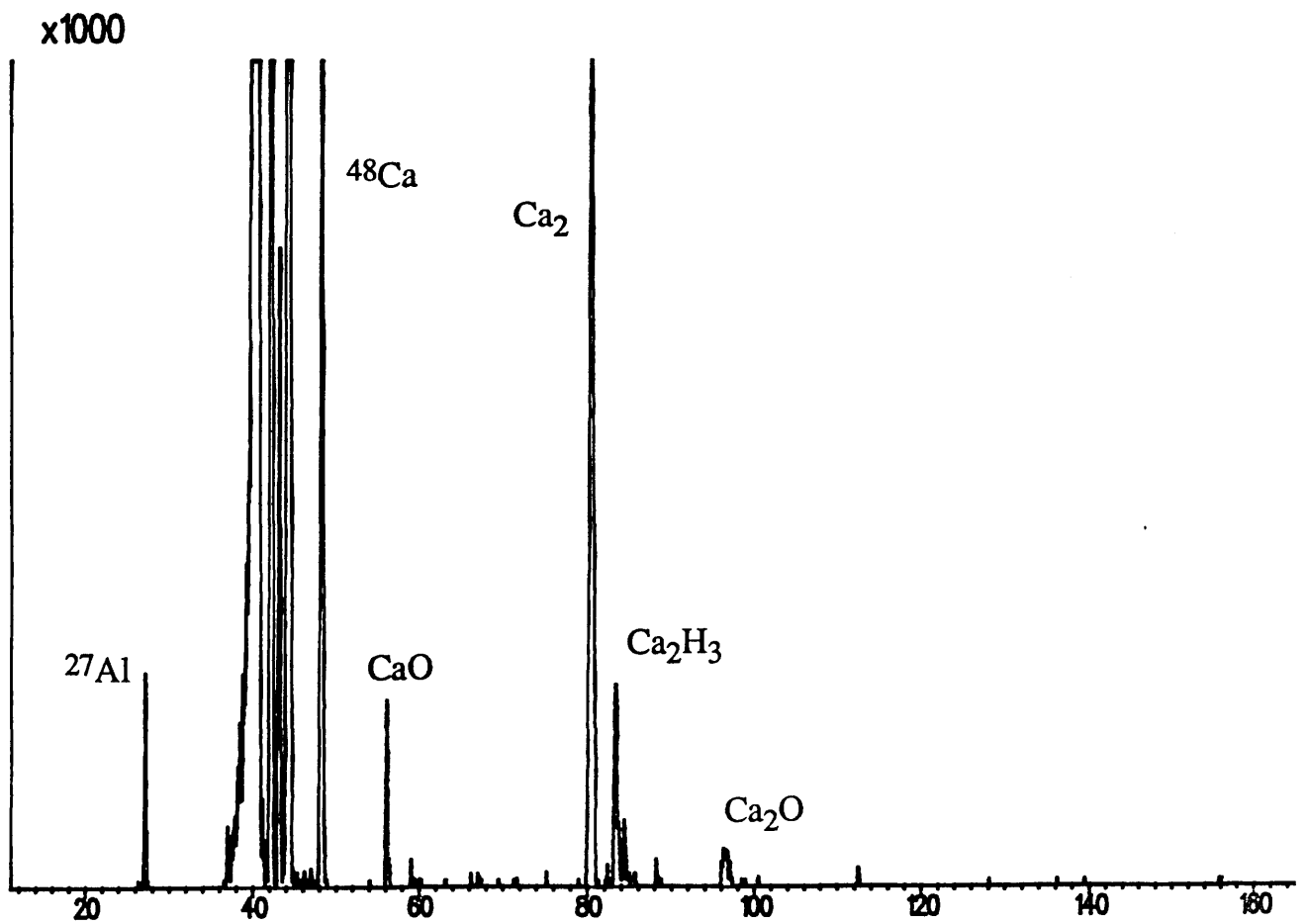

Fig. 5.3.3 (b) RLA spectrum of Calcium (x1000), 600.1nm

(ii) SALI

Following the 1.06μm LIMA experiment described above, a second laser beam was introduced to the ion source region, above and parallel to the sample surface. This second laser allowed ablated neutral species to be ionized. The second laser beam was provided by a frequency quadrupled Nd:YAG at 266nm, with a pulse energy of ≈20mJ. Most elements can be ionized through a non-resonant two-photon process with this wavelength. The laser was focussed into the ionization region, giving a fluence of ≈1J/mm^2, this high value being required to drive the low cross-section process with any degree of efficiency. This technique of non-resonant laser postionization has been developed by Becker and Gillen, [54-57], principally for sensitive surface analysis (hence the acronym SALI, 'surface analysis by laser ionization', see Chapter 1).

The mass spectrometer was set to accept SALI ions whilst rejecting ions created in the ablation process (reflect potential < sample potential). The resulting mass spectrum is shown in Figs.5.3.4 (a, b), again note the scale factor (x100) in the expanded figure (b). Since the sample was vapourized using the same ablation process, this figure should be compared to Fig. 5.3.2. Generally, the spectrum is much cleaner with fewer molecular species observed, and somewhat lower relative intensities for 'interfering' features which do reproduce. Note the absence of Na and K peaks in the SALI spectrum, indicating that these elements are ionized with very high efficiency in the ablation process. The background laser ionization signal, arising from hydrocarbons in the vacuum, discussed in Chapter 3, (Fig. 3.1.1), is at a much lower level than the principal features visible here. The benefits of separating the atomization and ionization processes are readily apparent in the SALI spectrum, but the limitations of a non-selective ionization mechanism remain.

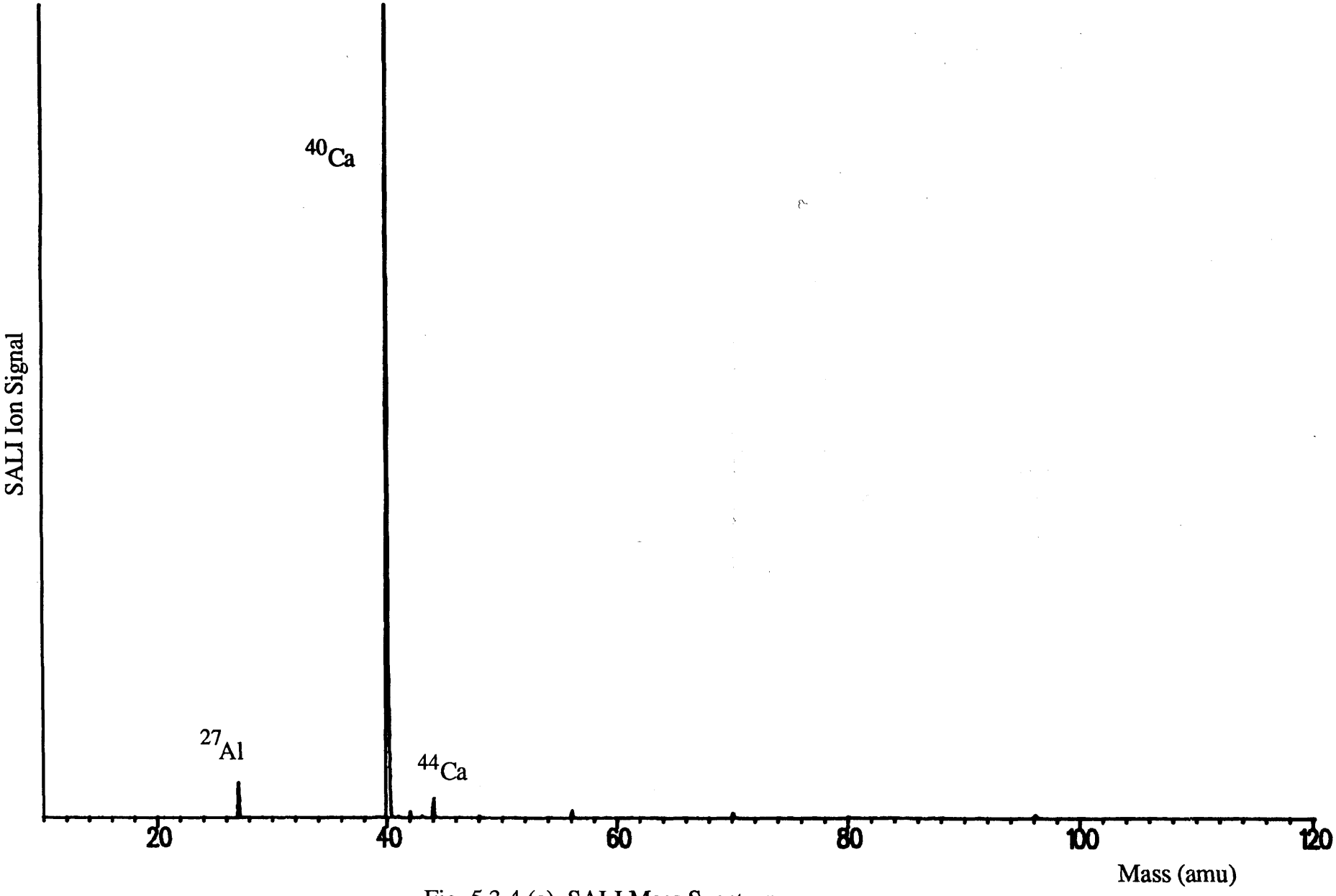

Fig. 5.3.4 (a) SALI Mass Spectrum

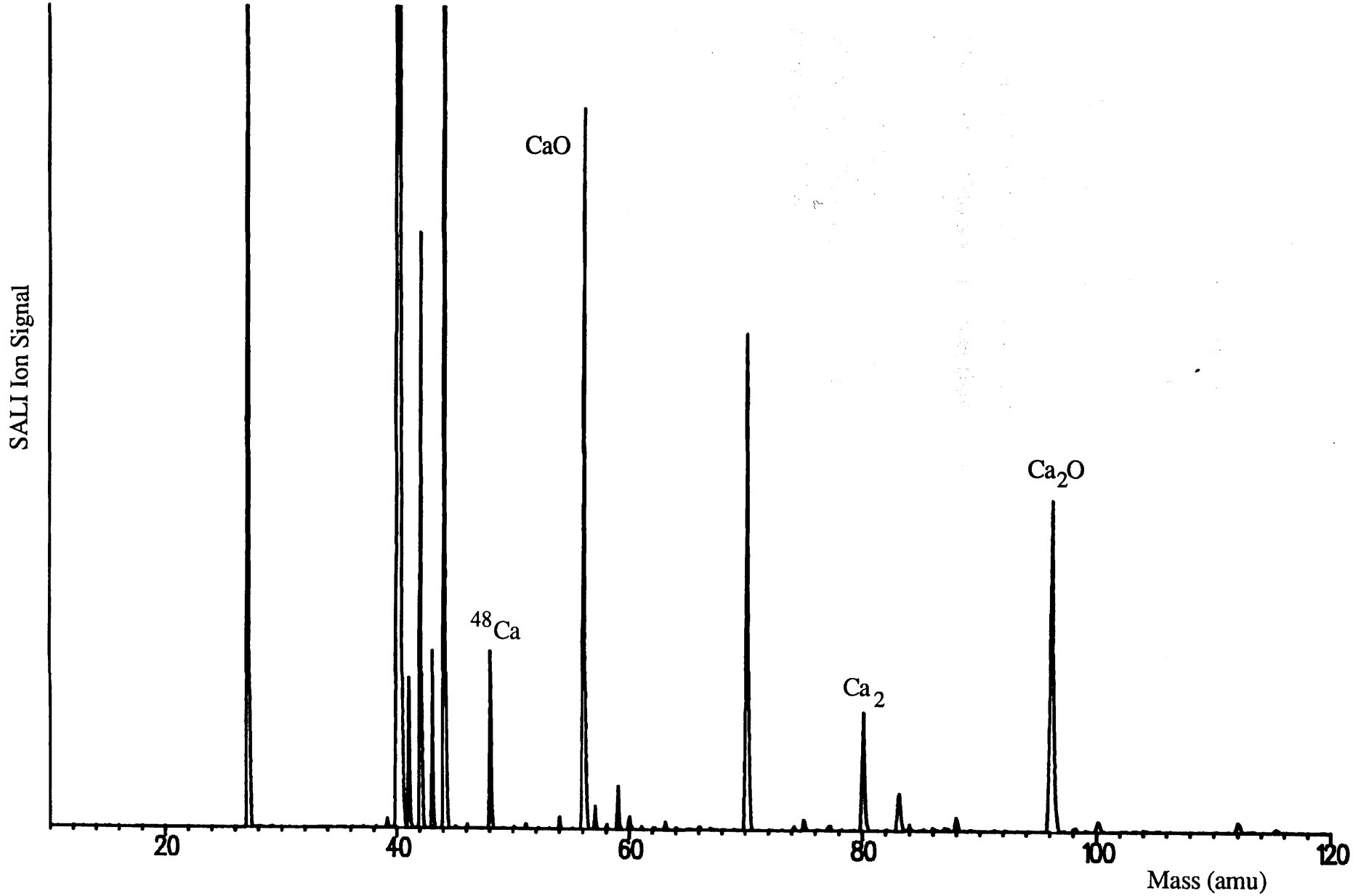

Fig.5.3.4 (b) SALI Mass Spectrum, Expanded x100

(iii) RIMS

Finally, resonant post-ionization laser beams were introduced to the source region. The ablation beam was again at 1.06μm, 4mJ/mm^2. Mass spectra were obtained for two different two-photon resonant, three-photon ionization schemes: in the blue at 421.5nm and in the red at 600.1nm, Figs. 5.3.5(a, b) and Figs. 5.3.6 (a, b), respectively. Again note that the scale factor in the expanded figures is x1000. As one would hope, there is very little in the RIMS spectra other than calcium to discuss. These spectra are clearly much 'cleaner' than those obtained by any of the non-resonant laser ionization methods, with only the RLA spectrum having comparable selectivity. The only molecular species evident on the RIMS spectra are those assigned to Ca species (eg. CaO at 56 amu), demonstrating well the relative freedom from isobaric interferences that is attainable with RIMS utilizing visible wavelengths. The minor isotope ^{46}Ca is clearly visible in both spectra, Figs. 5.3.7 (a, b). The spectra obtained at the different wavelengths are, however, quite distinct. Aluminium is observed quite clearly in the blue, but not at all in the red. In both cases three photons are required to effect multi-photon ionization of the Al ground state, a very low cross-section process. No coincidental resonance with a known Al transition could be deduced from atomic energy level tables [191]. Possibly the blue wavelength overlaps with an absorption/dissociative ionization band of a small Al molecule (eg. Al_2O_3). Considerably greater Ca molecular ion signal is observed in the blue, principally CaO and Ca_2H_3. This may simply indicate these species can be ionized by a single blue photon whilst requiring two photons in the red, or could be due to resonant molecular excitation. Little is known of the spectroscopy of small calcium molecules, some investigations of the Ca_2 dimer have been carried out [217, 218], but not at wavelengths of relevance here. Whilst it would be simple to investigate any degree of

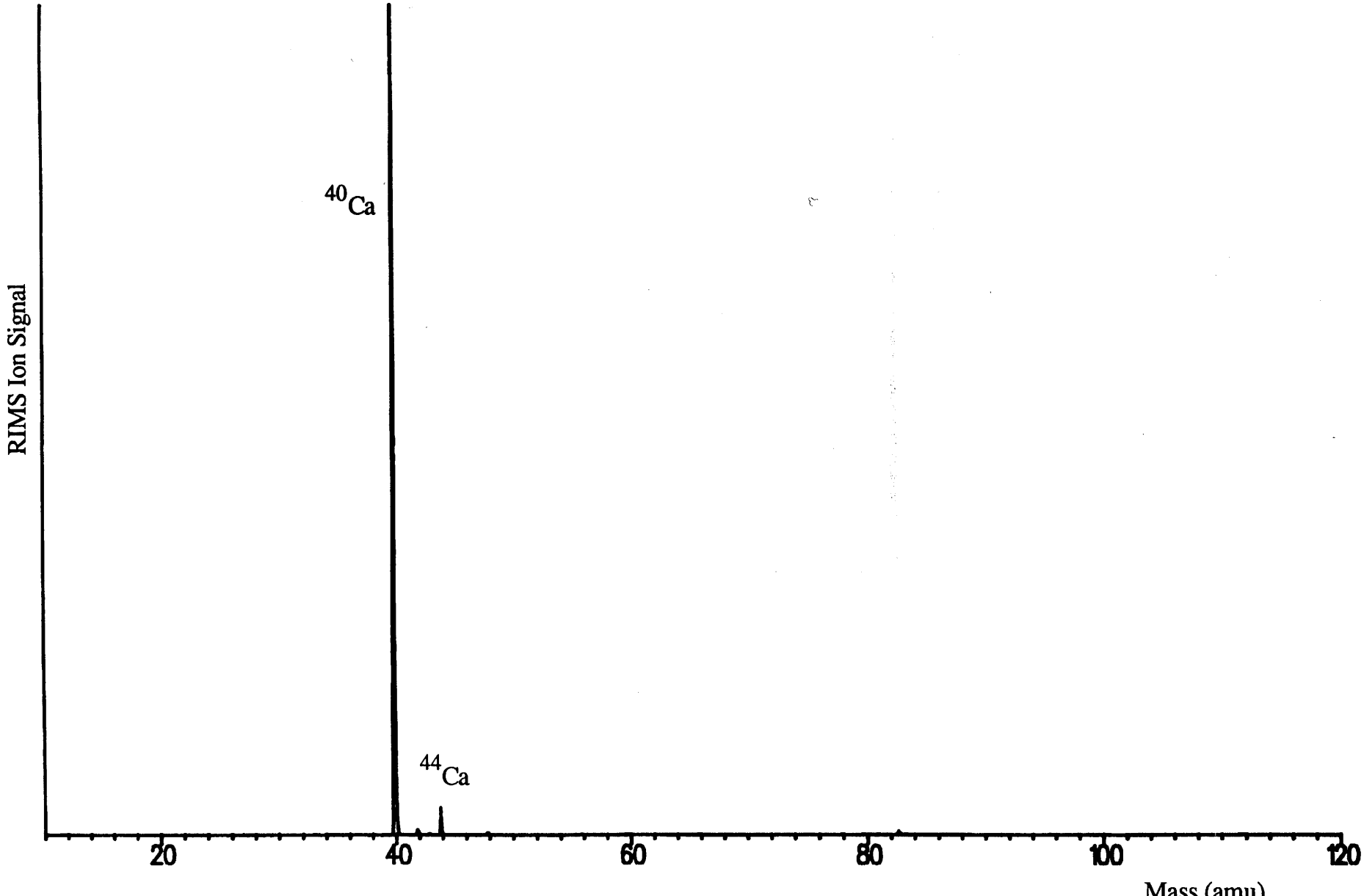

Fig. 5.3.5 (a) RIMS Mass Spectrum of Calcium, 421.5nm

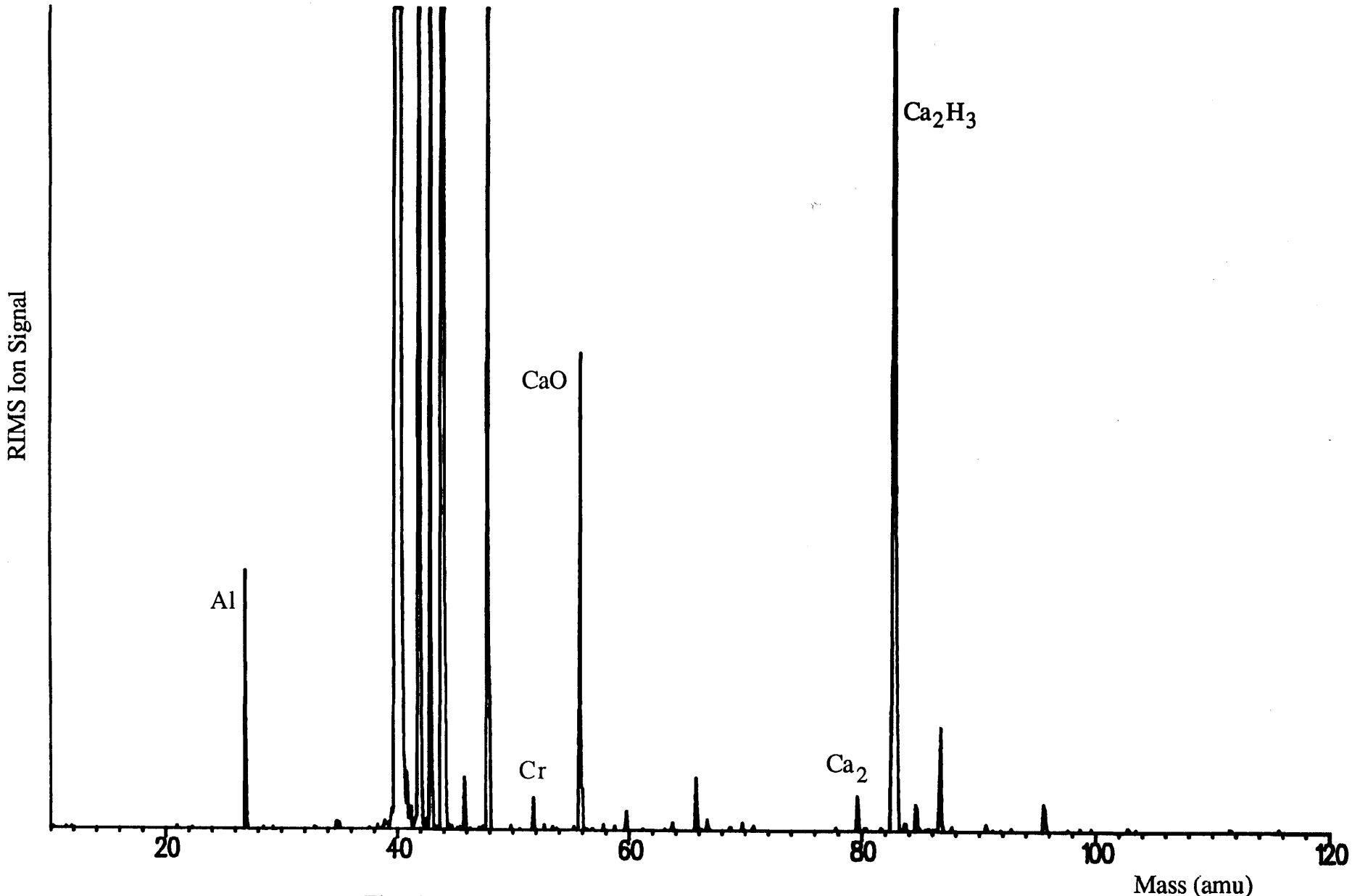

Fig. 5.3.5 (b) RIMS Mass Spectrum, 421.5nm, Expanded x1000

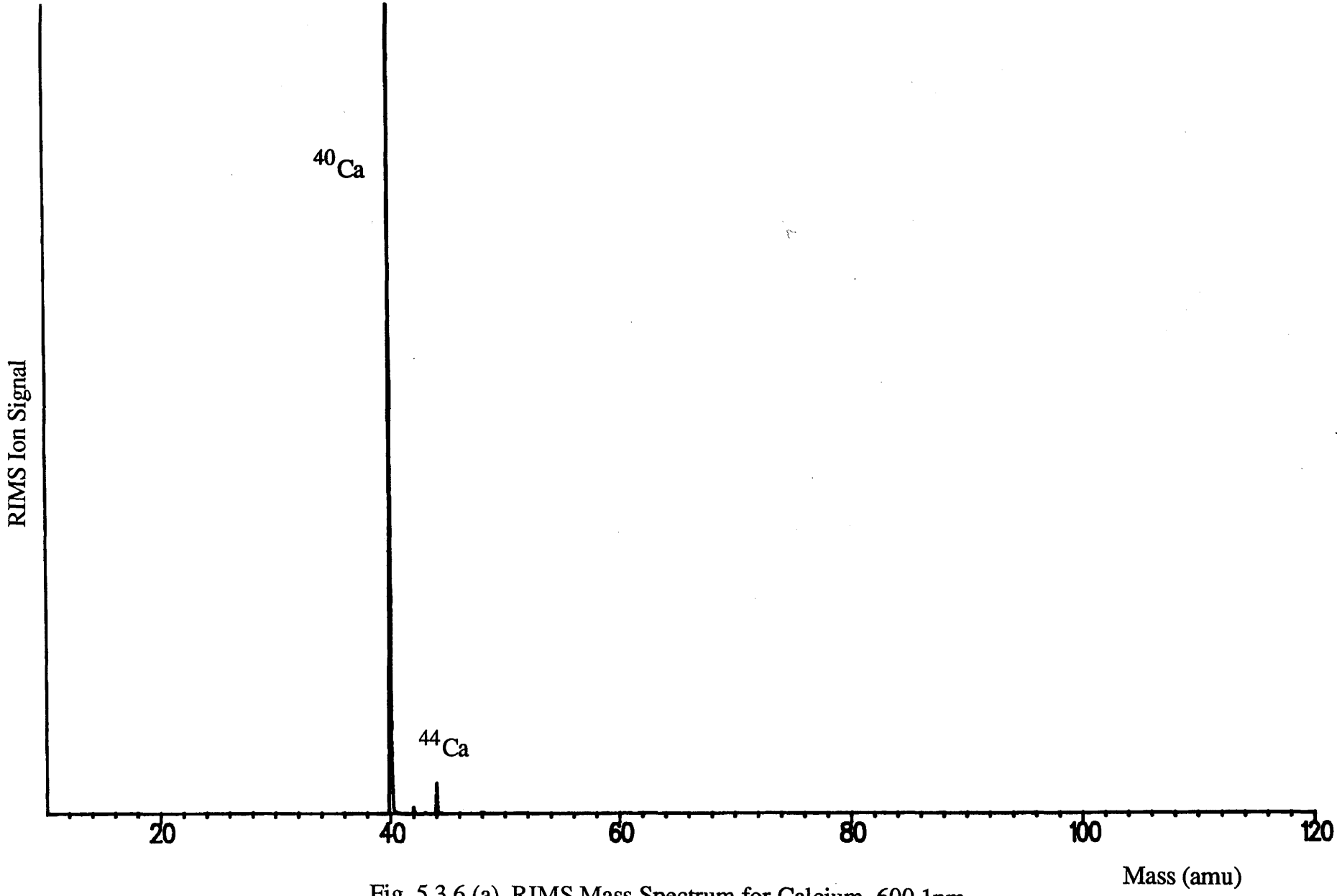

Fig. 5.3.6 (a) RIMS Mass Spectrum for Calcium, 600.1nm

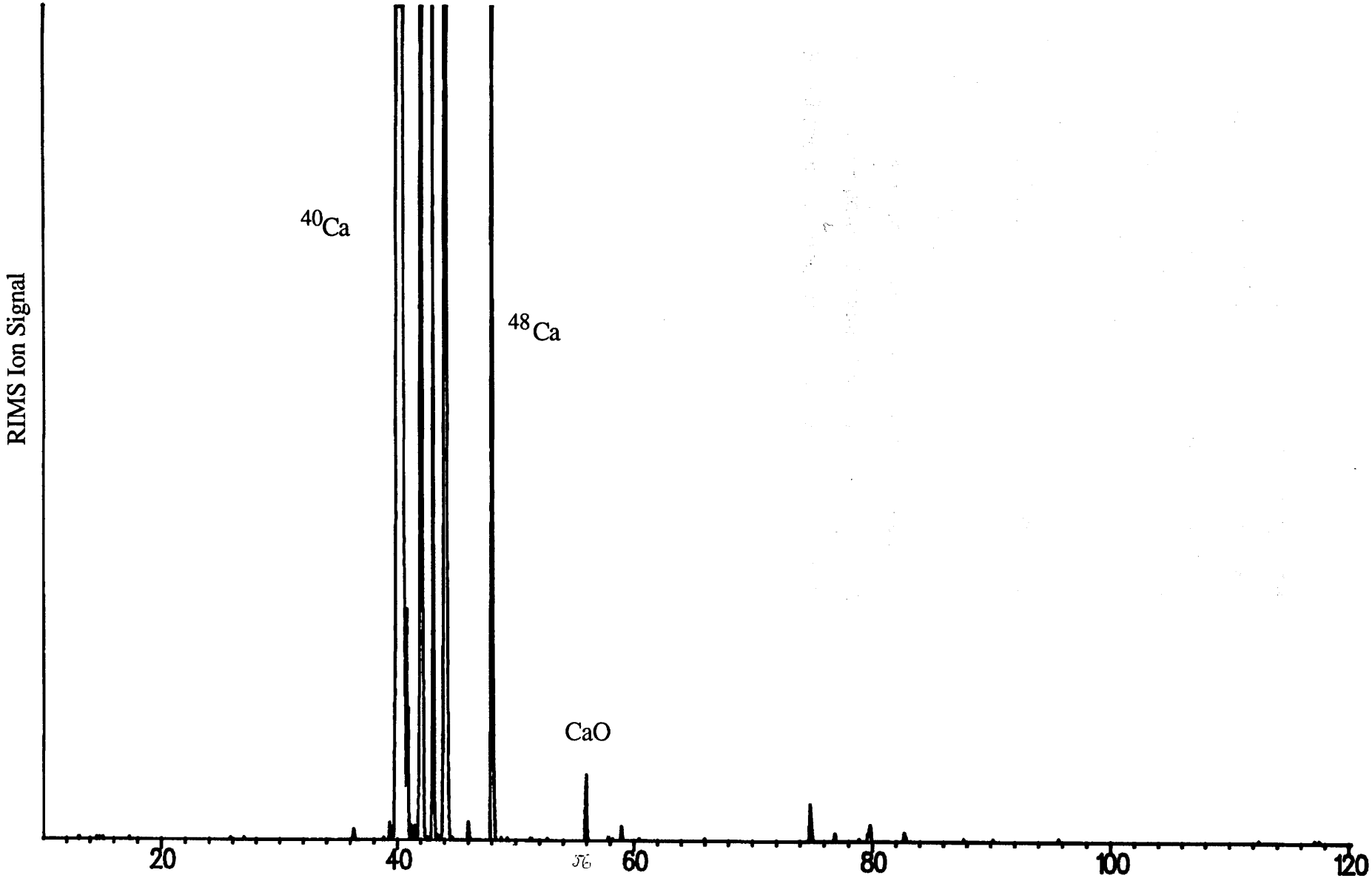

Fig. 5.3.6 (b) RIMS Mass Spectrum, 600.1nm, Expanded x1000

resonance behaviour for such ions, by setting a mass window at the appropriate peak in SPEC, the relatively low intensity, <1%, indicates that such peaks would not be of importance in most RIMS analyses. The formation of $^{40}CaH^+$ would, however, be of significance in any attempt to measure ^{41}Ca. Whilst there is no large mass-41 signal apparent in Figs. 5.3.7 (a, b) the electrical ringing emanating from the base of the ^{40}Ca peak at present precludes any firm conclusions on this point.

(iv) Summary

This simple series of qualitative investigations has demonstrated well many of the points discussed in Chapter 1. Comparison of the LIMA and SALI spectra demonstrates that significant gains can be made by separating the atomization and ionization processes. The ability of RLA to provide a high degree of selectivity in a simple ITV process, and the consequent potential for high sensitivity surface analysis relatively free from isobaric interferences is readily apparent. RIMS has been demonstrated to be capable of both high sensitivity and high selectivity for calcium analysis, indicating that, with further development, a RIMS instrument could tackle many of the challenging analytical problems outlined in Chapter 1. The next step must be to repeat these investigations in a much more controlled and quantifiable fashion, eg. using multi-element standard reference materials.

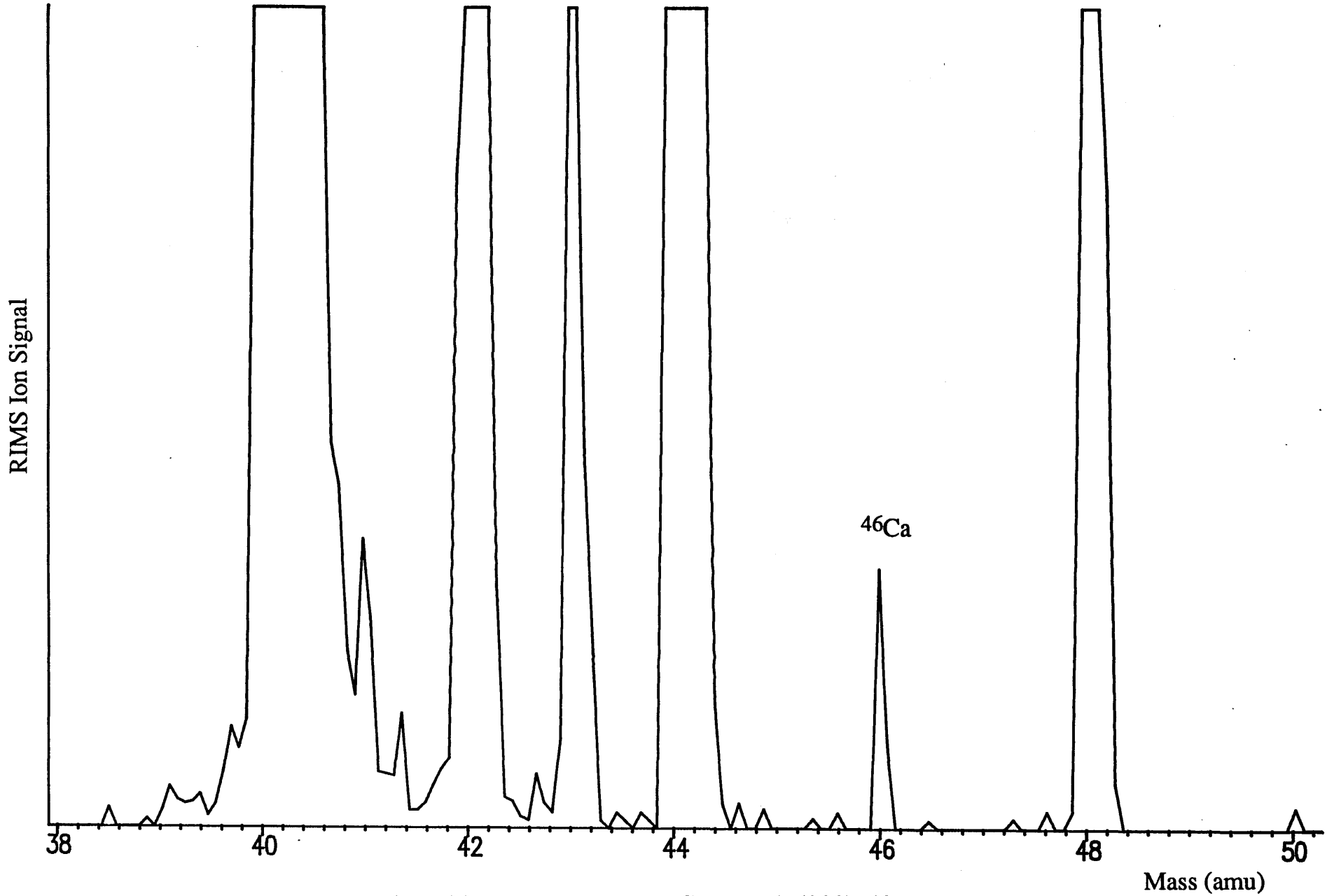

Fig. 5.3.7 (a) RIMS spectrum of Calcium (x5000), 421.5nm, 38 - 50amu

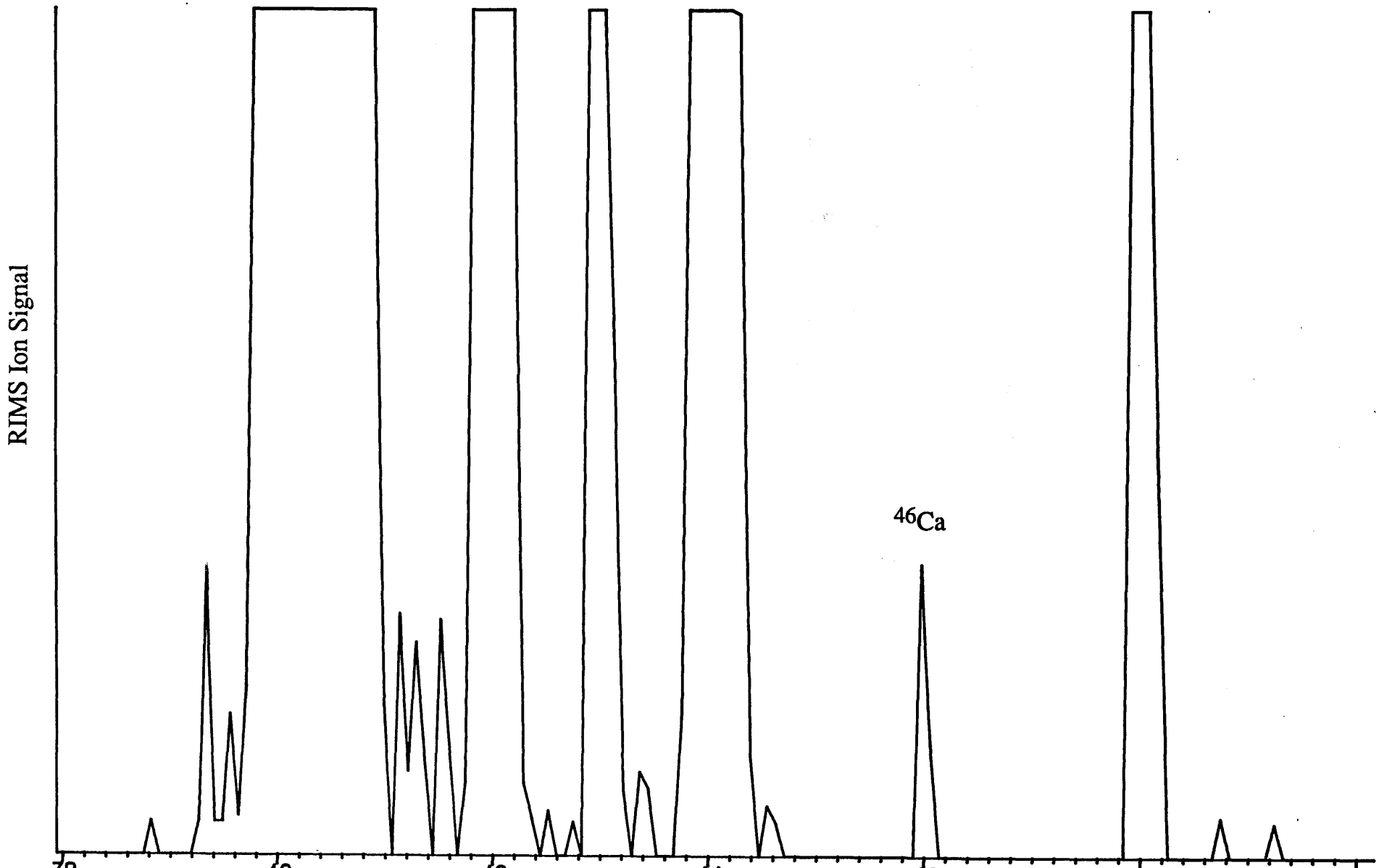

Fig. 5.3.7 (b) RIMS spectrum of Calcium (x16000), 600.1nm, 38 - 50amu

Appendix A: Atomic Theory

This appendix will briefly summarize some of the basic atomic theory used throughout this work. The emphasis will be on trying to present a consistent set of equations in a form that is of direct use in making real calculations. The quantity of most interest in a RIMS experiment is the transition cross-section. We either require to know this quantity to assess laser power requirements for efficient RIMS analysis, or from experimental knowledge of the cross-section, we can look to derive fundamental atomic quantities, eg. state lifetimes. Transition cross-sections are the most important input parameter for the Population Rate Equation computer model to be discussed in Appendix B.

(1) One-Photon Transitions

(i) Transition Cross-Sections

Most basic atomic physics textbooks provide useful discussions on the simple two-level, one-photon absorption case, see, for example, Woodgate, "Elementary Atomic Structure", [221] and Corney "Atomic and Laser Spectroscopy", [205]. For the simple two level sytem, shown in Fig. A.1.1, the Einstein coefficients provide a useful starting point.

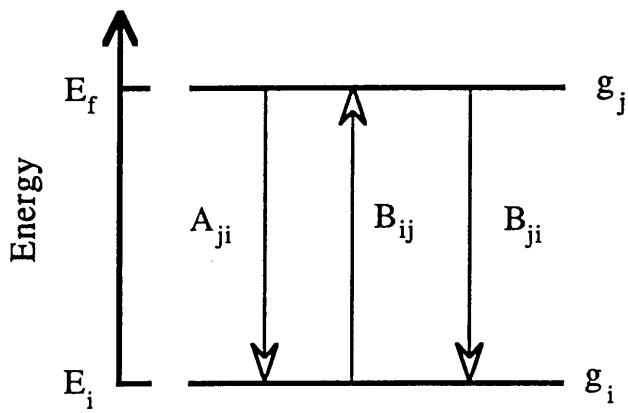

Fig. A.1.1 One-photon transition schematic

The Einstein A-coefficient is directly related to the natural radiative lifetime of an excited state by,

$$A_{ji} = 1 / \tau_{ji} \qquad (1.1)$$

Also, the natural atomic linewidth, $\Delta\nu_a$, is related to the state lifetime by the Uncertainty Principle,

$$\Delta E \Delta t \geq \frac{\bar{h}}{2} \quad \Rightarrow \quad \Delta\nu_a = \frac{1}{4\pi\tau_{ji}} \qquad (1.2)$$

The Einstein B-coefficients for stimulated emission and absorption are related to each other and the A-coefficient by,

$$B_{ij} = \frac{g_i}{g_j} B_{ji} = \frac{g_j}{g_i} \frac{\pi^2}{\bar{h}} \left(\frac{c}{\omega_{ij}} \right)^3 A_{ji} \qquad (1.3)$$

Under the electric dipole approximation, it is helpful to define an "oscillator strength" for the transition, which can be related directly to the state wavefunctions,

$$f_{ij} = \frac{2}{3} \frac{\omega_{ij}}{\bar{h}} \left(\frac{m_e}{e^2} \right) \left| \langle i | e \vec{r} | j \rangle \right|^2 \qquad (1.4)$$

Frequently, it is the oscillator strength, f_{ij}, for a transition which is tabulated in resource listings, even if the dipole approximation is inappropriate. The oscillator strength can be related to the Einstein coefficents through the relationship,

$$f_{ij} = \frac{2\varepsilon_0}{\pi}\left(\frac{m_e}{e^2}\right)\bar{h}\omega_{ij}B_{ij} \qquad (1.5)$$

In order to relate these fundamental quantities to experimental parameters it is helpful to introduce the concept of transition 'cross-section'. The absorption cross-section, σ_{ij}, is defined in terms of the transition rate, P_{ij}, for excitation under illumination with laser photon flux ϕ,

$$\sigma_{ij}(cm^2) = \frac{P_{ij}(sec^{-1})}{\phi\ (photons / cm^2\ sec)} \qquad (1.6)$$

It can be shown that the cross-section can be related to the fundamental Einstein A-coefficient by,

$$\sigma_{ij} = \frac{g_j}{g_i}\frac{\lambda_{ij}^2}{8\pi}\frac{A_{ji}}{\Delta\nu_a} \qquad (1.7)$$

The saturation requirement for laser photon flux is given by,

$$P_{ij} = \phi\sigma_{ij} >> \frac{1}{\tau} \qquad (1.8)$$

Where, τ is the shorter of the laser pulse length and the upper state lifetime.

Letokhov [1], gives the following requirement for the laser fluence required to saturate a transition,

$$\Phi_{sat} = \frac{E_{ij}}{2\sigma_{ij}}\frac{\Delta\nu_L}{\Delta\nu_a} \qquad (1.9)$$

(The ratio of laser to atomic linewidths represents the 'wasted' laser photons which do not contribute to the excitation process.) This expression closes the loop between the basic experimental and theoretical quantities of relevance to RIMS analyses. Conditions (1.8), (1.9) allow laser power requirements for efficient excitation to be assessed theoretically. Experimental knowledge of the saturation fluence allows the cross-section to be estimated, a more precise method of determining cross-sections using a Population Rate Equation model will be presented in Appendix B.

(ii) Selection Rules

The basic theory outlined in (i) above has neglected the subtleties introduced through the interaction of polarised light with magnetic substates. This interaction has important consequences for the efficiency of excitation, eg. some transitions may be 'forbidden' for a given polarisation of light, whilst others may be significantly enhanced through appropriate choice of polarisation [205, 222].

The selection rules for electric dipole transitions are summarized by the following, (stepwise excitations are considered through sequential application of the one-photon rules).

The most basic and absolute rule for all one-photon transitions is that *parity* of the upper and lower states must be different (for a single electron transition this equivalent to $\Delta l = \pm 1$, eg. 4s4p - 4s5d).

For all one-photon transitions, irrespective of the form of coupling, we also have [221],

$$\Delta J = \pm 1, 0; \quad J=0 \rightarrow J'=0, \text{ forbidden} \qquad (1.10)$$

For magnetic substates, m_J,

$\Delta m_J = \pm 1, 0$; $m_J = 0 \rightarrow m_{J'} = 0$, forbidden for $\Delta J = 0$ (1.11)

Linear, π, polarisation promotes $\Delta m_J = 0$ (1.12 (a))

Circular, $\sigma^{\pm}$, polarisations promote $\Delta m_J = \pm 1$, repectively (1.12 (b))

Fairbanks et al [44] give a good illustration of the importance of these rules. Linearly polarised light can be used to excite the transition $5p^2\ ^3P_0 \rightarrow 5p6p\ ^3P_1$ ($\Delta J=1$), however, only the $m_{J'}=0$ substate of the $^3P_1$ state will be populated through application of (1.12 (a)). Subsequent excitation to the $5p6s\ ^3P_1$ ($\Delta J=0$) state would then be forbidden by (1.11).

For LS-coupled systems, in which L and S are good quantum numbers, these rules are augmented by the following,

$\Delta S = 0$ (1.13 (a))

$\Delta L = \pm 1, 0$; $L = 0 \rightarrow L' = 0$, forbidden (1.13 (b))

As noted in Chapter 4, calcium follows the LS-coupling constraints very closely, with spin-flip transitions ($\Delta S=1$) being strongly suppressed.

For atoms with nuclear spin, I, then the total angular momentum is now $F=I+J$, and all rules for J and m_J must now be applied to F and m_F, for example, Eq. (1.10) becomes: $\Delta F = \pm 1, 0$; $F = 0 \rightarrow F' = 0$, forbidden.

This important distinction is the basis of the angular momentum isotope selection scheme proposed by Balling and Wright, [216], mentioned in Chapter 5. For an atom with I=0, the sequential excitation $^1S_0 \rightarrow {}^1P_1 \rightarrow {}^1S_0$ is forbidden for circularly polarised light beams of the same handedness,

since the selection rule $\Delta m_J=\pm 1$ applies for each transition. However, for I=3/2 isotopes (eg. Yb) it is possible to excite population from the $m_F=-3/2$ and $m_F=-1/2$ substates through to $m_F''=1/2$ and $m_F''=3/2$, respectively.

(2) Two- Photon Transitions

(i) Transition Cross-Sections

Goppert-Mayer [223] derived the basic expression for the two-photon transition rate using second order perturbation theory in 1931. The fundamental expression can be written in the form (see also Fig. A.2.1),

$$P_{if} = \frac{2\pi}{\hbar^2}\left|\sum_k \frac{\langle f|H_1|k\rangle\langle k|H_2|i\rangle + \langle f|H_2|k\rangle\langle k|H_1|i\rangle}{\delta\omega_k}\right|^2 \frac{\Delta\nu_a}{4\delta\omega_f^2 + \pi^2\Delta\nu_a^2} \qquad (2.1)$$

Where, the summation is over all possible intermediate states k, $\delta\omega_k$ is the detuning from intermediate resonance k, H_i is the electric dipole interaction Hamiltonian for the atom with beam i, $\Delta\nu_a$ is the atomic linewidth for the transition, and $\delta\omega_f$ is the detuning from the two-photon resonance.

For excitation using only one laser beam, tuned to resonance ($\delta\omega_f=0$), this reduces to [200],

$$P_{if} = \left|\sum_k \frac{\langle f|H|k\rangle\langle k|H|i\rangle}{\delta\omega_k}\right|^2 \frac{8}{\pi\Delta\nu_a I^2} \qquad (2.2)$$

If we make the assumption that one intermediate resonance, *r*,

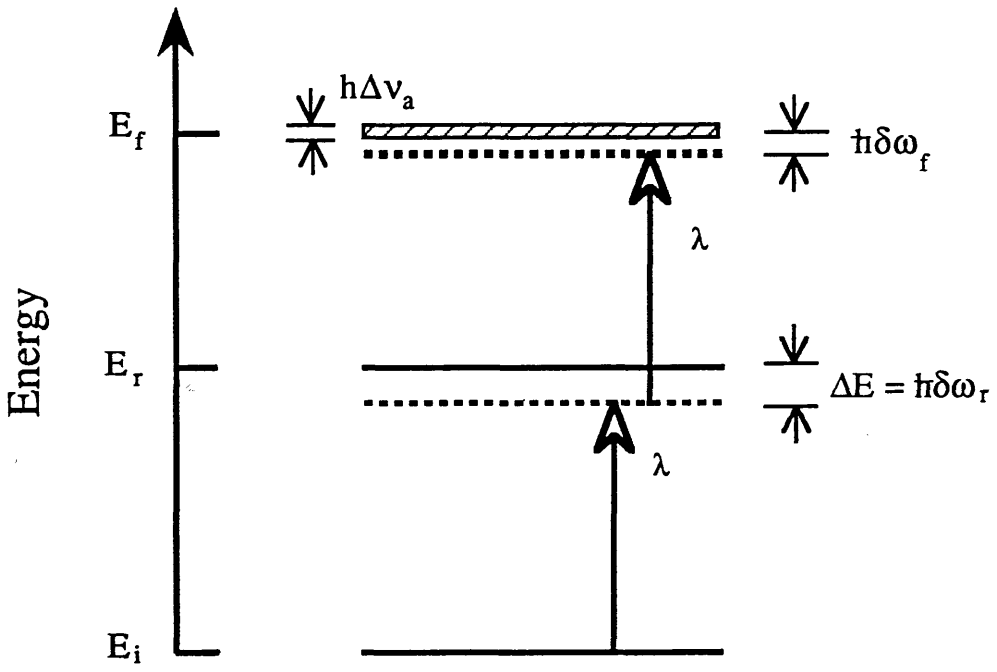

Fig. A.2.1 Two-photon transition schematic

dominates, and substitute explicitly for the Hamiltonian, then this expression becomes [200],

$$P_{if} = \frac{I_o^{\,2}}{\Delta\nu_a}\left(\frac{3r_e}{\pi\bar{h}c}\right)^2(\lambda_{ir}\lambda_{rf})^2\left(\frac{\omega_{ir}\omega_{rf}}{\delta\omega_r^2}\right)(f_{ir}f_{rf})\left|(C_{ir}C_{rf})\right|^2 \qquad (2.3)$$

Where, I_o is the laser intensity, r_e is the classical radius for the electron, f_{ij} is the oscillator strength for transition i→j, and C_{ij} is the Clebsch-Gordan coefficient for transition i→j.

We now need to put this expression into a form that is more directly useful for experimental investigation. We can define the two-photon cross-section to be given by,

$$\sigma_{if}(\mathrm{cm}^4\mathrm{s}) = \frac{P_{if}\,(\mathrm{s}^{-1})}{\phi^2\,(\mathrm{photons}/\mathrm{cm}^2\,\mathrm{sec})^2} \qquad (2.4)$$

Frequently, the laser linewidth, Γ_L, will be greater than natural atomic linewidths involved in the excitation. Hence, we replace the term $\Delta\nu_a$ with Γ, which is now taken to be the greater of the laser and atomic linewidths, which gives [65],

$$\sigma_{if} = \frac{K}{\Gamma}(\lambda_{ir}\lambda_{rf})^2\left(\frac{\omega_{ir}\omega_{rf}}{\delta\omega_r^2}\right)(f_{ir}f_{rf})\left|(C_{ir}C_{rf})\right|^2 \qquad (2.5)$$

Where K is a known constant.

Also, it may be possible for several magnetic substates, m_n, to become involved in the excitation process, consequently the expression must be summed over all such states. We can now write the two-photon transition

cross-section in the simple form,

$$\sigma_{if} = \left(\frac{K}{\Gamma\lambda^2}\right)\frac{f_{ir}f_{rf}}{E_{ir}E_{rf}(\Delta E)^2}\sum_n\left|C_{ir}C_{rf}\right|^2 \qquad (2.6)$$

(The radial frequencies have been replaced by their corresponding energies (eg. $\Delta E=h\Delta\omega$), and λ is the laser wavelength). For energies in units of cm^{-1}, wavelengths in nm and the linewidth in Hz, and the cross-section in cm^4 sec, we find $K\approx 2.88\times10^{-10}$. This is the expression used to calculate the expected two-photon cross-sections for the intermediate resonance enhancement experiments described in Chapter 4.

The saturation requirement for laser photon flux for a two-photon transition is given by,

$$P_{if} = \sigma_{if}\phi^2 >> \frac{1}{\tau} \qquad (2.7)$$

Where, τ is the shorter of the laser pulse length and the upper state lifetime.

The Clebsch-Gordan coefficients were calculated using the methods given by Edmonds [203]. In the most general case we can relate the Clebsch-Gordan coefficient to the Wigner 3-j symbol by,

$$C^{j_1\ j_2\ j_3}_{m_1\ m_2\ m_3} = (-1)^{-m_3-j_1+j_2}\sqrt{(2j_3+1)}\begin{pmatrix} j_1 & j_2 & j_3 \\ m_1 & m_2 & m_3 \end{pmatrix} \qquad (2.8)$$

For each one-photon transition i→j we need to calculate,

$$C_{ij} = C^{J_i\ 1\ J_j}_{m_i\ -q\ m_j} \qquad (2.9)$$

Where q=0 for linear polarisation and q=±1 for $\sigma^{\pm}$ polarisations, respectively. The required Wigner 3-j symbols can be evaluated from tables in Edmonds [203], (similar listing are given by several other authors).

(ii) Selection Rules

The selection rules for two-photon transitions are more complex than those for the simpler one-photon case. Comprehensive discussions and tabulation of results are given by Melikechi and Allen [224] and Bonin and McIlrath [225]. The results of the latter are reproduced in Fig. A.2.2.

Several important points arise from these results. The transition F=0 → F'=0 is allowed for linearly polarised beams, but forbidden for beams having the same handedness of circular polarisation. This was demonstrated in Chapter 4, where the series of transitions $^1S_0 \rightarrow {}^1S_0$ were observed for ^{40}Ca (I=0, F=J) with linearly polarised light, but not with circularly. As discussed in Chapter 5, ^{43}Ca has a non-zero nuclear spin (I=7/2) and consequently the $^1S_0 \rightarrow {}^1S_0$ transitions, forbidden for ^{40}Ca, are allowed for this isotope, leading to isotope selectivity in a manner very similar to that suggested by Balling and Wright [216].

The selection rules can also be 'harnessed' to provide doppler free excitation with high efficiency over an entire Maxwellian velocity distribution. For counter-propagating beams with polarisations σ^+ and σ^-, respectively, the transition F=0 → F'=0 is only allowed for the combination $\sigma^+\sigma^-$. That is, a photon must be absorbed from each beam for the transition to be allowed, making the excitation completely Doppler-free to first order. The potential of such schemes for RIMS applications in high abundance sensitivity isotope ratio measurements are discussed by Lucatorto et al [29].

Fig. A.2.2 Two-Photon Selection Rules

(Reproduced from Bonin and McIlrath [225])

General Rules		
$\|\Delta F\| \leqslant 2, \|i\rangle, \|f\rangle,$	same parity,	$F_i + F_f =$ integer

Particular Polarization Rules		
Polarizations		
Photon ω_1	Photon ω_2	Forbidden Transitions
σ^+	σ^-	$\Delta M \neq 0$
σ^+	π	$\Delta F: \ 0 \rightarrow 0; \quad \Delta M \neq -1$
σ^-	π	$\Delta F: \ 0 \rightarrow 0; \quad \Delta M \neq 1$
π	σ	$\Delta F: \ 0 \rightarrow 0; \quad \Delta M \neq \pm 1$
π	π	$\Delta F: \ 0 \leftrightarrow 1; \quad \Delta M \neq 0$
σ^+	σ^+	$\Delta F: \ 0 \leftrightarrow 1, \quad 0 \rightarrow 0, \quad \frac{1}{2} \rightarrow \frac{1}{2}; \quad \Delta M \neq -2$
σ^-	σ^-	$\Delta F: \ 0 \leftrightarrow 1, \quad 0 \rightarrow 0, \quad \frac{1}{2} \rightarrow \frac{1}{2}; \quad \Delta M \neq 2$

Additional Rules for Equal-Frequency Photons	
$\Delta F: \ 0 \leftrightarrow 1$	Forbidden for all polarizations
If $\|\Delta F\| = 1$,	$\Delta M: \ 0 \rightarrow 0$ Forbidden for all polarizations

Definitions: $\Delta F = F_f - F_i$, $\Delta M = M_f - M_i$; π is the light polarised along the quantization axis, σ is the linearly polarised light orthogonal to π, and $\sigma^{+,-}$ is the circularly polarised light

Appendix B: Population Rate Equation Model

This section will outline the basics of the Population Rate Equation (PRE) model developed in the LIS group at Glasgow. Much of this has already been presented in Singhal, Land, Ledingham and Towrie, 1990, [202]. The motivation behind the development of the model was to allow an estimate of expected ion yields to be made for known transition cross-sections and given laser powers. Conversely, the PRE model can also be used to calculate cross-sections from experimentally measured dependencies for ion yield on laser flux. The PRE computer model was developed to cover the most general case likely to be encountered in a RIMS analysis, a four-level system with three independent laser pulses exciting resonant transitions between them. The model can be applied to both atomic and molecular systems, and can be used to calculate both fluorescence and ionization yields.

The PRE model builds on the simple atomic theory outlined in Appendix A. The validity of simple PRE models for describing multiphoton ionization dynamics has been considered by Ackerhalt and Eberly [227] and by Ackerhalt and Shore [228]. Their findings suggest that it is reasonable to assume that the PRE model will provide a good approximation under the experimental conditions commonly encountered in RIMS analyses utilizing pulsed laser excitation (eg. laser coherence time << atomic lifetimes).

Similar models have been developed by several other authors, most notably Zakheim and Johnson [229] and Miller and Nogar [230]. The emphasis of the former authors' was very much towards molecular multiphoton spectroscopy. The latter authors' comparisons between CW and pulsed laser excitations for RIMS anlysis are particularly interesting, highlighting the potential high sensitivity available with quite modest CW laser intensities. However, neither of these models was felt to be suitably

flexible enough for the needs of the LIS group.

(1) The Glasgow PRE Model

The system under consideration is shown in Fig. B.1.The model allows for both stimulated and spontaneous emissions from excited states, and also for decay channels which 'remove' population from states of interest (eg. atomic collisions or molecular dissociation). Multiphoton processes can be considered simply by choosing appropriate exponents for the laser flux on the relevant resonance and corresponding dimensions for the cross-section. That is, for an m-photon process, the appropriate flux would be ϕ^m and the cross-section would have units of $cm^{2m}\ sec^{m-1}$. Although the uppermost level in Fig. B.1 is shown to be below the ionization continuum, the transition to any state can be made a photoionization process simply by closing all decay channels from this level. For this initial analysis, the laser pulse is assumed to have a uniform intensity over its duration ('top-hat' pulse). Also, the laser pulse is assumed to have a uniform geometric cross-section and the analyte atoms are assumed to have a uniform spatial density.

The rate equations for the system shown in Fig. B.1 are given by,

$$\frac{dn_0(t)}{dt} = -An_0 + Bn_1$$

$$\frac{dn_1(t)}{dt} = An_0 - (B + C + CP)n_1 + Dn_2$$

$$\frac{dn_2(t)}{dt} = Cn_1 - (D + E + EP)n_2 + Fn_3$$

$$\frac{dn_3(t)}{dt} = En_2 - (F + G)n_3$$

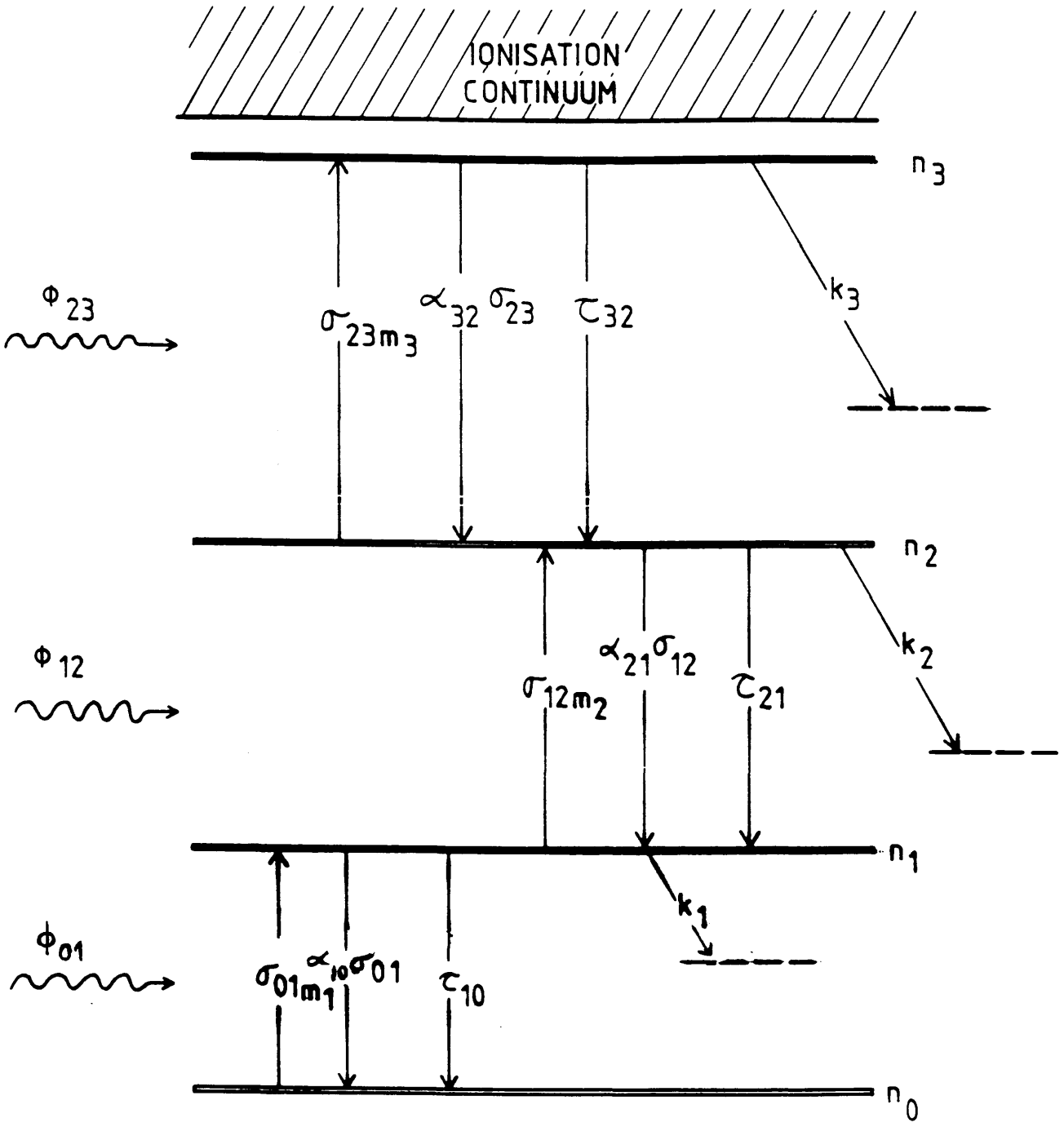

Fig. B.1 Four-Level System for PRE Model, see text for details

Where,

$$A = \sigma_{01m_1}\phi_{01}^{m_1} \quad ; \quad B = \alpha_{10}A + \tau_{10}^{-1}$$

$$C = \sigma_{12m_2}\phi_{12}^{m_2} \quad ; \quad CP = k_1$$

$$D = \alpha_{21}C + \tau_{21}^{-1} \quad ; \quad E = \sigma_{23m_3}\phi_{23}^{m_3}$$

$$EP = k_2 \quad ; \quad F = \alpha_{32}E + \tau_{32}^{-1} \quad ; \quad G = k_3$$

(All terms have their previously defined meanings.)

The basic rate equations can be manipulated algebraically to give a fourth order differential equation in terms of n_3 and constants only,

$$\begin{aligned} &n_3'''' + (A + B + C + CP + E + EP + F + G)n_3''' \\ &\quad + \{(A + B + C + CP + D + E + EP)(F + G) + \\ &\qquad (A + B + C + CP)(D + E + EP) + A(C + CP) - EF - CD\}n_3'' \\ &\quad + [\{(A + B + C + CP)(D + E + EP) + A(C + CP) - CD\}(F + G) + \\ &\qquad A(C + CP)(D + E + EP) - (A + B + C + CP)EF - ACD]n_3' \\ &\quad + [\{(A(C + CP)(D + E + EP) - ACD\}(F + G) - AEF(C + CP)]n_3 = 0 \end{aligned}$$

This equation has four real, positive roots, p_i, yielding a solution for $n_3(t)$ of the form,

$$n_3(t) = \sum_i \beta_i \exp(-p_i t)$$

Standard computer software subroutines are readily available to calculate the roots p_i. If we now assume that the total population, N_0, is in the ground state at time t=0, then we have,

$$\beta_i = (ACE)\, N_0\, [(p_j - p_i)(p_k - p_i)(p_l - p_i)]^{-1}$$

We can now write down solutions for the time evolution of the population in each of the system's levels,

$$n_2(t) = \frac{1}{E} \sum_i \beta_i (F + G - p_i) \exp(-p_i t)$$

$$n_1(t) = \frac{1}{CE} \sum_i \beta_i [(F + G - p_i)(D + E + EP - p_i) - EF] \exp(-p_i t)$$

$$n_0(t) = \frac{1}{ACE} \sum_i \beta_i \{ [(F + G - p_i)(D + E + EP - p_i)] (B + C + CP - p_i) - CD(F + G - p_i) - EF \} \exp(-p_i t)$$

These expressions can be programmed into a computer to allow simple and rapid evaluation of population changes under different conditions.

The model outlined above has two important omissions, no consideration has been given to either temporal variations in the laser pulse intensity or to spatial variations in the laser intensity/analyte density over the interaction region.

The problem of temporal variation in the laser pulse intensity is quite simply solved with computer model outlined above. The laser pulse length can be divided into a number of time 'bins' (say, one hundred bins over a 10ns pulse) during which the variation in intensity is small. The equations developed above are then valid over the duration of each bin, and the calculated level populations at the end of each bin can then serve as the starting populations for the next time bin in the sequence. Obviously, the constants A-G are also now time dependent, and must be recalculated for each time bin.

As discussed in Singhal et al [202], this more sophisticated model allowed the effect of different laser pulse temporal profiles on ion yields to

be investigated. For one- and two-photon excitation processes and standard pulse lengths (≈10ns), very little variation was calculated for quite extreme cases, from a perfectly uniform flat-top pulse through to a series of sharp spikes. However, for multiphoton processes ($m \geq 3$) or for subnanosecond laser pulses, quite considerable variations in ion yield were predicted. As noted in Chapter 2, the pulse shape from the Spectron dye lasers was observed to be far from uniform in profile. However, in light of the above findings on the model's relative insensitivity to temporal structure, it was felt that a simple Gaussian profile would be adequate for analysis of the one-and two-photon processes of interest in this programme of research.

The question of variation in the geometric profile of the laser pulse has not yet been examined in the LIS group. Both Zakheim and Johnson [229] and Miller and Nogar [230] have considered the effect of focussing the laser beam into a uniform gas. To be entirely relevant to the RIMS analysis carried out in the LIS group, however, such a model would also have to allow for the nonuniform density of gas phase atoms within a sputtered/ablated plume, a demanding, but entirely feasible, project.

(2) PRE Model Analysis of Yb RIS Data

As an early test of the model's abilities, a set of data from the RIS analysis of Yb carried out by Bekov et al [231] was analyzed. The experiment involved the stepwise excitation of three excited states followed by field ionization from the upper level. The RIS scheme involved is shown in Fig. B.2 . Sufficient laser power was available to saturate each of the transitions.

It is known analytically, [13], that the population of the upper excited state under saturation conditions is given by,

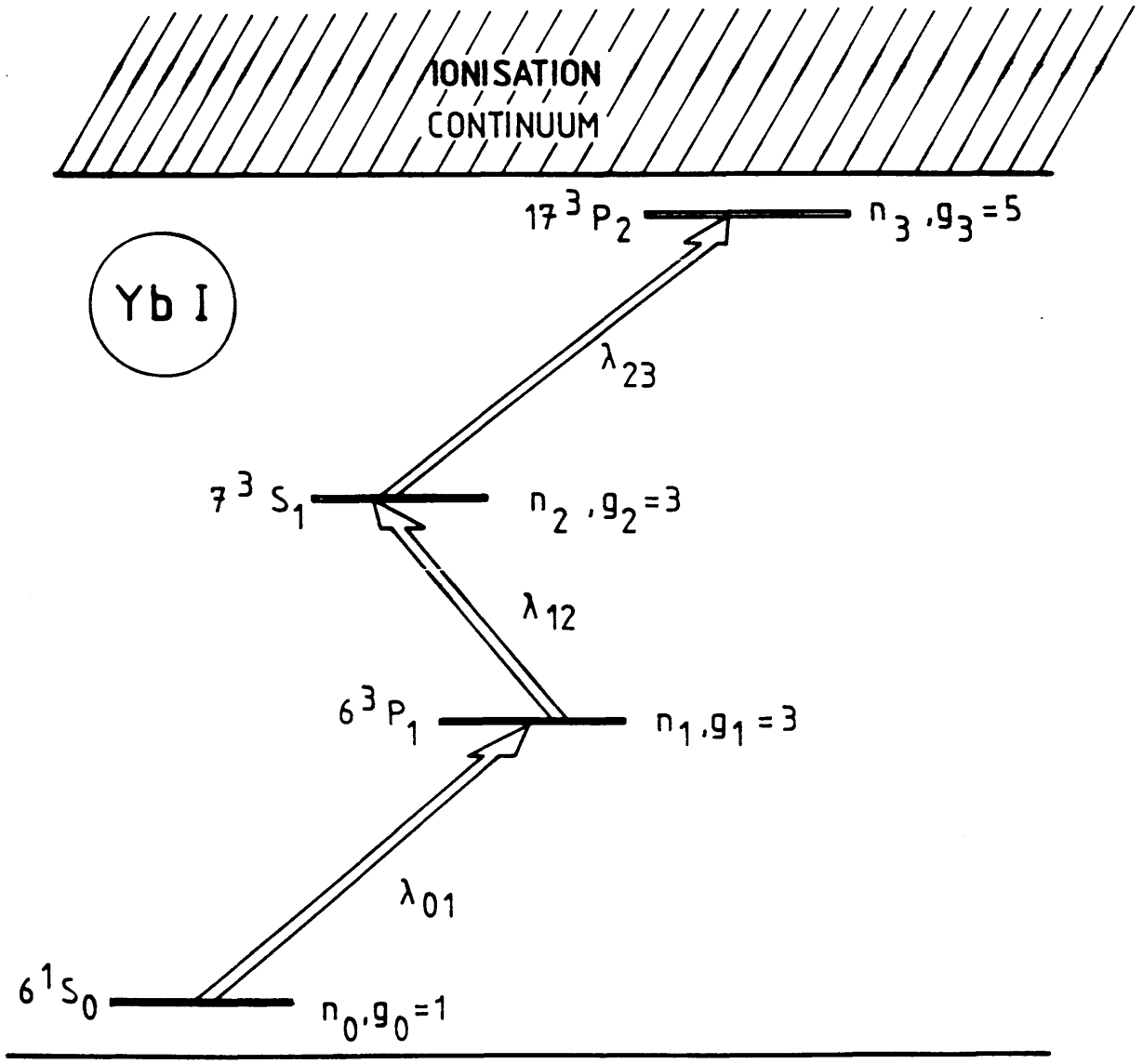

Fig. B.2 RIS scheme for Yb, Bekov et al [231]

$$n_3 = N_0 g_3 / \sum_{i=0}^{3} g_i$$

For the RIS scheme for Yb shown in Fig. B.2, this has a value of 0.417. The PRE model calculated a value of 0.416, suggesting that the computer model has no fundamental flaws.

The available data set consisted of three plots of the variation in relative ion yield as the intensity of light on one resonance was varied whilst the other transitions were kept in saturation [1, 231]. These 'power-dependence' plots are shown on Fig. B.3.

Bekov et al [231] give absolute absorption cross-sections for two of the transitions (σ_{01} and σ_{12}). With these values, the PRE model generated the solid curves shown in Fig. B.3. Although both of these curves lie above the experimental data, their shape reproduces the form of the data well. In fact, reducing the values of the cross-sections by factors of 4.0 and 3.5, respectively, yields the dashed curves shown in the figure. Since the quantity of direct relevance to the experimental data is actually the effective cross-section ($\sigma_{ij} \Delta\nu_L/\Delta\nu_a$) [202], this can be explained through uncertainties in the atomic and laser linewidths involved in the transitions.

The model was then used to calculate a value for the cross-section for the third transition. It was possible to obtain a good fit to data using an effective cross-section of $\sigma_{23}=7.5\text{x}10^{-15}$ cm^2. As noted above, the absolute cross-sections for the first two transitions were noted to be factors of 4.0 and 3.5 higher, respectively, than their effective values. Hence, this calculated effective value was multiplied by 3.75 to yield an absolute value for the transition cross-section of $2.81\text{x}10^{-14}$ cm^2, with an estimated uncertainty of 10%. This value is much as would be expected for excited state transitions of this nature [232].

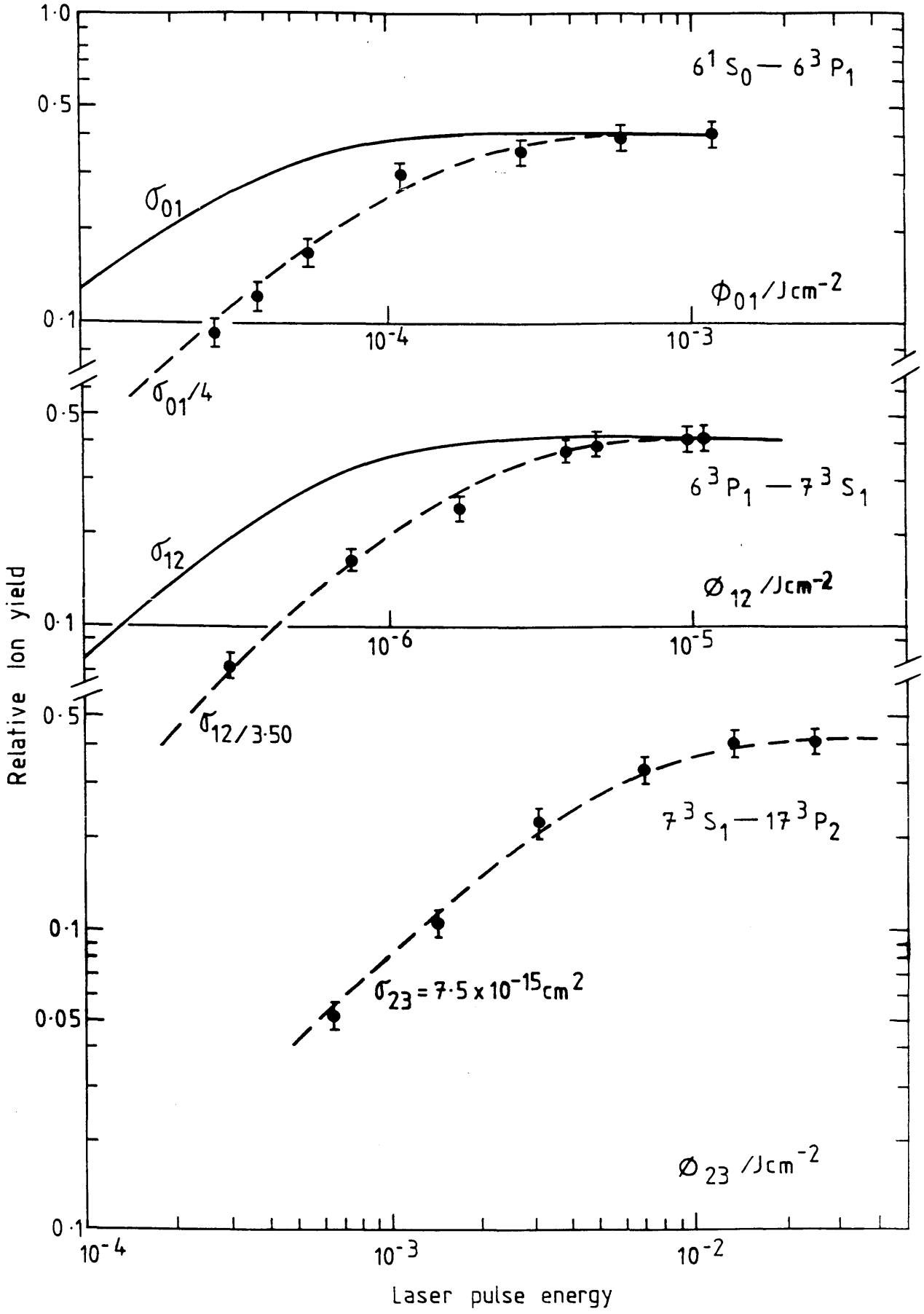

Fig. B.3 Power dependence curves for RIS of Yb,
see text for details

Bibliography

[1] V.S. Letokhov (1987), *Laser Photoionization Spectroscopy.* Academic Press Inc.(London) Ltd. 1987

[2] G.S. Hurst and M.G. Payne (1988), *Principles and Applications of Resonance Ionisation Spectroscopy.* Adam Hilger, Bristol, U.K. 1988

[3] J.P. Young, R.W. Shaw and D.H. Smith (1989), "Resonance Ionization Mass Spectrometry", Anal. Chem. 61(22), 1271A

[4] G.S. Hurst and M.G. Payne (1988), "Elemental analysis using resonance ionization spectroscopy", Spectrochimica Acta, 43B, 715

[5] J.D. Fassett and J.C. Travis (1988), "Analytical applications of resonance ionisation Mass spectrometry (RIMS)", Spectrochimica Acta, 43B, 1409

[6] R.P. Singhal and K.W.D. Ledingham (1987), "How to count atoms", New Scientist 26, 52

[7] K.W.D. Ledingham (1987), "RIMS: Counting Atoms", Spectrum 25, 20

[8] J.C. Travis, J.D. Fassett and T.B. Lucatorto (1986), "Resonance ionization Mass spectrometry", In *Resonance Ionization Spectroscopy 1986*, Eds. G.S. Hurst and C. Grey Morgan. Inst. Phys. Conf. Ser. No. 84, (1987), p.91

[9] M.G. Payne, C.H. Chen, G.S. Hurst and G.W. Foltz (1985), "Applications of resonance ionization spectroscopy in atomic and molecular phyiscs", Adv. At. Mol. Phys. 17, 229

[10] V.S. Letokhov (1985), "Laser photoionization spectroscopy of single atoms and molecules", Optica Acta 32(9/10), 1191

[11] J.D. Fassett, L.J. Moore, J.C. Travis and J.R. DeVoe (1985), "Laser Resonance Ionization Mass Spectrometry", Science 230, 262

[12] V.S. Antonov, V.S. Letokhov and A.N. Shibanov (1984), "Laser resonance photoionization spectroscopy of molecules", Sov. Phys. Usp. 27(2), 81

[13] G.I. Bekov and V.S. Letokhov (1983), "Laser Atomic Photoionization Spectral Analysis of Element Traces", Appl. Phys. B30,161

[14] D.H. Parker (1983), "Laser Ionization Spectroscopy and Mass Spectrometry", In *Ultrasensitive Laser Spectroscopy*, Ed. D.S. Kliger. Academic Press, Inc. (London) . (1983), Chpt. 4, p. 233

[15] G.S. Hurst, M.G. Payne, S.D. Kramer and J.P. Young (1979), "Resonance ionization spectroscopy and one atom detection", Rev. Mod. Phys. 51(4), 767

[16] D.W. Koppenaal (1988), "Atomic Mass Spectrometry",
Anal. Chem. 60(12), 113R

[17] O. Axner (1987), *Laser-Enhanced Ionisation Spectrometry and Its Principles*, PhD. Thesis, Dept. of Physics, Chalmers University of Technology, Goterborg, Sweden

[18] V.S. Letokhov (1969) Report of the P.N. Lebedev Institute, "On the possibilities of isotope separating by the methods of the resonant photoionization of atoms and photodissociation of molecules by laser radiation"
Published by Inst. of Spectroscopy, 1979.

[19] A. Einstein (1917), Phys. Zeit. 18, 121 (In German)

[20] A. Bohm (1979), *Quantum Mechanics: Foundations and Applications*, 2nd Edition, pp. 563-567, Springer-Verlag 1986.

[21] F. Bloch (1946), Phys. Rev. 70, 460

[22] R.V. Ambartsumyan, V.N. Kalinin and V.S. Letokhov (1971),
Zh. Eksp. Teor. Fiz. Pis'ma Red. 13 (6), 305
(English trans.) R.V. Ambartsumyan and V.S. Letokhov (1972),
Appl. Opt. 11 (2), 354

[23] G.S. Hurst, M.H. Nayfeh and J.P. Young (1977), Appl. Phys. Lett. 30(5), 229

[24] S.V. Andreev. V.S. Letokhov and V.I. Mishin (1987),
Phys. Rev. Letts. 59(12), 1274

[25] K. Niemax, J. Lawrenz, A. Obrebski and K-H. Weber (1986),
Anal. Chem. 58, 1566

[26] J. Lawrenz, A. Obrebski and K. Niemax (1988),
In *Resonance Ionization Spectroscopy 1988*. Eds. T.B. Lucatorto and J. E. Parks.
Inst. Phys. Conf. Ser. No. 94, (1989), p.301

[27] S. Chu and A.P. Mills (1982), Phys. Rev. Lett. 48, 1333

[28] C.W. Clark, J.D. Fassett. T.B. Lucatorto (1984),
In *Resonance Ionization Spectroscopy 1984*, Eds. G.S. Hurst and M.G. Payne.
Inst. Phys. Conf. Ser. No. 71, (1984), p.107

[29] T.B. Lucatorto, C.W. Clark and L.J. Moore (1984), Optics Comm. 48(6), 406

[30] T.J. Whitaker, B. A. Bushaw and B.D. Cannon (1988)
Laser Focus/Electro-Optics, February 1988.

[31] B.J. Comaskey et al (1986), "Atomic vapor laser isotope separation using resonance ionisation", In *Resonance Ionization Spectroscopy 1986*,
Eds. G.S. Hurst and C. Grey Morgan.Inst. Phys. Conf. Ser. No. 84, (1987), p.245

[32] K.W.D. Ledingham (1987), Personal communication.

[33] J. Wen, J.C. Travis, T.B. Lucatorto, B.C. Johnson and C.W. Clark (1988), Phys. Rev. A 37(11), 4207

[34] U. Kronert, S. Becker, G. Bollen, M. Gerber, T. Hilberath, H.-J. Kluge and G. Passler (1988), In *Resonance Ionization Spectroscopy 1988*. Eds. T.B. Lucatorto and J. E. Parks. Inst. Phys. Conf. Ser. No. 94, (1989), p.155

[35] B.L. Fearey, D.C. Parent, R.A. Keller and C.M. Miller (1988), In *Resonance Ionization Spectroscopy 1988*. Eds. T.B. Lucatorto and J. E. Parks. Inst. Phys. Conf. Ser. No. 94, (1989), p.285

[36] B.L. Fearey, J.E. Anderson, M.W. Rowe, C.M. Miller and N.S. Nogar (1988), In *Resonance Ionization Spectroscopy 1988*. Eds. T.B. Lucatorto and J. E. Parks. Inst. Phys. Conf. Ser. No. 94, (1989), p.259

[37] D.L. Donohue, J.P. Young and D.H. Smith (1985), Appl. Spectrosc. 39(1), 93

[38] J.P.Young, D.L. Donohue and D.H. Smith (1989), Spectrochimica Acta 44B(2), 147

[39] G.S. Janes, I. Itzkan, C.T. Pike, R.H. Levy and L. Levin (1976), IEEE J. Quant. Electr. QE-12(2), 111

[40] L.R. Carlson, J.A. Paisner, E.F. Worden, S.A. Johnson, C.A. May and R.W. Solarz (1976), J. Opt. Soc. Am. 66(8), 846

[41] R.W. Solarz, C.A. May, L.R. Carlson, E.F. Worden, S.A. Johnson, J.A. Paisner and L.J. Radziemski Jr. (1976), Phys. Rev. A 14(3), 1129

[42] D.L. Donohue, D.H. Smith, J.P. Young, H.S. McKown and C.A. Pritchard (1984), Anal. Chem. 56, 379

[43] A.Steudel (1967), In *Hyperfine Interactions*, Eds. A.J. Freeman and R.B. Frankel. Academic Press Inc., New York 1967.

[44] W.M. Fairbank Jr., M.T. Spaar, J.E. Parks and J.M.R. Hutchinson (1989), Phys. Rev. A 40(4), 2195

[45] P. Lambropoulos and A. Lyras (1989), Phys. Rev. A 40(4), 2199

[46] J. Grotemeyer, U. Boesl, K. Walter and E.W. Schlag (1986), Org. Mass Spectrom. 21, 645

[47] V. Vaida, M.B. Robin and N.A. Kuebler (1978), Chem. Phys. Lett. 58, 557

[48] H. Faidas and L.G. Christophorou (1988), In *Resonance Ionization Spectroscopy 1988*. Eds. T.B. Lucatorto and J. E. Parks. Inst. Phys. Conf. Ser. No. 94, (1989), p.315

[49] G. Cherbit, N. Albayaty and D. Vekhoff (1988), In *Resonance Ionization Spectroscopy 1988*. Eds. T.B. Lucatorto and J. E. Parks. Inst. Phys. Conf. Ser. No. 94, (1989), p.319

[50] P. Williams and L.A. Streit (1986), Nucl. Inst. Meth. B 15, 159

[51] J. Tumpner, R. Wilsch and A. Benninghoven (1987), J. Vac. Sci. Technol. A 5(4), 1186

[52] W.W. Harrison, K.R. Hess, R.K. Marcus and F.L. King (1986), Anal. Chem. 58(2), 341A

[53] C.T. Tye, R. Henry, I.D. Abell and D. Gregson (1989), Research and Development, April, 1989.

[54] C.H. Becker and K.T. Gillen (1984), Appl. Phys. Lett. 45(10), 1063

[55] C.H. Becker and K.T. Gillen (1984), J. Vac. Sci. Tecnol. A 3(3), 1347

[56] C.H. Becker and K.T. Gillen (1985), J. Opt. Soc. Am. B 2(9), 1438

[57] C.H. Becker (1986), J. Vac. Sci. Tecnol. A 5(4), 1181

[58] J.D. Fassett, J.C. Travis, L.J. Moore and F.E. Lytle (1983), Anal. Chem. 55, 765

[59] D.W. Beekman and T.A. Callcott (1984), In *Resonance Ionization Spectroscopy 1984* . Eds. G.S. Hurst and M.G. Payne. Inst. Phys. Conf. Ser. No. 71, (1984), p.143

[60] N.S. Nogar, R.C. Estler and C.M. Miller (1985), Anal. Chem. 57, 2441

[61] J.E. Parks (1986), Personal communication.

[62] J.D. Fassett, L.J. Moore, J.C. Travis and F.E. Lytle (1983), Int. J. Mass Spectrom. Ion Proc. 54, 201

[63] J.D. Fassett and P.J. Paulsen (1989), Anal. Chem. 61, 643A

[64] L.J. Moore, J.D. Fassett and J.C. Travis (1984), Anal. Chem. 56, 2770

[65] E.C. Apel, J.E. Anderson, R.C. Estler, N.S. Nogar and C.M. Miller (1987), Appl. Opts. 26, 1045

[66] R.J. Walker and J.D. Fassett (1986), Anal. Chem. 58, 2923

[67] M.N. Saha (1920), Philos. Mag. 40, 472

[68] I. Langmuir and J.B. Taylor (1933), Phys. Rev. 44, 423

[69] G.V. Marr (1967), *Photoionization Processes in Gases*, Academic Press Inc. (London) Ltd.1967

[70] J.D. Fassett, L.J. Moore, R.W. Shiedler and J.C. Travis (1984), Anal. Chem. 56, 203

[71] U. Kronert, J. Bonn, H.-J. Kluge, W. Ruster, K. Wallmeroth, P. Peuser and N. Trautmann (1985), Appl. Phys. B 38, 65

[72] G.K. Gerke, B.A. Bushaw and T.J. Whitaker (1988), In *Resonance Ionization Spectroscopy 1988*. Eds. T.B. Lucatorto and J. E. Parks. Inst. Phys. Conf. Ser. No. 94, (1989), p.311

[73] J.A. Holcombe and D.A. Bass (1988), "Atomic Absorption, Atomic Fluoresence, and Flame Emission Spectrometry", Anal. Chem. 60, 226R

[74] R.A. Keller and J.J. Snyder (1986), Laser Focus, March 1986

[75] N. Omenettto (1988), " Analytical characterisation of resonance ioniszation and optogalvanic spectroscopy in atmospheric pressure atomizers", In *Resonance Ionization Spectroscopy 1988*. Eds. T.B. Lucatorto and J. E. Parks. Inst. Phys. Conf. Ser. No. 94, (1989), p.141

[76] O. Axner, I. Magnusson, J. Petersson and S. Sjostrom (1987), Appl. Spectrosc. 41(1), 19

[77] N.F. Ramsey (1956), *Molecular Beams*, Oxford University Press, 1956

[78] G. Bekov, V. Radaev, J. Likonen, R. Zilliacus, I. Auterinen and E.-L. Lakomaa (1987), Anal. Chem. 59, 2472

[79] B.A. Bushaw and G.K. Gerke (1988), In *Resonance Ionization Spectroscopy 1988*. Eds. T.B. Lucatorto and J. E. Parks. Inst. Phys. Conf. Ser. No. 94, (1989), p.277

[80] G.I. Bekov, V.S. Letokhov and V.N. Radaev (1985), J. Opt. Soc. Am. B 2(9), 1554

[81] G.I. Bekov, V.S. Letokhov, V.N. Radaev, D.D. Badyukov and M.A. Nazarov (1988), Nature 332, 146

[82] R. Zilliacus, E.-L. Lakomaa, I. Auterinen and J. Likonen (1988), In *Resonance Ionization Spectroscopy 1988*. Eds. T.B. Lucatorto and J. E. Parks. Inst. Phys. Conf. Ser. No. 94, (1989), p.159

[83] I. Magnusson, O. Axner, I. Lindgren and H. Rubinsztein-Dunlop (1986), Appl. Spect. 40(7), 968

[84] R. Kelly, J.J. Cuomo, P.A. Leary, J.E. Rothenberg, B.E. Braren and C.F. Aliotta (1984), Nucl. Inst. Meth. B 9, (1985), 329

[85] J.E. Rothenberg and R. Kelly (1984), Nucl. Inst. Meth. B 1, 291

[86] R. Kelly and J.E. Rothenberg (1985), Nucl. Inst. Meth. B 7/8, 755

[87] R. Kelly and R.W. Dreyfus (1988), Nucl. Inst. Meth. B 32, 341

[88] E. Denoyer, R. Van Grieken, F. Adams and D.F.S. Natusch (1982), "Laser Microprobe Mass Spectrometry. 1: Basic Principles and Performance Characteristics.", Anal. Chem. 54(1), 26A

[89] D.M. Hercules, R.J. Day, K. Balasanmugam, T.A. Dang and C.P. Li (1982), " Laser Microprobe Mass Spectrometry. 2: Applications to Structural Analysis", Anal. Chem. 54(2), 280A

[90] D.S. Simons (1983), Int. J. Mass Spec. Ion Proc. 55, 15

[91] D.W. Beekman, T.A. Calcott, S.D. Kramer, F.T. Arakawa, G.S. Hurst and E. Nussbaum (1980), Int. J. Mass Spec. Ion Phys. 34, 89

[92] S. Mayo, T.B. Lucatorto and G.G. Luther (1982), Anal. Chem. 54, 553

[93] D.W. Beekman and N. Thonnard (1988), In *Resonance Ionization Spectroscopy 1988*. Eds. T.B. Lucatorto and J. E. Parks. Inst. Phys. Conf. Ser. No. 94, (1989), p.163

[94] M.W. Williams, D.W. Beekman, J.B. Swan and E.T. Arakawa (1984), Anal. Chem. 56, 1348

[95] B. Schueler and R.W. Odom (1987), J. Appl. Phys. 61(9), 4652

[96] A. Benninghoven (1973), Surface Sci. 35, 427

[97] *Ion Formation From Organic Solids*, Ed. A. Benninghoven. Springer-Verlag 1983.

[98] M.T. Robinson (1984), "The Physics of Ion Sputtering", In *Resonance Ionization Spectroscopy 1984*. Eds. G.S. Hurst and M.G. Payne. Inst. Phys. Conf. Ser. No. 71, (1984), p.151

[99] B.J. Garrison and N. Winograd (1982), "Ion Beam Spectroscopy of Solids and Surfaces", Science 216(4548), 805

[100] N. Winograd (1988), "Surface studies using ion beams and MPRI", In *Resonance Ionization Spectroscopy 1988*. Eds. T.B. Lucatorto and J. E. Parks. Inst. Phys. Conf. Ser. No. 94, (1989), p.183

[101] W. Katz and J.G. Newman (1987), "Fundamentals of Secondary Ion Mass Spectrometry", Materials Research Bulletin XII(6), 40

[102] H.W. Werner and P.R. Boudewijn (1984), "A comparison of SIMS with other techniques based on ion-beam solid interactions", Vacuum 34(1/2), 83

[103] *Secondary Ion Mass Spectrometry: Basic Concepts, Instrumental Aspects, Applications*, Eds. A. Benninghoven, F.G. Rudenauer and W.H. Werner. John Wiley and Sons Ltd., England 1987.

[104] F.M. Kimock, J.P. Baxter and N. Winograd (1983), Surface Sci., 124, L41

[105] H. Oechsner, H. Schoof and E. Stumpe (1978), Surface Sci., 76, 343

[106] J.E. Parks, M.T. Spaar, D.W. Beekman, L.J. Moore and P.J. Cressman (1988), In *Resonance Ionization Spectroscopy 1988*. Eds. T.B. Lucatorto and J. E. Parks. Inst. Phys. Conf. Ser. No. 94, (1989), p.197

[107] S.A. Schwarz (1987), J. Vac. Sci. Technol. A 5(3), 308

[108] W.H. Christie and D.E. Goeringer (1986), In *Resonance Ionization Spectroscopy 1986*, Eds. G.S. Hurst and C. Grey Morgan. Inst. Phys. Conf. Ser. No. 84, (1987), p.169

[109] C.E. Young, M.J. Pellin, W.F. Callaway, B. Jorgensen, E.L. Schweitzer and D.M. Gruen (1987), "Laser-Based Secondary Neutral Mass Spectrometry: Useful Yield and Sensitivity", Nucl. Instr. Meth. B 27, 119

[110] F.M. Kimock, J.P. Baxter, D.L. Pappas, P.H. Kobrin and N. Winograd (1984), Anal. Chem. 56, 2782

[111] D.M. Hrubowchak, D.L. Pappas, M.H. Ervin, N.Winograd and L. Mitchell (1988), In *Resonance Ionization Spectroscopy 1988*. Eds. T.B. Lucatorto and J. E. Parks. Inst. Phys. Conf. Ser. No. 94, (1989), p.357

[112] S.W. Downey and R.S. Hozack (1989), to be published in SIMS VII Conference Proceedings. Springer-Verlag 1989.

[113] J.E. Parks, E.H. Taylor, D.W. Beekman and M.T. Spaar (1985), USNRC Report NUREC/CR-4419, 1986

[114] D.L. Donohue, W.H. Christie, D.E. Goeringer and H.S. McKown (1985), Anal. Chem. 57, 1193

[115] J.M.R. Hutchinson, K.W.G. Inn, J.E. Parks, D.W. Beekman, M.T. Spaar and W.M. Fairbank (1987), Nucl. Inst. Meth. B 26, 578

[116] J.E. Parks, D.W. Beekman, L.J. Moore, H.W. Schmitt, M.T. Spaar, E.H. Taylor, J.M.R. Hutchinson and W.M. Fairbank Jr., (1986), In *Resonance Ionization Spectroscopy 1986*, Eds. G.S. Hurst and C. Grey Morgan. Inst. Phys. Conf. Ser. No. 84, (1987), p.157

[117] M.J. Pellin, C.E. Young, W.F. Callaway, J.W. Burnett, B. Jorgensen, E.L. Schweitzer and D.M. Gruen (1987), Nucl. Instr. Meth. B 18, 446

[118] M.A. Rudat and G.H. Morrison (1979), Surface Sci. 82, 549

[119] "The VG9000 Glow Discharge Mass Spectrometer". VG Microtrace, Winsford, Cheshire, United Kingdom.

[120] K.R. Hess and W.W. Harrison (1986), Anal. Chem. 56, 1696

[121] W.R. Garrett, M.A. Moore, R.K. Wunderlich and M.G. Payne (1988), In *Resonance Ionization Spectroscopy 1988*. Eds. T.B. Lucatorto and J. E. Parks. Inst. Phys. Conf. Ser. No. 94, (1989), p.33

[122] J.E. Bayfield and P.M. Koch (1974), Phs. Rev. Lett. 33, 258

[123] C.M. Houston et al (1988), J. Phys. D: Appl. Phys. 21, S59

[124] M.H.C. Smyth et al (1988), In *Resonance Ionization Spectroscopy 1988*. Eds. T.B. Lucatorto and J. E. Parks. Inst. Phys. Conf. Ser. No. 94, (1989), p.73

[125] K.K. Smith and G.E. McGuire (1984), "Analysis Requirements in the Semiconductor Industry", In *Resonance Ionization Spectroscopy 1984*. Eds. G.S. Hurst and M.G. Payne. Inst. Phys. Conf. Ser. No. 71, (1984), p.175

[126] C.J. McLean et al (1988), In *Resonance Ionization Spectroscopy 1988*. Eds. T.B. Lucatorto and J. E. Parks. Inst. Phys. Conf. Ser. No. 94, (1989), p.193

[127] W. Mertz (1981), "The Essential Trace Elements", Science 213, 1332

[128] J. Versieck (1985), "Trace Elements in Human Body Fluids and Tissues", CRC Critical Reviews in Clinical Laboratory Sciences, 22(2), 97

[129] A. Albert (1987), *Xenobiosis: Food, Drugs and Poisons in the Human Body.* Chapman and Hall, London 1987.

[130] K.W.D. Ledingham (1989), Personal communication.

[131] L.J. Moore, J.E. Parks, E.H. Taylor, D.W. Beekman and M.T. Spaar (1986), In *Resonance Ionization Spectroscopy 1986*, Eds. G.S. Hurst and C. Grey Morgan. Inst. Phys. Conf. Ser. No. 84, (1987), p.239

[132] J.D. Fassett, L.J. Powell and L.J. Moore (1984), Anal. Chem. 56, 2228

[133] L.J. Moore, M.T. Spaar, E.H. Taylor, J.E. Parks and D.W. Beekman (1988), In *Resonance Ionization Spectroscopy 1988.* Eds. T.B. Lucatorto and J. E. Parks. Inst. Phys. Conf. Ser. No. 94, (1989), p.273

[134] M.S. Baxter (1983), Marine Pollution Bulletin 14, 126

[135] C.M. Houston (1986), *Laser Ionisation Spectroscopy - Applications in Nuclear Waste Monitoring*, PhD. Thesis, Dept. of Physics and Astronomy , University of Glasgow.

[136] H. Rimke et al (1988), In *Resonance Ionization Spectroscopy 1988.* Eds. T.B. Lucatorto and J. E. Parks. Inst. Phys. Conf. Ser. No. 94, (1989), p.351

[137] S.D. Kramer et al (1986), Nucl. Instr. Meth. B 17, 395

[138] J.J. Snyder, T.B. Lucatorto, P.H. Debenham and S. Geltman (1985), J. Opt. Soc. Am. B 2(9), 1497

[139] G.I. Bekov and V.S. Letokhov (1988), In *Resonance Ionization Spectroscopy 1988.* Eds. T.B. Lucatorto and J. E. Parks. Inst. Phys. Conf. Ser. No. 94, (1989), p.331

[140] B.A. Bushaw (1988), Personal communication

[141] M.S. Burns and D.M. File (1986), J. Microsc. 144(2), 157

[142] L.J. Moore (1986) Personal Communication

[143] X. Jiang and D.L. Smith (1987), Anal. Chem. 59, 2570

[144] G.O. Ramseyer, J.T. Brenna, G.H. Morrison and R. Schwartz (1984), Anal. Chem.56, 402

[145] L.J. Moore, L.A. Machlan, M.O. Lim, A.L. Yergey and J.W. Hansen (1985), Pediatric Research 19(4), 329

[146] W.D. Lehman and M. Kessler (1982), In *Stable Isotopes*, p.649, Eds. H.-L. Schmidt, H. Forstel and K. Heinzinger. Elsevier Scientific Publishing Co., Amsterdam 1982.

[147]W.A. Russell, D.A. Papanastassiou and T.A. Tombrello (1977), Geochimica et Cosmochimica Acta 42, 1075, 1978

[148] T. Lee, W.A. Russell and G.J. Wasserburg (1978), The Astrophysics J. 228, L93, 1979

[149] G.M. Raisbeck and F. Yiou (1979), Nature (Letters) 227, 42

[150] R.E. Taylor (1987), "Dating Techniques in Archaeology and Paleoanthropology", Anal. Chem. 59(4), 317A

[151] P.W. Kubik, D. Elmore, N.J. Conrad, K. Nishiizumi and J.R. Arnold (1986), Nature 319, 568

[152] D. Elmore and F.M. Phillips (1987), "Accelerator Mass Spectrometry for Measurements of Long-Lived Radioisotopes", Science 236, 543

[153] W. Henning et al (1987), Science 236, 725

[154] A. Andl, K. Bekk, S. Goring, A. Hanser, G. Nowicki, H. Rebel, G. Schatz and R.C. Thompson (1982), Phs. Rev. C 26(5), 2194

[155] C.R. Lagergren and J.J. Stoffels (1969), Int. J. Mass Spectrom. Ion Phys., 3, 429, 1970

[156] "Ultra Sensitive Isotope Ratio Mass Spectrometry", (1988). VG Isotopes, Manchester, United Kingdom

[157] W.C. Haxton and G.A. Cowan (1980), Science 210, 897

[158] B. Cleveland and R. Davis Jr. (1984), In *Resonance Ionization Spectroscopy 1984.* Eds. G.S. Hurst and M.G. Payne. Inst. Phys. Conf. Ser. No. 71, (1984), p.241

[159] B.A. Mamyrin, V.I. Karataev, D.V. Shmikk and V.A. Zagulin (1973), Sov. Phys. JETP, 37, 45

[160] W.C. Wiley and I.H. McLaren (1955), Rev. Sci. Instr. 26 (12), 1150

[161] *Advances in TOF-MS*, Ed. J.E. Campana (1987), Anal. Instr. 16 (1)

[162] N.S. Oakey and R.D. Macfarlane (1966), Nucl. Inst. Meth. 49, 220

[163] J.L. Wiza (1979), Nucl. Inst. Meth. 162, 587

[164] D. Rathmann, N. Exeler and B. Willerding (1985), Rev. E: Sci. Instrum. 18, 17

[165] R.J. Cotter (1984), Anal. Chem. 56 (13), 2595

[166] T. Dingle (1988), Personal communication

[167] N.J. Dovichi, D.S. Moore and R.A. Keller (1982), Appl. Opt. 21 (8), 1468

[168] J.R. Nestor (1982), Appl. Opt. 21 (22), 4154

[169] J. Reader, C.H. Corliss, W.L. Wiese and G.A. Martin (1980), N.B.S. publication, NSRDS-NBS 68

[170] B.A. Palmer, R.A. Keller and R. Engleman, Jr. (1980), L.A.N.L. informal report, LA-8251-MS, UC-34a

[171] J.T. Stults, C.A. Myerholtz, B.H. Newcome, C.G. Enke and J.F. Holland (1985), Rev. Sci. Inst. 56, 2267

[172] J.D. Fassett, R.J. Walker, J.C. Travis and F.C. Ruegg (1987), Int. J. Mass Spectrom. Ion Proc. 75, 111

[173] A. Vertes, R. Gijbels and F. Adams (1990), "Diagnostics and modelling of plasma processes in ion sources", Mass Spectrometry Reviews, 9(7), 71

[174] R.J. Conzemius and J.M. Capellen (1980), "A Review of the Applications to Solids of the Laser Ion Source in Mass Spectrometry", Int. J. Mass Spec. Ion Phys. 34, 197

[175] M. Towrie (1986), *Multiphoton Resonace Ionisation - Applications in High Energy Physics*. Ph.D. Thesis, University of Glasgow.

[176] K.W.D. Ledingham et al (1986). In *Resonance Ionization Spectroscopy 1986*, Eds. G.S. Hurst and C. Grey Morgan. Inst. Phys. Conf. Ser. No. 84, (1987), p.289

[177] J.D. Fassett, R.J. Walker, J.C. Travis and F.C. Ruegg (1988), Anal. Instrum. 17(1&2), 69

[178] P.T. McCombes, I.S. Borthwick, R. Jennings, A.P. Land, K.W.D. Ledingham, R.P. Singhal and M. Towrie (1990), Presented as a paper at the SPIE Technical Symposium on Laser Spectroscopy, Los Angeles, January, 1990.

[179] G. Chen and E.S. Yeung (1988), Anal. Chem. 60, 864

[180] J.F. Ready (1971),*Effects of High -Power Laser Radiation*, New York Academic Press.

[181] H. Pang and E.S. Yeung (1989), Anal. Chem. 61, 2546

[182] J.P. Maier (1989), *Ion and Cluster Ion Spectroscopy and Structure*, Elsevier, Amsterdam

[183] V.S. Ban and B.E. Knox (1969), Int. J. Mass Spec. and Ion Phys., 3, 131

[184] C.J. Mclean et al (1990), Int. J. Mass Spec. Ion Proc., 96(1), R1-R7

[185] F.R. Verdun, G. Krier and J.F. Muller (1987), Anal. Chem., 59, 1383

[186] M. Towrie et al (1988), In *Resonance Ionization Spectroscopy 1988*. Eds. T.B. Lucatorto and J. E. Parks. Inst. Phys. Conf. Ser. No. 94, (1989), p.267

[187] J.P. Connerade, M.A. Baig, W.R.S. Garton and G.H. Newsom (1979), Proc. R. Soc. Lond. A371, 295 (1980)

[188] N. Bohr (1923), see G. Wentzel (1923), Phys. Zeits. 24, 106

[189] H.N. Russell and F.A. Saunders (1925), Astrophys. J. 61, 38

[190] H.E. White (1934), *Introduction to Atomic Spectra*, McGraw-Hill Book Co. Inc., New York, 1934

[191] C.E. Moore (1958), *Atomic Energy Levels, Vol. 1*, U.S. Government Publication, NSRDS-NBS Circular 467

[192] G. Risberg (1967), Arkiv. F. Fysik, 37(18), 231 (1968)

[193] S.A. Borgstrom and J.R. Rubbmark (1977), J. Phys. B: Atom Molec. Phys. 10(18), 3607

[194] J.A. Armstrong, P. Esherick and J.J. Wynne (1976),
Phys. Rev. A 15(1), 180, (1977)

[195] J.A. Armstrong, J.J. Wynne and P. Esherick (1978),
J. Opt. Soc. Am. 69(2), 211, (1979)

[198] C.M. Brown, S.G. Tilford and M.L. Ginter (1973), J. Op. Soc. Am. 63(11), 1454

[199] J.J. Wynne (1988), Personal communication

[200] G. Grynberg and B. Cagnac (1977), "Doppler-Free Multiphotonic Spectroscopy",
Rep. Prog. Phys. 40, 791

[201] T.F. Gallagher (1987), "Doubly Excited States", J. Opt. Soc. Am. B 4(5), 794

[202] R.P. Singhal, A.P. Land, K.W.D. Ledingham and M. Towrie (1989),
J. Analytic and Atomic Spec. 7, 599

[203] A.R. Edmonds (1960), *Angular Momentum in Quantum Mechanics*, §3-,
Princeton University Press, New Jersey (1960)

[204] W. Hansen (1983), J.Phys. B: Atom. Mol/ Phys. 16, 2309

[205] A. Corney (1977), *Atomic and Laser Spectroscopy*, Oxford University Press

[206] R.W. Ditchburn and R.D. Hudson (1959), Proc. R. Soc. A 256, 53 (1960)

[207] P. Esherick, J.A. Armstrong, R.W. Dreyfus and J.J. Wynne (1975),
Phys. Rev. Letts. 36(22), 1296 (1976)

[208] D.A. Eastham (1986), *Atomic Physics of Lasers*, Taylor and Francis, London

[209] W.L. Wiese, M.W. Smith and B.M. Miles (1969),
Atomic Transition Probabilities Vol. II, NSRDS-NBS 22

[210] H.W. Messenger (1990), "Solid-State Lasers Tune Into Diverse Applications",
Laser Focus World, 26(6), 69 (June, 1990)

[212] M. Towrie et al (1990), Int. J. Mass Spectrom. Ion Proc., 96(3), 309

[213] A. Andl et al (1982), Phys. Rev. C 26(5), 2194

[214] U. Brinkmann, W. Hartig, H. Telle and H. Walther (1974), Appl. Phys. 5, 109

[215] L.W. Green and F.C. Sopchyshyn (1988),
Int. J. Mass Spec. and Ion Proc. 89, 81 (1989)

[216] L.C. Balling and J.J. Wright (1976), Appl. Phys. Letts. 29(7), 411

[217] R.T. Hofmann and D.O. Harris (1986), J. Chem. Phys. 85(7), 3749

[218] K. Sakurai and H.P. Broida (1976), J. Chem. Phys. 65, 1138

[219] E. A. Rohlfing, D.M. Cox and A. Kaldor (1984), J. Chem. Phys. 81(7), 3322

[220] H.W. Kroto, J.R. Heath, S.C. O'Brien, R.F. Curl and R.E. Smalley (1985),
Nature (Letters), 318, 162

[221] G.K. Woodgate (1980), *Elementary Atomic Structure*, 2nd Edition,
Oxford University Press

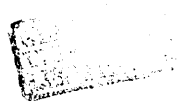

[222] W. Demtroder (1981), *Laser Spectroscopy*, Springer-Verlag, Berlin

[223] M. Goppert-Mayer (1931), Ann. Phys. Lpz. 9, 273

[224] N. Melikechi and L. Allen (1986), J. Opt. Soc. Am. B 3, 41

[225] K.D. Bonin and T.J. McIlrath (1984), J. Opt. Soc. Am. B 1, 52

[227] J. R. Ackerhalt and J.R. Eberly (1976), Phys. Rev. A 14, 1705

[228] J.R. Ackerhalt and B.W. Shore (1977), Phys. Rev. A 16, 277

[229] D.S. Zakheim and P.M. Johnson (1979), Chem. Phys. 46, 263

[230] C.M. Miller and N.S. Nogar (1983), Anal. Chem. 55, 481

[231] G.I. Bekov, V.S. Letokhov, O.I. Matveev and V.I. Mishin (1978), Opt. Lett. 3, 159

[232] J.A.C. Gallas, G. Leuchs, H. Walther and H. Figger (1985), "Rydberg Atoms: High-Resolution Spectroscopy and Radiation Interaction-Rydberg Molecules", Adv. At. Mol. Phys.(Ed. D. Bates), 20

[233] N.S. Nogar and R.A. Keller (1985), Anal. Chem. 57, 2992

[234] G.I. Bekov, E.P. Viablova-Angelova, L.N. Ivanov, V.S. Letokhov and V.I. Mishin (1980), Opt. Comm. 35, 194

[235] H. Rimke et al (1986), In *Resonance Ionization Spectroscopy 1986*, Eds. G.S. Hurst and C. Grey Morgan. Inst. Phys. Conf. Ser. No. 84, (1987), p.235

[236] A. Marshall, A. Clark, R. Jennings, K.W.D. Ledingham, R.P. Singhal and C.J. McLean (1990), Submitted to *Resonance Ionization Spectroscopy 1990.*

[237] R.P. Singhal, S.L.T. Drysdale, R. Jennings, A.P. Land, K.W.D. Ledingham, P.T. McCombes and M. Towrie (1990), Submitted to J. Phys. B: Atom Molec. Phys.

[238] S.C. O'Brien, J.R. Heath, R.F. Curl and R.E. Smalley (1988), J. Chem. Phys. 88, 220

[239] L. Wang, I.S. Borthwick, R. Jennings, P.T. McCombes, K.W.D. Ledingham, R.P. Singhal and C.J. McLean (1990), Submitted to *Resonance Ionization Spectroscopy 1990.*

[240] K.W.D. Ledingham and R.P. Singhal (1990), Submitted to J. Anal. Atom. Spectrosc.